Phase-field study of transient stages and fluctuations in solidification

Raúl Benítez Iglesias

Departament de Física Aplicada
Universitat Politècnica de Catalunya

A mi padre, y a
su nieta Clàudia.

Phase-field study of transient stages and fluctuations in solidification,

a thesis dissertation by

Raúl Benítez Iglesias

and supervised by

Laureano Ramírez de la Piscina

in partial fullfilment of the requirements for the degree of *Doctor en Ciències* in the doctoral program *Física Aplicada i Simulació en Ciències* of the Applied Physics Department at the Universitat Politècnica de Catalunya.

Barcelona, January 2005

Agradecimientos/Agraïments

Una vez superado el miedo a dejarse a alguien en el tintero, uno se percata de que lo auténticamente difícil de la sección de agradecimientos es el saber dar cuenta de los intersticios emocionales asociados a cada persona. En ese sentido, vaya por delante que tanto quienes aparecen a continuación como los que haya podido olvidar merecerían por mi parte varias páginas de sincera gratitud.

El primer agradecimiento es para mis padres, porque gracias a ellos he podido recorrer el incierto camino educativo y emocional que separa los cuadernos Rubio de las ecuaciones integrales.

En segundo lugar quiero agradecerle a Laure, mi director de tesis y amigo, el haberme llevado a visitar algunos de los rincones más interesantes del mundo de la física y del jazz.

A mis compañeros del Grupo de Sistemas Fuera del Equilibrio (Angelina, Anna, Blas, Carlota, Enric, Esteban, Inma, José, Pere, Víctor), el ser mi familia científica en Barcelona.

A en Jaume, per donar-me l'oportunitat de col·laborar amb ell i amb el professor L. Kramer a Bayreuth, i per haver-me posat posteriorment en contacte amb el grup d'en Laure.

Als companys de docència del Departament d'Electrònica de l'Escola Industrial (Alfonso, Beatriz, Fèlix, Francisco, Guillermo, Herminio, Javier E., Javier G., Joan D., Joan P., Jordi, José Luis, Josep María, Juan, Manolo, Manuel, Pablo), dels quals he après que l'art d'ensenyar requereix de grans dosis d'enginy, treball i honestedat intel·lectual.

Als companys del Departament d'Informàtica de l'Escola Industrial (Ferran, Gerard, Jesús, Jordi, Pedro, Samir, Sebas, Toni), per ser tant bons col·legues de feina i de penúries acadèmico-docents.

También a varios profesores de la Facultad de Física (Aurora, Esther, Francesc, Jordi, José María), porque constituyen una parte esencial del tejido intelectual que nutre la Diagonal barcelonesa de ciencia.

Al Pep, a la Montse, i a tots els companys del Departament d'Enginyeria de Sistemes, Automàtica i Informàtica Industrial, que han tolerat l'esquizofrènia interdisciplinar en la què m'he vist immers durant els últims anys.

A mis compañeros de departamento de Física Aplicada (Amador, David, Enric, Josep, Ricard), con los que he disfrutado y disfruto de memorables comidas QC y veladas HB.

A Enrique y Jose, así como al resto de mis compañeros de estudios en la Facultad de Física de la Universitat de Barcelona (Albert, Enric, Javi, Joan Manel, Miquel, Narciso, Pepe, Roger, Sandra, Toni, Valentín, Berto, Pascual, Arantxa, Yolanda), por haberme enseñado a estudiar con nocturnidad y alevosía.

A mis compañeros de estudios (Chus, Javi, Jose, Pep, Ramón), con los que he compartido mucho más que pisos, fiestas y libros de Bernini.

A mis amigos de la infancia (Amaya, Javier, José Luis, Josep Maria, Juan Manuel), a los que considero simples extensiones multidisciplinares de mi persona.

A mis hermanos (Letizia, José Luis, Iván), les agredezco el simple hecho de existir, porque no soy capaz de imaginar un mundo sin ellos.

A Pepita i Toni, l'una per la seva bondat infinita, l'altre per ser l'únic exemplar d'home renaixentista del segle vint-i-ú.

A Javier, por aportar una necesaria serenidad en el ámbito familiar.

Al personal d'administració i serveis (Esther, Fernando, Juan, Roser, Sílvia), sense els quals la universitat seria una joguina inoperant.

Per finalitzar, vull agrair-li molt especialment a la Meri tot el seu recolzament, perquè ha cregut en mí més que ningú i perquè ha sigut i és el meu cor, el meu cap i, en definitiva, la meva vida.

Acknowledgments

I would like to thank Lorenz Kramer and the people from the Physikalishes Institut at the Universität Bayreuth (Peter, Jürgen, Anke, Hong, Axel), for giving me the possibility of entering in the scientific research trough the world of pattern-forming systems.

I am also very grateful to Nigel Goldenfeld and his colleagues at the Physics Department of the University of Chicago in Urbana-Champaign (Y-Tae Kim, D. Ceperley, J. Dantzig), for suggesting me so many interesting research topics and for revealing me the excellences of the North American science.

I would also thank to Gabriel Faivre at the Group de Physique des Solides at the Pierre et Marie Curie-Denis Diderot University in Paris, for showing me the large amount of scientific knowledge which is necessary in order to carry out a good experiment in physics.

I also thank to my friends from Bayreuth (Aitor, Anna, Giuliano, María, Pascaline, Wolfgang, und so weiter), because they have shared with me some of the nicest moments of my life.

I am also very grateful to the friends I met during my stay in Urbana-Champaign (Amaya, David, José María), because my feelings haven't gone with the wind.

Resum en català

Motivació

Aquesta tesi doctoral té per objectiu l'estudi dels processos interfacials que es produeixen durant l'avanç d'un front de solidificació. El creixement d'un cristall és un procés dinàmic que succeeix en condicions termodinàmiques de no-equilibri. Anomenem processos interfacials a les deformacions morfològiques de la interfase de separació entre les fases sòlida i líquida. Durant un procés de cristal·lització, aquestes deformacions evolucionen de forma complexa i acaben donant lloc a estructures tan familiars com els flocs de neu.

Però la formació d'estructures en sistemes fora de l'equilibri no és un fenomen restringit a processos físics, sinó que també s'ha observat en sistemes químics, òptics o biològics. Desde el punt de vista científic, aquests problemes tenen un interès bàsic perquè tots els casos, independentment de la naturalesa del sistema, comparteixen una sèrie de característiques comunes. Aquesta universalitat recorda d'alguna forma a la que s'observa en els processos de transformació de fases, en els que el canvi de fase es produeix per un cert valor crític d'una variable termodinàmica com ara la temperatura o la pressió. D'una forma similar, els patrons que apareixen en sistemes fora de l'equilibri s'observen a partir d'un cert valor de la variable de control amb la que allunyem el sistema de l'equilibri. En el cas particular dels processos de solidificació, el creixement d'estructures dendrítiques com les de la Figura 1.3 s'observa a partir d'un cert valor del refredament del sistema per sota de la seva temperatura de cristal·lització. En uns altres règims, també es poden observar uns altres tipus d'estructures interfacials, com ara patrons cel·lulars que apareixen a la Figura 1.4.

Existeixen diverses maneres de caracteritzar les deformacions que pateix la interfase, i gairebé totes fan referència a l'amplitud de la deformació i a la separació entre les seves protuberàncies. Aquesta forma de caracteritzar el problema obre la possibilitat de fer-se la pregunta següent: Donada una determinada substància (posem per cas, l'aigua), i unes certes condicions de cristal·lització (p.e., mantenint la temperatura constant a -15^oC), podem saber quina és la forma precisa que tindrà la interfase uns minuts després d'haver-se iniciat el procés de solidificació?.

Qualsevol que observi detingudament la figura 1.3, se n'adonarà que la forma de la interfase és força complicada. De fet, l'aparició de complexes deformacions laterals (anomenades *sidebranches*) fa inviable qualsevol intent de solució del problema en termes determinístics. L'origen d'aquesta impredictibilitat es troba en les propietats microscòpiques del sistema: El moviment aleatori de les molècules del material produeix fluctuacions termodinàmiques que pertorben la interfase. Inicialment, aquestes pertorbacions són molt petites i la interfase no manifesta cap alteració morfològica. Aleshores, a mesura que el sòlid avança i depenent de les condicions de cristal·lització, pot arribar un moment en el que el sistema es torni inestable sota algunes de les pertorbacions. En aquest moment, les deformacions microscòpiques començaran a crèixer ràpidament, fent que la seva amplitud

s'incrementi en uns quants ordes de magnitud. Aquest procés d'amplificació és el que provoca que es formin les estructures dendrítiques que s'observen amb un microscopi.

Arribats a aquest punt, si volem continuar, necessitem una forma de conèixer les fluctuacions termodinàmiques del sistema. La forma més habitual és fer servir l'anomenat *teorema de fluctuació-dissipació*, que va ser deduït per Einstein en les seves investigacions sobre el moviment de les partícules brownianes. Aquest teorema estableix una relació directa entre els coeficients de transport del material i les seves fluctuacions microscòpiques, de forma que només haurem de conèixer propietats com ara el coeficient de difusió per determinar la magnitud del soroll. Una vegada conegudes les característiques de les fluctuacions, podem reformular la nostra primera pregunta:

Així doncs, assumint el caràcter estocàstic del problema, i per tant que no podrem determinar la forma exacta de la interfase, podem dir alguna cosa sobre l'amplitud i espaiat de les deformacions?. Aquest és el que s'anomena *problema de la selecció*, i actualment constitueix un nucli important d'activitat de recerca en l'àmbit teòric i experimental. Problemes de selecció n'hi ha tants com sistemes que presentin formació d'estructures fora de l'equilibri, i en cada cas els mecanismes que donen lloc a una estructura i no a un altra dependran, en general, dels detalls de cada sistema. En el fons, el fet que no poguèssim determinar el comportament del sistema no només és per causa del soroll, sinó que gran part de la responsabilitat recau en el fet que el sistema es trobi fora de l'equilibri. I és que, en general, no hi ha cap llei universal que determini la dinàmica d'evolució dels sistemes de no-equilibri.

La solidificació direccional és un procés metal.úrgic que permet controlar l'avanç del front de solidificació en aliatges binaris. En aquest cas, la solidificació es produeix com a conseqüència del rebuig de partícules de solut per part de la fase sòlida a mesura que el front avança. Per tal de controlar el procés, la mostra amb la solució binària es mou amb una velocitat constant vers la zona freda d'un gradient extern de temperatura que es manté constant. Aquesta situació es descriu a la figura 3.3 de la memòria. A mesura que la substància s'endinsa al gradient, la zona de la mostra que es troba a temperatures inferiors a la de solidificació es va fent més gran i, com a conseqüència, es produeix l'avanç del front.

Depenent de la velocitat amb la que es realitzi aquest procés, el front de solidificació presentarà l'aparició de interstabilitats morfològiques. S'observa que a partir d'un valor crític de la velocitat d'empenta, la interfase es torna inestable i presenta diferents tipus de deformacions. A mesura que augmentem la velocitat d'empenta, les deformacions interfacials es fan més pronunciades i poden arribar a donar lloc a estructures periòdiques de dendrites (*dendritic arrays*).

Metodologia

Potser no hi ha cap llei universal respecte a la seva dinàmica, però sí disposem d'un coneixement força acurat dels mecanismes físics que intervenen en els processos de

solidificació. He dedicat el **capítol 2** a donar una breu descripció dels que són més rellevants. Part dels mecanismes s'expliquen desde la termodinàmica de l'equilibri, mentre que uns altres fan referència a fenomens com ara la capił.laritat o la difusió del calor i de partícules al sistema.

El problema pot ser llavors formulat en termes d'aquests fenomens físics, donant lloc a un sistema d'equacions metemàtiques anomenat *problema de contorn mòbil*, que es discuteix amb més detall al **capítol 3** de la tesi. Els problemes de contorn mòbil consisteixen en equacions en derivades parcials que descriuen la difusió de calor i massa en les dues fases del sistema. Aquestes equacions són complementades per condicions de contorn que s'han de complir a la interfase, com ara que la quantitat d'energia o massa que es transfereixi entre les dues fases es mantingui en equilibri. El fet d'haver d'imposar condicions de contorn a la interfase mòbil presenta una clara dificultat: Per una banda, primer hem de resoldre totes les equacions per determinar la posició del front; per un altra, necessitem un coneixement previ de la posició de la interfase per tal de poder imposar les condicions de contorn i per tant per poder trobar una solució del sistema. El tractament analític d'aquest tipus de problemes només es pot dur a terme aplicant hipòtesis que simplifiquin el problema. Alguns dels procediments teòrics en relació als transitoris (*boundary integral methods*) i a les fluctuacions (*Warren-Langer theory*) es presenten al **capítol 4**. En general, si volem estudiar el comportament dinàmic del sistema, haurem de recòrrer a tècniques numèriques que solucionin les equacions diferencials acoblades del problema. Aquests procediments permeten simular la evolució de la interfase, però requereixen de la utilització d'uns algorismes de seguiment de la interfase (*front tracking algorithms)* que suposen un cost computacional força elevat. Malgrat que en aplicacions dins l'àmbit de l'enginyeria de materials aquests mètodes són sovint utilitzats, en situacions interfacials complexes com la que apareix a la figura 1.3 resulta més adient fer servir un altre tipus de descripció del sistema.

Els models de camp de fase (*phase-field models*) són una d'aquestes possibles descripcions, i consisteixen en un conjunt d'equacions diferencials que descriuen la dinàmica d'un camp continu $\phi(\mathbf{r}, t)$ acoblat a les equacions de difusió a les dues fases. El camp ϕ s'anomena camp de fase i assoleix valors constants a cadascuna de les fases, de forma que permet definir la posició de la interfase tan sols mirant en quins punts de l'espai pren un valor intermedi determinat. Com que la posició de la interfase vindrà determinada per l'evolució del camp ϕ, aquest procediment ens estalvia haver d'imposar les condicions de contorn mòbil i per tant evita la utilització d'algorismes de seguiment de la interfase. Durant els últims vint anys, els models de camp de fase s'han establert com una eina molt potent per estudiar sistemes interfacials complexos. La seva aplicació no només s'ha realitzat en el context de la solidificació, sinó també en uns altres àmbits com ara en la propagació de cracks en materials o en la dinàmica de membranes biològiques. Al **capítol 5** es deriven les equacions dels models de cap de fase per als processos de solidificació més habituals.

Resultats

Els resultats d'aquesta tesi poden dividir-se en dues seccions: La primera és de caràcter teòric i fa referència a la introducció de fluctuacions en models de camp de fase. En aquesta primera part, el resultat fonamental ha sigut el desenvolupament d'un mètode que permet d'incloure tant les fluctuacions termodinàmiques internes com les possibles pertorbacions incontrolades que puguin ser presents en el sistema experimental (impureses en la mostra, irregularitats en la superfície de contacte, etc). La incorporació de fluctuacions termodinàmiques en models de camp de fase ja s'havia realitzat prèviament, però la validesa del procediment quedava restringida a models simplificats amb els que no es podien obtenir resultats quantitatius. El nostre procediment, que es fonamenta en un anàlisi pertorbatiu asimptòtic (*hybrid asymptotic expasion*), es pot aplicar en qualsevol model i amb qualsevol font de soroll, i en aquest sentit permet la possibilitat de tractar el problema de la selecció amb aquestes tècniques. Els detalls del procediment i la comprovació de la seva validesa es descriuen al **capítol 6** de la tesi.

El segon bloc de resultats consisteix en estudis amb models de camp de fase de la dinàmica de transitoris i fluctuacions en processos de solidificació. En primer lloc, els resultats obtinguts amb els models de camp de fase es comparen amb prediccions analítiques derivades dels problemes de contorn mòbil. Els resultats es descriuen al **capítol 7**, on s'hi estudia la posició del front durant el transitori, així com la evolució dels perfils de concentració de solut en les dues fases. La segona part, la dels resultats numèrics, correspon als continguts del **capítol 8** i es dedica a l'estudi del problema de seleció en solidificació direccional. Per això s'hi analitza la estabilitat morfològica de la interfase durant el transitori, i es compara els resultats amb la predicció teòrica de la teoria proposada per Warren i Langer. Amb un anàlisi espectral de la dinàmica d'amplificació del soroll, es determina el temps de transició (*crossover time*), així com la longitud d'ona de la primera inestabilitat interfacial amb una amplitud observable. La part final de la tesi té per objectiu presentar resultats sobre l'evolució de la inestabilitat en el règim no-lineal, en el que estructures interfacials esdevenen complexes. Per finalitzar, al **capítol 9** es fa un breu resum dels resultats assolits en aquesta tesi, i es comenten les línies de recerca que segueixen obertes i que seran objecte de les nostres investigacions en el futur.

Contents

Chapter 1

Introduction

1.1 Pattern-forming systems

Under non-equilibrium conditions, some systems present the spontaneous apparition of spatio-temporal patterns [Cross93]. These *pattern-forming phenomena* have been observed in as diverse scenarios as hydrodynamics [Busse84, Buka96], solidification [Langer80b], nonlinear optics [Moloney92], chemical systems [Field85] or biology [Koch94, Murray02, Murray03]. When a pattern-forming system is driven out from equilibrium in a controlled way, it eventually becomes unstable under infinitesimal perturbations with a defined wave-vector q and frequency ω. If M is the control parameter used to drive the system away from equilibrium, this loose of stability occurs at a certain critical value $M = M_c$. The apparition of the instability introduces new space and time scales which are in general not related with the microscopical details of the particular system. If we continue increasing M a bit further, a well-defined pattern structure with wave-vector q and frequency ω will appear in the system. Although the mechanism of the instability depends on the particular details of the system, the pattern structure can often be described by means of q, ω and the relative distance to the instability threshold $\varepsilon = (M - M_c)/M_c$. This independence from the microscopical details of the system allows to stablish some equivalences between the pattern formation and a phase transition process [Haken75]. One possible way of classifying the pattern-forming instabilities is to distinguish between interfacial and bulk instabilities. *Bulk instabilities* affect to the system as a whole, whereas *interfacial or morphological instabilities* destabilize a front separating two different regions of the system (solid/liquid in solidification processes, nematic/smectic in liquid crystals, etc.). The main essential difference between bulk and interfacial patterns is perhaps the singular effect which plays the surface tension in the case of morphological instabilities.

Pattern-forming structures can also be classified in *spatially extended stationary patterns* ($q \neq 0$, $\omega = 0$) like the rolls observed in Rayleigh-Bénard convection

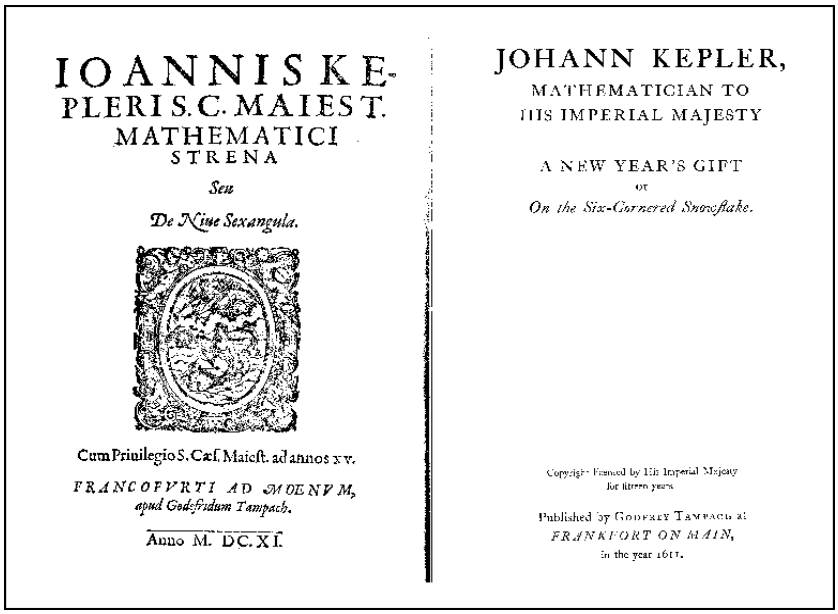

IOANNIS KE-
PLERI S.C. MAIEST.
MATHEMATICI
STRENA
Seu
De Nive Sexangula.

Cum Priuilegio S. Cæs. Maiest. ad annos XV.

FRANCOFVRTI AD MOENVM,
apud Godefridum Tampach.

Anno M. DC. XI.

JOHANN KEPLER,
MATHEMATICIAN TO
HIS IMPERIAL MAJESTY

A NEW YEAR'S GIFT
OR
On the Six-Cornered Snowflake.

Copyright Granted by His Imperial Majesty
for fifteen years

Published by GODFREY TAMPACH at
FRANKFORT ON MAIN,
in the year 1611.

Figure 1.1: Front page of the Johannes Kepler's *On the six-cornered snowflake* (De nive sexangula, 1611). In this work, Kepler asserts that behind the symmetric shape of a snowflake there is a basic, universal mechanism. It has taken four centuries of scientific thought to confirm his amazing neo-platonic intuition.

(see Fig.1.2), *oscillatory homogeneous* ($q = 0$, $\omega \neq 0$) as the Besulov-Zhabotinshky chemical reaction and *spatio-temporal structures* ($q \neq 0$, $\omega \neq 0$) like non-linear traveling waves in excitable media or the growth of a dendrite. For even larger values of the control parameter, some defects will appear in the pattern and the system will finally enter in a highly non-linear regime presenting a turbulent or chaotic behavior.

Non-equilibrium instabilities have been traditionally studied by using techniques which were already well established for the study of equilibrium phase transitions. Almost all of these approaches come from the critical dynamics field, and have been adapted to account for the universal properties of the system around the instability point. In order to study the different relevant aspects of pattern-forming systems, there are different methodological approaches and levels of description:

- The *microscopic* approach describes the evolution of the system in terms of the microscopic properties of its basic constitutive elements or particles. The microscopic dynamics is determined by a Hamiltonian which accounts for

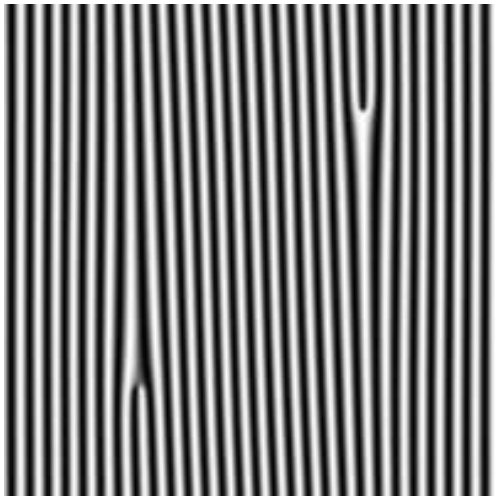

Figure 1.2: Topological defects in a convective roll pattern.

the particle interactions, and the probability distribution of the macroscopic states can be obtained by using standard statistical mechanics techniques. The system evolution can be numerically obtained by means of molecular dynamics or Monte-Carlo simulations. In pattern-formation, the molecular dynamics approach are mostly used either to determine some physical parameters which are difficult to determine experimentally (for instance, kinetic coefficient in solidification [Bragard02]) or when the macroscopic description of the system is not fully understood (Flame/crack propagation, etc.).

- *Phenomenological equations* provide a macroscopic description of the system in terms of kinetic processes (diffusion, convection, advection, chemical reaction) and conservation laws (conservation of mass, energy, momentum, etc.). In this level of description we have for instance the Navier-Stokes equations for hydrodynamic systems, the Maxwell-Bloch Equations in non-linear optics, the sharp-interface equations for solidification processes or the reaction rates in chemical reaction-diffusion systems. These constitutive equations usually take the form a non-linear set of partial differential equations, and few analytical or numerical work can be done in complex regimes where the instabilities are fully developed. We include in this level of description approaches like the Swift-Hohenberg equations, which are a simplified version of the phenomenological equations (Navier-Stokes) presenting the same linear instabilities under some restricted conditions.

- *Amplitude equations* can be used to describe the system near the critical point at which the instability occurs ($M \approx M_c$). They describe small spatio-

temporal modulations from the basic pattern by means of amplitude $|A|$ and phase ϕ variables which determine the amplitude of the pattern structure and the phase shift with respect with its basic periodicity. Amplitude equations are then constructed from the symmetry properties of the pattern without considering the details of the physical system. The details of the system are only reflected in the value of the amplitude equations parameters, which are determined by using singular perturbation techniques [Bender99]. In turn of the difficulty in determining the parameters, the equations can be easily simulated and allow to explore different ranges of the system parameters. The paradigmatic example of amplitude equations are the real and complex Ginzburg-Landau equations [Aranson02], which have been extensively used to study convection rolls in Rayleigh-Bénard convection or electrohydroconvection patterns in nematic liquid crystals [Buka96].

- *Phase equations* are similar to amplitude equations but only describe the phase shifts of long wavelength perturbations [Pomeau79]. The main idea is that the phase-shift $\delta\phi$ produced by a long wavelength perturbation ($\delta q \ll 1$) relaxes much slowly than the amplitude of the pattern $|A|$. Their validity is not necessary restricted to the vicinity of the instability threshold and the equations also reflect the basic symmetries of the pattern structure.

- *Field theories*: In some cases as crystal growth, nucleation or spinodal decomposition, an interfacial pattern is created by means of a first-order phase transition which separates two different phases of the system (solid/liquid, solute/solvent, α/β crystallographic structures, etc). In such situations, the non-equilibrium system can be described by means of a coarse-grained field ϕ which labels the two different phases and whose dynamics is determined by a free-energy functional $\mathcal{F}(\phi)$. The free-energy functional $\mathcal{F}$ is constructed in order to recover the equilibrium properties of the system, and its minima are associated with the two phases as stable states of the equilibrium system. This procedure was proposed in the context of dynamic critical phenomena [Hohenberg77], and provides a powerful description of the system whose validity is not necessarily restricted to the instability onset. In fact, this approach can also be used in systems presenting a second-order phase transition and even in heterogeneous systems where the two phases are different but no phase transition occurs like in Viscous Fingering or in Hele-Shaw cells. In this family of models we have the reaction-diffusion equations, Phase-Field methods, etc.

- *Bifurcation theory* uses the qualitative theory of differential equations to determine the universal properties of the system near the instability point, allowing to classify the different instabilities from the geometrical and topological universal properties of the system equations [Guckenheimer83]. This approach can be equally applied to the equations describing the system at different levels as to phenomenological equations or to amplitude equations.

One of the most important problems in pattern-forming systems is to understand the mechanisms by which the system selects a certain preferred wavelength and not other. In equilibrium systems, the selection of one phase is determined by the minimization of a thermodynamical free energy density. Under non-equilibrium conditions, however, there is no general variational principle which can be used in order to determine the selected properties of the system. This leads to the conclusion that there is no general selection mechanism, and that therefore every particular system will determine the final wavelength of the pattern depending on its particular properties. We can classify the different selection mechanisms by using some well defined scenarios:

- *Selection by boundary conditions*: The wavelength of the pattern is selected to be a integer fraction of the size of the system so that the periodic structure satisfies the boundary conditions of the system. This happens, for instance, in some bounded hydrodynamic instabilities such as Rayleigh-Benard convection.

- *Selection from a variational principle*: Extending the optimization principles which describe the dynamics of equilibrium systems (Lagrangian in mechanical systems, Gibb's free energy in equilibrium thermodynamics, etc.), it can be supposed that non-equilibrium systems select their wavelength by minimizing some generic magnitude or generalized action. Although variational descriptions of non-equilibrium systems have been demonstrated to be a very powerful techniques (Ginzburg-Landau, Swift-Hohenberg, Lyapunov function, etc.), nature usually behaves in a non-variational way.

- *Selection by noise amplification*: Pattern-forming systems are subjected to both internal thermodynamical fluctuations and to uncontrolled external perturbations. These stochastic forces might produce transitions between different stable states of the system, therefore selecting the features of the global pattern. Besides, small noise amplitudes present at microscopic scales can be amplified by a non-linear selection mechanism which, in combination with the probability distribution of the fluctuations, might determine the selected instability.

- *Dynamical selection from the initial conditions*: Many pattern-forming systems present a continuum range of stable stationary states. It might happen, however, that not all the stable states are dynamically accessible from a given choice of the initial conditions. This is for instance the case of the selection of the finger width in a Hele-Shaw cell. The main conclusion is that the surface tension acts as a singular perturbation, in the sense that even a infinitesimal amount of surface energy produces that the system selects a wavelength.

1.2 Pattern formation in solidification

During a solidification process, the solid-liquid interface can present a large variety of complex interfacial patterns [Langer80b, Langer87, Langer86, Boettinger00]. The most common phenomena are the apparition of cellular or dendritic structures, nucleation of phases, the creation of grain boundaries or the apparition of solute bands. These microstructures usually appear at length scales of the order of about 10 μm and determine the final mechanical and electrical properties of a manufactured material. Besides the technological applications for the characterization of processing materials, the study of the physical mechanisms underlying the formation of such microstructures has a fundamental interest. In order to fully understand the physics of a solidification process it is necessary to consider the interplay of three physical phenomena which appear at different physical scales:

- The *diffusion* of heat in pure systems and of solute particles in binary alloys are the processes which drive the motion of the solidification front. As we will see in Section 2.2, heat or mass diffusion are non-equilibrium kinetic processes by which the system minimizes its Gibbs' free energy. From the point of view of the morphological stability of the interface, this diffusion process acts as a destabilization force which tends to amplify small perturbations of the solid-liquid interface (cf. Sec. 3.3.4). Diffusion effects define a diffusion length scale of $\tilde{l} = \tilde{D}/\tilde{v}$, being $\tilde{D}$ the thermal/solutal diffusivity of the liquid phase and $\tilde{v}$ the front velocity or growth rate. For typical growth velocities of $\tilde{v} \sim 1$ μm/s, we have $\tilde{l} \sim 10$ cm for thermally driven fronts and $\tilde{l} \sim 1$ mm for alloy solidification processes.

- *Capillary effects* are due to the surface energy of the solid-liquid interface and act as a stabilization force for the interface deformations (cf. Sec. 3.3.4). As the surface energy is an anisotropic magnitude, the growth of unstable branches is directly related with the crystallographic properties of the solidified phase, giving rise to the six-cornered shape of the snowflake structures. Capillarity effects define a microscopic length scale which is of the order of $\tilde{d}_0^T = 1$ nm for pure systems and of $\tilde{\tilde{d}}_0 = 10$ nm for binary alloys. Although capillary effects appear in a microscopic scale, they have a macroscopic effect in the deformations of the solidification front. The reason is that they prevent the formation of cusped shapes associated with short wavelength perturbations, acting as a low-pass filter for the morphological modulations of the front.

- *Kinetic attachment* phenomena describe how the solute particles attach from the liquid phase to the crystalline structure of the solid phase. Kinetic effects become more important for large growth rates and, like the surface tension effects, might present an anisotropic behavior.

The interaction between these three physical processes produce a complex non-linear, non-local dynamics which is responsible of the morphological evolution of

the solidification front. In controlled solidification processes such as directional solidification, an *externally imposed thermal gradient* allows to control the advance of the front. The thermal gradient acts as a stabilizing force of the system and introduces an additional scale in the problem $\tilde{l}_T$ (thermal length) which, for typical values of the external gradient ($\tilde{G} \sim 10^3$ K/m) and of the sample solute concentration ($c_\infty \sim 10^{-2}$ mol), is of the order of $\tilde{l}_T \sim 10$ mm.
Besides the diffusion mechanism, the amount of heat and solute ahead of the front can be altered by convection flows which might be present in the liquid phase. These *convective effects* can eventually modify the stability conditions and even create new flow-induced instabilities [Davis01, Büeler98].

1.2.1 Dendritic growth

The formation of a growing dendrite is one of the most elegant and surprising pattern-forming systems in nature. For a long time, scientists have been studying the question of how such a complex structure can arise from a simple system like an undercooled pure melt. Dendrites constitute a suitable example of nature's complexity, combining the deterministic features of its six-folded shape with complex sidebranching structures. Dendrites can also form in alloy materials which solidify under the effect of small concentration gradients. For a general review on dendrite growth, we refer to Ref. [Glicksman93, Langer87]. The main physical problem concerning dendritic growth is to determine the selected shape and velocity of the growing dendrite for a given thermal undercooling. Ivantsov [Ivantsov47] was the first in obtaining a relation between the tip radius of the dendrite and the undercooling of the melt. Assuming that the interface at the tip was isothermal, and neglecting capillary effects, he approximated the steady-state shape of the dendrite tip by a paraboloid of revolution. The Ivantsov's theory, however, did not allow to determine the tip radius and velocity of the dendrite separately, but rather a product of this two quantities. This product was determined as a function of the thermal undercooling of the system, and could therefore be determined for a given set of solidification conditions. The validity of the Ivantsov's solution was experimentally confirmed by Huang and Glicksman in Refs. [Huang81a, Huang81b]. In these experimental investigations, the tip radius and velocity were measured independently, and that induced an important theoretical effort with the aim in understanding the selection mechanisms. These efforts [Langer87, Temkin60, Trivedi70] led to the *microscopical solvability theory* [Ben-Jacob84, Kessler85], which incorporated surface tension and anisotropy effects. Later on, this theory has been extended to three dimensions [Amar93] and gives a quantitative description of non-steady stages.

1.2.2 Cellular and dendritic arrays in directional solidification

In a directional solidification process, a binary mixture sample is pulled with a constant velocity through a fixed temperature gradient. Under fixed conditions

Figure 1.3: Dendritic growth and formation of sidebranches in a needle-crystal structure (Courtesy of Prof. Ken Libbrecht, Physics Dept., Caltech, Pasadena, USA).

of sample concentration and external gradient, the initially planar solid-liquid interface undergoes a planar to cellular morphological transition as the pulling velocity increases. For even larger growth rates, the cellular pattern enters in a highly non-linear regime giving rise to a complex dendritic array structure. The morphological stability of a planar interface was first studied by Mullins and Sekerka under a steady-state assumption [Mullins63]. By performing a linear stability analysis, they found an expression for the growth rate of the morphological perturbations. The Mullins-Sekerka instability predicted the instability wavelength of a steady-state planar interface. The wavelength of the instability, however, it is not selected when the planar front has reached its stationary state but during the initial solute redistribution transient [Trivedi85]. In order to account for these transients, Warren and Langer [Warren90, Warren93] proposed a linear stability analysis of the non-steady concentration profile and predicted rather different wavelengths than the steady-state theory. Recent investigations [Losert98a, Losert98b] have shown a quantitative agreement between the Warren and Langer predictions of the selected wavelength and the experimental observations. During the last decade, a large amount of theoretical work has been dedicated to the wavelength selection problem of the cellular structure [Kerszberg83a, Kerszberg83b, Kerszberg83c, Karma86, Dombre87, Amar88, Haug89, Kessler89a,

Kessler89b, Kessler90, Karma90, Mashaal90, Weeks91, Lu92, Kurze96]. The main question was to elucidate whether there is a selection mechanism or if the instability wavelength is selected by means of a dynamical process which depends on the initial conditions. Although there are different possible scenarios for the selection problem, it seems that the dynamical selection mechanism is the one which better describes the experimental observations. Some experimental works have been devoted to clarify the selection problem [Eshelman88a, Eshelman88b, Qian89].

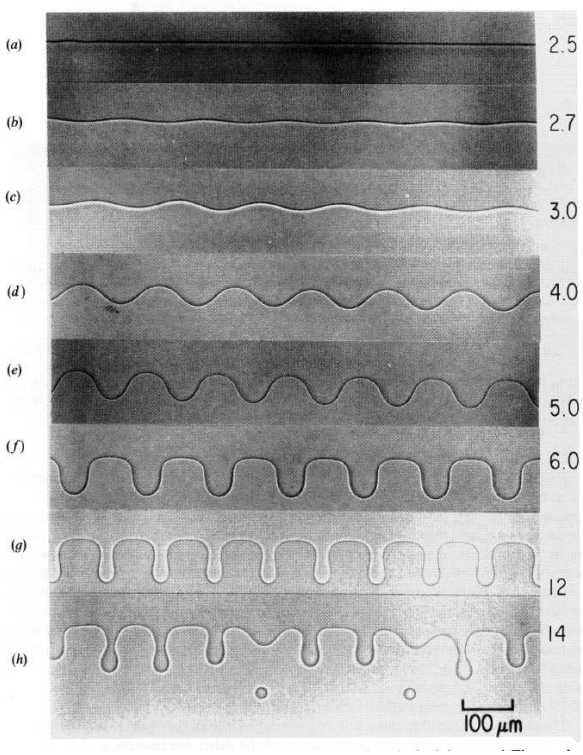

Figure 1.4: Destabilization of a planar solidification front. Taken from the experiments of A. J. Simon, J. Bechhoefer and A. Libchaber (Ref. [Simon88]).

1.2.3 Flow-induced instabilities

From a general point of view, the morphological instability of the solidification front is not uniquely driven by heat and mass diffusion. Under some situations, the effects of the advection and convection at the liquid phase might be equally important [Hurle93c, Davis01]. A description of the solidification problem taking into account the effects of the fluid flow at the liquid phase requires the coupling of

the heat and mass equations with the Navier-Stokes equations for the fluid velocity. In fact, convective patterns can also form during the advance of the solidification front, and two different pattern-forming instabilities (bulk and interfacial) will be present in the same physical system [Davis84].

1.2.4 Eutectic patterns

A binary eutectic system is a A-B binary alloy presenting a three-phase coexistence between the liquid phase and two distinct solid phases which are rich in either A (α phase) or B particles (β phase) [Davis01, Sinha03]. At the triple point, the the alloy melt has a eutectic concentration c_E and a melting temperature T_E. Below T_E, there is a equilibrium state between the α and β solid phases. Eutectic systems have a great technological importance because the melting temperature T_E is quite smaller than the melting temperatures of the pure A and pure B systems T_A, T_B and because their solidification microstructures have a smaller wavelength than the typical structures in dendritic growth. During eutectic growth, many different microstructures can appear in the system, and the solid phase presents some ordering between the α and β phases in the form of a lamellar pattern or a rod-like structure [Jackson66a, Jackson66b, Davis01]. Pattern-formation in eutectic systems has not been studied until recently [Langer80a, Karma96c, Kassner91a, Kassner91b, Caroli90]. There are other important physical metallurgy systems like monotectics or peritectics which present, as the eutectic system, different stable solid phases from the melt.

1.3 General objectives and outline of the work

1.3.1 General objectives

The work developed in this thesis deals with continuum models for solidification processes. The derivation and application of such models requires the combination of different theoretical and computational approaches. In particular, we will work with the so-called phase-field models, which constitute a relatively new approach to deal with complex interfacial phenomena.

The ultimate objective of this thesis is to quantitatively describe the pattern selection dynamics of the morphological instabilities which are present during a controlled directional solidification experiment. This pattern selection problem has important scientific and technological consequences; as basic research, a knowledge of the selection dynamics will clarify the underlying mechanisms which determine the apparition of different pattern-forming structures in the system. From the technological point of view, it provides a tool which can be used to predict and control the formation of microstructures in material processing engineering.

During the last fifteen years, it has been already well established from experimental [Eshelman88a, Eshelman88b, Losert98a, Losert98b] and theoretical results

[Warren90, Warren93] that the features of the final solidification pattern are determined during a history-dependent process at the initial transient stages of the solidification process. For this reason, the first objective of the work is addressed to decide whether the phase-field formulations allow to quantitatively predict the correct transient behavior of the solidification front during early mass and heat redistribution stages. This is a rather important question, because small differences in the value of the mass or heat fields might significantly modify the transient stability of the front and therefore the properties of the final selected pattern. This part of the thesis is described in Chapter 7, where phase-field simulation results are compared with standard analytical and theoretical predictions. In this section, we specifically study the transient behavior of the front, the non-steady formation of the mass and heat boundary layers, and the evolution of the morphological stability of the interface during the transient.

Once we have tested the validity of the approach and determined the proper simulation conditions, the next step is to include the effect of fluctuations in the dynamics of the advancing interface. The fluctuations in solidification are well characterized and play a very important role in the selection dynamics of the front. In fact, these microscopical perturbations constitute the initiation mechanism for the development of the morphological front instabilities. When the advancing interface is unstable, these noise perturbations are amplified by several orders of magnitude until the amplitude of the deformation reaches an observable value.

As a result of the sensibility of the system dynamics under small perturbations, fluctuations must be included in our field model in a very accurate way. To this extent, our second objective is twofold: It is not only that the system itself presents some internal stochastic behavior, but that the experimental set-up might also induce some additional uncontrolled sources of noise. For this reason, the second objective of the thesis is to properly account for fluctuations in phase-field models for solidification.

The third and last aim of this thesis is to use the stochastic phase-field approach in order to perform long simulations of the front evolution and characterize the different stages of the selection problem. We can divide the selection dynamics in different dynamical stages:

- Before the controlled solidification process starts at $t = 0$, the solid-liquid interface is morphologically stable and its planar shape is not altered by the microscopical fluctuations of the system.

- The first dynamical regime starts with the initiation of the solidification process at $t = 0$, and finishes when a first wavelength becomes unstable in the system. This happens at time t_i, which is known as the instability time, and immediately afterwards some of the spectral modes of the fluctuations will began to growth.

- The second regime starts at the instability time t_i and finishes at t_0 when the interfacial perturbations reach an observable size. The time t_0 is known

as the crossover time, and can be defined as the time at which the amplitude of the perturbation becomes comparable to its mean wavelength λ_0. During this regime, the microscopic noise spectrum is amplified by the instability mechanism and the amplitude of the perturbations present a linear growth. An unstable planar interface will then undergo a dynamical transition from planar to a cellular shape.

- Once the system has reached the crossover time t_0, its dynamical evolution becomes nonlinear and the interface presents a non-steady coarsening dynamics. At the end of this period, the system reaches the final steady-state pattern, which determine the final electro-mechanical features of the solidified material.

To summarize, we want to address the selection problem in directional solidification by means of using phase-field techniques which account for the effect of fluctuations and transients during the early redistribution stages.

1.3.2 Outline of the work

The outline by chapters of this thesis is structured as follows:

Chapter 2

The main physical phenomena which are relevant in a solidification process are introduced in this chapter. We first give a thermodynamical description of phase transformations in pure systems and binary alloys, determining the thermodynamical forces which drive the advance of the solidification front. We present the importance of interfacial capillary effects in the stability of the system, and introduce the spontaneous nucleation as the process which initiates the spontaneous solidification from the melt. Other important interfacial effects are introduced by the attachment dynamics by which the atoms are incorporated at the crystalline structure of the advancing solid phase. We also consider the internal thermodynamical fluctuations of the system, which result in mass and heat stochastic currents in the bulk phases and across the solid-liquid interface.

Chapter 3

The mathematical description of solidification processes is usually given in terms of a moving boundary problem. This formulation consists in diffusion equations for the mass and/or heat at the two phases, supplemented with convenient boundary conditions at the moving interface. These moving boundary conditions are derived from the conservation laws across the interface and by imposing the thermodynamical equilibrium conditions of the system. We introduce the sharp-interface equations for pure systems and dilute mixtures, and introduce the constitutional undercooling criterion as the basic stability condition for the interfacial stability.

In this chapter, we perform the Mullins-Sekerka linear stability analysis for the morphological stability of the interface, which predicts the growth or decay rate for the interfacial perturbations.

Chapter 4

There are some analytical methods for the study of transient stages in solidification. In this chapter, we derive the boundary integrals for different solidification situations and incorporate the initial recoil transients. Boundary integral methods provide an integro-differential formulation of the moving boundary problem. These integro-differential equations are simulated for different solidification problems (Symmetric system, one-sided, constant miscibility gap approximation). The second analytical approach to deal with transients and fluctuations in solidification is the Warren and Langer's theory of noise amplification during the initial transient. The main features and assumptions of this theory are presented, and numerical simulations will be carried out for some particular cases. The Warren-Langer approach can be combined with a transient dispersion relation in order to analytically predict the wavelength selection in directional solidification.

Chapter 5

During the last two decades, the phase-field approach has established as a quantitative method to simulate complex interfacial phenomena. The technique consists in equations for a continuous order parameter field coupled with the diffusive process which drives the motion of the interface. In addition to the microstructure formation in solidification processes, this technique has been applied to several interfacial problems such as nucleation, dynamics of grain boundaries, crack propagation or biological membranes. In this chapter we present the derivation of the phase-field equations for the solidification of a undercooled pure substance and for a supersaturated diluted binary solution. We distinguish between variational and non-variational phase-field formulations, and give a detailed derivation of the basic assumptions. At the end of this chapter, we show how to introduce internal fluctuations in variational formulations by using the fluctuation-dissipation theorem.

Chapter 6

The phase-field approach gives a diffuse-interface description of the front, and recovers the moving boundary dynamics in the limit of small interface thickness. The model consists in a non-linear set of coupled partial differential equations for the evolution of the order-parameter ϕ and for the mass or heat diffusion in the system. The sharp-interface limit is an asymptotic procedure which projects the field equations into a set of equations which have the structure of a moving boundary problem. The model parameters can then be obtained by comparing the projected equations with the standard sharp-interface equations for the solidification problem.

In this chapter, we present a hybrid sharp-interface projection of a generic phase-field model including fluctuations. This new procedure allows to include either internal or external noises in both variational and non-variational phase-field models. The asymptotic limit is taken by performing a small-noise expansion in combination with the standard expansion in terms of the interface thickness. This technique allows to determine the deterministic and stochastic phase-field parameters, and has been tested by evaluating the well-known stationary power spectrum of the interfacial fluctuations.

Chapter 7

The phase-field method can be used as a simulation technique, and this chapter begins by pointing out the computational difficulties which arise when trying to obtain quantitative results. The computational efficiency of the phase-field approach is studied, and the main solutions to improve it are commented.

The rest of the chapter is devoted to perform a quantitative comparison between the phase-field simulations of the transient stages and the results obtained by means of analytical or theoretical approaches. We first focus in the front position during the solute redistribution transient, and study the phase-field convergence to the sharp-interface dynamics. This procedure is presented for different models (symmetric, constant miscibility gap, one-sided, liquid crystals), and good quantitative agreement is found in all the cases. The second test of the phase-field transient behavior concerns to the diffusion profiles which are formed behind the advance of the solidification front. The last process studied in this chapter is the phase-field behavior under external perturbations. The simulations of the transient growth rate for different perturbation modes is then compared with the analytical prediction of the transient linear stability analysis introduced in Chapter 4.

Chapter 8

Once the transient linear stability behavior of the model has been checked, we perform stochastic simulations of the phase-field equations. Fluctuations are introduced in the model by following the procedure described in Chapter 6, and the noise amplification of the different Fourier modes is studied during the transient. During the initial stages, the amplitude of the deformations grow linearly until their amplitude becomes comparable with its wavelength. At this time, which is known as the crossover time, the spectral modes begin to interact and the linear regime finishes. After the crossover time, the system evolves by means of a coarsening process which selects different primary spacings until it reaches the final cellular or dendritic structure. In the first part of the chapter (Sec. 8.2), we present simulations of these initial transient stages and compare our results for the crossover time with the Warren and Langer's noise amplification theory. In the second part (Sec. 8.3), the coarsening process is studied by means of phase-field numerical experiments and the obtained results are compared with two experimental results for

the directional solidification of organic alloys.

Chapter 9

We present the main results and conclusions of the work, and some assumptions about the future applicability of the results obtained in this thesis.

Appendix A

Tables with the physical parameters of some relevant pure systems and binary alloys which have been used in the simulations presented in this thesis.

Appendix B

Differential operators in the orthogonal curvilinear system, which are necessary when performing the hybrid asymptotic expansion of Chapter 6.

Appendix C

As we introduce several different physical parameters along the thesis, we have included this abstract in order to provide a relation of the most important parameter definitions for the reader's convenience.

Chapter 2

The physics of solidification

In this chapter, we introduce the basic physical mechanisms which take place during a solidification process. Section 2.1 is devoted to introduce the basic thermodynamic arguments needed to describe phase transitions in pure substances (Sec. 2.1.1) and in binary mixtures (Sec. 2.1.2). In Section 2.1.1 we introduce the capillary effects associated to the surface energy of the solid-liquid interface, introducing the spontaneous nucleation of a solid seed as the initiation mechanism of a solidification process. The diffusion of mass (Sec. 2.2.2) and heat (Sec. 2.2.1) in the system are presented in Section 2.2 as the main non-equilibrium mechanisms driving the motion of the solidification front. Phenomenological equations for the mass and heat conservation laws will be provided. The last section Sec. 2.3 we focus in the study of the thermal (Sec. 2.3.1) and solute (Sec. 2.3.2) equilibrium internal fluctuations which are relevant in a solidification processes.

2.1 Thermodynamics of phase transformations

Solidification is a phase transformation process in which a stable solid phase grows into a metastable liquid. Although this growth process occurs when the system is driven out from equilibrium, most of its important features can be explained within the thermodynamical equilibrium theory.

As we will see in this section, the relative stability of the phases is defined in terms of a general principle which requires the minimization of the Gibbs' free energy of the system, which will be soon introduced. For a further introduction on thermodynamics of phase transformations and kinetic processes, we refer to the references that I have used in order to write this chapter, Refs. [Kurz85, Porter92, Sinha03, Davis01, Fermi56, Zemansky81, Landau80, Hurle93a, Hurle93b].

2.1.1 Pure substance systems

For a thermodynamical system with a constant number of identical particles, the Gibbs' Free Energy G is defined as

$$G = H - TS, \tag{2.1}$$

where H is the total enthalpy of the system, T the absolute temperature and S its entropy. The entropy S is a measure of the microscopic disorder of the system, and the enthalpy H is defined as

$$H = U + PV, \tag{2.2}$$

where U is the internal energy of the system, and V, P its volume and pressure respectively.

Let us consider an infinitesimal process at constant temperature and pressure in which the volume of the system changes by an amount dV. Using Eqs. 2.1, 2.2, the infinitesimal variation of the Gibbs' free energy is given by

$$dG = dU + PdV - TdS. \tag{2.3}$$

If the system is transformed from an initial state A to a final state B, the change in the Gibbs' free energy can be evaluated by integrating Eq. 2.3, leading to

$$\Delta G = \Delta U + P\Delta V - T\Delta S, \tag{2.4}$$

where $\Delta\varphi = \int_A^B d\varphi = \varphi(B) - \varphi(A)$. From the first principle of the thermodynamics, the mechanical work performed during the process W can only be transformed into a decrease of the internal energy of the system U or in the form of heat Q. For an infinitesimal process, this principle corresponds to

$$dW = -dU + dQ. \tag{2.5}$$

In a hydrostatic system which has been mechanically insulated, the work can only be performed by means of a volumetric expansion, and we have

$$dW = PdV. \tag{2.6}$$

Inserting the last expression into Eq. 2.5 and integrating over the process from state A to state B, we find

$$P\Delta V = -\Delta U + \Delta Q. \tag{2.7}$$

On the other hand, the second principle states that during an isothermal process between the states A and B, the amount of heat absorbed from or transferred to the system obeys the relation

$$\Delta Q \leq T\Delta S, \tag{2.8}$$

where the equality holds when the process which transforms the system from A to B is reversible. Using Eqs. 2.8, 2.7 and 2.4, we have that, for an isothermal, isobaric, irreversible process, the Gibbs' free energy decreases

$$\Delta G = G(B) - G(A) < 0, \tag{2.9}$$

and the final state B has always a smaller free energy than the initial state. If the transformation between A and B is reversible, the free energy remains unaltered and we have $G(A) = G(B)$. From the preceding arguments, it follows that the *thermodynamical system evolves until its Gibbs' free energy takes its minimum possible value.*

The last statement allows to define the *stable equilibrium state* of the system as the state with the lowest possible value of the Gibbs' free energy. If the system is not in the global minimum of the Gibbs' free energy but in a local one, we say that it is in a *metastable state*, and the system will evolve across different *unstable states* until it reaches its stable equilibrium state. The growth process by which a system evolves from a metastable state to a stable equilibrium state is called a *kinetic process*, and can not be described within the framework of the equilibrium thermodynamics theory. As we will see in Section 2.2, the diffusion of heat and mass in the system are the most relevant non-equilibrium processes which drive the advance of the solidification front.

The principle of the minimization of the free energy is so powerful that can be used to predict that matter adopts different phases depending on its temperature. Let us consider condensed systems such as solid or liquid phases. For these systems, the value of the product PV is typically small compared with the internal energy U and it can assumed that $G \sim U - TS$. At a given temperature, the system can minimize G by either increasing the entropy or decreasing its internal energy. For large temperatures $T \gg U/S$, the term $-TS$ will be more important and the equilibrium phases will be those with large entropy such as liquid and vapor phases. On the contrary, for low temperatures $T \ll U/S$, the internal energy U is the dominant term in the Gibbs' free energy, and the phases with small internal energies will be the stable ones. As the internal energy $U = U_{kin} - U_{pot}$ is defined as the difference between the kinetic energy of the particles U_{kin} (translational, rotational or vibrational motions) and the potential energy U_{pot} associated to the attractive interaction between them, phases with strong bonds between particles (like solids) will have a smaller internal energy, and will therefore be the more stable phase at low temperatures. These arguments point out that the value of the Gibbs' free energy determines the relative stability of the different phases in a thermodynamic system.

Phase equilibrium

After the introductory remarks presented in the last section, we now study the stability of the solid, liquid and vapor phases as the temperature of the system is increased. Figure 2.1 shows the value of the Gibbs' free energy for each of these

phases for different values of the system temperature. Following the principle of minimum free energy, at a given temperature, the stable state of the system will be the one with the smallest value of G.

At $T = 0\ K$, there is no kinetic energy ($U_{kin} = 0$) and the Gibbs' free energy is determined by the potential energy of the system $G \sim U = -U_{pot}$. At this temperature, the internal energies of the three phases satisfy the relation $U^S > U^L > U^V$, because the solid phase is the one which presents more interaction energies between the particles and therefore the largest value of the potential energy U_{pot}. From this follows that the free energies of the phases satisfy the relation $G^S < G^L < G^V$, which brings to the conclusion that the solid phase is the most stable one at low temperatures near $T = 0K$.

As the temperature increases, the kinetic energy and the entropy of the system will get larger producing the decrease of the Gibbs' free energy. The free energy of the phases will decrease monotonously with a slope determined by their corresponding entropies (note that $S = -\frac{\partial G}{\partial T}$) (see Fig. 2.1). As the entropies of the three phases satisfy the relation $S^S < S^L < S^V$, the decrement of G with T will be faster in the phases with larger entropies. The G-T lines will eventually cross at some temperatures T_M, T_V, and these points will determine the range of temperatures for which each of the phases is stable: Below the *melting temperature* T_M, we have that the solid phase is the stable one. Between T_M and the *vaporization temperature* T_V the stable phase of the system is the liquid, and for temperatures above T_V the system is a vapor.

At the critical temperatures T_M, T_V the energy required to produce the corresponding phase transformation is given by the enthalpy difference between the two phases. We then define $L = H^L(T_M) - H^S(T_M)$ as the *latent heat of melting*, and $L_{vap} = H^L(T_V) - H^S(T_V)$ the *latent heat of vaporization*, which are the amounts of energy needed by the system in order to perform the solid-liquid (melting) and liquid-vapor (vaporization) processes respectively.

The driving force for the solidification of an undercooled pure melt

When a pure liquid is undercooled by an amount $\Delta T = T - T_M$ below its melting temperature T_M ($\Delta T < 0$), the liquid phase becomes a metastable state and the solid turns out to be the stable equilibrium phase of the system. At the new temperature T, the free energies of the liquid and solid phases are given by

$$G^L(T) = H^L(T) - TS^L(T) \tag{2.10}$$
$$G^S(T) = H^S(T) - TS^S(T), \tag{2.11}$$

and the Gibbs' free energy difference between the solid and liquid phases is given by

$$\Delta G(T) = \Delta H(T) - T\Delta S(T), \tag{2.12}$$

where $\Delta H(T) = H^L(T) - H^S(T)$ and $\Delta S(T) = S^L(T) - S^S(T)$. For small undercoolings $\Delta T \ll 1$, we can approximate $\Delta H(T)$ by its equilibrium value at T_M and

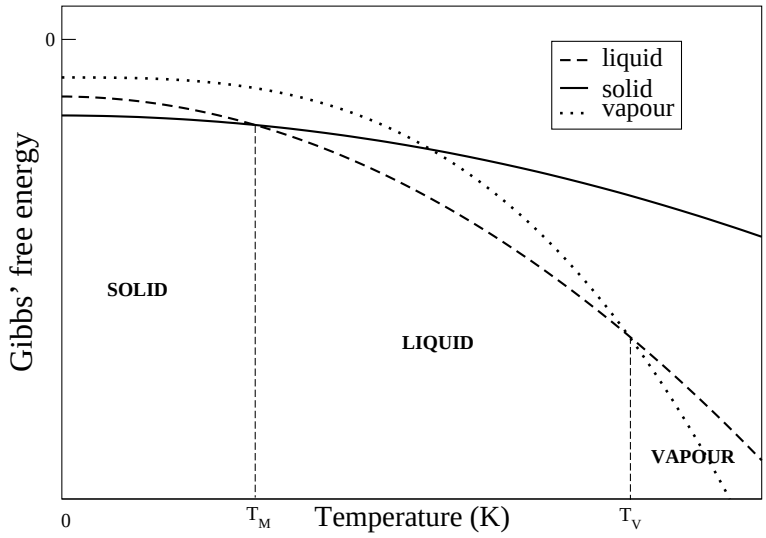

Figure 2.1: Gibbs' free energy and phase transformations

write

$$\Delta H(T) \approx \Delta H(T_M) = H^L(T_M) - H^S(T_M) = L. \tag{2.13}$$

For an isothermal reversible process, the absorbed heat is equal to the enthalpy ($\Delta Q = \Delta H = L$) and, as the relation $\Delta S = \Delta Q/T$ holds, we have

$$\Delta S(T) \approx \Delta S(T_M) = S^L(T_M) - S^S(T_M) = \frac{L}{T_M}. \tag{2.14}$$

Finally, inserting Eqs. 2.13 and 2.14 into Eq.2.12, the free energy difference produced by the undercooling of the system is given by

$$\Delta G(T) \approx -\frac{L\Delta T}{T_M}. \tag{2.15}$$

The Gibbs' free energy excess of Eq. 2.15 determines the driving force for the solidification from a undercooled pure melt. The larger the difference between the free energies of the solid and liquid phases at the undercooled temperature T, the larger the thermodynamical force which drives the stable solid phase to grow into the metastable liquid. It is of course proportional to the thermal undercooling ΔT, which is the main control parameter in a pure substance solidification experiment.

2.1.2 Mixtures and dilute alloys

We now consider systems which are composed of more than one type of particles. It is clear that a variation in the number of particles or a modification in the composition of the system will produce a variation of the Gibbs' free energy. As a consequence, the stability of the phases will not only depend on temperature as in pure substances, but also on the composition of the system.

Let us consider a mixture system composed by M different substances in such a way that it contains n_i moles of the substance i. The Gibbs' free energy G of the whole system will be now a function of the temperature, pressure and composition of the system given by

$$G = \sum_{i=1}^{M} \mu_i n_i, \tag{2.16}$$

where

$$\mu_i(T, P, n_1, n_2, ..., n_M) = \frac{\partial G}{\partial n_i} \tag{2.17}$$

is the *chemical potential* of the i-th component.

Note that as the chemical potentials μ_i represent energies per unit mol, they do not change when modifying the total number of moles in the system while maintaining its composition. For a pure system with n moles of a single component, we have $G = \mu n$ and the chemical potential μ is the free energy of one mole of the substance or its *molar free energy.*

For an isothermal, isobaric process in which the number of moles of the i-th component is infinitesimally changed by an amount dn_i, the Gibbs' free energy variation is given by

$$dG = \sum_{i=1}^{M} \mu_i dn_i, \tag{2.18}$$

and the equilibrium condition is that the change in the composition does not produce any free energy variation, i.e.

$$dG = \mu_1 dn_1 + \mu_2 dn_2 + \cdots \mu_M dn_M = 0. \tag{2.19}$$

Ideal binary mixtures

Let us consider a binary system, i.e, a mixture system composed by only two different species A and B. In this case, the total Gibbs' free energy is given by

$$G = \mu_A n_A + \mu_B n_B. \tag{2.20}$$

In an isothermal, isobaric process, the composition of the system can be modified by an infinitesimal change in the number of A and B moles of dn_A and dn_B, respectively. As the total number of moles in the system $n = n_A + n_B$ remains

constant, the infinitesimal variations dn_A and dn_B must be related by $dn_A = -dn_B$, and the equilibrium condition $dG = \mu_A dn_A + \mu_B dn_B = 0$ can be expressed as

$$\mu_A = \mu_B. \tag{2.21}$$

The last equation says that the system reaches the stable equilibrium state when the chemical potential of the two substances are equal.

If we call g_A,g_B to the molar free energies of the pure A and pure B substances respectively ($g_i = u_i - Ts_i + Pv_i$, $i = A, B$, where the lower case letters refer to molar magnitudes), the total free energy of the system can also be expressed as

$$G = g_A n_A + g_B n_B + \Delta G', \tag{2.22}$$

where $\Delta G' = G' - G$ accounts for the variation in the total free energy due to the mixing between the two substances, being G and G' the free energy of the system before and after the mixing process. This variation in the free energy can be expressed in terms of enthalpy and entropy variations as

$$\Delta G' = \Delta H' - T\Delta S', \tag{2.23}$$

where $\Delta H' = H' - H$, $\Delta S' = S' - S$ and the primes refer to the values after the mixing. Assuming that the volume during the mixing remains constant, the variation in the enthalpy is due to the variation of the internal energy of the system, accounting for the interactions between the two species. In a first approximation, we consider an *ideal solution* and suppose that the the enthalpy of the system do not change during the mixing, i.e. $\Delta H' = 0$. For ideal solutions, the change in the free energy is therefore due to variations in the entropy and we have

$$\Delta G' = -T\Delta S'. \tag{2.24}$$

The mixing entropy can be determined by using the Boltzmann's definition

$$\Delta S' = S' = k_B \ln \Omega, \tag{2.25}$$

where k_B is the Boltzmann's constant and Ω represents the number of possible microscopical configurations of the system. Ω must be understood as the number of microscopic dynamical states that correspond with the given thermodynamical state. At first sight it might seem that the number of possible microscopic configurations compatible with a certain thermodynamic state is infinite. This difficulty dissapears if the dynamical states are considered in the phase space of the system. Each state of the system is then represented by a point in a 2p-dimensional space, being p the number of degrees of freedom of the system. The phase space is then divided into identical small cells and each state of the system is characterized by specifying the cell at which the point belongs. When de size of the cells gets infinitesimally small, this technique to determine Ω will be exact. As the value of Ω

changes by a factor when changing the size of the cells, the entropy remains undetermined by an additive constant. This does not suppose any restriction because we are interested in entropy differences and not in absolute values.

From the last arguments, we can evaluate the entropy of a binary solution after the mixing by counting the number of distinguishable ways of arranging N_A particles of the kind A and N_B particles of the kind B. Using elementary combinatorial arguments, we get

$$\Omega = \frac{(N_A + N_B)!}{N_A! N_B!}, \tag{2.26}$$

and introducing Ω in Eq. 2.25, the entropy after the mixing is given by

$$\Delta S' = k_B \ln \frac{(N_A + N_B)!}{N_A! N_B!}. \tag{2.27}$$

As the number of A and B particles in the system is large ($N_A, N_B \gg 1$), we can use the Stirling formula $\ln p! \approx p \ln p - p$ for $p \gg 1$ to expand the logarithm in Eq. 2.27 and obtain

$$\Delta S' \approx k_B (N_A + N_B) \ln(N_A + N_B) - k_B N_A \ln N_A - k_B N_B \ln N_B. \tag{2.28}$$

If N_0 is the number of particles in a mol (Avogadro's number), a system with N_A, N_B particles correspond to a system with $n_A = N_A/N_0$ and $n_B = N_B/N_0$ moles of A and B, respectively. Therefore, grouping A and B terms in Eq. 2.28, we can rewrite the mixing entropy as

$$\Delta S' \approx -R n_A \ln \frac{n_A}{n} - R n_B \ln \frac{n_B}{n}, \tag{2.29}$$

where $R = k_B N_0 = 8,314$ J/K mol is the universal gas constant and $n = n_A + n_B$ is the total number of moles of the system.

We introduce here the *molar fractions of A and B*, x_A, x_B as

$$x_A = \frac{n_A}{n} \tag{2.30}$$

$$x_B = \frac{n_B}{n}, \tag{2.31}$$

and using Eqs. 2.24, 2.22 and 2.29, write the total free energy of the ideal binary system as

$$G = g_A n_A + g_B n_B + RT n_A \ln x_A + RT n_B \ln x_B. \tag{2.32}$$

The chemical potentials μ_A and μ_B for the ideal binary solution can be now calculated by differentiating Eq. 2.32 with respect to n_A and n_B

$$\begin{aligned} \mu_A &= \frac{\partial G}{\partial n_A} = g_A + RT \ln x_A \,, \\ \mu_B &= \frac{\partial G}{\partial n_B} = g_B + RT \ln x_B, \end{aligned} \tag{2.33}$$

where, due to the logarithmic dependence in Eq. 2.32, the variations in n_A, n_B occur without changing the molar fractions x_A, x_B.

As $x_A, x_B \in [0, 1]$, the logarithmic terms in Eqs. 2.33 are negative and the effect of the mixing entropy in an ideal mixture is to reduce the molar Gibbs' free energy of the system. This effect is shown in Fig. 2.2, where the dashed lines represent the molar free energy of the system before mixing $g = G/n = \mu_A x_A + \mu_B x_B$ at two different temperatures $T_1 < T_2$. As the free energies of the pure substances decrease when increasing the temperature, we have $g_A(T_1) > g_A(T_2)$ and $g_B(T_1) > g_B(T_2)$. The solid lines in Fig. 2.2 correspond to the molar free energies of the mixed systems at T_1, T_2, which are given by Eq. 2.32. For all the compositions, the molar free energy of the mixed system is smaller than the one for the system before the mixing. As it can be appreciated in the figure, this effect becomes more important as temperature increases.

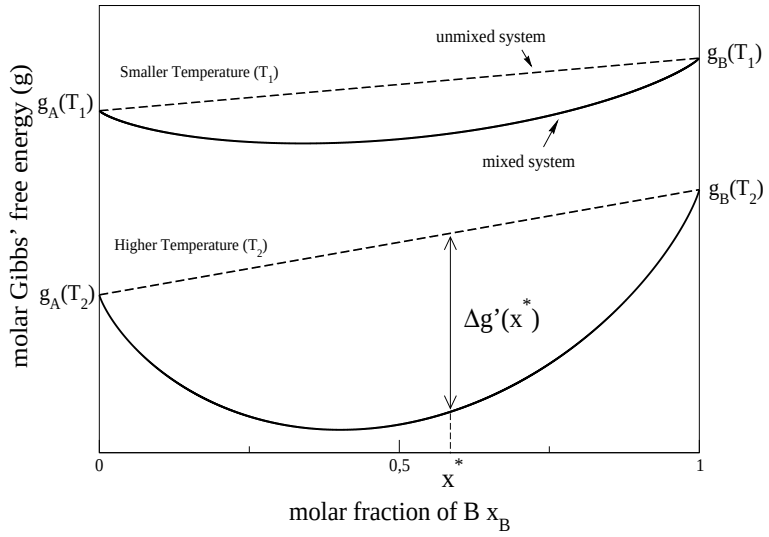

Figure 2.2: Molar Gibbs' free energy of a ideal binary system. The free energy decrement due to mixing becomes more relevant for higher temperatures ($T_1 < T_2$).

Regular binary solutions

So far, we have only considered ideal solutions, i.e., those with zero mixing enthalpy $\Delta H' = 0$. The description of binary systems can be improved by considering the effect of the interaction between particles during the mixing process. The simplest

description accounting for these effects is the so-called *regular solution model*. In this model, the entropy of mixing is calculated under the assumption of the ideality of the mixture, and the mixing enthalpy is evaluated by averaging the interactions between the particles. Let U_{AA}, U_{BB} and U_{AB} be the interaction energies between $A-A$, $B-B$ and $A-B$ particles respectively. The interaction energy is here defined as the negative value of the potential energy. For a binary solution with N_A particles of A and N_B of B, and with the internal energy before mixing is then given by

$$U = \frac{zN_A}{2}U_{AA} + \frac{zN_B}{2}U_{BB}, \tag{2.34}$$

where z is the number of bonds per particle or *coordination number* and the factor 2 in the denominator accounts for the fact that the interaction energy per bond is twice the interaction energy per particle (one bound for each two particles).

After the mixing, some A-B interactions occur and the internal energy takes the value

$$U' = P_{AA}U_{AA} + P_{BB}U_{BB} + P_{AB}U_{AB}, \tag{2.35}$$

where P_{AA},P_{BB} and P_{AB} are the number of bonds between $A-A$, $B-B$ and $A-B$ particles, respectively. As in a $A-A$ ($B-B$) interaction there is two A (B) particles and in a $A-B$ interaction there is only one A or B particle, we have

$$N_A z = 2P_{AA} + P_{AB} \tag{2.36}$$

$$N_B z = 2P_{BB} + P_{AB}, \tag{2.37}$$

and the enthalpy of mixing, which is equal to the change in the internal energy due to mixing, is given by

$$\Delta H' = \Delta U' = U' - U = P_{AB}\left(U_{AB} - \frac{U_{AA}+U_{BB}}{2}\right). \tag{2.38}$$

When the interaction energy U_{AB} is similar to $\frac{1}{2}(U_{AA}+U_{BB})$, it can be assumed than the particles are randomly arranged and we can approximate

$$P_{AB} \approx z(N_A+N_B)x_A x_B, \tag{2.39}$$

and then one obtains

$$\Delta H' \approx z(N_A+N_B)x_A x_B\left(U_{AB} - \frac{U_{AA}+U_{BB}}{2}\right). \tag{2.40}$$

Finally, using Eq. 2.23, Eq. 2.22 and Eq. 2.29, the molar Gibbs' free energy of a regular binary solution is given by

$$G = n_A g_A + n_B g_B + \nu\frac{n_A n_B}{n} + TR(n_A \ln x_A + n_B \ln x_B)\,, \tag{2.41}$$

with ν given by $\nu = zN_0(U_{AB} - \frac{1}{2}(U_{AA}+U_{BB}))$.

The ideality of the solution is recovered with the assumption $U_{AB} = \frac{1}{2}(U_{AA} + U_{BB})$, and the sign of ν determines if the process is exothermic ($\nu < 0$, $\Delta H' < 0$) or endothermic ($\nu > 0$, $\Delta H' > 0$). In exothermic processes and for all temperatures, the mixing of two substances results in a decrement of the free energy. This effect is shown in the Figure 2.3, which plots the molar free energies of an ideal and regular solution. For an endothermic processes, the situation is more complicated

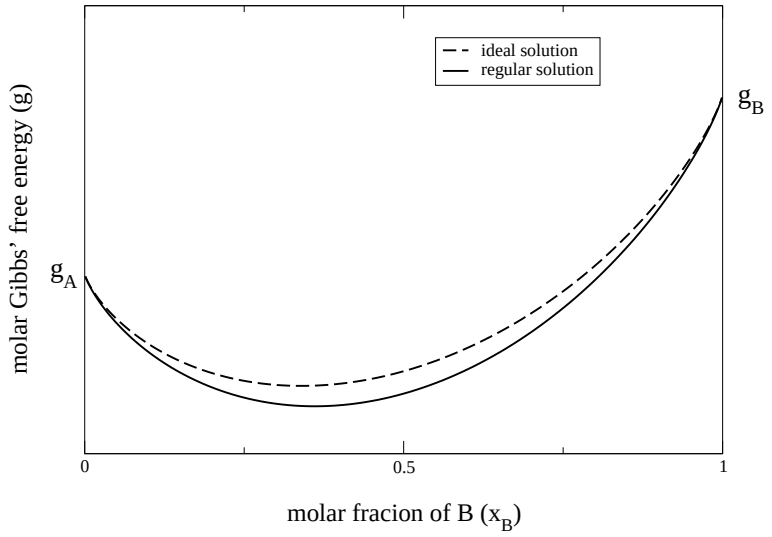

Figure 2.3: Molar free energy for ideal and regular solutions in the case of an exothermic process.

and the stability depends on the relative importance of the terms $\Delta H'$ and $-T\Delta S'$ in the free energy. Comparing Eq. 2.41 with Eq. 2.20, the chemical potentials for a regular binary solution can be determined and take the form

$$\mu_A = g_A + \nu(1 - x_A)^2 + RT \ln x_A \tag{2.42}$$
$$\mu_B = g_B + \nu(1 - x_B)^2 + RT \ln x_B, \tag{2.43}$$

where g_A, g_B are the molar free energies of the pure A and B substances, and it has been used the trivial relation $n_A n_B = n_A n_B (n_A + n_B)/n$.

Decrease of the freezing temperature in dilute solutions

In section 2.1.1, we studied the stability of the solid and liquid phases in the pure system as function of the temperature. The melting temperature T_M^A of the pure

A system was then determined from the G-T curve by the condition $g_A^S(T_M^A) = g_A^L(T_M^A)$. In a mixture, the stability of the phases not only depends on temperature, but also on the system composition.

As we have seen (cf. Fig. 2.2), the introduction of a small amount of solute B results in a decrement of the molar free energy due to the entropy of mixing. As a consequence, the G-T curves for the solid and liquid phases cross at a smaller temperature, resulting in a decrease of the melting temperature of the solution. This effect is shown in Fig. 2.4, where the temperature of the system is changed for a given value of the composition. It can be seen that the liquid and solid G-T curves cross at a smaller temperature in the presence of a solute than for a pure system.

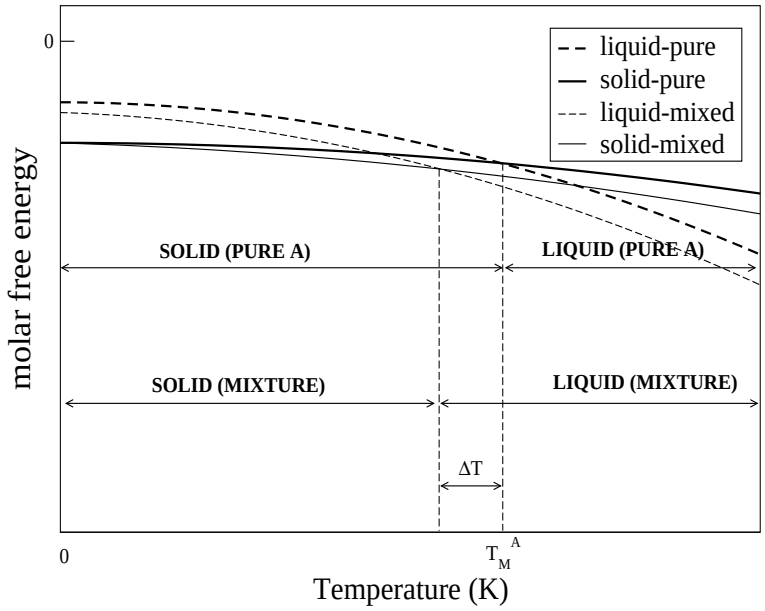

Figure 2.4: Molar free energy of the solid and liquid phases for a pure system and for an ideal mixture. The melting temperature of the solution is reduced as a consequence of the introduction of the solute.

Equilibrium conditions for heterogeneous systems

When modifying the composition at a constant temperature the situation is rather different. Figure 2.5 represents the molar free energy of the solid and liquid phases in terms of the molar fraction of B. The functions correspond to a temperature $T_M^A < T' < T_M^B$ between the melting temperatures of the pure A and pure B substances. For low concentrations of B, the liquid phase minimizes the free energy and is therefore the equilibrium state of the system, whereas for high B concentrations, the solid phase is the equilibrium one. In these two regions we have a liquid or solid *homogeneous system*.

In the intermediate region between the two minima of the solid and liquid molar free energies, however, the system can decrease its free energy by separating the two phases forming a *heterogeneous system* where solid and liquid phases coexist with different solute concentrations.

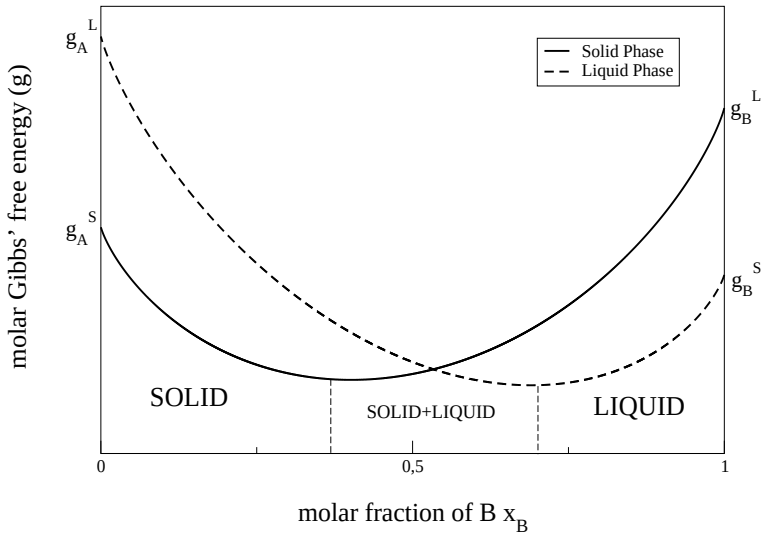

Figure 2.5: Molar free energies of the solid and liquid phases and their stability depending on the mixture composition

In the particular case of *dilute binary solutions*, it is interesting to quantify the reduction of the melting temperature produced by the introduction of a certain small amount of solute. A binary solution is said to be dilute when the number of particles of one of the species (solute) is small compared with the number of particles of the other substance (solvent). Being A the solvent and B the solute, this condition can be represented in terms of their molar fractions by $x_A \gg x_B$.

Noting that $x_A = 1 - x_B$, the chemical potentials of a ideal dilute solution are given by (cf. Eq. 2.33)

$$\mu_A = g_A - RTx_B \tag{2.44}$$
$$\mu_B = g_B - RT \ln x_B, \tag{2.45}$$

where we have approximated $\ln x_A = \ln(1 - x_B) \approx -x_B$.

In a heterogenous situation where solid and liquid phases coexist, the total free energy of the system is given by $G = G_S + G_L$, where G_S and G_L are the free energies of the solid and liquid regions respectively. As the two phases are in contact, their concentrations can be modified by the migration of particles from one phase to the other. Being n_A^S, n_B^S the respective number of moles of A and B in the solid, and n_A^L, n_B^L the number of moles of A and B in the liquid, the free energies of the solid and liquid phases are given, in the ideal approximation, by

$$G^S = g_A^S n_A^S + g_B^S n_B^S - RTn_B^S + RTn_B^S \ln \frac{n_B^S}{n_A^S + n_B^S} \tag{2.46}$$
$$G^L = g_A^L n_A^L + g_B^L n_B^L - RTn_B^L + RTn_B^L \ln \frac{n_B^L}{n_A^L + n_B^L}. \tag{2.47}$$

Let us consider a process in which the number of moles of the substance $i = A, B$ in the phase $\alpha = S, L$ is changed by an infinitesimal amount given by dn_i^α. If no chemical reactions occur, the number of moles of A and B $n_A = n_A^S + n_A^L$, $n_B = n_B^S + n_B^L$ remains constant. In such a process, it is clear that the relations $dn_A^S = -dn_A^L$ and $dn_B^S = -dn_B^L$ are fulfilled, and the equilibrium condition of the heterogeneous system, which is given by

$$dG = dG^S + dG^L = \mu_A^S dn_A^S + \mu_B^S dn_B^S + \mu_A^L dn_A^L + \mu_B^L dn_B^L = 0, \tag{2.48}$$

can be expressed as

$$\mu_A^S = \mu_A^L, \tag{2.49}$$
$$\mu_B^S = \mu_B^L. \tag{2.50}$$

The last relation states that a heterogeneous system reaches equilibrium when the chemical potential of the different species take the same value in the two coexisting phases.

The chemical potentials μ_A^S and μ_A^L can be now easily determined by differentiating the free energies Eqs. 2.47 with respect to the molar concentration n_A

$$\mu_A^S = \frac{\partial G^S}{\partial n_A^S} = g_A^S - RTx_B^S, \tag{2.51}$$
$$\mu_A^L = \frac{\partial G^L}{\partial n_A^L} = g_A^L - RTx_B^L. \tag{2.52}$$

Inserting the expressions for the chemical potentials Eqs. 2.52 in the first equilibrium condition Eq. 2.49, we arrive to

$$g_A^S - RTx_B^S = g_A^L - RTx_B^L. \tag{2.53}$$

When the amount of solute is small, we can suppose that the effect in the reduction in the melting temperature is also small. We can therefore expand in Taylor g_A^S and g_A^L around the melting point $T = T_M^A$ to obtain

$$g_A^S(T) \approx g_A^S(T_M^A) + \frac{\partial g_A^S}{\partial T}(T - T_M^A), \tag{2.54}$$

$$g_A^L(T) \approx g_A^L(T_M^A) + \frac{\partial g_A^L}{\partial T}(T - T_M^A), \tag{2.55}$$

where $g_A^L(T_M^A)$ and $g_A^S(T_M^A)$ are the molar free energies of the pure substances at the melting temperature, which we know that are equal from the equilibrium condition of a pure system $g_A^S(T_M^A) = g_A^L(T_M^A) = g_A$. We remind the definition of the molar entropy of a pure system as $s^S = -\frac{\partial g_A^S}{\partial T}$ and $s^L = -\frac{\partial g_A^L}{\partial T}$, which satisfies the relation $\Delta s = s^L - s^S = L_m/T_M^A$, where L_m is the latent heat per unit mole of the pure A substance defined by $L_m = L/n$ and n the total number of moles in the system. From the last arguments, the melting temperature of the solution T can be expressed as

$$T = T_M^A - \frac{RT^2}{L_m}(x_B^L - x_B^S), \tag{2.56}$$

expression which quantifies the decrease in the melting temperature due to the presence of a certain quantity of solute in the solid and liquid phases.

Inserting Eq. 2.45 into the second equilibrium condition Eq. 2.50, we arrive to

$$\frac{x_B^S}{x_B^L} = k(T) = \exp\left\{\frac{\Delta g_B}{RT}\right\}, \tag{2.57}$$

where $k(T)$ is the *partition coefficient* of the solution, and $\Delta g_B = g_B^L - g_B^S$. The partition coefficient relates the ratio of solute in the solid and liquid phases in order to satisfy the thermodynamical equilibrium condition.

Inserting Eq. 2.57 into Eq. 2.56, we find a simpler expression for the decrease of the melting temperature

$$T = T_M^A - \frac{RT^2}{L_m}x_B^L(1 - k). \tag{2.58}$$

The last equation allows to introduce the *absolute value of the liquidus slope* of the binary solution m_L as a positive constant defined by

$$m_L = \frac{RT^2(1 - k)}{L_m}. \tag{2.59}$$

Introducing the latent heat per unit volume as $L_v = L_m/v_m$, where v_m is the *molar volume* of the substance (i.e., the volume of 1 mol of substance, defined as $v_m = Z/\rho$ being Z the molecular weight and ρ the density), the previous expression can be written as

$$m_L = \frac{RT^2(1-k)}{v_m L_v}. \tag{2.60}$$

The last expression is known as the *Clausius-Clapeyron relation* , and allows to write the shift in the melting temperature due to solute concentration as

$$T = T_M^A - m_L x_B^L. \tag{2.61}$$

Although the liquidus slope $m_L(T)$ is a function of the temperature, we will assume that for solutions with a small amount of solute it can be approximated by its value at the equilibrium melting temperature of the solution $T_E = T_M^A - m_L x_B^{0,L}$, i.e.,

$$m_E = m_L(T_E) = \frac{RT_E^2(1-k)}{v_m L_v}. \tag{2.62}$$

In the same way we can introduce the equilibrium partition coefficient k_E defined as

$$k_E = k(T_E) = \exp\left\{\frac{\Delta g_B}{RT_E}\right\}. \tag{2.63}$$

From the last arguments follows that, at a given temperature and pressure, the local equilibrium conditions at the solid-liquid interface is ensured by the two conditions:

i) The shift in the melting temperature due to the addition of solute is given by Eq. 2.61.

ii) For an equilibrium solution at a given temperature T, the ratio of the solute concentrations at the solid and liquid sides of the interface is constant, and given by Eq. 2.57.

Isothermal solidification of a supersaturated melt

The phase diagram of a dilute system is represented in figure 2.6, and describes the stability of the different phases in a system as a function of the temperature and solute concentration. As it can be observed in the figure, a dilute binary solution with solute concentration x_∞ will be liquid for temperatures above $T_1 = T_M^A - m_L x_\infty$ and solid for temperatures below $T_2 = T_M^A - m_L x_\infty/k$.

At a intermediate temperature T^* between T_1 and T_2, the liquid solution is in a metastable state. The solution is then said to be *supersaturated* because its equilibrium concentration x_0 is larger than the actual concentration of the alloy x_∞. In such a situation, a solid seed with concentration kc_0 can be spontaneously formed in the system. The mechanisms of this nucleation process will be described in Section 2.1.3. After this initiation mechanism, and depending on the level of

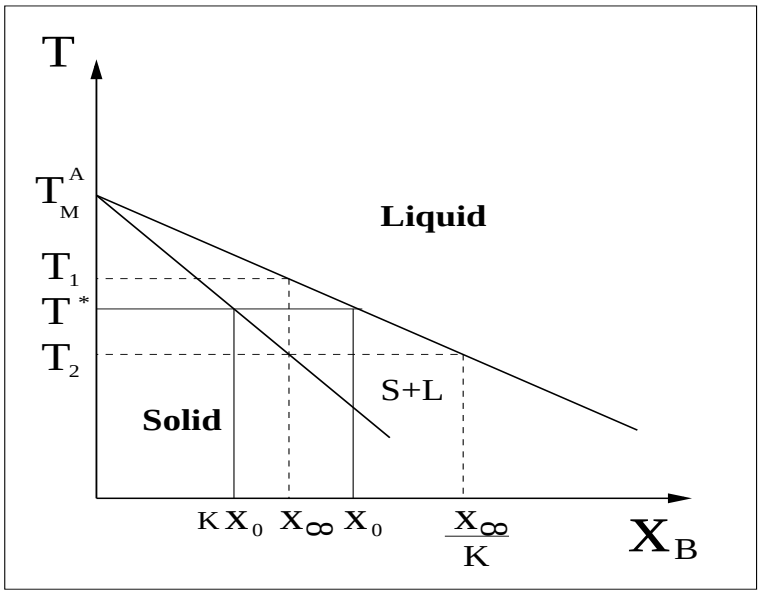

Figure 2.6: Phase diagram of a dilute binary solution. For a given solute concentration x, the system is liquid for temperatures above T_1 and solid for temperatures below T_2. For intermediate temperatures, solid and liquid phases coexist in a heterogeneous state.

supersaturation of the alloy, the solid nucleus will grow until the whole system solidifies.

As the solid phase advances, some solute particles are rejected to the liquid phase, and a boundary layer of accumulated solute builds up near the interface. As local equilibrium is preserved at the interface, the ratio between the solid and liquid concentrations is maintained constant ($x_S/x_L = k$), and the growing solid phase increases its concentration. This *solute redistribution transient* process continues until the solid reaches a concentration x_∞, which corresponds to a concentration x_∞/k at the liquid side of the interface.

One possible way of defining the *level of supersaturation* of the solution is

$$\delta x = x_0 - x_\infty, \tag{2.64}$$

which corresponds to a *supersaturation undercooling* below the melting temperature of the initial melt T_1 given by

$$\Delta T = T^* - T_1 = -m_L \delta x. \tag{2.65}$$

The magnitude ΔT is the equivalent in alloy solidification to the thermal undercooling of a pure melt.

We can introduce here the *miscibility gap* of the alloy as

$$\Delta x_0 = \frac{x_\infty(1-k)}{k}, \tag{2.66}$$

which determines the total amount of solute which has accumulated at the liquid side of the front at the end of the redistribution transient. In the same way that the freezing of pure substances occurred by undercooling the liquid below its melting temperature, the solidification of a binary alloy happens when the system is supersaturated.

The driving force for the solidification of binary solutions

We can determine the driving force of the solidification of a supersaturated alloy by determining the Gibbs' free energy difference between the liquid and solid phases. We can actually use the same relations obtained in section 2.1.1 for the case of the pure substance system, using the Clausius-Clapeyron relation Eq. 2.60 to determine the ΔG in terms of the physical parameters of the alloy system. For n moles of a pure system, the free energy per unit mole $\Delta g = \Delta G/n$ is given by

$$\Delta g = -\frac{L_m \Delta T}{T_M}. \tag{2.67}$$

where $L_m = L/n$ is the latent heat per unit mole and ΔT the undercooling of the system below its melting temperature. In the case of a supersaturated solution with solute concentration x_∞, ΔT the undercooling in Eq. 2.67 is given by $\Delta T = T^* - T_1 = -m_L \delta x$ (cf. Eq. 2.65). On the other hand, using the Clausius-Clapeyron relation in molar units

$$\frac{L_m}{T_M} = \frac{RT_M(1-k)}{m_L}, \tag{2.68}$$

we arrive to an expression for the Gibbs' free energy excess for alloys Δg given by

$$\Delta g = RT_M(1-k)\delta x. \tag{2.69}$$

Note that for a supersaturated solution Δg is a positive magnitude ($k < 1$, $\delta x > 0$) which can be understood as the driving force for the alloy solidification process. From the last equation it follows that no solidification process will occur when $k = 1$ (no solute rejection occurs at the interface) or when $\delta x = 0$ (the solution is not supersaturated, so the system is not metastable).

2.1.3 Interface thermodynamics and nucleation

As far, we have assumed that heterogeneous systems are bulk solid and liquid coexisting phases. In practice, however, these bulk phases are separated by an interface across which the particles arrange from an ordered structure in the solid to a disordered motion in the liquid. Let us introduce the *interfacial surface energy*

$\tilde{\sigma}$ as the energy per unit area needed to create this solid-liquid interface. As a general indication for the rest of this thesis, we will use tilded letters to refer to dimensional value of the parameters. As a free solidification processes begins with the spontaneous formation of a small seed of solid in a metastable liquid, the energy associated to the creation of the solid-liquid interface will modify the equilibrium conditions of the system.

Let us consider a solid spherical seed of radius r embedded into a metastable liquid phase. The metastability can be produced by either the undercooling of a pure substance or by the supersaturation of a solution. In both cases, the formation of the solid seed produces a change of the Gibbs' free energy density G_v given by

$$\Delta G_{bulk} = -\Delta G_v \frac{4\pi}{3} r^3 \tag{2.70}$$

where $\Delta G_v = (G_v^L - G_v^S)$ is the difference between the solid and liquid free energies per unit volume. Note that as the liquid is metastable, we have $\Delta G_v > 0$ and the formation of the solid seed results in a decrease of the free energy of the system. In the solidification of a pure substance, ΔG_v depends on the undercooling and is given by $\Delta G_v = \frac{L_v \Delta T}{T_M}$, where $L_v = L_m / v_m$ is the latent heat per unit volume of the substance.

On the other hand, as a consequence of the tension produced by the solid-liquid interface, there is a increment in the pressure inside the solid seed given by

$$\Delta P = \tilde{\sigma}\tilde{\kappa}, \tag{2.71}$$

where $\tilde{\kappa} = \frac{2}{r}$ is the *surface curvature*, defined as positive when the center of the radius of curvature is located at the liquid side of the interface. This pressure variation produces a change in the Gibbs' free energy given by

$$\Delta G_{int} = V \Delta P = \frac{4\pi}{3} r^3 \Delta P = \frac{8\pi\tilde{\sigma}}{3} r^2. \tag{2.72}$$

The total free energy change due to the formation of the seed is therefore given by

$$\Delta G_{Total} = \Delta G_{bulk} + \Delta G_{int}. \tag{2.73}$$

The total free energy of the previous equation is represented in terms of the seed radius in Fig. 2.7. When a seed of radius $r < r_c$ is created, the system will decrease its free energy by decreasing the radius of the seed until it dissolves in the liquid. For spontaneous seeds of radius $r > r_c$, the system decreases its free energy by growing the seed and a solidification process will be initiated. The critical radius for nucleation r_c can be easily determined by imposing the condition

$$\left. \frac{d\Delta G_{Total}}{dr} \right|_{r=r_c} = 0, \tag{2.74}$$

and is given by

$$r_c = \frac{2\tilde{\sigma}}{\Delta G_v}. \tag{2.75}$$

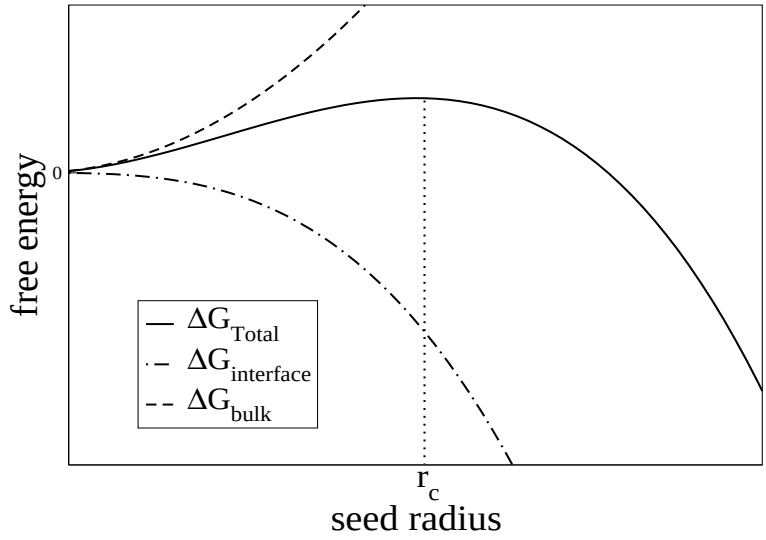

Figure 2.7: The spontaneous formation of a solid seed in a metastable liquid only grows when its radius is larger than the critical nucleation radius r_c

The Gibbs-Thomson effect

Besides determining the conditions for spontaneous nucleation, the pressure variation in the solid due to the surface energy has another important effect: As the interface curvature increases the free energy of the system, the melting temperature of the system will be reduced when curved interfaces are present in the system. It is easy to see that this decrease is given by

$$T = T_M^A - m_L x_B - \tilde{d}_0 \tilde{\kappa}, \tag{2.76}$$

where $\tilde{\kappa}$ is the curvature of the front and

$$\tilde{d}_0 = \frac{\tilde{\sigma} T_M^A}{L_v} \tag{2.77}$$

is the *capillary length* of the system, being $\tilde{\sigma}$ the surface energy of the substance. The last equation Eq. 2.76 is known as the *Gibbs-Thomson equation*, and determines the temperature of a solid-liquid interface in terms of its curvature and the amount of solute in the system.

2.1.4 Attachment kinetics

Besides surface energy effects, there are other interfacial processes which might be important in the dynamics of the solidification front. In many cases, the most relevant among them is the efficiency by which the particles in the liquid attach to the atomic structure of the growing solid phase [Nozières91, Chernov04, Aziz88, Aziz94, Aziz96]. This efficiency can be ideally approximated as infinite, assuming that the system attaches the particles instantaneously as the solidification front advances. This might be the case in some situations such as in slow solidification processes or during the growth of crystal facets where the attachment dynamics is fast because it is limited by nucleation and defects. In general, however, it is reasonable to expect that the efficiency of the interface attachment process decreases as the front velocity increases, thus limiting the velocity of the solidification front.

As the solidification growth rate is related with the Gibbs' molar free energy difference between the phases Δg, the actual front velocity can be expressed as

$$\tilde{v} = \tilde{v}_{max}[1 - e^{-\frac{\Delta g}{RT_M}}], \tag{2.78}$$

where $\tilde{v}_{max}$ is the maximum velocity of the front for a hypothetically infinite driving force ($\Delta G \to \infty$). Expanding Eq. 2.78 for $\tilde{v} \ll \tilde{v}_{max}$, we have

$$-\frac{\Delta g}{RT_M} = \ln(1 - \frac{\tilde{v}}{\tilde{v}_{max}}) \approx -\frac{\tilde{v}}{\tilde{v}_{max}}. \tag{2.79}$$

Recovering the expression for Δg for pure substances (cf. Eq. 2.15), we have

$$\Delta g_{pure} = -\frac{L_m \Delta T}{T_M}, \tag{2.80}$$

Inserting the last expressions into Eq. 2.79 and noting that $\Delta T = T - T_M < 0$, we arrive to the conclusion that the kinetic attachment results in a reduction of the melting temperature given by

$$T = T_M - \frac{RT_M^2}{L_m \tilde{v}_{max}} \tilde{v}. \tag{2.81}$$

In the case of alloys, using the Clausius-Clapeyron in molar units $RT_M^2/L_m = m_L/(1-k)$, we can write the last expression in a more convenient form

$$T = T_M - \frac{m_L}{(1-k)\tilde{v}_{max}} \tilde{v}. \tag{2.82}$$

This effect is known as the *kinetic undercooling*, and the value of $\tilde{v}_{max}$ will be determined by the physical origin of the process which limits the attachment of the particles to the solid front. This attachment process might be more effective along some crystallographic planes of the solid, thus producing a *kinetic anisotropy* in the growth of the front. The Continuous Growth Model presented by Aziz and

Kaplan [Aziz88] and developed by Aziz, Kaplan and Boettinger in [Aziz94, Aziz96] presents two different scenarios for the limiting process: The first one appears when the *growth is limited by the diffusion* of the particles, and assumes that $\tilde{v}_{max}$ is proportional to the diffusivity at the liquid side

$$\tilde{v}_{max} \sim \frac{\tilde{D}}{\tilde{d}_0}, \tag{2.83}$$

predicting values for $\tilde{v}_{max}$ of the order of about 1 m/s. The second regime is called the *collision limited growth* and describes situations in which the particles attach to the solid crystalline structure following a fast collision process. In this case, $\tilde{v}_{max}$ is supposed to be proportional to the sound velocity in the liquid phase of the material, i.e.

$$\tilde{v}_{max} \sim \tilde{v}_{sound}, \tag{2.84}$$

predicting values of $\tilde{v}_{max}$ in the range of 10^3 m/s and therefore having a small effect in the kinetic undercooling of the front. We can now introduce the *interface mobility* $\tilde{\mu}$ as the proportionality constant relating the undercooling ($\Delta T < 0$) and the front velocity

$$\tilde{v} = -\tilde{\mu}\Delta T, \tag{2.85}$$

and its value, written for pure systems and alloys, is respectively given by

$$\tilde{\mu}_{pure} = \frac{L_m \tilde{v}_{max}}{R T_M^2} \tag{2.86}$$

$$\tilde{\mu}_{alloy} = \frac{(1-k)\tilde{v}_{max}}{m_L}. \tag{2.87}$$

Note that we have used the same Greek letter μ for the interface mobility and for the chemical potential. We have considered that as their meanings are rather different, it should not create any confusion.

2.2 Growth driven by diffusion

Once that the nucleation barrier has been exceeded by the initial seed (i.e., the seed has a radius larger than the critical radius), a stable solid phase grows into the metastable liquid. As we have seen, the force driving this growth is the free energy difference between the two phases. As the front evolves, this free energy excess is minimized by the system by means of a non-equilibrium process also called a *kinetic process*. Kinetic processes occur outside of equilibrium and are studied within the theoretical frame of the non-equilibrium statistical mechanics. In systems without other mass or energy flows (fluid, chemical, electrical, etc.), the kinetic process which allows the decrease of the free energy is diffusion. We can then say that a diffusion process controls the rate at which the solidification occurs. In the freezing of pure substances, the process is governed by thermal diffusion of the

heat released at the interface. In the solidification of mixtures, however, thermal diffusion is not the relevant process because the thermal diffusivity is typically of the order of $\tilde{D}_T \sim 10^{-5}$ m^2/s, whereas solute diffusivity is normally in the range of $\tilde{D}_{solutal} \sim 10^{-10}$ m^2/s. It can be therefore assumed that the temperature field adapts quasi-adiabatically to the alloy solidification front, and the diffusion of the solute concentration rejected by the solid and accumulated in the liquid can be considered as the main diffusive process driving the evolution of the front.

2.2.1 Heat diffusion

As the solidification front of a pure substance advances, the latent heat of the solid-liquid transformation is released to the system at the position of the interface. If the front moves with a velocity $\tilde{\mathbf{v}}$, the flux of heat is in the growth direction is given by $L_v \tilde{\mathbf{v}} \cdot \hat{n}$, being L_v the latent heat per unit volume of the substance. This flux is balanced with the heat flux produced by thermal diffusion, given by

$$[\tilde{\kappa}_S \nabla T|_S - \tilde{\kappa}_L \nabla T|_L]_{int} \cdot \hat{n}, \tag{2.88}$$

where $\tilde{\kappa}_S$ and $\tilde{\kappa}_S$ are the *thermal conductivities* of the solid and liquid phases respectively. Thermal conductivities are related with the thermal diffusivities by the relations

$$\tilde{D}_T^S = \frac{\tilde{\kappa}_S}{c_v^S}, \tag{2.89}$$

$$\tilde{D}_T^L = \frac{\tilde{\kappa}_L}{c_v^L}, \tag{2.90}$$

where c_v^S and c_v^L are the *specific heat per unit volume* of the solid and liquid respectively. The first term in Eq. 2.88 accounts for diffusive flux of heat going from the liquid to the solid, and the second one the corresponds to the thermal flux from the solid to the liquid. Imposing the *heat conservation law* across the interface, we arrive to the *moving boundary* condition

$$L_v \tilde{\mathbf{v}} \cdot \hat{n} = [\tilde{\kappa}_S \nabla T|_S - \tilde{\kappa}_L \nabla T|_L]_{int} \cdot \hat{n}, \tag{2.91}$$

where the gradients are evaluated at the solid-liquid interface. The heat released to the solid and liquid phases is distributed following the corresponding diffusion equations

$$\partial_t T_\alpha = \tilde{D}_T^\alpha \nabla^2 T_\alpha, \tag{2.92}$$

with $\alpha = S, L$. The solidification problem is determined by Eq.2.91 and Eq. 2.92, together with the local equilibrium condition at the interface, which is given by

$$T_{int}^S = T_{int}^L = T_M - \tilde{d}_0 \tilde{\kappa} - \frac{1}{\tilde{\mu}_{pure}} \tilde{v}. \tag{2.93}$$

2.2.2 Solute diffusion

In the solidification of mixtures, the solute rejected by the solid accumulates in a boundary layer ahead of the interface at the liquid side. If the velocity of the solidification front is $\mathbf{v}$, the flux of solute rejected from the solid to the liquid, is given by

$$(x_L - x_S)\tilde{\mathbf{v}} \cdot \hat{n} = x_L(1-k)\tilde{\mathbf{v}} \cdot \hat{n}, \tag{2.94}$$

where the right side term has been written by using the local equilibrium at the interface $x_S/x_L = k$. This flux of solute is balanced by the flux produced by the diffusion of the solute in the solid and liquid phases

$$[\tilde{D}_S \nabla x|_S - \tilde{D}_L \nabla x|_L] \cdot \hat{n}. \tag{2.95}$$

Imposing the *mass conservation condition* across the interface, we arrive to

$$x_L(1-k)\tilde{\mathbf{v}} \cdot \hat{n} = [\tilde{D}_S \nabla x|_S - \tilde{D}_L \nabla x|_L] \cdot \hat{n}. \tag{2.96}$$

The problem is the completed with the equations describing the diffusion of the solute in the solid and liquid

$$\partial_t x_\alpha = \tilde{D}_\alpha \nabla^2 x_\alpha, \tag{2.97}$$

with $\alpha = S, L$, and with the thermodynamical local equilibrium condition at the interface

$$T_{int}^L = T_M - m_L x_L - \tilde{d}_0 \tilde{\kappa} - \frac{1}{\tilde{\mu}_{alloy}} \tilde{v}, \tag{2.98}$$

where T_{int}^L indicates that the temperature is taken at the liquid side of the interface.

2.3 Thermodynamical equilibrium fluctuations

Real systems are always exposed to the effects of noise. The physical origin of the noise can be very diverse and ranges from the internal thermodynamical fluctuations to uncontrolled perturbations due to imperfections in the experimental set-up. In the description given in the preceding chapters, all the thermodynamical magnitudes characterizing the state of the system referred to the mean value of the real fluctuating variables.

As a consequence of the microscopical motion of the particles in the system, the real value of the thermodynamical magnitudes change continously around a certain mean value. In a near-equilibrium situation, it is possible to describe the system with the mean values and quantify the effect of the fluctuations by means of a proper probability distribution. In the case of a noise of internal origin, this probability distribution is usually Gaussian and it can be obtained from the statistical properties of the equilibrium fluctuations in the system. In order to characterize the equilibrium internal fluctuations for a given system, we use the

so-called *Fluctuation-Dissipation theorem*, which was proposed in 1902 by Einstein in his works on the Brownian motion [Einstein56]. This theorem, which is one of the most important results of thermodynamics and statistical physics, establishes a connection between the internal fluctuations of a system and the microscopic forces which determine the motion of its particles. In the particular case of a Brownian particle, it states that the fluctuations producing the random motion of the particle have the same origin than the dissipation of energy by friction which is produced when the particle is moved inside the system.

Crystal growth is a process in which the presence of fluctuations can modify significantly the dynamical evolution of the solid-liquid interface. Due to its non-linear and non-local nature, the dynamics of the solidification front is subjected to morphological instabilities which deform its shape and give rise to complex structures and patterns. In the presence of fluctuations, the apparition of these instabilities might be altered, and the properties of the final pattern will generally depend on the statistical properties of the noises present in the system. This is for instance the case of the formation of microstructures during alloy solidification; in this system, the wavelength of the final pattern is selected during early transient stages by means of a noise amplification process.

The preceding arguments point out the necessity of introducing thermal and solutal fluctuations into the phenomenological description of the system. Therefore, the Sharp-Interface description must include fluctuations into both the heat and mass diffusion equations and in the conservation laws across the interface. As an additional source of interfacial noise, we will consider the fluctuations produced by the random attachment kinetics of atoms from the liquid to the solid phase.

2.3.1 Temperature bulk fluctuations

For a given thermodynamical magnitude ϕ, the probability that the system takes a value of ϕ between ϕ and $\phi + d\phi$ is given by $\Omega(\phi)d\phi$, where $\Omega(\phi)$ is given by

$$\Omega(\phi) = Ae^{-\Delta W(\phi)/k_B T}, \tag{2.99}$$

where A is a constant and $\Delta W(\phi)$ stands for the minimum amount of work needed to produce an infinitesimal reversible change in ϕ. In a reversible process, this amount of work is given by the variation of the Gibbs' free energy ΔG

$$\Delta W = \Delta G = \Delta U - T\Delta S + P\Delta V, \tag{2.100}$$

where ΔV, ΔU and ΔS are the volume, internal energy and entropy variations respectively. Expanding ΔW up to second order around the equilibrium values, we have, at second order in Δn,

$$\Delta W \approx \frac{1}{2}\left(\frac{\partial^2 U}{\partial S^2}\right)(\Delta S)^2 + 2\left(\frac{\partial^2 U}{\partial S \partial V}\right)\Delta S \Delta V + \left(\frac{\partial^2 U}{\partial V^2}\right)(\Delta V)^2. \tag{2.101}$$

For a process at constant volume ($\Delta V = 0$), and using the thermodynamical relations

$$\left(\frac{\partial^2 U}{\partial S^2}\right) = \frac{T}{c_v} \tag{2.102}$$

$$\Delta S = \frac{c_v \Delta T}{T}, \tag{2.103}$$

where c_v is the specific heat at constant volume, we obtain an expression for Ω in Eq. 2.99

$$\Omega = A e^{-\frac{c_v (\Delta T)^2}{2 k_B T^2}}. \tag{2.104}$$

Assuming that the statistics of the fluctuations of ϕ obey a Gaussian distribution, we have

$$\Omega(\phi) = \frac{1}{\sqrt{2\pi \langle \phi^2 \rangle}} e^{-\frac{(\phi - \langle \phi \rangle)^2}{2\langle \phi^2 \rangle}}. \tag{2.105}$$

Taking $\phi = \Delta T$ and comparing Eq. 2.104 with Eq. 2.105, we obtain the mean and the variance of the thermal fluctuations

$$\langle \Delta T \rangle = 0 \tag{2.106}$$

$$\langle (\Delta T)^2 \rangle = \frac{k_B T^2}{c_v}. \tag{2.107}$$

2.3.2 Solute bulk fluctuations

We can use the same procedure to determine the statistical properties of the solute fluctuations in the system. Let us consider a fluctuation consisting in the isothermal, isobaric reversible change of the solute concentration in an amount Δn moles. The work ΔW to produce this fluctuation is now given by

$$\Delta W = \Delta G - \mu \Delta n, \tag{2.108}$$

where ΔG is the change in the Gibbs' free energy and $\mu \Delta n$ accounts for the work which has been done in order to change the concentration. Expanding the Gibbs' free energy around equilibrium, we have

$$\Delta G \approx \left(\frac{\partial G}{\partial n}\right) \Delta n + \frac{1}{2}\left(\frac{\partial^2 G}{\partial n^2}\right) (\Delta n)^2, \tag{2.109}$$

and noting that $\mu = \frac{\partial G}{\partial n}$, we obtain

$$\Delta W = \frac{1}{2}\left(\frac{\partial \mu}{\partial n}\right) (\Delta n)^2, \tag{2.110}$$

which, substituted in Eq. 2.99, gives

$$\Omega = A e^{-\frac{\left(\frac{\partial \mu}{\partial n}\right)}{2 k_B T} (\Delta n)^2}. \tag{2.111}$$

Identifying this with Eq. 2.105 for $\phi = \Delta n$, we obtain the statistical properties of the solute fluctuations

$$\langle \Delta n \rangle = 0 \tag{2.112}$$

$$\langle (\Delta n)^2 \rangle = \frac{k_B T}{(\frac{\partial \mu}{\partial n})}. \tag{2.113}$$

For a n mol solution with n_B moles of solute, we define the solute concentration as the molar fraction of the solute $x = n_B/n$, and the fluctuations in the concentration are determined by

$$\langle \Delta x \rangle = 0 \tag{2.114}$$

$$\langle (\Delta x)^2 \rangle = \frac{k_B T}{n(\frac{\partial \mu}{\partial x})}. \tag{2.115}$$

In the case of a dilute solution, we have $\frac{\partial \mu}{\partial x} \approx RT/x$ (cf. Eq. 2.33), and the solute fluctuations are given by

$$\langle (\Delta x)^2 \rangle = \frac{x}{N}, \tag{2.116}$$

where $N = nN_0$ is the total number of particles in the system and N_0 the Avogadro's number. If we prefer to write the solute concentration as the number of solute molecules per unit volume $\tilde{c}$, we use the transformation

$$\tilde{c} = \frac{N_0}{v_m} x, \tag{2.117}$$

where $v_m = Z/\rho$ is the molar volume of this substance, being Z and ρ the molecular weight and density of the dissolvent. We can then write Eq. 2.116 in terms of $\tilde{c}$, obtaining

$$\langle (\Delta \tilde{c})^2 \rangle = \frac{\tilde{c}}{n v_m}, \tag{2.118}$$

and noting that nv_m is the total volume of the system ΔV, we finally obtain

$$\langle (\Delta \tilde{c})^2 \rangle = \frac{\tilde{c}}{\Delta V}. \tag{2.119}$$

2.3.3 Heat and mass stochastic currents

Thermal and solute fluctuations result in additional heat and mass stochastic currents at the bulk phases which must be considered in the description of the system. In a first approximation, these noises can be assumed to be uncorrelated in space (white noise) and time (Markov process). During the solidification of a pure substance, the effect of thermal fluctuations is a stochastic heat current $\mathbf{q}_\alpha(\mathbf{r}, t)$ which acts at each point of the system and whose statistical properties are given by the fluctuation-dissipation theorem [Rytov56, Cherepanova76]

$$\langle q_\alpha^i(\mathbf{r}, t) q_\alpha^j(\mathbf{r}', t') \rangle = \frac{2\tilde{D}_T^\alpha k_B T^2}{c_v^\alpha} \delta_{ij} \delta(\mathbf{r}' - \mathbf{r}) \delta(t' - t), \tag{2.120}$$

where $\alpha = S, L$ and i, j denote components of $\mathbf{q}_\alpha$. The diffusion equation Eq. 2.92 is then modified by adding the stochastic current to the diffusion current, and the temperature field obeys the stochastic diffusion equation

$$\partial_t T_\alpha = \tilde{D}_T^\alpha \nabla^2 T_\alpha - \nabla \cdot \mathbf{q}_\alpha. \tag{2.121}$$

The heat conservation at the interface Eq. 2.91 must also be modified to account for the extra stochastic current across the interface in the total heat balance

$$L_v \tilde{\mathbf{v}} \cdot \hat{n} = [\tilde{\kappa}_S \nabla T|_S - \tilde{\kappa}_L \nabla T|_L]_{int} \cdot \hat{n} - [c_v^S \mathbf{q}_S - c_v^L \mathbf{q}_L] \cdot \hat{n} \tag{2.122}$$

where $\mathbf{q}_S$ and $\mathbf{q}_L$ are the fluctuating currents at the solid and liquid phases respectively.

In alloys, we proceed in a similar way by modifying both the diffusion equation Eq. 2.97 and the mass conservation equation Eq. 2.96 in order to include the corresponding solute stochastic current $\mathbf{j}$. The fluctuating version of the problem is then given by

$$\partial_t x_\alpha = \tilde{D}_\alpha \nabla^2 x_\alpha - \nabla \cdot \mathbf{j}_\alpha, \tag{2.123}$$

$$x_L(1-k)\tilde{\mathbf{v}} \cdot \hat{n} = [\tilde{D}_S \nabla x_\alpha|_S - \tilde{D}_L \nabla x_\alpha|_L] \cdot \hat{n} - [\mathbf{j}_S - \mathbf{j}_L] \cdot \hat{n}, \tag{2.124}$$

where $\alpha = S, L$ and the properties of the solute stochastic current $\mathbf{j}_\alpha$ are given by

$$\langle j_\alpha^i(\mathbf{r}, t) j_\alpha^j(\mathbf{r}', t') \rangle = \frac{2\tilde{D}_\alpha x_\alpha v_m}{N_0} \delta_{ij} \delta(\mathbf{r}' - \mathbf{r}) \delta(t' - t). \tag{2.125}$$

The heat and solute stochastic processes introduced in the last expressions account for bulk fluctuations which has an effect in the heat and mass balance across the interface.

2.3.4 Interfacial fluctuations associated to kinetic attachment

The heat and mass stochastic currents which have been introduced in the last two sections must be considered as bulk currents which affect to a large number of particles in the system. However, as pointed out by A. Karma in Ref. [Karma93a], the interfacial kinetic attachment process described in section 2.1.4 has associated a stochastic interfacial force which must also be taken into account. After some theoretical arguments concerning the analytical description of the interface, he arrived to the result that the effect of the interfacial fluctuations results as an additive noise $\eta(\mathbf{r}, t)$ in the local equilibrium condition Eq.2.61, which reads

$$T = T_M^A - m_L x_B^L - \frac{\tilde{v}}{\tilde{\mu}} + \eta(\mathbf{r}, t), \tag{2.126}$$

where $\tilde{\mu}$ is the interface mobility anf the statistical properties of the noise are given by

$$\langle \eta(\mathbf{r},t)\eta(\mathbf{r}',t')\rangle = 2\frac{k_B T^2}{\tilde{\mu}L}\frac{\delta(\mathbf{r}-\mathbf{r}')\delta(t-t')}{\sqrt{1+|\nabla z_s(\mathbf{r},t)|^2}}, \tag{2.127}$$

being $z = z_s(\mathbf{r},t)$ the implicit equation for the position of the solid-liquid surface.

Chapter 3

Moving Boundary problems for solidification

This chapter is devoted to introduce the mathematical equations governing the dynamics of a solidification process. Section 3.2 is dedicated to describe the free solidification of an undercooled pure substance, and Section 3.3 is devoted to the directional solidification of a supersaturated mixture. In both cases, we will study the moving boundary equations and their basic solutions in the case of having a planar solidification front. The case of directional solidification will be studied with more detail, and in Sec. 3.3.4 the constitutional undercooling criterion is introduced in order to explain the basic mechanisms by which the interface becomes morphologically unstable. At the end of the chapter, a basic linear stability analysis of the directional solidification problem is performed (Mullins-Sekerka), obtaining the stationary growth rate for the different perturbation wavelengths.

3.1 Introduction

As we have seen in the previous chapter, the phenomenological formulation of a solidification problem involved equations for:

i) Heat/mass diffusion at the solid and liquid bulk phases (Eq. 2.92 for pure substances and Eq. 2.97 for alloys).

ii) Local thermodynamic equilibrium conditions at the interface (Eq. 2.93 for pure systems and Eq. 2.98 for alloys).

iii) Heat/mass conservation across the interface (Eq. 2.91 for pure systems and Eq. 2.96 for alloys).

These sort of mathematical problems are called *moving boundary problems* , since the solution of the diffusion bulk equations (i) is found by imposing the boundary

conditions (ii) at the moving boundary whose motion is determined by (iii). In such a problems, the bulk and interfacial equations are dynamically related and must be solved simultaneously. The above equations (i-iii), supplemented with the convenient initial and boundary conditions, define a quantitative physical description of the solidification process. Moving boundary problems are also called *Stefan problems*, in reference to the Austrian physicist Josef Stefan, who derived a differential equation for the position of a polar ice front by imposing the heat balance across the solid-liquid interface [Stefan91]. For this reason, condition (iii) is also known as the *Stefan condition*. In fact, the problem of a growing phase transformation was already proposed by Lamé and Clapeyron in Ref. [Lamé31]. An improved analytical solution by means of a similarity analysis was obtained by F. Neumann in 1860 [Carlslaw50].

Besides solidification systems, moving boundary problems are suited to describe many scientific and technological processes such as flame propagation, crack dynamics or oil drilling. For a detailed description of analytical and numerical techniques for moving boundary problems, we refer to Ref. [Crank84]. In the context of solidification processes, the moving boundary formulations are called *Sharp-Interface models*, because they describe the solid-liquid interface as an atomically thin interface. The next sections are dedicated to describe the Sharp-Interface equations for the most relevant solidification processes, namely the solidification of an undercooled pure melt and the directional solidification of a dilute binary alloy.

3.2 Free growth from an undercooled pure melt

3.2.1 Sharp-Interface equations

Grouping the results presented in the previous sections, the equations describing the solidification of an undercooled pure melt are given by

$$\partial_{\tilde{t}} T_\alpha = D_T^\alpha \tilde{\nabla}^2 T_\alpha, \tag{3.1}$$

$$L_v \tilde{\mathbf{v}} \cdot \hat{n} = [\tilde{\kappa}_S \tilde{\nabla} T|_S - \tilde{\kappa}_L \tilde{\nabla} T|_L] \cdot \hat{n}, \tag{3.2}$$

$$T_{int} = T_M - \tilde{d}_0 \tilde{\kappa} - \frac{1}{\tilde{\mu}} \tilde{v}, \tag{3.3}$$

where $\tilde{d}_0 = \tilde{\sigma} T_M / L_v$ is the *thermal capillary length* introduced in Section 2.1.3 and $\tilde{\mu} = L_m v_{max}/(R T_M^2)$ is the kinetic mobility introduced in section 2.1.4.

3.2.2 Analytical similarity solution

Only in few simple cases, analytical solutions can be obtained for Stefan problems. We shall consider the simplest Stefan problem, which describes the one dimensional solidification of an undercooled pure melt. A pure substance occupies a

semi-infinite region $\tilde{z} \geq 0$ as shown in Figure 3.1. An infinitesimally thin sheet of solid at temperature $T = T_M$ is initially located a $\tilde{z} = 0$, and the liquid at $\tilde{z} > 0$ is undercooled at a temperature T_∞ below its melting temperature with an undercooling $\Delta T = T_M - T_\infty$. The liquid phase is in a metastable state, and the solid phase will grow in the $\tilde{z} > 0$ direction occupying the semi-infinite region. As the temperature at the solid is maintained constant, there is no heat flux in the solid. If $\tilde{z} = \tilde{\xi}(\tilde{t})$ is the position of the solid-liquid interface at time $\tilde{t}$, the equations describing this process are given by

$$\partial_{\tilde{t}} T_L = \tilde{D}_L^T \, \partial_{\tilde{z}}^2 T_L, \tag{3.4}$$

at the liquid bulk $\tilde{z} > \tilde{\xi}(\tilde{t})$, and

$$L_v \frac{d\tilde{\xi}(\tilde{t})}{d\tilde{t}} = -\tilde{\kappa}_L \partial_{\tilde{z}} T_L|_{\tilde{z}=\tilde{\xi}(\tilde{t})} \tag{3.5}$$

$$T_S(\tilde{z} = \tilde{\xi}(\tilde{t}), \tilde{t}) = T_L(\tilde{z} = \tilde{\xi}(\tilde{t}), \tilde{t}) = T_M \tag{3.6}$$

at the interface $\tilde{z} = \tilde{\xi}(\tilde{t})$. Additionally, we have the far-field conditions

$$T_L(\tilde{z} \to \infty) = T_\infty \tag{3.7}$$

$$T_S(\tilde{z} \leq \tilde{\xi}(\tilde{t})) = T_M. \tag{3.8}$$

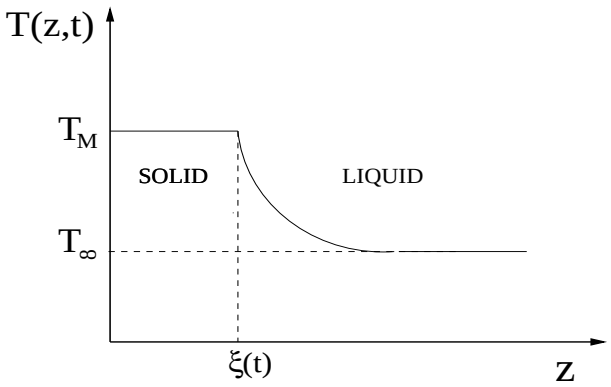

Figure 3.1: Temperature profile during the solidification of an undercooled pure melt in a semi-infinite region

It is easy to check that equations 3.4 and 3.7 are satisfied by the similarity solution

$$T_L(\tilde{z}, \tilde{t}) = T_\infty + A \, \mathrm{erfc}\left(\frac{\tilde{z}}{2\sqrt{\tilde{D}_L^T \tilde{t}}}\right), \tag{3.9}$$

where $\mathrm{erfc}(x) = \frac{2}{\sqrt{\pi}} \int_x^\infty e^{-y^2} dy$ is the complementary error function. The constant A in Eq. 3.9 is determined by imposing $T_L(\tilde{z} = \tilde{\xi}(\tilde{t})) = T_M$ from Eq. 3.6, and is given by

$$A = \frac{\Delta T}{\mathrm{erfc}\left(\frac{\tilde{\xi}(\tilde{t})}{2\sqrt{\tilde{D}_L^T \tilde{t}}}\right)}. \tag{3.10}$$

As A is a constant, we have, for consistency, that

$$\frac{\tilde{\xi}(\tilde{t})}{\sqrt{\tilde{D}_L^T \tilde{t}}} = \alpha, \tag{3.11}$$

where α is a constant which determines the growth velocity of the front for a given undercooling $\Delta T = T_M - T_\infty$. In order to determine the value of α, we impose the Stefan condition Eq. 3.5 to the solution Eq. 3.9. Noting that $\tilde{D}_L^T = \tilde{\kappa}_L / c_v^L$ and using Eq. 3.11, we obtain the relation

$$\sqrt{\pi}\ \alpha\ \mathrm{erfc}(\alpha)\ e^{\alpha^2} = \frac{\Delta T c_v^L}{L_v}. \tag{3.12}$$

It is interesting to note here that the term at the right side of Eq. 3.12 coincides with the expression obtained in section 2.1.1 for the Gibbs' free energy variation driving the solidification process of an undercooled pure substance. Relation Eq. 3.12 can be understood as the law which determines the growth velocity α for a given driving force $\Delta T c_v^L / L_v$, and the ratio $S = L_v / \Delta T c_v^L$ is also known as the *Stefan number*. The validity of the relation 3.12 is restricted to values of the inverse of the Stefan number $S^{-1} \in [0, 1]$ and therefore for undercoolings ΔT smaller than L_v / c_v^L. This is shown in Fig. 3.2, where it can be observed that Eq. 3.12 has no solutions for $S^{-1} \geq 1$. Moreover, for $S^{-1} \to 1^-$, the value of α tends to infinity and the solution predicts erroneously infinitely large growth velocities for a finite undercooling ΔT. These limitations are due to the breakdown of the local equilibrium condition and can be overcame by introducing finite interfacial attachment dynamics described in section 2.1.4. Following identical procedure, a similarity solution for the resulting model with the modified local equilibrium condition can be easily obtained [Davis01], predicting three different growth regimes depending on the value of the Stefan number

$$\tilde{\xi}(\tilde{t}) \sim \sqrt{\tilde{t}}\ , \text{ for } S^{-1} < 1, \tag{3.13}$$

$$\tilde{\xi}(\tilde{t}) \sim \tilde{t}\sqrt{\tilde{t}}\ , \text{ for } S^{-1} = 1, \tag{3.14}$$

$$\tilde{\xi}(\tilde{t}) \sim \tilde{t}\ , \text{ for } S^{-1} > 1. \tag{3.15}$$

In spite of their fundamental interest, the analytical approaches for moving boundary problems are limited to relatively simple situations. In fact, Stefan

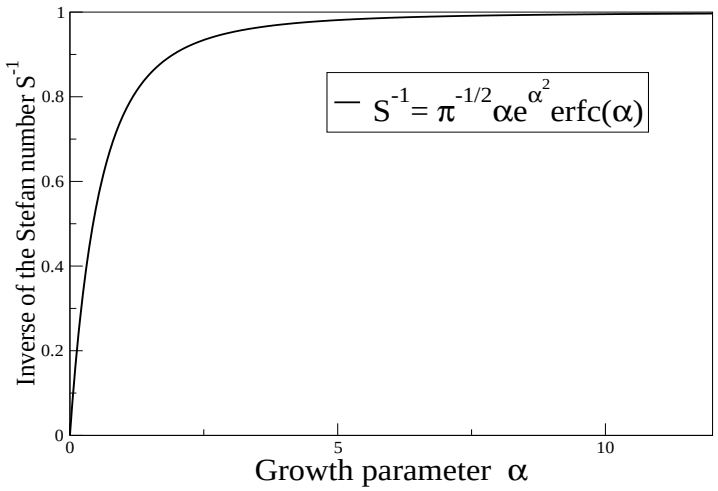

Figure 3.2: Dependence of the growth parameter α with the inverse of the Stefan number S^{-1}. The validity of the similarity solution is restricted to undercoolings satisfying $S^{-1} < 1$.

problems are in general three-dimensional and, as a consequence of their non-linear and non-local character, present complex interfacial structures such as dendrites or spikes, making it necessary to use quasi-analytical, perturbative or numerical approaches to study its dynamical evolution.

3.3 Directional solidification of a dilute binary solution

3.3.1 The directional solidification process

Directional solidification is a technological process which allows to control the advance of an alloy solidification front. The set-up for a directional solidification experiment is shown in Fig. 3.3. A dilute binary solution sample is pulled with a constant velocity $\tilde{\mathbf{v}}_p = -\tilde{v}_p\hat{\mathbf{z}}$ towards the cold region of an externally imposed stationary temperature gradient $\tilde{\nabla}T = \tilde{G}\hat{\mathbf{z}}$. If the initial stationary melt has a uniform concentration c_∞, the regions located at temperatures smaller than $T = T_M - m_L c_\infty$ will solidify creating a solid-liquid interface separating the two bulk phases. Then the sample is pulled towards the cold region of the gradient,

producing the controlled advance of the solid-liquid front. As it will be discussed in Section 3.3.4, the planar solid-liquid interface remains morphologically stable for small pulling velocities, whereas for larger growth rates the front becomes instable presenting different kinds of interfacial instabilities.

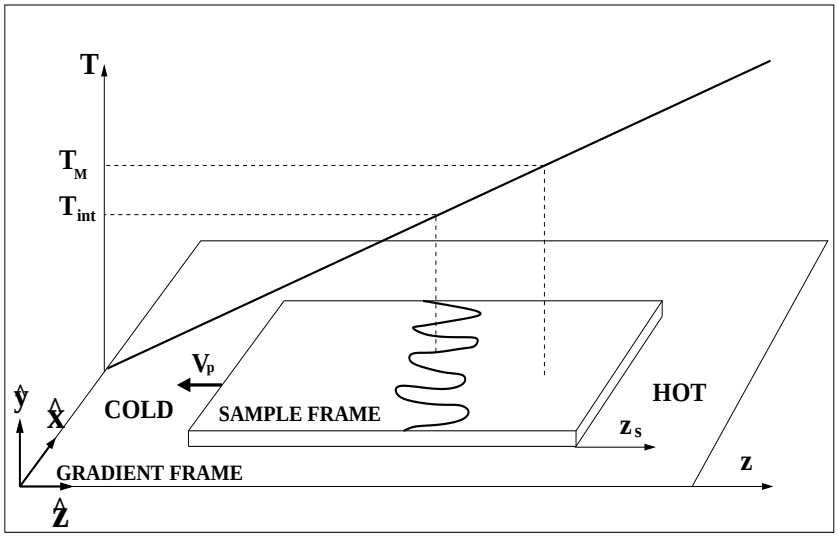

Figure 3.3: Experimental set-up of a directional solidification experiment. The mixture sample is pulled at constant velocity v_p under an externally imposed temperature gradient.

Problem setting and definitions

Before entering in the mathematical description of the problem, we would like to remark some issues related with the choice of fields, reference frames and scaling of the variables:

i) We describe the solute concentration at a certain point of the sample $c(\tilde{\mathbf{r}}, \tilde{t})$ as the molar fraction of solute, defined in Sec. 2.1.2 as the ratio between the number of moles of solute n_B and the total number of moles of the solution, n, i.e.,

$$c(\tilde{\mathbf{r}}, \tilde{t}) = \frac{n_B}{n}. \tag{3.16}$$

This measure of the solute concentration can be easily related with the *physical concentration* $\tilde{c}(\tilde{\mathbf{r}}, \tilde{t})$, denoted with a tilde and defined as number of solute molecules per unit volume of the solution. Noting that 1 mol of solute has N_0 particles of solute and that the volume of 1 mol of solution is given by the molar volume $v_m = Z/\rho$, these two measures for the concentration can

be easily related by

$$\tilde{c}(\tilde{\mathbf{r}},\tilde{t}) = \frac{N_0}{v_m} c(\tilde{\mathbf{r}},\tilde{t}). \tag{3.17}$$

ii) We will use the gradient frame to refer to all the distances and velocities, adding explicitely the subscript "s" when referring to variables measured in the moving frame of the sample. Positions and velocities in the sample and gradient frames are therefore related by the Galilean transformations

$$\tilde{\mathbf{r}} = \tilde{\mathbf{r}}_s - \tilde{\mathbf{v}}_p \tilde{t}, \tag{3.18}$$
$$\tilde{\mathbf{v}} = \tilde{\mathbf{v}}_s - \tilde{\mathbf{v}}_p. \tag{3.19}$$

iii) The origin of the moving sample frame is chosen in such a way that the initial value of the system temperature at the origin ($\tilde{z}=0$, $\tilde{t}=0$) is equal to

$$T(\tilde{z}=0,\tilde{t}=0) = T_M - m\frac{c_\infty}{k}. \tag{3.20}$$

iv) Tilted variables and parameters refer to the physical, unscaled values of the magnitudes.

The initial recoil transient

Let us now consider a more detailed description of the directional solidification process. Figures Fig. 3.4, Fig. 3.5 and Eq. 3.6 describe the main idea of the experimental procedure. At $\tilde{t}=0$, a sample with concentration c_∞ is located under a fixed external temperature profile given by

$$T(\tilde{\mathbf{r}}) = T_M - m_L\frac{c_\infty}{k} + \tilde{G}\tilde{z}. \tag{3.21}$$

Figure Fig. 3.4 shows the sample frame under the external gradient at $\tilde{t}=0$. Under the effect of the external gradient, the system reaches equilibrium by creating an interface which separates a solid region with concentration kc_∞ and a liquid region with concentration c_∞. This initial equilibrium interface, as can be shown in Fig. 3.4, is located at

$$\tilde{z} = \tilde{l}_T = \frac{m_L \Delta c_0}{\tilde{G}}, \tag{3.22}$$

which is the position of the sample at a temperature of $T_i = T_M - m_L c_\infty$. The parameter $\tilde{l}_T$ is known as the *thermal length* and defines a new physical length in the solidification problem. The bulk regions at the left and right of this position will be therefore occupied by solid and liquid phases respectively. Once the planar solidification front is created, the sample is pulled at a constant velocity $-\tilde{v}_p$ towards the cold region of the gradient. This motion results in a progressive introduction of the sample into the cold region of the gradient, therefore producing the growth of the solid phase in the system and the consequent advance of the solidification front.

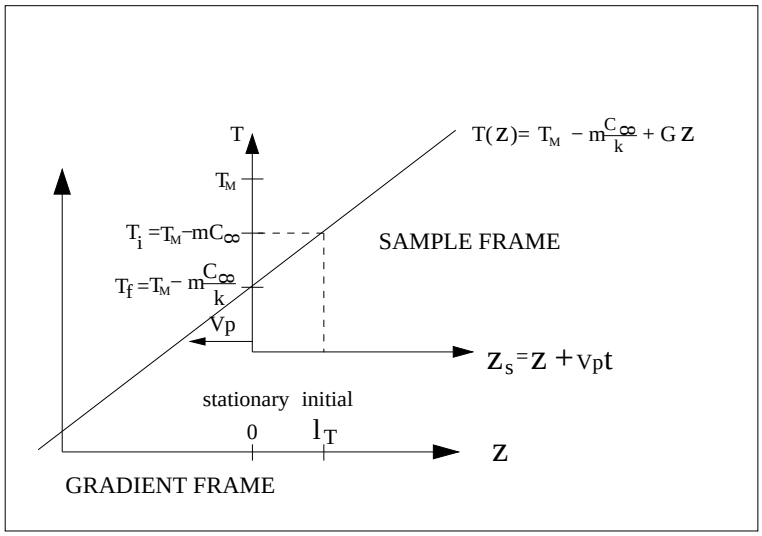

Figure 3.4: Motion of the sample under the temperature gradient. The frames are represented here at $\tilde{t} = 0$. In the gradient frame, the initial front position is $\tilde{\xi}(\tilde{t} = 0) = \tilde{l}_T$, and the stationary position is $\tilde{\xi}(\tilde{t} \to \infty) = 0$.

As the solidification front evolves, not all the solute particles of the liquid phase can be incorporated at the structure of the solid phase. A certain amount of solute is then rejected from the solid, producing the creation of a boundary layer at the liquid side of the advancing front as indicated in Fig. 3.6. As a consequence of this phenomena, the solute concentration is increased in the solid and liquid regions near the interface. The accumulation of solute continues until the concentration at the solid and liquid sides of the front reach solute concentrations of c_∞ and c_∞/k, respectively (cf. Eq. 2.57). The values of the final concentrations and the temperature at the front position are determined by the phase diagram shown in Fig. 3.5. At the end of this transient process, the solute boundary layer is totally formed and the solid-liquid interface is located at $\tilde{z} = 0$ where the temperature is T_f. As shown in Fig. 3.6, an observer at the gradient frame will see that the front moves back from $\tilde{z} = \tilde{l}_T$ to $\tilde{z} = 0$. This solute redistribution process in known as the *initial recoil transient*. We can describe the position of the solidification surface in the gradient frame with the implicit relation $\tilde{z} = \tilde{\xi}(\tilde{\rho}, \tilde{t})$, and the points at the solid-liquid surface are pointed by the vector

$$\tilde{\mathbf{r}}^{int}(\tilde{t}) = \tilde{\rho} + \tilde{\xi}(\tilde{\rho}, \tilde{t})\hat{\mathbf{z}}, \tag{3.23}$$

where we have used the notation $\tilde{\mathbf{r}} = \tilde{\rho} + \tilde{z}\hat{\mathbf{z}}$, being $\tilde{\rho} = \tilde{x}\hat{\mathbf{x}} + \tilde{y}\hat{\mathbf{y}}$ the spatial components in the orthogonal directions to $\hat{\mathbf{z}}$. For a planar front, the interface position will not depend on $\tilde{\rho}$ and we have $\tilde{z} = \tilde{\xi}(\tilde{t})$. At $\tilde{t} = 0$, the planar front is

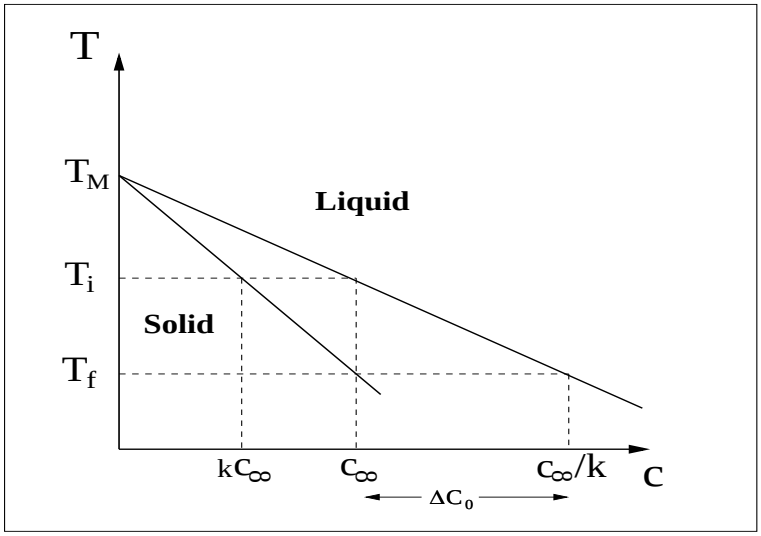

Figure 3.5: Phase diagram of a dilute alloy. The initial and final temperatures are determined by the initial and final solute concentrations at the liquid side of the interface.

located at

$$\tilde{\xi}(\tilde{t}=0)=\tilde{l}_T, \tag{3.24}$$

and as time evolves it moves back until its position for $\tilde{t}\to\infty$ is given by

$$\tilde{\xi}(\tilde{t}\to\infty)=0. \tag{3.25}$$

From the sample reference frame, the position of the front ranges from $\tilde{\xi}_s(0)=\tilde{l}_T$ at $\tilde{t}=0$, to $\tilde{\xi}_s(\infty)=-\tilde{v}_p\tilde{t}$ at $\tilde{t}\to\infty$. Equivalently, the gradient and sample frame velocities range from $\dot{\tilde{\xi}}(0)=-\tilde{v}_p$ to $\dot{\tilde{\xi}}(\infty)=0$ and from $\dot{\tilde{\xi}}_s(0)=0$ to $\dot{\tilde{\xi}}_s(\infty)=\tilde{v}_p$.

3.3.2 Sharp-Interface equations

In the sample frame, the diffusion equations at the bulk phases are given by

$$\partial_{\tilde{t}}c_\alpha-\tilde{v}_p\partial_{\tilde{z}}c_\alpha=\tilde{D_\alpha}\tilde{\nabla}^2c_\alpha, \tag{3.26}$$

where $\alpha=S,L$ labels the solid and liquid phases respectively.

The local equilibrium conditions at the interface, taking into account capillary and kinetic effects (cf. Eqs. 2.57, 2.76 and 2.85), are given by

$$c_S(\tilde{\mathbf{r}}^{int},\tilde{t})=kc_L(\tilde{\mathbf{r}}^{int},\tilde{t}) \tag{3.27}$$

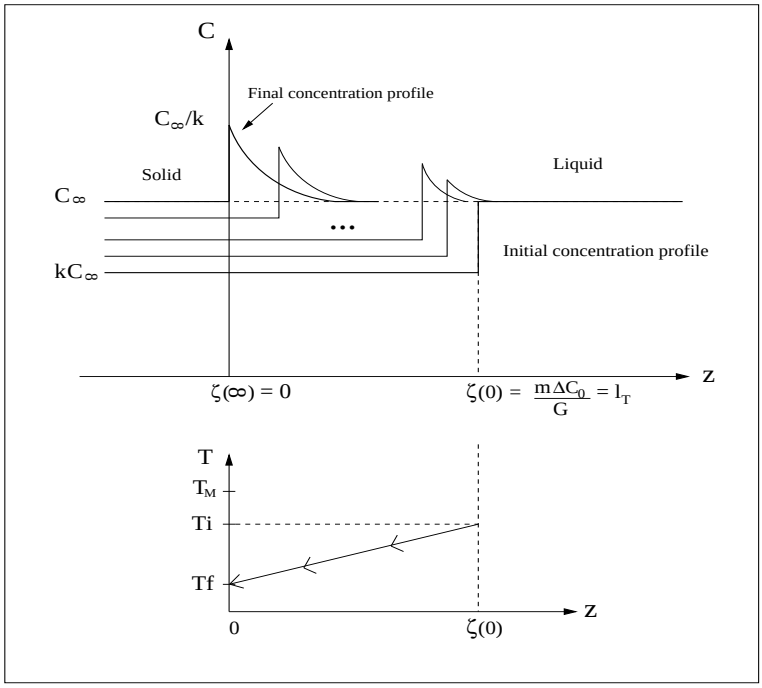

Figure 3.6: Solute profiles and front positions during the initial solute redistribution transient in directional solidification.

$$T(\tilde{\mathbf{r}}^{int},\tilde{t}) = T_M - m_L c_L(\tilde{\mathbf{r}}^{int},\tilde{t}) - \tilde{d}_0\tilde{\kappa}(\tilde{\mathbf{r}}^{int},\tilde{t}) - \frac{1}{\tilde{\mu}}\,(\dot{\tilde{\xi}}(\tilde{\rho},\tilde{t}) + \tilde{v}_p), \tag{3.28}$$

where $\tilde{d}_0 = \frac{\tilde{\sigma}T_M}{L_v}$ is the capillary length introduced in Section 2.1.3, $\tilde{\sigma}$ is the surface energy, $\tilde{\kappa}$ the local interface curvature and $\tilde{\mu} = (1-k)v_{max}/m_L$ the interface mobility defined in section 2.1.4 (cf. Eq. 2.87).

Note that the Gibbs-Thomson equation Eq. 3.28 accounts for kinetic effects during the whole transient. At $\tilde{t} = 0$ there is no kinetic effects ($\dot{\tilde{\xi}}(0) = -\tilde{v}_p$), and in the stationary regime are determined by the pulling velocity ($\dot{\tilde{\xi}}(\infty) = 0$).

The last equation accounts for the mass conservation across the interface

$$\hat{\mathbf{n}}\cdot[\tilde{D}_S\tilde{\nabla}C_S - \tilde{D}_L\tilde{\nabla}c_L]_{\tilde{\mathbf{r}}=\tilde{\mathbf{r}}^{int}} = c_L(\tilde{\mathbf{r}}^{int},\tilde{t})\;(1-k)(\dot{\tilde{\xi}}(\tilde{\rho},\tilde{t}) + \tilde{v}_p). \tag{3.29}$$

Combining Eq. 3.28 and Eq. 3.21, a closed expression can be obtained for the solute concentration at the liquid side of the interface

$$c_L(\tilde{\mathbf{r}}^{int},\tilde{t}) = \frac{c_\infty}{k} - \frac{\tilde{G}}{m_L}\tilde{\xi}(\tilde{t}) - \tilde{d}_0^c\tilde{\kappa} - \tilde{\beta}\;(\dot{\tilde{\xi}}(\tilde{\rho},\tilde{t}) + \tilde{v}_p), \tag{3.30}$$

where we have introduced the *kinetic coefficient* defined by

$$\tilde{\beta} = \frac{1}{m_L \tilde{\mu}}, \tag{3.31}$$

and the *chemical capillary length* by

$$\tilde{d}_0^c = \frac{\tilde{d}_0}{m_L}. \tag{3.32}$$

From Eq. 3.30 it is clear that, for a planar interface ($\tilde{\kappa} = 0$), the kinetic undercooling produces a reduction of the final position of the front, which instead of being located $\tilde{\xi}(\infty) = 0$, is now located at

$$\tilde{\xi}(\infty) = -\frac{\tilde{\beta} m_L}{\tilde{G}} \tilde{v}_p. \tag{3.33}$$

Dimensionless equations

The values of the diffusion coefficient at the liquid $\tilde{D}_L$ and the pulling velocity $\tilde{v}_p$ permit to define natural space and time scales for the solidification problem. We introduce the *diffusion length* $\tilde{l}$ and the *diffusion time* $\tilde{\gamma}$ as

$$\tilde{l} = \frac{\tilde{D}_L}{\tilde{v}_p} \tag{3.34}$$

$$\tilde{\gamma} = \frac{\tilde{D}_L}{\tilde{v}_p^2}, \tag{3.35}$$

and use them to define the new scaled variables $\mathbf{r} = \tilde{\mathbf{r}}/\tilde{l}$ and $t = \tilde{t}/\tilde{\gamma}$. Writing the model defined by Eqs. 3.26-3.29 in terms of the scaled variables, we obtain

$$\begin{aligned}
\partial_t c_S - \partial_z c_S &= D_s \nabla^2 c_S, && (3.36)\\
\partial_t c_L - \partial_z c_L &= \nabla^2 c_L && (3.37)\\
k \cdot c_L^{int} &= c_S^{int} && (3.38)\\
T^{int} &= T_M - m_L c_l^{int} - d_0 \kappa(\mathbf{r}) - \frac{1}{\mu}(1 + \dot{\xi}(\rho, t)), && (3.39)\\
\hat{\mathbf{n}} \cdot [D_s \nabla c_S - \nabla c_L]^{int} &= c_l^{int}(1-k)(1 + \dot{\xi}(\rho, t)),, && (3.40)
\end{aligned}$$

where we the new scaled parameters are written without the tilde and are defined by the relations

$$\mu = \tilde{\mu}\frac{\tilde{l}}{\tilde{\gamma}}, \tag{3.41}$$

$$d_0 = \frac{\tilde{d}_0}{l}, \tag{3.42}$$

$$D_s = \tilde{D}_s\frac{\tilde{\gamma}}{\tilde{l}^2}, \tag{3.43}$$

$$\kappa = \frac{\tilde{\kappa}}{\tilde{l}} \tag{3.44}$$

$$\xi = \frac{\tilde{\xi}}{\tilde{l}}, \tag{3.45}$$

$$\dot{\xi} = \dot{\tilde{\xi}}\frac{\tilde{\gamma}}{\tilde{l}}, \tag{3.46}$$

The temperature profile in the new variables takes the form

$$T(\mathbf{r},t) = T_M - m_L\frac{c_\infty}{k} + Gz(t), \tag{3.47}$$

where $G = \tilde{G}\tilde{l}$ and z is the scaled position in the gradient frame. The scaled equation for the interface concentration is therefore

$$c_L^{int} = \frac{c_\infty}{k} - \frac{G}{m_L}\xi(t) - d_0^c\kappa - \beta\ (1+\dot{\xi}(\rho,t)), \tag{3.48}$$

where $d_0^c = \tilde{d}_0^c/\tilde{l}$.

3.3.3 The planar stationary solution

In order to know the steady-state profile of the moving planar interface, we search for stationary solutions of the Eq. (3.26)

$$-\tilde{v}_p\partial_{\tilde{z}}c_\alpha = \tilde{D}_\alpha\tilde{\nabla}^2c_\alpha. \tag{3.49}$$

In the stationary regime, the motion of the interface is only due to the translation of the sample along the external temperature gradient, and the interface position is therefore located at the origin of the gradient frame $\tilde{z}^{int} = \tilde{\xi}(\tilde{t}\to\infty) = 0$.
As the solute diffusion in the solid is typically five orders of magnitude smaller than in the liquid, we can assume that the diffusion of the concentration profile only occurs in the liquid side of the interface (one-sided model). We then have

$$\tilde{D}_L\tilde{\nabla}^2c_L + \tilde{v}_p\partial_{\tilde{z}}c_L = 0. \tag{3.50}$$

A general solution for this ordinary differential equation is given by

$$c_L(z) = A + B\ e^{-\frac{\tilde{v}_p}{\tilde{D}_L}\tilde{z}}. \tag{3.51}$$

where A and B are integration constants. We introduce at this point the *diffusion length*

$$\tilde{l} = \frac{\tilde{D}_L}{\tilde{v}_p}, \tag{3.52}$$

which is a measure of the thickness of the solute boundary layer formed ahead of the solidification front. We note that for a given substance, the thickness of the boundary layer decreases for increasing growth velocities.

We now impose a condition requiring that the value of the concentration profile away from the interface must be equal to the original composition of the alloy c_∞. This can be imposed by means of the far-field condition $c_L(\tilde{z} \to \infty) = c_\infty$, which allows to find a value of the integration constant A

$$A = c_\infty. \tag{3.53}$$

Similarly, the value of the integration constant B can be found by imposing the solute conservation equation Eq. 3.29, which brings to

$$B = \frac{c_\infty(1-k)}{k} = \Delta c_0. \tag{3.54}$$

The final stationary concentration profile is then given by

$$c_L(\tilde{z}) = c_\infty + \Delta c_0\ e^{-\frac{\tilde{z}}{\tilde{l}}}, \tag{3.55}$$

which is represented in Fig. 3.6.

3.3.4 Morphological stability of a planar front

Due to the local character of the problem, the solid-liquid interface might be morphologically unstable and front deformations may grow resulting in the formation of cellular or dendritic patterns. This section is devoted to the study of the physical mechanisms which give rise to a morphological destabilization of the front. We first present the constitutional undercooling as the basic physical process destabilizing the interface, and then introduce the Mullins-Sekerka analysis which determines the decay or growth of sinusoidal perturbations with different wavelengths.

The constitutional undercooling criterion

When a directionally solidified sample has reached its stationary state (i.e., the diffusion boundary layer is formed) , there is a simple thermodynamical argument which qualitatively determines the morphological stability of the solidification

front. As shown in Fig. 3.7, the boundary layer formed ahead of the solid-liquid interface has a solute concentration which decreases from c_∞/k at the liquid side of the interface, to c_∞ at distances of order of the diffusion length $\tilde{l} = \tilde{D}/\tilde{v}_p$. As the concentration at the liquid decreases, the temperature at which it solidifies increases following $T = T_M - m_L c_L$. The melting temperatures for the points in the boundary layer is represented as a dashed line in Fig. 3.7. On the other hand, the external temperature gradient imposes a temperature at each of the sample points given by

$$T(\tilde{\mathbf{r}}) = T_M - m_L \frac{c_\infty}{k} + \tilde{G}\tilde{z}, \tag{3.56}$$

which is plotted in Fig. 3.7 as a solid line.

It turns now clear that the points in the region between the solid and dashed lines have a temperature below its melting temperature, and therefore at these points the liquid phase is metastable. This local undercooling which produces the instability of the interface is known as *constitutional undercooling*, and was first proposed by Rutter and Chalmers in Ref. [Rutter53] and latter by Tiller *et al.* in Ref. [Tiller53]. For a recent historical review of the constitutional undercooling criterion, we refer to Ref. [Jackson04]. When the value of the temperature gradient

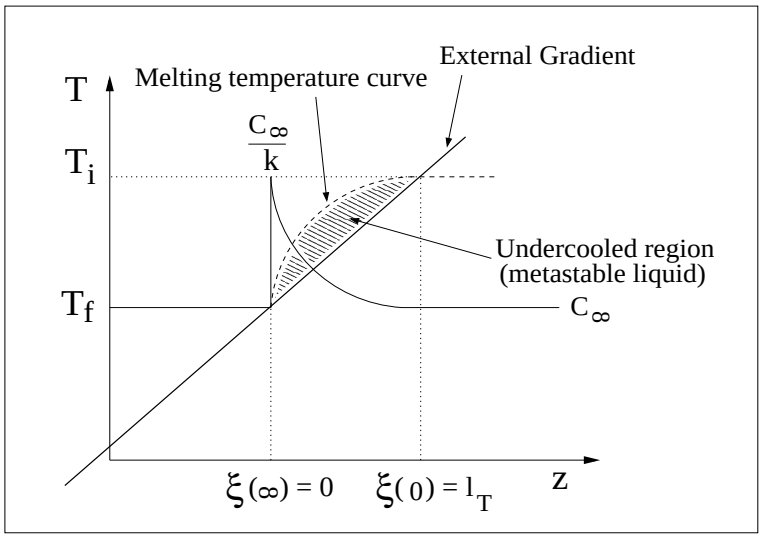

Figure 3.7: Constitutional undercooling criterion for the morphological stability of the solidification front. The region between the solid and the dashed line defines a metastable liquid phase.

$\tilde{G}$ is increased, the constitutionally undercooled region gets smaller. This can be appreciated in Fig. 3.8, where the undercooled region is plotted for three different gradients $G_1 > G_2 > G_3$. For gradients larger than G_1, there is no undercooled

region and the front becomes morphologically stable. So the external gradient has a stabilizing effect for the interface.

The mathematical condition which determines the front stability can be obtained by comparing the external temperature gradient $\tilde{G}$ with the slope of the melting temperature curve at $\tilde{z} = 0$. Using Eq. 3.55, this slope can be easily determined as

$$\left|\frac{dT}{d\tilde{z}}\right|_{\tilde{z}=0} = m_L \Delta c_0 \frac{\tilde{v}_p}{\tilde{D}}, \tag{3.57}$$

and the condition for the stability of the front can then be written as

$$\tilde{G} > m_L \Delta c_0 \frac{\tilde{v}_p}{\tilde{D}}. \tag{3.58}$$

The last condition can be expressed in terms of the gradient length $\tilde{l}_T = m_L \Delta c_0 / \tilde{G}$ introduced in Eq. 3.24 and the diffusion length $\tilde{l} = \tilde{D}/\tilde{v}_p$ of Eq. 3.52, and the morphological stability criterion is then written as

$$\tilde{l} > \tilde{l}_T, \tag{3.59}$$

namely that the interface will be morphologically stable when the diffusion length $\tilde{l}$ is larger than the gradient length $\tilde{l}_T$. From the last equation it turns clear that, whereas the increase of the external gradient has a stabilizing effect because it decreases $\tilde{l}_T$, increasing the pulling velocity has a destabilizing influence because it increases the diffusion length $\tilde{l}$. For a given sample concentration c_∞, the two main control parameters in a directional solidification experiment are the external temperature gradient $\tilde{G}$ (stabilizing) and the pulling velocity $\tilde{v}$ (destabilizing). The constitutional undercooling criterion can be used as a rule of thumb for determining the interface stability, but it does not take into account important phenomena such as surface energy or kinetic attachment effects. Capillary effects, however, have a very important influence in the morphological stability of the interface. We have seen in section 2.1.3 that a positive interfacial curvature (i.e., with its center located at the solid side), results in a decrease of the melting temperature in the liquid side of the front. This undercooling by curvature turns in a reduction of the melting temperature in the diffusive boundary layer, producing a stabilization of the front. The effect is represented in Fig. 3.8, where the planar and curved fronts present different curves for the temperature of melting in the boundary layer. In particular, for a given external temperature gradient G_2, the curved front becomes stable (there is no undercooled region) whereas the plane front was clearly unstable. Following the same argument, as the kinetic attachment produces an effective undercooling at the interface, it also contributes to the stabilization of the front.

Due to the competition between stabilizing forces (external gradient, capillary effects, kinetic effects) and destabilizing effects (front velocity, diffusion, solute concentration), the solidification front in alloys presents a wide spectrum of morphological instablilties such as dendrites, banded structures, cellular patterns, traveling waves, oscillatory modes, etc.

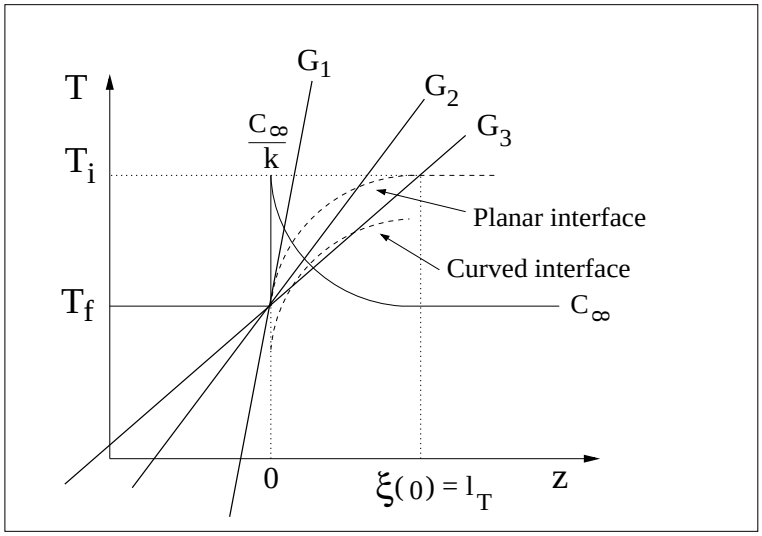

Figure 3.8: The effect of capillarity in the interface stability is a reduction of the melting temperature. For the same external gradient G_2, the curved surface becomes stable whereas the planar interface was constitutionally unstable.

The Mullins-Sekerka stability analysis

The above arguments describe the qualitative mechanism by which the front destabilizes, but do not say anything about the amplification or decay of the different perturbations which might be applied to the system. This analysis was first done by Mullins and Sekerka in Ref. [Mullins63]. They performed a linear stability analysis of the stationary front by applying different sinusoidal perturbations and obtaining an expression for the growth rate at which they growth or decay. We will turn to this point later in section 4.2, where we will develop the mathematical stability analysis but not in the stationary regime but during the initial transient stages in directional solidification.

The analysis starts from the planar stationary solution Eq. 3.55,

$$c_S^0(\tilde{z}) = c_\infty, \tag{3.60}$$

$$c_L^0(\tilde{z}) = c_\infty + \Delta c_0 \, e^{-\frac{\tilde{v}_p}{\tilde{D}_L}\tilde{z}}. \tag{3.61}$$

which is located at $\tilde{z} = 0$. By perturbing this stationary solution with a sinusoidal interfacial deformation, we have the perturbed concentration profiles at the liquid

and solid c'_L, c'_S, and the perturbed interface is located at the position $\tilde{\xi}'$, given by

$$c'_S(\tilde{\mathbf{r}},\tilde{t}) = c^0_S + \delta c_S(\tilde{\mathbf{r}},\tilde{t}) \quad (3.62)$$
$$c'_L(\tilde{\mathbf{r}},\tilde{t}) = c^0_L(\tilde{z}) + \delta c_L(\tilde{\mathbf{r}},\tilde{t}) \quad (3.63)$$
$$\tilde{\xi}'(\tilde{\rho},\tilde{t}) = \delta\tilde{\xi}(\tilde{\rho},\tilde{t}), \quad (3.64)$$

where the perturbations are given by

$$\delta c_S(\tilde{\mathbf{r}},\tilde{t}) = c_2 e^{i\tilde{\mathbf{k}}\cdot\tilde{\rho}+\tilde{q}'\tilde{z}+\tilde{w}\tilde{t}} \quad (3.65)$$
$$\delta c_L(\tilde{\mathbf{r}},\tilde{t}) = c_1 e^{i\tilde{\mathbf{k}}\cdot\tilde{\rho}-\tilde{q}\tilde{z}+\tilde{w}\tilde{t}} \quad (3.66)$$
$$\delta\tilde{\xi}(\tilde{\rho},\tilde{t}) = z_1 e^{i\tilde{\mathbf{k}}\cdot\tilde{\rho}+\tilde{w}\tilde{t}} = \tilde{\xi}_k(\tilde{t})e^{i\tilde{\mathbf{k}}\cdot\tilde{\rho}}. \quad (3.67)$$

In the stationary state, and neglecting kinetic effects, the perturbed front satisfies the set of quasi-stationary equations

$$\tilde{D}_S\tilde{\nabla}^2 c'_S + \tilde{v}_p\partial_{\tilde{z}}c'_S = 0, \quad (3.68)$$
$$\tilde{D}_L\tilde{\nabla}^2 c'_L + \tilde{v}_p\partial_{\tilde{z}}c'_L = 0, \quad (3.69)$$
$$c'_L(\tilde{\mathbf{r}}^{int},\tilde{t}) = \frac{c_\infty}{k} - \frac{\tilde{G}}{m_L}\tilde{\xi}'(\tilde{\rho},\tilde{t}) - \tilde{d}^c_0\tilde{\kappa}' \quad (3.70)$$
$$\hat{\mathbf{n}}\cdot[\tilde{D}_S\tilde{\nabla}c'_S - \tilde{D}_L\tilde{\nabla}c'_L]_{\tilde{\mathbf{r}}=\tilde{\mathbf{r}}^{int}} = c'_L(\tilde{\mathbf{r}}^{int},\tilde{t})\ (1-k)(\tilde{v}_p + \dot{\tilde{\xi}}'). \quad (3.71)$$

Inserting the expressions for the perturbed fields Eqs. 3.65, 3.66 into the diffusion equations Eqs. 3.68 and 3.69, we obtain the relations

$$\tilde{D}_S(\tilde{q}'^2 - \tilde{k}^2) + \tilde{v}_p\tilde{q}' = 0, \quad (3.72)$$
$$\tilde{D}_L(\tilde{q}^2 - \tilde{k}^2) - \tilde{v}_p\tilde{q} = 0, \quad (3.73)$$

where $\tilde{k}^2 = \tilde{k}_x^2 + \tilde{k}_y^2$.

By Taylor expanding the perturbed fields c'_L, c'_S around $\tilde{z}=0$, we obtain a first order approximation in z_1, c_1, c_2 of the concentration at the solid and liquid sides of the perturbed front

$$c'_S(\tilde{\mathbf{r}},\tilde{t})|_{z=\tilde{\xi}'} \approx c'_S(\tilde{\mathbf{r}},\tilde{t})|_{z=0} + \partial_{\tilde{z}}c'_S(\tilde{\mathbf{r}},\tilde{t})|_{z=0}\cdot\delta\tilde{\xi}(\tilde{\mathbf{r}},\tilde{t}), \quad (3.74)$$
$$c'_L(\tilde{\mathbf{r}},\tilde{t})|_{z=\tilde{\xi}'} \approx c'_L(\tilde{\mathbf{r}},\tilde{t})|_{z=0} + \partial_{\tilde{z}}c'_L(\tilde{\mathbf{r}},\tilde{t})|_{z=0}\cdot\delta\tilde{\xi}(\tilde{\mathbf{r}},\tilde{t}). \quad (3.75)$$

Inserting Eq. 3.66 into Eq. 3.75, the concentration at the liquid side is given by

$$c'_S(\tilde{\mathbf{r}},\tilde{t})|_{z=\tilde{\xi}'} \approx c_\infty + \Delta c_0\left(1 - \frac{\tilde{v}_p}{\tilde{D}_L}\delta\tilde{\xi}\right) + c_1 e^{i\tilde{\mathbf{k}}\cdot\tilde{\rho}+\tilde{w}\tilde{t}}. \quad (3.76)$$

We can expand in the same way the right side of Eq. 3.70, obtaining

$$\frac{c_\infty}{k} - \frac{\tilde{G}}{m_L}\tilde{\xi}'(\tilde{\rho},\tilde{t}) - \tilde{d}^c_0\tilde{\kappa}' \approx \frac{c_\infty}{k} - \left(\frac{\tilde{G}}{m_L} + \tilde{d}^c_0\tilde{k}^2\right)\delta\tilde{\xi}(\tilde{\rho},\tilde{t}) \quad (3.77)$$

Inserting the last expressions Eqs. 3.76 and 3.76 into Eq. 3.76, we find a first relation between the amplitudes of the perturbations c_1 and z_1

$$c_1 = z_1\left(\frac{\tilde{v}_p}{\tilde{D}_L}\Delta c_0 - \frac{\tilde{G}}{m_L} - \tilde{d}_0^c\tilde{k}^2\right). \tag{3.78}$$

A second relation between c_1 and z_1 can be found by expanding the fields in the local equilibrium condition $k \cdot c_L^{'int} = c_S^{'int}$, which brings to

$$c_2 = kc_1 - k\frac{\tilde{v}_p}{\tilde{D}_L}\Delta c_0 z_1. \tag{3.79}$$

The third and last relation needed to determine the perturbation amplitudes can be obtained by expanding the derivatives $\partial_{\tilde{z}}c'_L(\tilde{\mathbf{r}},\tilde{t})$, $\partial_{\tilde{z}}c'_S(\tilde{\mathbf{r}},\tilde{t})$ and inserting them into the mass conservation condition Eq. 3.71. After some algebraic manipulations, we have, at first order

$$\tilde{D}_s\tilde{q}'c_2 + \left[\tilde{D}_L\tilde{q}c_1 - (1-k)\tilde{v}_p\right] = z_1\Delta c_0\left[\tilde{\omega} + k\frac{\tilde{v}_p^2}{\tilde{D}_L}\right] \tag{3.80}$$

We can now introduce Eqs. 3.78, 3.79 into Eq. 3.80 and obtain the stationary dispersion relation for directional solidification

$$\begin{aligned}\frac{\tilde{D}_L}{\tilde{v}_p^2}\tilde{\omega}(\tilde{\mathbf{k}},\tilde{t}) = -k - \frac{\tilde{D}_S\tilde{D}_L}{\tilde{v}_p^2}q'k\cdot\left[\frac{\tilde{G}}{m_L\Delta c_0} + \hat{\tilde{d}}_0\tilde{k}^2\right] + \\ \frac{\tilde{D}_L^2}{\tilde{v}_p^2}\left[q + (k-1)\frac{\tilde{v}_p}{\tilde{D}_L}\right]\cdot\left[\frac{\tilde{v}_p}{\tilde{D}_L} - \frac{\tilde{G}}{m_L\Delta c_0} - \hat{\tilde{d}}_0\tilde{k}^2\right],\end{aligned} \tag{3.81}$$

where $\hat{\tilde{d}}_0$ has been defined as the *reduced chemical capillary length*

$$\hat{\tilde{d}}_0 = \frac{\tilde{d}_0^c}{\Delta c_0}, \tag{3.82}$$

and q, q' are given by the solutions of Eqs. 3.73, which take the form

$$q' = -\frac{\tilde{v}_p}{\tilde{D}_S} \pm \sqrt{\frac{\tilde{v}_p^2}{4\tilde{D}_S^2} - \tilde{k}^2} \tag{3.83}$$

$$q' = \frac{\tilde{v}_p}{\tilde{D}_L} \pm \sqrt{\frac{\tilde{v}_p^2}{4\tilde{D}_L^2} - \tilde{k}^2}. \tag{3.84}$$

By using the diffusion time $\tilde{\gamma} = \frac{\tilde{D}_L}{\tilde{v}_p^2}$ introduced in Eq. 3.35, we rewrite the dispersion relation in a more compact form

$$\begin{aligned}\tilde{\omega}(\tilde{\mathbf{k}},\tilde{t}) = -\frac{k}{\tilde{\gamma}} - \tilde{D}_S q'k\cdot\left[\frac{1}{\tilde{l}_T} + \hat{\tilde{d}}_0\tilde{k}^2\right] + \\ \tilde{D}_L\left[q + (k-1)\frac{1}{\tilde{l}}\right]\cdot\left[\frac{1}{\tilde{l}} - \frac{1}{\tilde{l}_T} - \hat{\tilde{d}}_0\tilde{k}^2\right].\end{aligned} \tag{3.85}$$

The Mullins-Sekerka stability analysis can be written as a linear equation for the evolution of the Fourier modes of the perturbation $\tilde{\xi}_k(\tilde{t})$ introduced in Eq. 3.67

$$\frac{d\tilde{\xi}_k(\tilde{t})}{dt} = \tilde{\omega}(\tilde{\mathbf{k}})\tilde{\xi}_k(\tilde{t}). \tag{3.86}$$

From the last equation, it becomes clear that the Mullins-Sekerka analysis does not contain any information about the physical initiation for the perturbations. If the system departs from a non perturbed initial condition $\tilde{\xi}'_k(\tilde{t} = 0) = 0$, the predicted future evolution of the system will be unperturbed. In order to account for realistic experimental situations, Warren and Langer introduced in Refs. [Warren90, Warren93] the internal fluctuations as the initiation process which activates the perturbation of the front. As we will see in Sec. 4.2.2 of the next chapter, they proposed a Langevin equation by introducing a fluctuation term in Eq. 3.86. As the effect of fluctuations will be noted by the front at very early stages, they extended the Mullins-Sekerka analysis to account for the stability of the front during the the initial recoil transient where the boundary layer builds up.

Chapter 4

Analytical methods for the study of transient stages in directional solidification

In the study of solidification fronts, there are two important analytical approaches to deal with transients and fluctuations. The first technique is known as the *Boundary Integral Method* (Sec. 4.1), and uses the Green's function theory to transform the moving boundary equations into an integro-differential formulation of the problem. The numerical solution of these integro-differential equations will be used as a benchmark for further simulations results. Some of the integral equations presented in this chapter cannot be found in the previous literature and have been derived for the particular purposes of this thesis. We report the complete derivation of these models in order to provide the necessary expressions needed to account for other solidification systems in the future.

The second theoretical analysis (Sec. 4.2) is the *Warren and Langer's theory* on noise amplification during the initial transient stages. The main idea is to incorporate fluctuations as the physical mechanism which perturbs the interface at early times. In order to know how these perturbations grow or decay, a linear stability analysis similar to the Mullins-Sekerka is performed in Sec. 4.2.1, but incorporating the effects of the solute build-up process during the initial transient. The main difference is that while the Mullins-Sekerka theory perturbed the stationary front, the Warren-Langer procedure takes the transient profile ansatz as the unperturbed state.

4.1 Boundary integral methods for solidification

4.1.1 Introduction

Boundary integral methods have shown great success for the study of engineering problems such as crack propagation, acoustics, elasticity or solid mechanics. In solidification problems, Green's functions techniques allow to formulate the moving boundary problem in terms of a closed set of integro-differential equations known as boundary integral equations. For a general introduction to this technique in solidification problems, we refer to Ref. [Caroli92], and for a more detailed description and applications to Refs. [Caroli86a, Caroli86b, Caroli93, Tiller53, Huang97, Karma92, Karma93d, Karma86, Barber87]. In practice, however, these techniques are often used under some quasistationary approximation, and formulations accounting for transient stages are difficult to find.

The solutions obtained by the numerical simulation of the boundary integral equations should be considered as analytical solutions of the problem within the limits of the computational accuracy of the numerical integration method. This section is devoted to find this integral equations for different solidification problems such as directional or symmetric solidification. All the boundary integral problems will take into account the transient stages from an initial time t_0. Equations for the profile of the diffusive field (temperature or solute concentration) at a certain time t will be expressed as an integral equation involving the retarded Green's function of the problem and the past values (i.e., from the initial time t_0 to t) of the profiles and front positions and velocities. By using the boundary conditions at the interface, these integral equation for the diffusive field can be transformed in a closed integral equation for the front position during the solidification process. This transformation, however, can only be performed in the case of one-sided systems (no diffusion at the solid) or in a symmetric situation (equal diffusivities in the solid and liquid). For the case of having different positive diffusivities in both phases, no closed integral equation for the front position can be obtained as a consequence of the asymmetry in the conservation across the interface of the diffusion field. This approach describes the front dynamics during the solute redistribution transient and it is capable of including capillary and kinetic effects. The numerical simulation of these equations will be used as a benchmark in the following chapter for the results obtained with other computational techniques (phase-field methods). Although the derivation is presented in the most general case for a 2D surface including curvature effects, the simulations will be performed in the case of having a planar interface.

4.1.2 Formulation of the problem

Let us consider two semi-infininite media $i = 1, 2$, separated by a moving interface $\tilde{z} = \tilde{\xi}(\rho, t)$. For the solidification problem, $i = 1$ corresponds to the solid phase and

$i = 2$ to the liquid phase. The two bulk regions are then defined by

$$\begin{aligned} &\text{Phase 1 (Solid)}: && -\infty < \tilde{z} < \tilde{\xi}(\rho, t), \\ &\text{Phase 2 (Liquid)}: && \tilde{\xi}(\rho, t) < \tilde{z} < \infty. \end{aligned} \tag{4.1}$$

In the sample reference frame, which moves with constant velocity $\tilde{v}_p$, the physical variables can be scaled using the time and space scales $\tilde{\gamma}_i = \frac{\tilde{D}_i}{\tilde{v}_p^2}$ and $\tilde{l}_i = \frac{\tilde{D}_i}{\tilde{v}_p}$, where $\tilde{D}_i$ is the diffusivity at the phase i. The scaled distances and times are then defined as

$$t_i = \frac{\tilde{t}}{\tilde{\gamma}_i} \qquad \mathbf{r}_i = \frac{\tilde{\mathbf{r}}_i}{\tilde{l}_i}. \tag{4.2}$$

For the sake of clarity, we will use in this section the compact notation

$$x_i = (\rho_i, t_i) \qquad p_i = (\mathbf{r}_i, t_i) \qquad p_{iS} = (x_i, \xi_i(x_i)), \tag{4.3}$$

where

$$\mathbf{r}_i = \rho_i + z_i \hat{k} \qquad \rho_i = x_i \hat{i} + y_i \hat{j}, \tag{4.4}$$

and $\xi_i(x_i)$ is the equation for the interface at the side of the phase (i). We now introduce a normal unitary vector pointing to the liquid side as shown in Fig. 4.1

$$\hat{n}(x_2) = \frac{-\nabla_\perp \xi(x_2) + \hat{k}}{\sqrt{1 + |\nabla_\perp \xi(x_2)|^2}}, \tag{4.5}$$

where $\nabla_\perp = \partial_x \, \hat{i} + \partial_y \, \hat{j}$. The unitary normal vector with origin in the phase (i) and pointing to phase (ii) is then defined as

$$\hat{n}_i = (-1)^{i+1} \hat{n}, \tag{4.6}$$

We now introduce in each medium a diffusion field $u_i(p_i)$ which satisfies the limit boundary conditions

$$\lim_{z_i \to (-)^i \infty} u_i(p_i) = \lim_{z_i \to (-)^i \infty} \nabla_i u_i(p_i) = 0. \tag{4.7}$$

In the moving frame, the fields evolve according to the diffusion equation for each phase

$$\left(\frac{\partial}{\partial t_i} - \frac{\partial}{\partial z_i} - \nabla_i^2 \right) u_i(p_i) = 0. \tag{4.8}$$

The formalism presented in this section can be applied to both pure and alloy solidification processes. In the case of alloy solidification, as the initial liquid melt has a concentration of c_∞, the reduced diffusion field will be defined by

$$u_i(p) = \frac{c_i(p) - c_\infty}{\Delta c_0}, \tag{4.9}$$

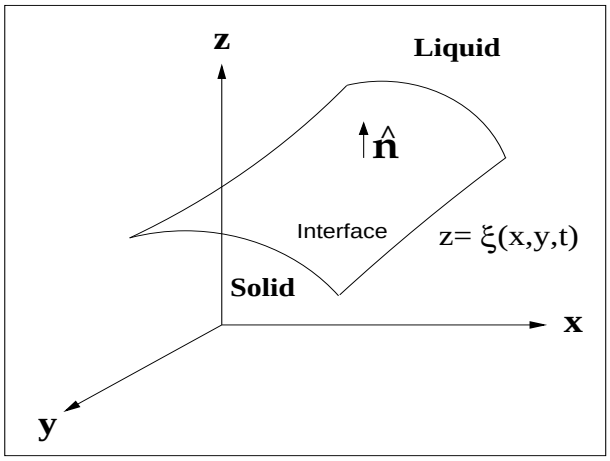

Figure 4.1: Unitary vector normal to the interface and pointing to the liquid phase

whereas for pure substances, we have

$$u_i(p) = \frac{T_M - T_\infty}{L/c_p}, \tag{4.10}$$

where T_∞ is the temperature below the melting temperature T_M at which the liquid melt has been undercooled.

Green's function of the diffusion problem

The retarded Green's function associated to the diffusion problem Eq. 4.8 is determined by the equations

$$\begin{aligned} \left(\nabla_i'^2 - \frac{\partial}{\partial z_i'} + \frac{\partial}{\partial t_i'}\right) G_i(p_i, p_i') = -\delta(p_i - p_i'), \qquad & t_i > t_i', \\ G_i(p_i, p_i') = 0, \qquad & t_i < t_i' \ . \end{aligned} \tag{4.11}$$

Eqs. 4.11 can be solved to find the retarded Green's function associated to the diffusion problem, which is given by

$$G_i(p_i, p_i') = \frac{\theta(t_i - t_i')}{[4\pi(t_i - t_i')]^{\frac{3}{2}}} \exp\left\{-\frac{(\rho_\mathbf{i} - \rho_i')^2 + (z_i - z_i' + t_i - t_i')^2}{4(t_i - t_i')}\right\}, \tag{4.12}$$

and satisfies the limit

$$\lim_{\varepsilon \to 0} G_i(\mathbf{r_i}, t_i; \mathbf{r}_i', t_i - \varepsilon) = \delta(\mathbf{r_i} - \mathbf{r}_i'). \tag{4.13}$$

Equation for the diffusion field $u_i(p_i)$

Let's now find an expression for the concentration at the interface $u_i(p_i)$. Multiplying (4.8) by $G_i(p_i, p_i')$ and Eq. 4.11 by $u_i(p_i')$ and adding the two terms, we obtain, after some arrangements

$$\begin{aligned}\frac{\partial}{\partial t_i'}[G(p_i,p_i')u(p_i')] &= \frac{\partial}{\partial z_i'}[G(p_i,p_i')u(p_i')] - u(p_i')\delta(p_i-p_i') \\ &- u(p_i')\nabla_i'^2 G(p_i,p_i') + G(p_i,p_i')\nabla_i'^2 u(p_i').\end{aligned} \tag{4.14}$$

We introduce the space and time integration domain Ω defined by

$$\Omega = \begin{cases} t_{i0} < t_i' < t_{i-}\ , \qquad t_{i-} \equiv t_i - \varepsilon \\ V_1(t_1') : -\infty \le x_1', y_1' \le \infty,\ -\infty < z_1' < \xi_1(x_1') \\ V_2(t_2') : -\infty \le x_2', y_2' \le \infty,\ \xi_2(x_2') < z_2' < \infty, \end{cases} \tag{4.15}$$

being $V_i(t_i')$ the volume of the region (i) at time t_i'. Integrating equation 4.14 over Ω and imposing the first limit condition in Eq. 4.7, we get

$$\begin{aligned}&\int_{t_{i0}}^{t_{i-}} dt_i' \int_{V_i(t_i')} d\mathbf{r}_i'\ \frac{\partial}{\partial t_i'}[G(p_i,p_i')u(p_i')] = \\ &\int_{t_{i0}}^{t_{i-}} dt_i' \int_{V_i(t_i')} d\mathbf{r}_i' \left[\frac{\partial}{\partial z_i'}[G(p_i,p_i')u(p_i')]\right. \\ &\left. + \nabla_i' \cdot [G(p_i,p_i')\nabla_i' u(p_i') - u(p_i')\nabla_i' G(p_i,p_i')]\right].\end{aligned} \tag{4.16}$$

The first term in left hand side of Eq. 4.16 can be simplified by using Leibnitz's rule for the derivation under the integral sign and write

$$\begin{aligned}&\int_{t_{i0}}^{t_{i-}} dt_i' \int_{V_i(t_i')} d\mathbf{r}_i'\ \frac{\partial}{\partial t_i'}[G(p_i,p_i')u(p_i')] = \\ &\int_{t_{i0}}^{t_{i-}} dt_i' \frac{d}{dt_i'} \int_{V_i(t_i')} d\mathbf{r}_i' G(p_i,p_i')u(p_i') + (-)^i \int_{t_i}^{t_{i-}} dt_i' \int d\rho_i' \frac{d\xi_i(x_i')}{dt_i'} G(p_i,p_{iS}')u(p_{iS}'),\end{aligned} \tag{4.17}$$

and evaluating the first integral at the right side we obtain

$$\begin{aligned}&\int_{t_{i0}}^{t_{i-}} dt_i' \int_{V_i(t_i')} d\mathbf{r}_i'\ \frac{\partial}{\partial t_i'}[G(p_i,p_i')u(p_i')] = \\ &\left[\int_{V_i(t_i')} d\mathbf{r}_i' G(p_i,p_i')u(p_i')\right]_{t_{i0}}^{t_{i-}} + (-)^i \int_{t_i}^{t_{i-}} dt_i' \int d\rho_i' \frac{d\xi_i(x_i')}{dt_i'} G(p_i,p_{iS}')u(p_{iS}'),\end{aligned} \tag{4.18}$$

which, using Eq. 4.13 reads

$$\int_{t_{i0}}^{t_{i-}} dt_i' \int_{V_i(t_i')} d\mathbf{r}_i' \; \frac{\partial}{\partial t_i'}[G(p_i,p_i')u(p_i')] =$$
$$u_i(p_{iS}) - \int_{V_i(t_{i0}')} d\mathbf{r}_i' G(p_i;\mathbf{r}_i',t_{i0})u(\mathbf{r}_i',t_{i0}) + (-)^i \int_{t_i}^{t_{i-}} dt_i' \int d\rho_i' \frac{d\xi_i(x_i')}{dt_i'} G(p_i,p_{iS}')u(p_{iS}'). \tag{4.19}$$

The first integral at the right side of Eq. 4.16 can directly be solved by noting that

$$\int_{t_{i0}}^{t_{i-}} dt_i' \int_{V_i(t_i')} d\mathbf{r}_i' = \int_{t_i}^{t_{i-}} dt_i' \int d\rho_i' \int_{z_i'>(-)^i\xi_i(x_i')} dz_i' =$$
$$(-)^i \int_{t_i}^{t_{i-}} dt_i' \int d\rho_i' \int_{\xi_i(x_i')}^{(-)^i\infty} dz_i', \tag{4.20}$$

and gives

$$(-)^i \int_{t_i}^{t_{i-}} dt_i' \int d\rho_i' \Big[G(p_i,p_i')u(p_i') \Big]_{\xi_i(x_i')}^{(-)^i\infty}, \tag{4.21}$$

which can be simplified using Eq. 4.7 to give

$$(-)^{i+1} \int_{t_i}^{t_{i-}} dt_i' \int d\rho_i' G(p_i,p_{iS}')u(p_{iS}'). \tag{4.22}$$

Finally, by applying Gauss's theorem to the second term at the right side of Eq. 4.16, and using the previous results Eqs. 4.19, 4.22, an integral equation for the diffusion field $u_i(p_i)$ can be found

$$\begin{aligned} u_i(p_i) = & \int_{V_i(t_{i0})} d\mathbf{r}_i' \cdot G(p_i;\mathbf{r}_i',t_{i0}) \cdot u_i(\mathbf{r}_i',t_{i0}) \\ & + (-)^{i+1} \int_{t_i}^{t_{i-}} dt_i' \cdot \int d\rho_i' [1+\dot{\xi}_i(x_i')] \cdot u_i(p_{iS}') \cdot G(p_i,p_{iS}') \\ & + (-)^{i+1} \int_{t_{i0}}^{t_{i-}} dt_i' \int dS_i' \cdot [\hat{n}_i' \cdot \nabla_i' u_i(p_{iS}')] \cdot G(p_i,p_{iS}') \\ & + (-)^{i} \int_{t_{i0}}^{t_{i-}} dt_i' \int dS_i' \cdot u_i(p_{iS}') \cdot \hat{n}_i' \cdot \nabla_i' G(p_i,p_{iS}') \end{aligned} \tag{4.23}$$

The last equation constitutes an integral equation for the diffusive profile $u_i(p_i)$ at each time t_i. The first integral term accounts for the initial conditions of the problem. The second one involves the past values of the front velocity and of the past profiles. The third one accounts for the evolution of the gradients of the diffusive field, which can be evaluated by means of the conservation law of the diffusive field across the interface. The last one can be directly evaluated by using the result for the Green's function Eq. 4.12.

Equation for the diffusion field at the interface $u(p_{iS})$

Once we have obtained the integral equation for the diffusion profile, the next step is to apply the limit $p \to p_S$ to Eq. 4.23 in order to obtain an integral equation for the value of the diffusion field at the interface $u(p_{iS})$. This value will then be used in combination with the Gibbs-Thomson equation to find a closed equation for the interface position during the solidification process.

Before performing the limit, we need some mathematical relations of the Green's function $G(p, p')$. The first relation is the so called Friedman's theorem. The second can easily be derived and relates integrals of the Green's function.

i) **The Friedman's theorem**:

The Friedman's theorem helps us to perform the limit of this equation in order to get an expression for the concentration at the interface $u_i(p_{iS})$. This theorem is also known as the theorem on the discontinuity of a double layer and is based on a regularization of the singular kernel as proposed in Ref. [Dee83]. The main idea is to regularize the limit of the integral by using the Hadamard's finite part integral [Hadamard23]. More information about regularization techniques for hypersingular integral equations can be found in Ref. [Niu04, Hamina00, Guiggiani95]. In our case, the Friedman's theorem adopts the form

$$\begin{aligned}\lim_{z_i \to \xi_i(x_i)+(-)^i 0} \int_{t_{i0}}^{t_i} dt_i' \int dS_i'\, f_i(p_{iS}')\, \hat{n}' \cdot \nabla_i' G(p_i, p_{iS}') = \\ \frac{(-)^i}{2} f_i(p_{iS}') + \int_{t_{i0}}^{t_i} dt_i' \int dS_i'\, f_i(p_{iS}')\, \hat{n}' \cdot \nabla_i' G(p_{iS}, p_{iS}')\end{aligned} \tag{4.24}$$

and determines the value of the limit of the first integral as we approach to the interface position.

ii) **Relations between integrals of the Green's function**:

By integrating over space and time equation Eq. 4.11, and using condition Eq. 4.13 and Gauss theorem, one finds

$$\begin{aligned}&\int_{t_{i0}}^{t_i} dt_i' \int dS_i' \cdot \hat{n}_i' \cdot \nabla_i' G(p_i, p_{iS}') - \int_{t_{i0}}^{t_i} dt_i' \int d\rho_i' \cdot [1 + \dot{\xi}_i(x_i')] \cdot G_i(p_i, p_{iS}') \\ &+ \int d\rho_i' \int_{\xi_i(\rho_i', t_{i0})}^{(-)^i \infty} dz_i' G_i(p_i; \mathbf{r}_i', t_{i0}) = (-)^i.\end{aligned} \tag{4.25}$$

To evaluate the last term at the left hand side, we introduce the function

$$J(p_i, t_{i0}) = \int d\rho_i' \int_{\xi_i(\rho_i', t_{i0})}^{(-)^i \infty} dz_i' G_i(p_i; \mathbf{r}_i', t_{i0}) = \lim_{z_{i1} \to (-)^i \infty} J_i(p_i; z_{i1}, t_{i0}), \tag{4.26}$$

where

$$J_i(p_i; z_{i1}, t_{i0}) = \int d\rho_i' \int_{\xi_i(\rho_i', t_{i0})}^{z_{i1}} dz_i' G_i(p_i; \mathbf{r}_i', t_{i0}). \tag{4.27}$$

Introducing Eq. 4.12 into Eq. 4.27 and integrating after performing the change of variable $\mathbf{y} = \frac{\rho' - \rho}{\sqrt{4(t_i - t_{i0})}}$, we get

$$J_i(p_i; z_{i1}, t_{i0}) = \frac{1}{2\pi} \int d\mathbf{y}\ e^{-y^2} [\mathrm{erf}(\alpha) - \mathrm{erf}(\beta)], \tag{4.28}$$

where $\mathrm{erf}(x) = \frac{2}{\sqrt{\pi}} \int_0^x e^{-u^2} du$, and

$$\begin{aligned} \alpha &= \frac{z_i - \xi_i(\rho_i', t_{i0}) + 2(t_i - t_{i0})}{\sqrt{4(t_i - t_{i0})}}, \\ \beta &= \frac{z_i - z_{i1} + 2(t_i - t_{i0})}{\sqrt{4(t_i - t_{i0})}}. \end{aligned} \tag{4.29}$$

Taking now the limit $z_{i1} \to (-)^i \infty$ to Eq. 4.28, and noting that $\mathrm{erf}(\infty) = 1$, one finds an expression for $J(p_i, t_{i0})$

$$J(p_i, t_{i0}) = \frac{(-)^i}{2} + \frac{1}{2\pi} \int d\mathbf{y}\ e^{-y^2} \mathrm{erf}(\alpha). \tag{4.30}$$

Introducing the function

$$F(p_i, t_{i0}) = \frac{1}{2\pi} \int d\mathbf{y}\ e^{-y^2} \mathrm{erf}(\alpha), \tag{4.31}$$

Eq. 4.25 can then be written as

$$\begin{aligned} &\int_{t_{i0}}^{t_i} dt_i' \int dS_i' \cdot \hat{n}_i' \cdot \nabla_i' G(p_i, p_{iS}') - \int_{t_{i0}}^{t_i} dt_i' \int d\rho_i' \cdot [1 + \dot{\xi}_i(x_i')] \cdot G_i(p_i, p_{iS}') = \\ &\frac{1}{2}(-)^i - F(p_i, t_{i0}). \end{aligned} \tag{4.32}$$

Performing the limit $p_i \to p_{iS}$ to the last expression Eq. 4.32, and using Friedman's theorem Eq. 4.24, it is possible to write Eq. 4.32 as

$$\begin{aligned} &\int_{t_{i0}}^{t_i} dt_i' \int dS_i' \cdot \hat{n}_i' \cdot \nabla_i' G(p_{iS}, p_{iS}') - \int_{t_{i0}}^{t_i} dt_i' \int d\rho_i' \cdot [1 + \dot{\xi}_i(x_i')] \cdot G_i(p_{iS}, p_{iS}') = \\ &-\frac{1}{2} F(p_{iS}, t_{i0}) = \frac{(-)^i}{2} - \int d\rho_i' \int_{\xi(\rho_i', t_{i0})}^{(-)^i \infty} dz_i' G_i(p_{iS}; \mathbf{r}_i', t_{i0}). \end{aligned} \tag{4.33}$$

Note that in the stationary limit $t_{i0} \to -\infty$, we have

$$\lim_{t_{i0}\to-\infty} F(p_i, t_{i0}) = 1. \tag{4.34}$$

Using Eq. 4.33, it is possible to perform the limit $p_i \to p_{iS}$ of Eq. 4.23 and obtain an integro-differential equation for the diffusion field at the interface $u_i(p_i)$

$$\begin{aligned}\frac{1}{2}u_i(p_{iS}) = &\int_{V_i(t_{i0})} d\mathbf{r}'_i \cdot G_i(p_{iS}, \mathbf{r}'_i, t_{i0}) \cdot u_i(\mathbf{r}'_i, t_{i0}) \\ &+(-)^{i+1}\int_{t_{i0}}^{ti-} dt'_i \int d\rho'_i \cdot [1 + \dot{\xi}_i(x'_i)] \cdot u_i(p'_{iS}) \cdot G_i(p_{iS}, p'_{iS}) \\ &+(-)^{i+1}\int_{t_{i0}}^{t_{i-}} dt'_i \int dS'_i \cdot G_i(p_{iS}, p'_{iS}) \cdot \hat{n}'_i \cdot \nabla'_i u_i(p'_{iS}) \\ &+(-)^{i}\int_{t_{i0}}^{t_{i-}} dt'_i \int dS'_i \cdot u_i(p'_{iS}) \hat{n}'_i \cdot \nabla'_i G_i(p_{iS}, p'_{iS})\end{aligned} \tag{4.35}$$

4.1.3 Integral equations for the front position

As we have commented, a closed integral equation for the front position can only be obtained in the case of one-sided or symmetric models. This section is dedicated to use the moving boundary conditions at the interface to construct the integral equation in these two cases. Whereas the one-sided model is only considered for dilute alloy solidification, the symmetric model can be used for both pure substances and dilute alloys.

One-sided model for dilute alloys

For clarity of exposition, and as in the one-sided model the diffusion in the solid phase is neglected, we will write variables and fields in the liquid phase without sub-indexes. In one-sided alloys, the diffusion field is then defined by $u(\mathbf{r}, t) = (c(\mathbf{r}, t) - c_\infty)/\Delta c_0$, with $\Delta c_0 = c_\infty(1-k)/k$. Note that this field satisfies the condition Eq.4.7 because the initial supersaturated melt has a homogeneous concentration c_∞. The dimensionless moving boundary conditions at the interface (cf.Eqs.3.39, 3.40), written for the reduced field u, are given by

$$\begin{aligned}&\hat{n} \cdot \nabla u(p_S) = n_z \cdot [1 + \dot{\xi}(x)] \cdot [(k-1)u(p_S) - k] \\ &u(p_S) = 1 - \frac{1}{l_T}\xi(x) - \hat{d}_0\kappa(x), \\ &u_1(p_S) = k u_2(p_S).\end{aligned} \tag{4.36}$$

where $\hat{d}_0 = d_0^c/\Delta c_0$ and $l_T = m_L \Delta C_0/G$.

Writing Eq. 4.35 in the liquid side ($i = 2$), we get

$$\begin{aligned}\frac{1}{2}u(p_S) = &\int_{V(t_0)} d\mathbf{r}' \cdot G(p_S, \mathbf{r}', t_0) \cdot u(\mathbf{r}', t_0) \\ &- \int_{t_0}^{t-} dt' \int d\rho' \cdot [1 + \dot{\xi}(x')] \cdot u(p'_S) \cdot G(p_S, p'_S) \\ &+ \int_{t_0}^{t-} dt' \int dS' \cdot u(p'_S) \cdot \hat{n}' \cdot \nabla_{\mathbf{r}'} G(p_S, p'_S) \\ &- \int_{t_0}^{t-} dt' \int dS' \cdot G(p_S, p'_S) \cdot \hat{n}' \cdot \nabla_{\mathbf{r}'} u(p'_S)\end{aligned} \tag{4.37}$$

Introducing in the last equation the moving boundary conditions at the interface Eqs. 4.36, 4.36 and using Gauss' Theorem, we can derive an integro-differential equation for the position of the interface $\xi(x)$

$$\begin{aligned}&\frac{1}{2}(1 - \frac{1}{l_T}\xi(x) - \hat{d}_0\kappa(x)) = \int_{V(t_0)} d\mathbf{r}' \cdot G(p_S, \mathbf{r}', t_0) \cdot u(\mathbf{r}', t_0) \\ &- \int_{t_0}^{t-} dt' \int d\rho' \cdot [1 + \dot{\xi}(x')] \cdot \left[1 - \frac{1}{l_T}\xi(x') - \hat{d}_0\kappa(x')\right] \cdot G(p_S, p'_S) \\ &+ \int_{t_0}^{t-} dt' \int dS' \cdot \left[1 - \frac{1}{l_T}\xi(x') - \hat{d}_0\kappa(x')\right] \cdot \hat{n}' \cdot \nabla_{\mathbf{r}'} G(p_S, p'_S) \\ &- \int_{t_0}^{t-} dt' \int dS' \cdot n_z \cdot [1 + \dot{\xi}(x)] \cdot \left[(k-1)(1 - \frac{1}{l_T}\xi(x') - \hat{d}_0\kappa(x')) - k\right] \cdot G(p_S, p'_S)\end{aligned} \tag{4.38}$$

In the particular case of the evolution of a planar interface, the curvature $\kappa(x) = 0$ and there's no integration over the variable ρ. The volume of integration $V(t_0)$ is defined now as $\xi(t_0) < z' < \infty$ and $p_S = (\xi(t), t)$. After these considerations, we get

$$\begin{aligned}\frac{1}{2}\left[1 - \frac{1}{l_T}\xi(t)\right] = &\int_{\xi(t_0)}^{\infty} dz' \cdot G(p_S, z', t_0) \cdot u(z', t_0) \\ &- \int_{t_0}^{t-} dt'[1 + \dot{\xi}(t')] \cdot (1 - \frac{1}{l_T}\xi(t')) \cdot G(p_S, p'_S) \\ &+ \int_{t_0}^{t-} dt' \int dS' \cdot (1 - \frac{1}{l_T}\xi(t')) \cdot \hat{n}' \cdot \nabla_{\mathbf{r}'} G(p_S, p'_S) \\ &- \int_{t_0}^{t-} dt' \int dS' \cdot n_z \cdot [1 + \dot{\xi}(t)] \cdot \left[(k-1)(1 - \frac{1}{l_T}\xi(t')) - k\right] \cdot G(p_S, p'_S)\end{aligned} \tag{4.39}$$

separating factors in the equation, we have

$$\begin{aligned}
&\frac{1}{2}\left[1-\frac{1}{l_T}\xi(x)\right] = \int_{\xi(t_0)}^{\infty} dz' \cdot G(p_S, z', t_0) \cdot u(z', t_0) \\
&+\int_{t_0}^{t-} dt'[1+\dot{\xi}(t')]\frac{1}{l_T}\xi(t') \cdot G(p_S, p'_S) \\
&-\int_{t_0}^{t-} dt'[1+\dot{\xi}(t')] \cdot G(p_S, p'_S) \\
&+\int_{t_0}^{t-} dt' \int dS' \cdot \hat{n}' \cdot \nabla_{\mathbf{r}'} G(p_S, p'_S) \\
&-\int_{t_0}^{t-} dt' \int dS' \cdot \frac{1}{l_T}\xi(t') \cdot \hat{n}' \cdot \nabla_{\mathbf{r}'} G(p_S, p'_S) \\
&-\int_{t_0}^{t-} dt' \int dS' \cdot n_z \cdot [1+\dot{\xi}(t)] \cdot \left[-k\frac{1}{l_T}\xi(t') - 1 + \frac{1}{l_T}\xi(t')\right] \cdot G(p_S, p'_S).
\end{aligned} \tag{4.40}$$

We now make use of relation 4.33 which, written in the liquid side ($i = 2$), takes the form

$$\int_{t_0}^{t-} dt' \int dS' \cdot \hat{n}' \cdot \nabla' G(p_S, p'_S) - \int_{t_0}^{t-} dt' \int d\rho' \cdot [1+\dot{\xi}(t')] \cdot G(p_S, p'_S) = -\frac{1}{2}F(p_S, t_0) \tag{4.41}$$

where

$$F(p_S, t_0) = -1 + 2\int_{\xi(t_0)}^{\infty} dz' G(p_s; z', t_0). \tag{4.42}$$

Introducing the last relation to simplify Eq. 4.40, we get

$$\begin{aligned}
&\frac{1}{2}\left[1-\frac{1}{l_T}\xi(x)\right] = \int_{\xi(t_0)}^{\infty} dz' \cdot G(p_S, z', t_0) \cdot u(z', t_0) - \frac{1}{2}F(p_S, t_0) \\
&-\int_{t_0}^{t-} dt' \int dS' \cdot \frac{1}{l_T}\xi(t') \cdot \hat{n}' \cdot \nabla_{\mathbf{r}'} G(p_S, p'_S) \\
&+\int_{t_0}^{t-} dt' \int dS' \cdot n_z \cdot [1+\dot{\xi}(t)] \cdot [1+k\frac{1}{l_T}\xi(t')] \cdot G(p_S, p'_S)
\end{aligned} \tag{4.43}$$

Using the Green's function Eq. 4.12, the expression for $\hat{n}' \cdot \nabla_{\mathbf{r}'} G(p_S, p'_S)$ is given by

$$\hat{n}' \cdot \nabla_{\mathbf{r}'} G(p_S, p'_S) = n'_z \left[\frac{1}{2} + \frac{\xi(t) - \xi(t')}{2(t-t')}\right] G(p_S, p'_S) \tag{4.44}$$

Introducing Eq. 4.41 into Eq. 4.40 we get

$$\begin{aligned}\frac{1}{2}\left[1-\frac{1}{l_T}\xi(t)\right] &= \int_{\xi(t_0)}^{\infty} dz' \cdot G(p_S, \mathbf{r}', t_0)\cdot u(z', t_0) - \frac{1}{2}F(p_S, t_0)\\ -\int_{t_0}^{t-} dt' \frac{1}{l_T}\xi(t')\cdot &\left[\frac{1}{2}+\frac{\xi(t)-\xi(t')}{2(t-t')}\right] G(p_S, p_S')\\ +\int_{t_0}^{t-} dt' \int dS'\cdot n_z \cdot [1+\dot{\xi}(t)]\cdot &[1+k\frac{1}{l_T}\xi(t')]\cdot G(p_S, p_S')\end{aligned} \tag{4.45}$$

and simplifying we finally get

$$\begin{aligned}\frac{1}{l_T}\xi(t) &= 2\int_{\xi(t_0)}^{\infty} dz' \cdot G(p_S, z', t_0)\cdot [1-u(z', t_0)]\\ -\frac{1}{2}F(p_S, t_0) &+ \int_{t_0}^{t-} dt' \frac{1}{l_T}\xi(t')\cdot\left[1+\frac{\xi(t)-\xi(t')}{(t-t')}\right] G(p_S, p_S')\\ -2\int_{t_0}^{t-} dt' &\cdot [1+\dot{\xi}(t)]\cdot [1+k\frac{1}{l_T}\xi(t')]\cdot G(p_S, p_S').\end{aligned} \tag{4.46}$$

Introduction of the initial conditions: We can integrate Eq. 4.46 from different initial conditions for the concentration profile. If we are interested in early transient stages, the initial condition at $t = t_0$ is an equilibrium solid-liquid system with concentration c_∞ at the liquid and kc_∞ at the solid. In this case we have

$$u(z, t_0) = 0, \tag{4.47}$$

and the integral equation for the planar front adopts a simpler form given by

$$\begin{aligned}\frac{1}{l_T}\xi(t) &= \left[1+\mathrm{erf}\left(\frac{\xi(t)-\xi(t_0)+t}{2\sqrt{t}}\right)\right] + \int_{t_0}^{t-} dt' \frac{1}{l_T}\xi(t')\cdot\left[1+\frac{\xi(t)-\xi(t')}{(t-t')}\right] G(p_S, p_S')\\ -2\int_{t_0}^{t-} dt' &\cdot [1+\dot{\xi}(t)]\cdot [1+k\frac{1}{l_T}\xi(t')]\cdot G(p_S, p_S').\end{aligned} \tag{4.48}$$

Numerical Simulations: The last equation Eq.4.46 can be discretized in time between an initial time $t_0 = 0$ and the final time t. It results in a set of nonlinear equations which can be solved numerically in order to determine the position of the front at each time. As an example of this calculation procedure, Fig. 4.2 plots the evolution of the front position in time during the one-sided solidification for a certain value of the control parameter $l_T = \tilde{l}_T/\tilde{l} = 3.125$ and for three different values of the partition coefficient $k = 0.15, 0.5, 0.75$. It is interesting to note that, the larger the value of the partition coefficient k, the slower the initial recoil transient, indicating that the steady state for the front position occurs on a time scale $\tilde{\tau}_{front} \approx \tilde{D}/(k\tilde{v}_p^2)$ which is proportional to $1/k$.

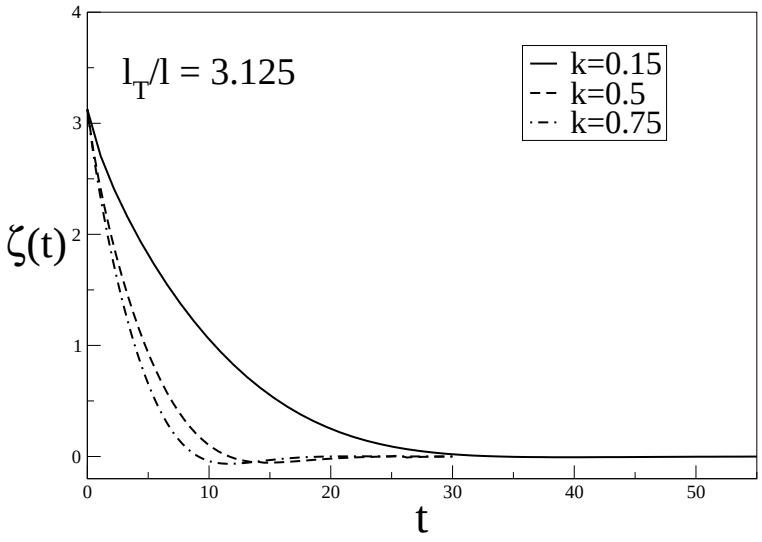

Figure 4.2: Front position during the transient in one-sided directional solidification. The curves have been obtained by solving the boundary integral equation Eq. 4.48 with $l_T = 3.125$ and for three different values of the partition coefficient $k = 0.15, 0.5, 0.75$.

Symmetric models

Equations for the symmetric model can be found in a similar way than in the one-sided model. In order to satisfy the limiting relation Eq. 4.7, and noting that the initial concentration of the melt is c_∞, the diffusion field is defined as

$$c_i = \frac{c_i - c_\infty}{\Delta c_0}, \tag{4.49}$$

We shall distinguish between two different cases:

- ***Constant miscibility gap approximation***: This approximation assumes that the solid and liquid slopes are equal $m_L = m_S$, and is valid when the value of the partition coefficient is near 1 ($k \approx 1$). The solid and liquid lines are then parallel, and at the initial temperature, the initial concentrations are

$$c_1^0 = c_\infty, \tag{4.50}$$
$$c_2^0 = c_\infty + \Delta c_0, \tag{4.51}$$

  where the solvability gap is considered here to be constant in the phase diagram ($\Delta c_0 = c_L^0 - c_S^0 \approx constant$). This approximation can be used with

organic binary mixtures such as liquid crystals where the partition coefficient is large. The initial conditions in this model are given by

$$c_1(z,t_0) = c_\infty - \Delta c_0, \tag{4.52}$$
$$c_2(z,t_0) = c_\infty. \tag{4.53}$$

For the reduced fields, the previous choice corresponds to

$$u_1(z,t_0) = -1, \tag{4.54}$$
$$u_2(z,t_0) = 0. \tag{4.55}$$

On the other hand, the boundary equations at the front are

$$\begin{aligned} &u_2(p_{2S}) = 1 - \frac{1}{l_T}\xi(x_2) - \hat{d}_0\kappa(x_2) \\ &\hat{n}\cdot\Big[\nabla_2 u(p_{2S}) - \nabla_1 u(p_{1S})\Big] = -[1+\dot{\xi}(x_2)] \\ &u_1(p_{1S}) = u_2(p_{2S}) - 1. \end{aligned} \tag{4.56}$$

Adding Eq. 4.35 for $i=1$ and $i=2$, and imposing the boundary equations Eqs. 4.56, we obtain a integro-differential equation for the front position in the symmetric model in the constant gap approximation

$$\begin{aligned} &\frac{1}{2} - \frac{1}{l_T}\xi(t) = \int_{-\infty}^{\xi(t_0)} dz'\cdot G(p_S,z',t_0)\cdot u_1(z',t_0) + \\ &\int_{\xi(t_0)}^{\infty} dz'\cdot G(p_S,z',t_0)\cdot u_2(z',t_0) - \frac{1}{2}\int_{\xi(t_0)}^{-\infty} dz' G(p_S,z',t_0) \\ &-\frac{1}{2}\int_{\xi(t_0)}^{\infty} dz' G(p_S,z',t_0) + \int_{t_0}^{t_-} dt'(1+\dot{\xi})G(p_S,p'_S). \end{aligned} \tag{4.57}$$

Evaluating the third and fourth integrals at the right side of the previous equation, we obtain

$$\int_{\xi(t_0)}^{-\infty} dz' G(p_S,z',t_0) = -\frac{1}{2}\left[1 - \mathrm{erf}\left(\frac{\xi(t)-\xi(0)+t}{2\sqrt{2}}\right)\right] \tag{4.58}$$
$$\int_{\xi(t_0)}^{\infty} dz' G(p_S,z',t_0) = \frac{1}{2}\left[1 + \mathrm{erf}\left(\frac{\xi(t)-\xi(0)+t}{2\sqrt{2}}\right)\right], \tag{4.59}$$

and inserting the last expressions together with the initial conditions Eqs. 4.55 into Eq. 4.57, we arrive to the simplified expression

$$\frac{1}{l_T}\xi(t) = 1 - \int_{t_0}^{t_-} dt'(1+\dot{\xi})G(p_S,p'_S). \tag{4.60}$$

- ***Normal miscibility gap***: In this case, the solid and liquid slopes are related by $km_L = m_S$, and the equilibrium final concentrations are given by

$$c_1^0 = c_\infty \tag{4.61}$$
$$c_2^0 = c_\infty/k, \tag{4.62}$$

whereas the initial profile at $t = t_0$ is

$$c_1(z, t_0) = kc_\infty \tag{4.63}$$
$$c_2(z, t_0) = c_\infty. \tag{4.64}$$

From the last equations, the miscibility gap is $\Delta c_0 = c_1^0 - c_2^0 = c_\infty/k - c_\infty$, and depends on temperature through the partition coefficient k. The initial condition is given by the same expression than in the constant gap approximation

$$u_1(z, t_0) = -1 \tag{4.65}$$
$$u_2(z, t_0) = 0. \tag{4.66}$$

In this model, the boundary equations satisfied at the liquid side of the interface are given by

$$\begin{aligned} &u_2(p_{2S}) = 1 - \frac{1}{l_T}\xi(x_2) - \hat{d}_0\kappa(x_2) \\ &\hat{n}\cdot\Big[\nabla_2 u(p_{2S}) - \nabla_1 u(p_{1S})\Big] = n_z\cdot[1+\dot{\xi}(x_2)]\cdot[(k-1)u_2(p_{2S}) - k] \\ &u_1(p_{1S}) = k[u_2(p_{2S}) - 1]. \end{aligned} \tag{4.67}$$

where $\hat{d}_0 = d_0^c/\Delta c_0$ and $l_T = m_L\Delta C_0/G$. Following the same procedure than in the constant gap approximation model, the integral equation for the front position in the symmetric model (without the constant gap approximation and departing from the initial conditions Eqs. 4.66), are

$$\begin{aligned} &\frac{1}{l_T}\xi(t) = 1 - \frac{(k-1)}{(1+k)}\,\mathrm{erf}\left(\frac{\xi(t) - \xi(0) + t}{2\sqrt{2}}\right) \\ &- \frac{2}{(1+k)}\int_{t_0}^{t_-} dt'(1+\dot{\xi})G(p_S, p_S') \\ &+ \frac{(1-k)}{(1+k)}\int_{t_0}^{t_-} dt'\frac{1}{l_T}\xi(t')\cdot\left[1 + \frac{\xi(t) - \xi(t')}{(t-t')}\right]G(p_S, p_S'). \end{aligned} \tag{4.68}$$

Note that the integral equation Eq. 4.68 recovers exactly the integral equation obtained for the constant gap approximation Eq. 4.60 in the limit $k = 1$.

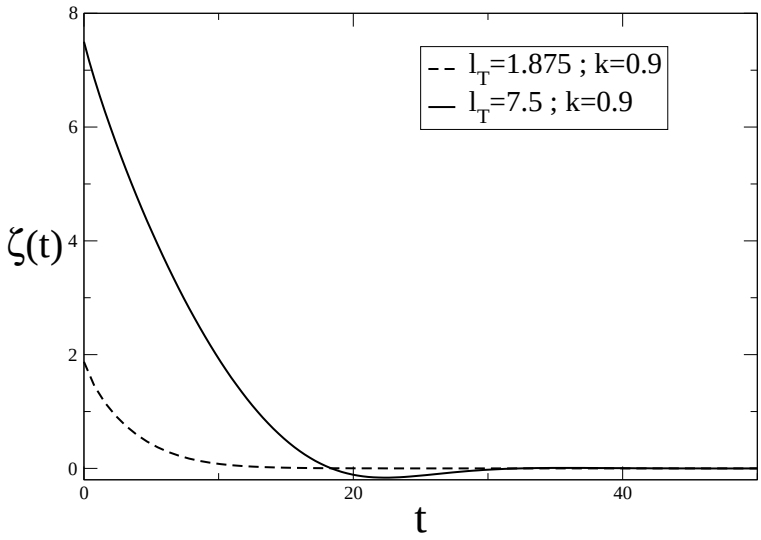

Figure 4.3: Front position during the transient in the symmetric model directional solidification (normal gap). The curves have been obtained by solving the boundary integral equation Eq. 4.68 with $k = 0.9$ and for two different values of the control parameter $l_T = 1.875, 7.5$.

4.2 Noise amplification during directional solidification transients

4.2.1 Morphological stability during the solute redistribution transient

Once we have derived an integro-differential equation for the evolution of the planar front position $\xi(t)$, we want to study the morphological stability of the planar interface under sinusoidal perturbations. The analysis presented in this section is the extension to transient stages of the Mullins-Sekerka analysis described in section 3.3.4. Contrary than in Sec. 3.3.4, we will consider here that the solute diffusion in the solid can be neglected ($\tilde{D}_S = 0$, one-sided approximation). For this purpose, we will work in a frame moving at the same velocity than the front during the transient. In this system of reference, the sharp-interface equations scaled with

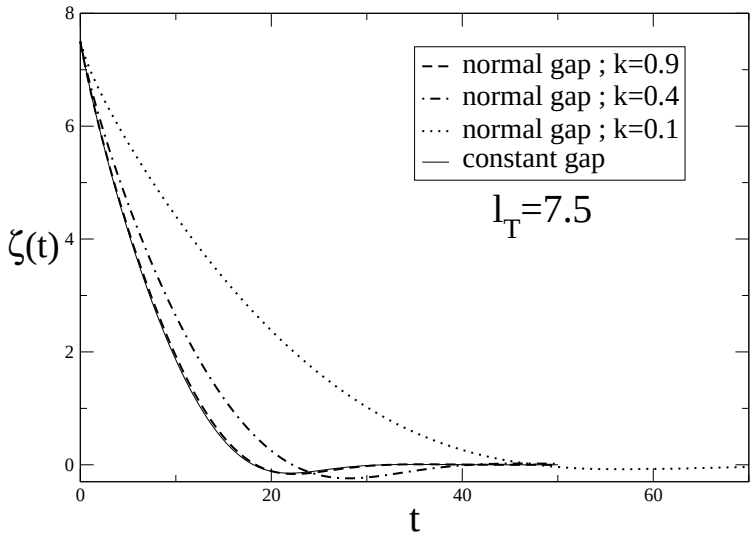

Figure 4.4: Validity of the constant gap approximation. Comparison between the constant gap result (solid line) calculated from Eq. 4.60, and three different values of $k = 0.1, 0.4, 0.9$ in the normal gap model Eq. 4.68. As the value of k approaches to the unity, the results of the normal gap simulations become similar to the constant gap model.

$\tilde{l} = \tilde{D}_L/\tilde{v}_p$ and $\tilde{\gamma} = \tilde{D}_L/\tilde{v}_p^2$ take the form

$$\frac{\partial u}{\partial t} - (1+\dot{\xi})\frac{\partial u}{\partial z} = \nabla^2 u \tag{4.69}$$

$$u(\mathbf{r}_{int}, t) = 1 - \frac{1}{l_T}\xi - \hat{d}_0\kappa(\mathbf{r}_{int}, t) \tag{4.70}$$

$$\hat{n}\cdot\nabla u\big|_{\mathbf{r}_{int}} = (1+\dot{\xi})\Big[(k-1)u(\mathbf{r}_{int}, t) - k\Big], \tag{4.71}$$

where $u(\mathbf{r}, t) = (c(\mathbf{r}, t) - c_\infty)/\Delta c_0$, $\hat{d}_0 = d_0^c/\Delta c_0$, $\Delta c_0 = c_\infty(1-k)/k$, and $l_T = m_L\Delta c_0/G$.

Unperturbed situation: The transient planar front

As we are looking for a transient dispersion relation , we should take into account the initial solute redistribution transient from the initial condition to the final stationary state. Let's assume, following Warren and Langer in Ref. [Warren90, Warren93], that the concentration profile during the transient is an exponential

with a time-dependent decay length l(t)

$$u^0(z,t) = u^0(\xi,t)\ e^{-((z-\xi(t))/l(t)}, \tag{4.72}$$

where ξ is the position of the planar front during the transient and $l(t)$ a time-dependent dimensionless diffusion length. Equation 4.72 must recover the stationary concentration profile $u(z) = e^{-z/l}$ for $t \to \infty$, so in the stationary regime $l(t)$ recovers the value of the diffusion length in the stationary regime $l(t \to \infty) = 1$ ($\tilde{l}(\tilde{t} \to \infty) = \tilde{D}/\tilde{v}_p$). Solution 4.72 must obey the set of equations given by

$$\frac{\partial u^0}{\partial t} - (1+\dot{\xi})\frac{\partial u^0}{\partial z} = \frac{\partial^2 u^0}{\partial z^2} \tag{4.73}$$

$$u^0(\xi(t),t) = 1 - \frac{1}{l_T}\xi(t) \tag{4.74}$$

$$\left.\frac{\partial u^0}{\partial z}\right|_{z=\xi(t)} = (1+\dot{\xi}(t)) \cdot [(k-1)u^0(\xi,t) - k]. \tag{4.75}$$

Equations Eqs.4.74 and 4.75 can be used to derive differential equations governing the dynamics of the position $\xi(t)$ and diffusion length $l(t)$ of the planar interface

$$1+\dot{\xi}(t) = \frac{\left[1-\frac{1}{l_T}\xi(t)\right]}{l(t)\left[1-\frac{1}{l_T}(1-k)\xi(t)\right]} \tag{4.76}$$

$$\dot{l}(t) = \frac{l(t)\dot{\xi}(t)}{\left[1-\frac{1}{l_T}\xi(t)\right]} + \frac{k\xi(t)}{l(t)\left[1-\frac{1}{l_T}(1-k)\xi(t)\right]} \tag{4.77}$$

The last equations are known as the *Warren and Langer equations*, and can be used to determine the front position $\xi(t)$ within the validity of the *Warren and Langer approximation* Eq. 4.72. Contrary to the Green's function solutions presented in the last section Sec. 2.1.1, the Warren and Langer equations do not constitute an analytical solution of the moving boundary problem.

Introduction of the perturbation

We will perform a linear stability analysis of a moving planar interface located at $z = \xi(t)$ and with a concentration profile given by Eq. 4.72.
Let's introduce a perturbation in the system consisting in slight sinusoidal modulations of the interface position. After the perturbation, the position of the front is given by $z = \xi'(\rho,t)$, where

$$\xi'(\rho,t) = \xi(t) + \delta z(\rho,t), \tag{4.78}$$

and the prime accounts for the perturbed value. We introduce perturbations which take the form

$$\delta z(\rho,t) = z_1\ e^{i\mathbf{k}\cdot\rho+\omega(\mathbf{k},t)t} = \xi_k(t)e^{i\mathbf{k}\cdot\rho}, \tag{4.79}$$

describing an exponential growth or decay of the sinusoidal perturbations depending on the value and sign of $\omega(\mathbf{k},t)$. That means that perturbations with a wavevector $\mathbf{k}$ will grow or decay exponentially in time with a growth rate $\omega(\mathbf{k},t)$, which can be expressed with a differential equation for the evolution of the Fourier modes similar to Eq. 3.86 but where ω depends now on time

$$\frac{d\xi_k(t)}{dt} = \omega(k,t)\xi_k(t). \tag{4.80}$$

The objective of this section is to find a closed expression for the dispersion relation $\omega(\mathbf{k},t)$.

Similarly, we consider perturbations in the transient plane front adapted to the form of the profile

$$u(\mathbf{r},t) = u^0(z,t) + \delta u(\mathbf{r},t), \tag{4.81}$$

where δu is given by

$$\delta u(\mathbf{r},t) = u_1\ e^{i\mathbf{k}\cdot\rho+\omega t-q(z-\xi)}. \tag{4.82}$$

The transient dispersion relation $\omega(\mathbf{k},t)$

In order to find closed relations which allow to determine ω and q, we write two relations in the perturbed situation: i) the diffusion equation and ii) the solute conservation condition together with the Gibbs-Thomson equation. These two relations will be conveniently arranged so that it would be possible to determine ω and q.

i) Bulk condition

The first condition will come from the expression of the bulk diffusion equation after the system is perturbed. The concentration field after the perturbation takes the form

$$u(\mathbf{r},t) = u^0(z,t) + \delta u(\mathbf{r},t). \tag{4.83}$$

The concentration gradient in the z direction is given by

$$\frac{\partial u}{\partial z} = \frac{\partial u^0}{\partial z} + \frac{\partial \delta u}{\partial z}, \tag{4.84}$$

which, considering Eq. 4.82,

$$\frac{\partial \delta u}{\partial z} = -q\delta u, \tag{4.85}$$

take the form

$$\frac{\partial u}{\partial z} = \frac{\partial u^0}{\partial z} - q\delta u. \tag{4.86}$$

Similarly, the time derivative of the perturbed field is given by

$$\frac{\partial u}{\partial t} = \frac{\partial u^0}{\partial t} + \frac{\partial \delta u}{\partial t} = \frac{\partial u^0}{\partial t} + \omega \delta u, \tag{4.87}$$

and the diffusion term

$$\nabla^2 u = \frac{\partial^2 u}{\partial x^2} + \frac{\partial^2 u}{\partial y^2} + \frac{\partial^2 u}{\partial z^2} = \nabla^2 u^0 + (q^2 - k^2)\delta u. \tag{4.88}$$

Inserting Eqs. 4.83, 4.86, 4.87 and 4.2.1 into the diffusion equation Eq. 4.69 and simplifying terms noting that u^0 is solution of Eq. 4.69, we obtain

$$\omega = (q^2 - k^2) - q(1 + \dot{\xi}) \tag{4.89}$$

ii) Interface conditions

The next step is to evaluate the moving boundary conditions Eqs. 4.70 and Eq.4.71 at the perturbed interface.

We first proceed by evaluating the mass conservation equation Eq. 4.71 at the perturbed interface $z_{int} = \xi'$

$$\left.\frac{\partial u}{\partial z}\right|_{\xi'} = (1 + \dot{\xi}') \cdot [(k-1)u(\rho, \xi', t) - k]. \tag{4.90}$$

In order to evaluate the terms $\left.\frac{\partial u}{\partial z}\right|_{\xi'}$ and $u(\rho, \xi', t)$ at the left side of Eq.4.90, we expand both functions in Taylor for $\xi' - \xi = \delta z \ll 1$ to obtain

$$u(\rho, \xi', t) \approx u^0(\rho, \xi, t) + \left.\frac{\partial u}{\partial z}\right|_{\xi} \delta z + O(\delta z^2) + \delta u|_{\xi}, \tag{4.91}$$

$$\left.\frac{\partial u}{\partial z}\right|_{\xi'} \approx \left.\frac{\partial u}{\partial z}\right|_{\xi} + \left.\frac{\partial^2 u}{\partial z^2}\right|_{\xi} \delta z + O(\delta z^2). \tag{4.92}$$

Using that $u = u^0 + \delta u$ and keeping terms up to first order in the perturbations we have

$$u(\rho, \xi', t) \approx u(\rho, \xi, t) + \left.\frac{\partial u^0}{\partial z}\right|_{\xi} \delta z + \delta u|_{\xi} \tag{4.93}$$

$$\left.\frac{\partial u}{\partial z}\right|_{\xi'} \approx \left.\frac{\partial u^0}{\partial z}\right|_{\xi} + \left.\frac{\partial \delta u}{\partial z}\right|_{\xi} + \left.\frac{\partial^2 u^0}{\partial z^2}\right|_{\xi} \delta z. \tag{4.94}$$

Evaluating Eq. 4.73 at $z = \xi$ and isolating $\left.\frac{\partial^2 u^0}{\partial z^2}\right|_{\xi}$ it is possible to rewrite Eq. 4.94 as

$$\left.\frac{\partial u}{\partial z}\right|_{\xi'} \approx \left.\frac{\partial u^0}{\partial z}\right|_{\xi} + \left.\frac{\partial \delta u^0}{\partial z}\right|_{\xi} + \left[\frac{\partial u^0}{\partial t} - (1 + \dot{\xi})\frac{\partial u^0}{\partial z}\right]_{\xi} \delta z, \tag{4.95}$$

and as $u^0 = 1 - \frac{1}{l_T}\xi(t)$, $\frac{\partial u^0}{\partial t} = -\frac{1}{l_T}\dot{\xi}(t)$ and we are left with

$$\left.\frac{\partial u}{\partial z}\right|_{\xi'} \approx \left.\frac{\partial u^0}{\partial z}\right|_{\xi} + \left.\frac{\partial \delta u}{\partial z}\right|_{\xi} - \left[\frac{1}{l_T}\dot{\xi}(t) + (1+\dot{\xi})\left.\frac{\partial u^0}{\partial z}\right|_{\xi}\right]\delta z. \tag{4.96}$$

Inserting Eqs. 4.93 and 4.96 into the solute conservation equation Eq. 4.90 we obtain the relation

$$\left.\frac{\partial u^0}{\partial z}\right|_{\xi} + \left.\frac{\partial \delta u}{\partial z}\right|_{\xi} - \left[\frac{1}{l_T}\dot{\xi}(t) + (1+\dot{\xi})\left.\frac{\partial u^0}{\partial z}\right|_{\xi}\right]\delta z = (1+\dot{\xi}')\cdot\left[(k-1)\left(u(\rho,\xi,t) + \left.\frac{\partial u^0}{\partial z}\right|_{\xi}\delta z\right) - k\right], \tag{4.97}$$

which can be simplified using Eq. 4.75 and $\dot{\xi}' = \dot{\xi} + \dot{\delta z}$ to obtain

$$\begin{aligned} \left.\frac{\partial \delta u}{\partial z}\right|_{\xi} - \left[\frac{1}{l_T}\dot{\xi}(t) + (1+\dot{\xi})\left.\frac{\partial u^0}{\partial z}\right|_{\xi}\right]\delta z = \\ (1+\dot{\xi})(k-1)\left[\delta u|_{\xi} + \left.\frac{\partial u^0}{\partial z}\right|_{\xi}\delta z\right] + \dot{\delta z}\left[(k-1)u^0(\xi,t) - k\right]. \end{aligned} \tag{4.98}$$

Using Eqs. 4.79 and 4.82 to evaluate the terms $\dot{\delta z}$ and $\left.\frac{\partial \delta u}{\partial z}\right|_{\xi}$ we have the relations

$$\left.\frac{\partial \delta u}{\partial z}\right|_{\xi} = -q\delta u|_{\xi} = -qu_1 e^{i\mathbf{k}\cdot\rho+\omega t} \tag{4.99}$$

$$\dot{\delta z} = \omega z_1 e^{i\mathbf{k}\cdot\rho+\omega t}, \tag{4.100}$$

which can be used to simplify Eq. 4.98 to get

$$-\left[\frac{1}{l_T}\dot{\xi} + (1+\dot{\xi})\left.\frac{\partial u^0}{\partial z}\right|_{\xi}\right]z_1 - qu_1 = (1+\dot{\xi})(k-1)\left[u_1 + \left.\frac{\partial u^0}{\partial z}\right|_{\xi} z_1\right] + \omega z_1\left[(k-1)u^0(\xi,t) - k\right] \tag{4.101}$$

and arranging terms

$$\begin{aligned} &\left[q + (1+\dot{\xi})(k-1)\right]u_1 \\ &+ \left\{\frac{1}{l_T}\dot{\xi} + (1+\dot{\xi})\left.\frac{\partial u^0}{\partial z}\right|_{\xi} + (1+\dot{\xi})(k-1)\left.\frac{\partial u^0}{\partial z}\right|_{\xi} + \omega\left[(k-1)u^0(\xi,t) - k\right]\right\}z_1 = 0 \end{aligned} \tag{4.102}$$

To complete the interfacial condition, we need another equation relating u_1 and z_1. For this purpose, let's evaluate the Gibbs-Thomson equation Eq. 4.70 at $z_{int} = \xi'$

$$u(\rho,\xi',t) = 1 - \frac{1}{l_T}\xi' - \hat{d}_0\kappa(\xi'). \tag{4.103}$$

The curvature of the perturbed interface can be written as

$$\kappa(\xi') = \kappa(\xi) - k^2\delta z, \tag{4.104}$$

and as the unperturbed interface is a plane front, we have $\kappa(\xi) = 0$. The concentration at the interface is then given by

$$u(\rho, \xi', t) = 1 - \frac{1}{l_T}\xi - (\frac{1}{l_T} + \hat{d}_0 k^2)\delta z, \tag{4.105}$$

and using the Taylor expansion Eq. 4.93 we have

$$u^0(\rho, \xi, t) + \left.\frac{\partial u^0}{\partial z}\right|_\xi \delta z + \delta u|_\xi = 1 - \frac{1}{l_T}\xi - (\frac{1}{l_T} + \hat{d}_0 k^2)\delta z, \tag{4.106}$$

which, using Eq. 4.74 gives

$$u_1 + \left\{ \left.\frac{\partial u^0}{\partial z}\right|_\xi + (\frac{1}{l_T} + \hat{d}_0 k^2) \right\} z_1 = 0 \tag{4.107}$$

We can now combine Eqs. 4.102 and 4.107 to get a closed relation which, together with Eq. 4.89 will determine the dispersion relation of the perturbations during the transient

$$\begin{aligned} -\big[q + (1+\dot{\xi})(k-1)\big] \left[\left.\frac{\partial u^0}{\partial z}\right|_\xi + \frac{1}{l_T} + \hat{d}_0 k^2 \right] + \frac{1}{l_T}\dot{\xi} + (1+\dot{\xi}) \left.\frac{\partial u^0}{\partial z}\right|_\xi \\ +(1+\dot{\xi})(k-1) \left.\frac{\partial u^0}{\partial z}\right|_\xi + \omega\big[(k-1)u^0(\xi,t) - k\big] = 0 \end{aligned} \tag{4.108}$$

simplifying we have

$$\omega\big[(k-1)u^0(\xi,t) - k\big] = \big[q + (1+\dot{\xi})(k-1)\big] \left[\left.\frac{\partial u^0}{\partial z}\right|_\xi + \frac{1}{l_T} + \hat{d}_0 k^2 \right] - \frac{1}{l_T}\dot{\xi} - k(1+\dot{\xi}) \left.\frac{\partial u^0}{\partial z}\right|_\xi, \tag{4.109}$$

and inserting Eqs. 4.74 and 4.75 into Eq. 4.109 we finally obtain

$$\begin{aligned} &\omega\big[(k-1)\big(1 - \frac{1}{l_T}\xi\big) - k\big] = \\ &\big[q + (1+\dot{\xi})(k-1)\big] \left[(1+\dot{\xi}(t)) \cdot \big[(k-1)\big(1 - \frac{1}{l_T}\xi\big) - k\big] + \frac{1}{l_T} + \hat{d}_0 k^2 \right] \\ &- \frac{1}{l_T}\dot{\xi} - k(1+\dot{\xi})^2 \cdot \big[(k-1)\big(1 - \frac{1}{l_T}\xi\big) - k\big], \end{aligned} \tag{4.110}$$

which, together with

$$\omega = (q^2 - k^2) - q(1+\dot{\xi}), \tag{4.111}$$

can be used to determine the transient dispersion relation of the interfacial perturbations during the transient.

Numerical example and limits

Fig. 4.5 shows the value of $\omega(k,t)$ at different times. The substance parameters for this simulation has been taken for the organic mixture CBr_4-C_2Cl_6 (see Section A.2.1 of Appendix A), and the experimental parameters are $\tilde{G} = 5.6\times10^3$ K/m and $\tilde{v}_p = 0.001$ m/s. As time evolves, the growth rate for a certain wavelength increases from a negative value (stable situation), to a positive one, and the interface becomes morphologically unstable under perturbations with this wavelength. As it can be observed in the figure, there is an important difference between the wavelength of the first unstable mode and the wavelength with maximum growth rate at the stationary state. This reveals the importance of considering the initial transient stages when studying the wavelength selection of the final cellular pattern.

As limits of particular interest, we shall remark the equilibrium ($t < 0$) and stationary ($t \to \infty$) situations, which are represented with solid thick lines in the figure. Equations 4.110 and 4.111 permit to obtain analytical expressions for the

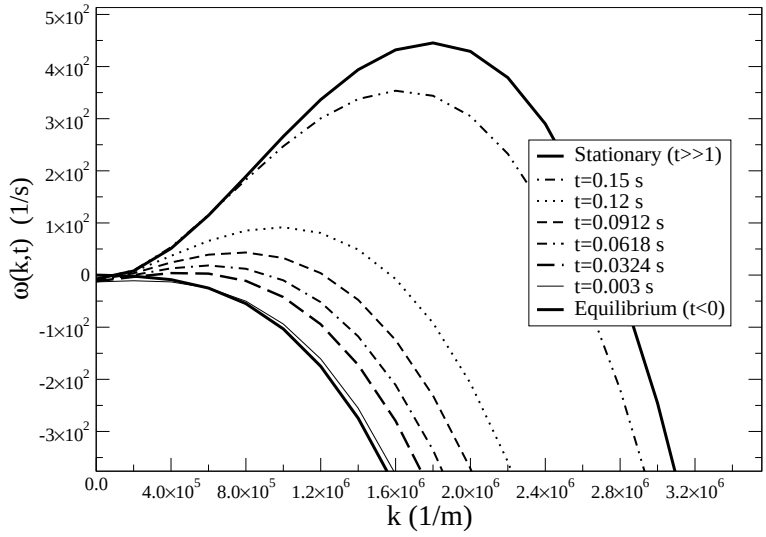

Figure 4.5: Transient dispersion relation at different times calculated from Eqs. 4.110 and 4.111 using the parameters for the organic mixture CBr_4-C_2Cl_6 and the experimental values $\tilde{G} = 5.6 \times 10^3$ K/m and $\tilde{v}_p = 0.001$ m/s. The lower and upper curves correspond to the equilibrium and stationary dispersion relations respectively

growth rate in these two particular limiting cases:

i) Equilibrium interface ($t < 0$)

At $t < 0$, before the external gradient begins to move $\tilde{v}_p = 0$, , we have a stationary ($\dot{\xi}(0) = 0$) flat interface in equilibrium at $z = \xi(0) = l_T$. The velocity of the front in the moving frame is $1 + \dot{\xi}(0) = 0$, and the dispersion relation Eqs. 4.110 takes the form

$$\begin{aligned} \omega_{eq} &= -\frac{q}{k}\left[\frac{1}{l_T} + \hat{d}_0 k^2\right] \\ \omega_{eq} &= (q^2 - k^2). \end{aligned} \tag{4.112}$$

ii) Stationary interface ($t \to \infty$)

At $t \to \infty$ we are in the stationary situation where the solute boundary layer is formed and the interface is located at $z = \xi(t \to \infty) = 0$ and with velocity $\dot{\xi}(t \to \infty) = 0$. The front velocity in the moving frame is now $1 + \dot{\xi}(\infty) = 1$, and we recover the results of the Mullins-Sekerka analysis presented in section 3.3.4 in the one-sided case

$$\begin{aligned} \omega_{st} &= \left[q + k - 1\right]\left[1 - \frac{1}{l_T} - \hat{d}_0 k^2\right] - k. \\ \omega_{st} &= (q^2 - k^2) - q, \end{aligned} \tag{4.113}$$

Miscellaneous topics

i) Transient dispersion relation in physical units

In order to change to physical units, we should use the following relations

$$\xi = \frac{\tilde{\xi}}{\tilde{l}} \tag{4.114}$$

$$\dot{\xi} = \frac{\dot{\tilde{\xi}}}{\tilde{v}_p} \tag{4.115}$$

$$q = \tilde{q}\tilde{l} \tag{4.116}$$

$$k = \tilde{k}\tilde{l} \tag{4.117}$$

$$\omega = \frac{\tilde{D}}{\tilde{v}_p^2}\tilde{\omega} \tag{4.118}$$

$$\hat{d}_0 = \frac{\tilde{\hat{d}}_0}{\tilde{l}} \tag{4.119}$$

$$l_T = \frac{\tilde{l}_T}{\tilde{l}}. \tag{4.120}$$

Writing the system equations Eqs. 4.110 in terms of the physical variables we obtain

$$\tilde{\omega}\left[(1-k)\tilde{\xi}-\tilde{l}_T\right]=\left[\tilde{D}\tilde{q}+(\tilde{v}_p+\dot{\tilde{\xi}})(k-1)\right]\left[(\tilde{v}_p+\dot{\tilde{\xi}})\cdot[(1-k)\tilde{\xi}-\tilde{l}_T]+1+\tilde{l}_T\tilde{d}_0\tilde{k}^2\right]$$

$$-\dot{\tilde{\xi}}-\frac{k\tilde{l}_T}{\tilde{D}}(\tilde{v}_p+\dot{\tilde{\xi}})^2\cdot[(1-k)\tilde{\xi}-\tilde{l}_T]. \tag{4.121}$$

$$\tilde{\omega}=(\tilde{q}^2-\tilde{k}^2)-\tilde{q}(\tilde{v}_p+\dot{\tilde{\xi}}), \tag{4.122}$$

ii) Changing the origin of the reference frame

In some important references (for instance, Refs. [Warren90, Warren93]), the distances in the growth direction are measured in the gradient frame with a variable z' which takes its origin at the initial position of the front instead of the final stationary one.

The relation between $\tilde{z}$ and $\tilde{z}'$ is therefore given by

$$\tilde{z}'=\tilde{z}-\frac{m_L c_\infty}{\tilde{G}k}, \tag{4.123}$$

and consequently the transient front moves from $\tilde{z}'=\tilde{\xi}_L(0)=-\frac{m_L c_\infty}{\tilde{G}}$ at $\tilde{t}=0$ to $\tilde{z}'=\tilde{\xi}_L(\infty)=-\frac{m_L c_\infty}{\tilde{G}k}$ at $\tilde{t}\to\infty$.

The temperature is now given by

$$T(\tilde{\mathbf{r}})=T_M+G\tilde{z}', \tag{4.124}$$

instead by

$$T(\tilde{\mathbf{r}})=T_M-m_L\frac{c_\infty}{k}+\tilde{G}\tilde{z}, \tag{4.125}$$

which has been our standard choice during the preceding chapters. Using these relations, it is possible to write down the equations determining the transient dispersion relation in terms of $\tilde{z}'$ and its time derivatives. From Eq.4.122 we find, in physical units

$$\tilde{q}\left[\tilde{D}+(1-k)\tilde{v}_0\tilde{\xi}_L+\tilde{d}_0 l_T\tilde{k}^2\right]= \tag{4.126}$$

$$\dot{\tilde{\xi}}+(1-k)\left[\frac{\tilde{v}_0^2\tilde{\xi}_L}{\tilde{D}}+\tilde{\omega}\tilde{\xi}_L,+\tilde{v}_0(1+\tilde{d}_0\tilde{l}_T\tilde{k}^2)\right] \tag{4.127}$$

$$\tilde{\omega}=\tilde{D}(\tilde{q}^2-\tilde{k}^2)-\tilde{q}\tilde{v}_0, \tag{4.128}$$

where $\tilde{v}_0$ is given by $\tilde{v}_0=\tilde{v}_p+\dot{\tilde{\xi}}_L$.

iii) The adiabatic approximation

In order to simplify the problem of solving the non-linear set of equations given by Eqs. 4.110, a quasi-stationary approximation can be done by assuming $\partial_t u=0$

in the derivation of the bulk condition. This assumption implies taking $\omega = 0$ in Eq.4.89, which brings to a second order equation to determine q

$$q^2 - q(1 + \dot{\xi}) - k^2 \approx 0, \tag{4.129}$$

and therefore

$$q \approx \frac{(1 + \dot{\xi}) \pm \sqrt{(1 + \dot{\xi})^2 + 4k^2}}{2} \tag{4.130}$$

Note that although we have assumed $\partial_t u = 0$, there is still a time-dependent contribution coming from the transient motion of the front.As a limiting case, the stationary front in the quasi-stationary approximation ($t \to \infty$, $\dot{\xi} = 0$) satisfies

$$q \approx \frac{1 \pm \sqrt{1 + 4k^2}}{2}. \tag{4.131}$$

4.2.2 Noise amplification during transient stages

The last element of the Warren and Langer's theory is to include internal thermodynamical fluctuations as the initiation mechanism for the front perturbations. The departing point is a stochastic version of the equation Eq. 4.80 for the evolution of the Fourier modes,

$$\frac{d\xi_k(t)}{dt} = \omega(k, t)\xi_k(t) + \nu_k(t), \tag{4.132}$$

where the additive noise term $\nu_k(t)$ has the properties

$$\langle \nu_k(t) \rangle = 0, \tag{4.133}$$

$$\langle \nu_k(t)\nu_{k'}(t') \rangle = R_0(k)\delta^2(\mathbf{k} - \mathbf{k}')\delta(t - t') \tag{4.134}$$

The correlation amplitude $R_0(k)$ in Eq. 4.134 has taken to be time independent because $\nu_k(t)$ accounts for thermodynamical equilibrium fluctuations in the system. Equation Eq. 4.132 describes a time-dependent Ornstein-Uhlenbeck process, and a general solution is given by (see Ref. [Gardiner04])

$$\xi_k(t) = \int_{-\infty}^{t} dt' \exp\left\{ \int_{t'}^{t} \omega(k, s)ds \right\} \nu_k(t), \tag{4.135}$$

where it has been assumed that $\xi_k(-\infty) = 0$. The external gradient begins to move at $t = 0$, and the interface is at equilibrium for $t \in [-\infty, 0)$. The statistical properties for the interfacial correlations can be easily calculated from Eq. 4.135

$$\langle \xi_k(t)\xi_{k'}(t) \rangle = R_0(k)\delta^2(\mathbf{k} - \mathbf{k}') \int_{-\infty}^{t} dt' \exp\left\{ \int_{t'}^{t} 2\omega(k, s)ds \right\}. \tag{4.136}$$

As the interface correlation for a planar solid-liquid equilibrium interface is given by

$$\langle \xi_k \xi_{k'} \rangle_{eq} = (2\pi)^2 \delta^2(\mathbf{k} - \mathbf{k}') \frac{k_B T_M}{\sigma} \frac{1}{k^2}, \tag{4.137}$$

we can evaluate the second integral in Eq. 4.136 for $t \in [-\infty, 0)$ where the dispersion relation takes its equilibrium negative value $\omega(k,t) = \omega_{eq}(k) < 0$ given by Eqs.4.112, obtaining

$$\langle \xi_k \xi_{k'} \rangle_{eq} = \frac{R_0(k)}{2|\omega_{eq}(k)|} \delta^2(\mathbf{k} - \mathbf{k}'), \tag{4.138}$$

and comparing Eq. 4.138 with Eq. 4.138 we arrive to

$$R_0(k) = (2\pi)^2 2|\omega_{eq}(k)| \frac{k_B T_M}{\sigma} \frac{1}{k^2}. \tag{4.139}$$

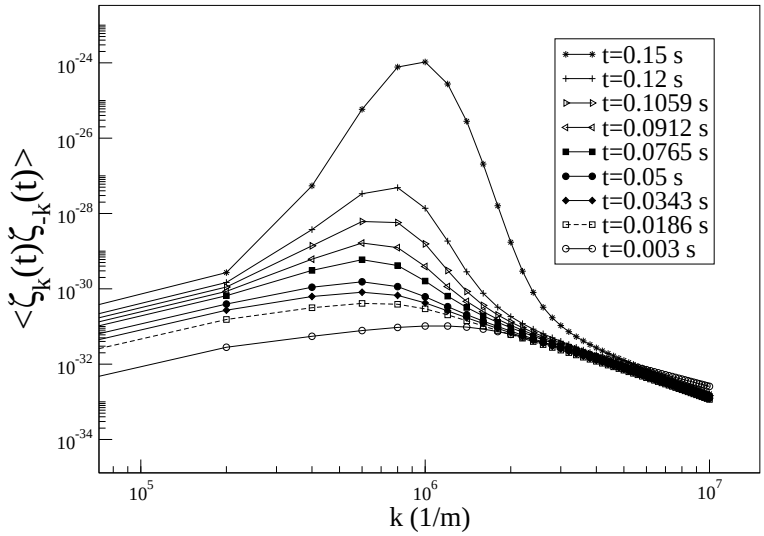

Figure 4.6: Noise amplification during early stages in the directional solidification of CBr_4-C_2Cl_6 ($\tilde{G} = 5.6 \times 10^3$ K/m, $\tilde{v}_p = 0.001$ m/s). The interfacial correlations increase by seven orders of magnitude in a fraction of a second.

Once we have determined the value of $R_0(k)$, Eq. 4.136 can be integrated to obtain the growth or decay of the Fourier modes during the transient. In order to evaluate this integral, we need to solve Eqs. 4.110 and 4.111 to determine the dispersion relation $\omega(k,t)$ at each time. This procedure allows to study the noise

amplification of the system during the initial transient. The mean square amplitude of the interfacial deformations is given by

$$\langle \xi^2(t) \rangle = \int \frac{d^2k}{(2\pi)^2} \langle \xi_k(t) \xi_{-k}(t) \rangle, \tag{4.140}$$

where $\langle \xi_k(t) \xi_{-k}(t) \rangle$ is defined as

$$\langle \xi_k(t) \xi_{-k}(t) \rangle = \int \frac{d^2k'}{(2\pi)^2} \langle \xi_k(t) \xi_{k'}(t) \rangle = \frac{R_0(k)}{(2\pi)^2} \int_{-\infty}^{t} dt' \exp \left\{ \int_{t'}^{t} 2\omega(k,s) ds \right\}. \tag{4.141}$$

Figure Fig. 4.6 shows the time evolution of the interfacial correlations at nine different times during the very early redistribution transient. The integration of Eq. 4.141 have been performed using the parameters of the CBr_4-C_2Cl_6 and for the experimental values $\tilde{G} = 5.6 \times 10^3$ K/m and $\tilde{v}_p = 0.001$ m/s. Fig. 4.6 shows the rapid amplification of these wavelengths from the initial interfacial noise. A remarkable fact is that the dynamically selected wavelength is about $\tilde{k} \approx 10^{-6}$ m^{-1}, whereas the dispersion relation in Fig. 4.5 shows that other wavelengths have much larger growth rates. This shows that the wavelength selection occurs at very early times during the transient stages, and that the selected wavelength is maintained by the system even in later stages when the growth rate for other perturbations have higher values.

Chapter 5

Phase-field models for solidification

In the last years, phase-field models have emerged as an efficient technique to simulate interfacial phenomena in non-equilibrium systems [González-Cinca04]. This method has successfully been applied to several problems such as solidification [Wheeler92a, Wheeler92b, Karma98], domain growth, grain boundaries [Warren03], crack propagation [Aranson00], viscous fingering [Folch99] or vesicle dynamics [Biben03]. The phase-field approach introduces an equation for a continuous variable $\phi(\mathbf{r}, t)$, which appears as an order parameter and takes distinct constant values in the different phases. The interface is then described by the level set $\phi = constant$, and the transition between both phases takes place in a diffuse interface of thickness W. The model is completed by coupling the ϕ equation with a diffusion field which acts as a driving force. The behavior of the diffuse interface can then be computed by the integration of a set of partial differential equations for the whole system, therefore avoiding the explicit tracking of the interface position. This has practical advantages over using the free boundary conditions characteristic of a moving boundary description.

5.1 Introduction

Phase-field models were first proposed by J.S. Langer as a method to describe the dynamics of first-order phase transitions [Langer78, Langer86]. At the same time, Collins and Levine [Collins85] derived independently a diffuse interface approach and studied the basic solutions of the equations, and Fix [Fix83] applied the idea of introducing a continuous field in order to avoid the tracking of the front in the numerical simulation of a moving boundary problem.

The Langer's original formulation was based in classical models for phase transitions such as the Ginzburg-Landau theory [Ginzburg50] or the Cahn-Hilliard

[Cahn58] models. Langer described the advance of the solidification front by means of a continuous order parameter ϕ which took different constant values at the solid and liquid phases of the system. The dynamics of this order parameter or *phase-field* obeys a variational principle determined by the optimization of a general free energy functional. In particular, he started from the C model of Hohenberg, Halperin and Ma [Halperin74] which incorporated the coupling of the order parameter ϕ with an auxiliary conserved field like temperature or solute concentration. Using general thermodynamical considerations, Langer derived the form of the system's free energy in the case of the solidification of an undercooled pure melt. In particular, he related the thickness of the diffuse region between the two phases with the surface energy of the solid-liquid interface. With this approach, Langer recovered the physical dynamics of the solidification front in the limit where the space and time variations of the diffusion field occur in a larger and slower scale than the phase-field variations. Therefore, the phase-field evolution recovers the moving boundary solutions in the limit of small interface thickness and a quasistationary evolution of the diffusion field with respect to the phase-field dynamics.

A major advantage of the phase-field approach is that the resulting model equations were much simpler than the moving boundary equations of the sharp-interface problem. One of the main computational advantages of the phase-field over the moving boundary description is that it avoids the use of interface tracking algorithms. As soon as phase-field models where first formulated, an important amount of work was done in order to define them from solid mathematical and physical grounds. Caginalp [Caginalp84, Caginalp86a, Caginalp89, Caginalp88, Caginalp90] proposed a formal asymptotic limit in terms of the interface thickness which allowed to determine the model parameters so that the phase-field dynamics recovers the different versions of the moving boundary problem. This asymptotic procedure was known as the *sharp-interface limit*, and established the physical and mathematical grounds of the phase-field technique. Fife and Penrose [Fife95] studied how the finite thickness effects produced a deviation from the dynamics of the physical moving boundary description.

The first phase-field simulations were performed by Kobayashi [Kobayashi93a] and Wheeler [Wheeler93], who used the model to simulate solidification patterns as the growth of dendritic structures. At about the same time, some authors [Penrose90, Wang93, Penrose93] noticed that the phase-field method presented some thermodynamical inconsistencies. Specifically, they proposed a formulation which ensured the increase of the local entropy production by deriving the model in terms of an entropy functional instead using a free energy functional.

Phase-field methods, which were first formulated for the solidification of pure substances, were soon extended to account for the solidification of supersaturated melts [Wheeler92a, Wheeler92b] by introducing the solute concentration of a dilute binary mixture as the conserved diffusive field in the problem.

The introduction of surface tension anisotropy was already proposed in the early phase-field formulations [Langer86, Caginalp86b, Caginalp86c, Caginalp86d], and opened the possibility of performing dendritic growth simulations. Some later

works [Karma98] also included anisotropy in the kinetic attachment, which becomes relevant in the kinetic regime at high growth rates. Three-dimensional simulations of the tip radius selection in dendritic growth were performed by Karma and Rappel [Karma96a, Karma97] confirming the validity of the phase-field approach in selection problems and supporting the conclusions of the microscopic solvability theory for the growing dendrite. Qualitative comparison of the phase-field results with experimental results were proposed by Murray, Wheeler and Glicksman [Murray95].

The main drawback of the phase-field approach was that obtaining quantitative results from the simulations presented some important computational difficulties. The first versions of this asymptotic procedure (classical sharp-interface limit) were very restrictive in the values of W, which meant a drastic reduction of the computational efficiency of the method. By performing the asymptotic expansion using the Pélcet number instead of the interface thickness, Karma and Rappel [Karma96b, Karma98] presented a modified asymptotic procedure (*thin interface limit*) which presented better convergence in W, allowing quantitative results to be obtained. This procedure relaxed the restrictive conditions of the ratio between the interface thickness and the capillary length of the substance, resulting in an important improvement of the computational power of the technique.

From the first article of Langer, phase-field models were formulated with the possibility of having a variational structure, i.e., in such a way that the equations of both the phase-field and the coupled conserved diffusion field could be derived *from the same free energy functional*. Some computational works [Kim99, Karma98], however, have pointed out that non-variational formulations allow for more flexibility and provide an improvement in computational efficiency.

The importance of noise in the wavelength selection during initial stages [Qian89] and its relevance in the formation of dendritic sidebranches [Karma99, González-Cinca01, Pocheau01, Li99] resulted in the necessity of introducing thermodynamical fluctuations in the phase-field approach. Thermodynamical fluctuations were first introduced by following the Hohenberg and Halperin models for critical dynamics and introducing additive stochastic terms in the model equations. For a complete introduction to noise in pattern-forming extended systems, we refer to Ref. [García-Ojalvo99]. The statistical properties of the additive noises in the phase and diffusive field equations were then determined by using the fluctuation-dissipation relation. Other approaches based on the statistical properties of the system where proposed by Pavlik and Sekerka [Pavlik99, Pavlik00], which used the free energy functional as a partition function for the system, and derived the statistical properties of the noises from statistical mechanics arguments. In all these works, however, the introduction of noise was restricted to variational models. In non-variational formulations, fluctuation-dissipation relation cannot be used in order to determine the noise properties and a stochastic asymptotic limit is required to project the noise dynamics of the phase-field into a fluctuating sharp-interface description [Benítez04c]. We will turn to this point in Chapter 6, where we present a sharp-interface projection of a generic stochastic phase-field model.

Another important problem of the phase-field approach was to account for one-sided systems. In such cases, the sharp interface limit presented some pathological problems which resulted in the form of finite thickness effects. Almgren was the first in determining the form of these spurious terms arising from the sharp-interface limit [Almgren99], concluding that the finite thickness effects could not be canceled by simply choosing the convenient interpolation functions in the free energy functional. Following a similar procedure proposed by Folch [Folch99], Karma proposed a one-sided model which included an additional anti-trapping current term which allowed to cancel these spurious terms [Karma01].

5.2 Variational Formulations

5.2.1 Non-symmetric dilute binary alloys

Let us introduce the phase-field variable ϕ as a continuous order parameter which takes different constant values at the solid and liquid bulk phases. Consider, for instance, that $\phi = 1$ in the solid and $\phi = -1$ in the liquid phase. In the intermediate region between the two phases, the phase field defines a diffuse zone of a certain thickness $\tilde{W}$. The dynamics of ϕ will be determined by a phenomenological free energy functional $\tilde{\mathcal{F}}$ which should include the basic thermodynamical features of the system. For a dilute binary solution, for instance, the system can be thermodynamically described in terms of its molar fraction of solute c_B and its temperature T, and the general expression for the free energy functional, written in dimensional units, is given by

$$\tilde{\mathcal{F}}[\phi, c_B, T] = \int d\tilde{\mathbf{r}} \left[\frac{\tilde{K}}{2} |\tilde{\nabla}\phi|^2 + \tilde{h}_0 f(\phi) + \tilde{g}_v(\phi, c_B, T) \right], \tag{5.1}$$

In the last expression, $\tilde{\mathcal{F}}$ represents the total Gibbs' free energy of the system and the integration domain extends to the total volume of the system. The $\frac{\tilde{K}}{2}|\tilde{\nabla}\phi|^2$ term accounts for the free energy excess due to the presence of interfaces in the system, being $\tilde{K}$ the energy per unit length associated to a solid-liquid interface. The second term is a symmetric double-well potential with two minima located at $\phi = \pm 1$, and separated by a barrier of height $\tilde{h}_0$. The standard choice for this potential is given by

$$f(\phi) = -\frac{1}{2}\phi^2 + \frac{1}{4}\phi^4, \tag{5.2}$$

which is represented in Fig. 5.1. The last term in the integral $\tilde{g}_v(\phi, c_B, T)$ is a function of ϕ which recovers the Gibbs' free energy per unit volume of the system at the solid and liquid phases for $\phi = \pm 1$. This function $\tilde{g}_v$ includes the particular thermodynamic features of the system such as the phase diagram and the equilibrium conditions for heterogeneous phases. By changing the parameters in the free energy density $\tilde{g}_v$, it is possible to modify the relative stability of the solid and

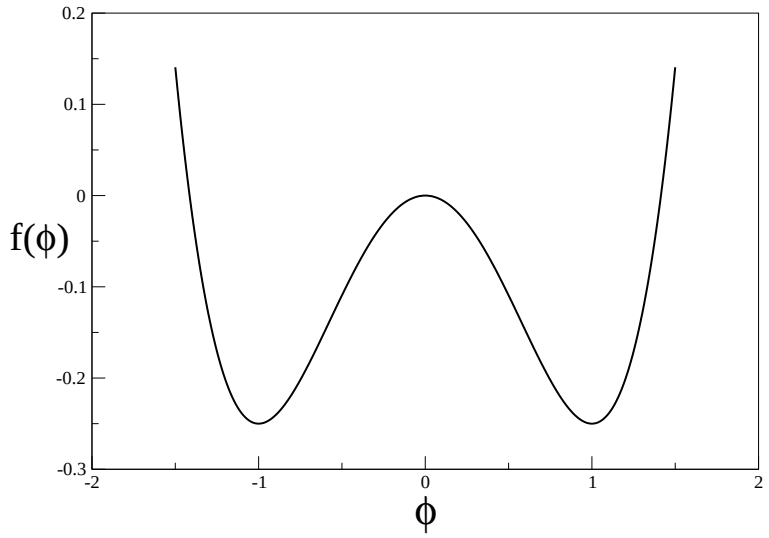

Figure 5.1: The double-well potential $f(\phi)$ which determines the solutions $\phi = \pm 1$ as the two stable phases in the system.

liquid phases, thus producing the metastability of one of the phases and imposing a non-equilibrium situation in the system which will act as a driving force for the solidification process.

Once we have determined the form of $\tilde{\mathcal{F}}$, its dynamics can then be described by imposing the variational minimization of $\tilde{\mathcal{F}}$

$$\tilde{\tau}\partial_{\tilde{t}}\phi = -\frac{1}{\tilde{h}_0}\left(\frac{\delta\tilde{\mathcal{F}}}{\delta\phi}\right) \tag{5.3}$$

$$\partial_{\tilde{t}} c_B = -\tilde{\nabla}\cdot\tilde{\mathbf{j}}, \tag{5.4}$$

where $\tilde{\tau}$ is a certain time scale, $\tilde{h}_0$ the height of the double-well barrier, and the solute current $\tilde{\mathbf{j}}$ is given by the Fick's Law

$$\tilde{\mathbf{j}} = -M(\phi, c_B)\tilde{\nabla}\mu_v, \tag{5.5}$$

where μ_v is the chemical potential per unit volume of the system, which can be calculated from the free energy functional $\tilde{\mathcal{F}}$ as

$$\mu_v = \frac{\delta\tilde{\mathcal{F}}}{\delta c_B} = \frac{\partial\tilde{g}_v}{\partial c_B}. \tag{5.6}$$

The quantity $M(\phi, c_B)$ in Eq. 5.5 is the atomic mobility of the substance, defined as

$$M(\phi, c) = c(1-c)\frac{\tilde{D}_L v_m}{RT} q(\phi), \tag{5.7}$$

where the dimensionless function $q(\phi)$ satisfies $q(\phi = +1) = \tilde{D}_S/\tilde{D}_L$ and $q(\phi = -1) = 1$ and accounts for systems with different diffusivities in the solid and liquid phases (non-symmetric models). Note that this model can also account for symmetric substances by simply taking $q(\phi) = 1$ in the model equations. From Eqs. 5.3, 5.4 it follows that the phase-field obeys a non-conserved dynamics whereas the solute concentration is governed by a conserved equation.

Being d the spatial dimensionality of the system, the dimensions of the parameters and fields which have appeared so far are

$$[\tilde{\mathcal{F}}] \sim E \tag{5.8}$$

$$[\tilde{K}] \sim \frac{E}{L^{d-2}} \tag{5.9}$$

$$[\tilde{g}_v] \sim [\tilde{h}_0] \sim \left[\frac{\delta\tilde{\mathcal{F}}}{\delta\phi}\right] \sim \left[\frac{\delta\tilde{\mathcal{F}}}{\delta c}\right] \sim \frac{E}{L^d} \tag{5.10}$$

$$[M] \sim \frac{L^{d+2}}{ET} \tag{5.11}$$

$$[\mu_v] \sim \frac{E}{L^d} \tag{5.12}$$

$$[\tilde{\tau}] \sim T, \tag{5.13}$$

where E, T, L denote energy, time and length, respectively.

Thermodynamics of dilute regular binary solutions

As we have seen in the first chapter (Sec. 2.1.2), the Gibbs' free energy for a dilute regular binary solution is given by (cf. Eq. 2.41)

$$G = n_A g_A + n_B g_B + \nu n_A n_B + TR(n_A \ln c_A + n_B \ln c_B)\ , \tag{5.14}$$

where $\nu = \frac{zN_0}{n}(U_{AB} - \frac{1}{2}(U_{AA} + U_{BB}))$, $n = n_A + n_B$ the total number of moles, n_i is the number of moles of the $i = A, B$ specie, $c_i = n_i/n$ its molar fraction, and g_i the molar free energy of the pure i substance.

The molar free energy density g_v can then be obtained by dividing Eq. 5.14 by the molar density v_m and the total number of moles n, resulting

$$g_v = c_A g_v^A + c_B g_v^B + \nu_v c_A c_B + \frac{TR}{v_m}(c_A \ln c_A + c_B \ln c_B)\ , \tag{5.15}$$

with $\nu_v = \frac{zN_0}{v_m}(U_{AB} - \frac{1}{2}(U_{AA} + U_{BB}))$.

In the dilute approximation, we can assume that

$$\ln c_A \approx -c_B \tag{5.16}$$

$$c_A c_B = (1 - c_B)c_B \approx c_B, \tag{5.17}$$

and the resulting molar free energy density is

$$g_v = c_A g_v^A + c_B g_v^B + \nu_v c_B + \frac{TR}{v_m}(c_B \ln c_B - c_B). \tag{5.18}$$

If our system is taken slightly away from equilibrium, the molar Gibbs' free energy density of the pure A substance $g_v^A(T)$ can be expanded around the melting temperature T_M^A having

$$g_v^A(T) \approx g_v^A(T_M^A) - s_v(T_M^A)(T - T_M^A), \tag{5.19}$$

where $s_v(T) = -\frac{\partial g_v^A(T)}{\partial T}$ is the molar entropy density. Inserting the last expression into Eq. 5.18, we get the final expression for the free energy density

$$g_v(T, c_B) = c_A\left[g_v^A(T_M^A) - s_v^A(T_M^A)(T - T_M^A)\right] + c_B g_v^B(T) + \nu_v c_B + \frac{TR}{v_m}c_B(\ln c_B - 1). \tag{5.20}$$

In a heterogeneous system, assuming that the molar volumes are equal in the solid and liquid phases ($v_m^S = v_m^L = v_m$), the value of the free energy density is given by

$$\begin{aligned} g_v^S(T, c_B^S) =& c_A^S\left[\tilde{g}_A - s_v^S(T_M^A)(T - T_M^A)\right] + c_B^S g_v^{B,S}(T) \\ &+ \nu_v^S c_B^S + \frac{TR}{v_m}c_B^S(\ln c_B^S - 1) \\ g_v^L(T, c_B^L) =& c_A^L\left[\tilde{g}_A - s_v^L(T_M^A)(T - T_M^A)\right] + c_B^L g_v^{B,L}(T) \\ &+ \nu_v^L c_B^L + \frac{TR}{v_m}c_B^L(\ln c_B^L - 1), \end{aligned} \tag{5.21}$$

where we have introduced $\tilde{g}_A = g_v^{A,S}(T_M^A) = g_v^{A,L}(T_M^A)$ by noting that the molar free energy density of A have the same value at the solid and the liquid, which is the equilibrium condition for the pure A substance system. Observing the form of Eq. 5.21, we note that for regular solutions in the dilute approximation, the thermodynamical magnitudes which take different values at the two phases are:

1. The entropy density s_v^α,
2. the regular solution parameter $\nu_v^\alpha = \frac{zN_0}{v_m}(U_{AB}^\alpha - \frac{1}{2}(U_{AA}^\alpha + U_{BB}^\alpha))$, and
3. the pure solute free energy density $g_v^{B,\alpha}(T)$.

Equilibrium conditions for a regular dilute system

For a dilute regular solution, the chemical potentials per unit volume ($\mu_v = \mu/v_m$) are given by (cf. Eq. 2.52)

$$\begin{aligned} \mu_v^A &= g_v^A - \frac{RT}{v_m} c_B \\ \mu_v^B &= g_v^B + \nu_v + \frac{RT}{v_m} \ln c_B. \end{aligned} \tag{5.22}$$

The equilibrium conditions for the system are given by (cf. Eq.2.49 and 2.50) are

$$\mu_v^{A,S} = \mu_v^{A,L} \tag{5.23}$$

$$\mu_v^{B,S} = \mu_v^{B,L}. \tag{5.24}$$

Inserting μ_A in Eq. 5.22 into the first equilibrium condition Eq. 5.23, and expanding as usual $g_A^\alpha(T) \approx g_A^\alpha(T_M^A) - s_A^\alpha(T - T_M^A)$, we find the decrease in the melting temperature for a regular dilute solution

$$T = T_M^A - \frac{RT^2}{L_m}(c_B^L - c_B^S), \tag{5.25}$$

where L_m is the latent heat per unit mol of the substance or molar latent heat. From the second equilibrium condition Eq.5.24, it results

$$\frac{c_B^{0,S}}{c_B^{L,0}} = k = \exp\left\{\frac{v_m}{RT}(\Delta g_v^B + \Delta\nu_v)\right\}, \tag{5.26}$$

being $c_B^{0,S}$ and $c_B^{L,0}$ the solid and liquid equilibrium concentrations, $\Delta g_v^B = g_v^{B,L} - g_v^{B,S}$, $\Delta\nu_v = \nu_v^L - \nu_v^S$, and k the partition coefficient of the system.

Constructing the $\tilde{g}_v(\phi, c_B, T)$ potential

Now that we know the expressions for the free energy density at each phase Eqs. 5.21, we can construct the function $\tilde{g}_v(\phi, c_B, T)$ in the free energy functional $\tilde{\mathcal{F}}$ in Eq. 5.1. As $\tilde{g}_v(\phi, c_B, T)$ changes continously between the solid and liquid phases, let us consider the next ansatz expression

$$\tilde{g}_v(\phi, c_B, T) = c_A\left[\tilde{g}_A - a(\phi)(T - T_M^A)\right] + b(\phi)c_B + \frac{TR}{v_m} c_B(\ln c_B - 1). \tag{5.27}$$

where $a(\phi)$ and $b(\phi)$ are continuous functions of ϕ which allow to recover the thermodynamical properties of the system at each of the phases. In the dilute limit, we can assume $c_A \approx 1$ in Eq. 5.27 and write

$$\tilde{g}_v(\phi, c_B, T) = \tilde{g}_A - a(\phi)(T - T_M^A) + b(\phi)c_B + \frac{TR}{v_m} c_B(\ln c_B - 1). \tag{5.28}$$

In order to recover the solid and liquid molar entropy and enthalpy densities at $\phi = \pm 1$, i.e.

$$a(\phi = +1) = s_v^S(T_M) \tag{5.29}$$
$$a(\phi = -1) = s_v^L(T_M) \tag{5.30}$$
$$b(\phi = +1) = \nu_v^S + g_v^{B,S}(T) \tag{5.31}$$
$$b(\phi = -1) = \nu_v^L + g_v^{B,L}(T), \tag{5.32}$$

the functions $a(\phi)$ and $b(\phi)$ in Eq. 5.28 should be given by

$$a(\phi) = \frac{\Sigma s_v}{2} - \frac{\Delta s_v}{2} g(\phi) \tag{5.33}$$
$$b(\phi) = \frac{(\Sigma \nu_v + \Sigma g_v^B)}{2} - \frac{(\Delta \nu_v + \Delta g_v^B)}{2} p(\phi), \tag{5.34}$$

where we have defined

$$\Sigma s_v = s_v^S(T_M) + s_v^L(T_M) \tag{5.35}$$
$$\Sigma \nu_v = \nu_v^S + \nu_v^L \tag{5.36}$$
$$\Sigma g_v^B = g_v^{B,S}(T) + g_v^{B,L}(T) \tag{5.37}$$
$$\Delta \nu_v = \nu_v^L - \nu_v^S \tag{5.38}$$
$$\Delta s_v = s_v^L(T_M^A) - s_v^S(T_M^A) \tag{5.39}$$
$$\Delta g_v^B = g_v^{B,L} - g_v^{B,S}, \tag{5.40}$$

and the functions $p(\phi)$ and $p'(\phi)$ satisfy the relations

$$g(\phi = \pm 1) = p(\phi = \pm 1) = \pm 1 \tag{5.41}$$
$$\partial_\phi g(\phi = \pm 1) = \partial_\phi p(\phi = \pm 1) = 0. \tag{5.42}$$

Let us consider again the pure A substance case, which is recovered from Eq. 5.28 by taking $c_B = 0$ (and $c_A = 1$). Its free energy density $\tilde{g}_v$ is then given by

$$\tilde{g}_v^{pure}(\phi, T) = \tilde{g}_A - a(\phi)(T - T_M^A), \tag{5.43}$$

When the pure substance is not undercooled (i.e. $T = T_M^A$), the system will be at equilibrium obeying the equilibrium condition $\tilde{g}_v^{pure}(\phi = \pm 1, T_M^A) = \tilde{g}_A$. When the system is undercooled, the free energy density difference between the solid and liquid phases can easily be calculated from Eq. 5.43 to be

$$\Delta \tilde{g}_v^{pure} = \tilde{g}_v^{pure,L} - \tilde{g}_v^{pure,S} = \tilde{g}_v^{pure}(\phi = -1, T) - \tilde{g}_v^{pure}(\phi = +1, T) = -\Delta s_v (T - T_M^A), \tag{5.44}$$

and noting that $\Delta s_v = L_v / T_M^A$, we recover the driving force for the solidification of an undercooled melt introduced in Sec. 2.1.1

$$\Delta \tilde{g}_v^{pure} = -\frac{L_v}{T_M^A}(T - T_M^A), \tag{5.45}$$

recovering the result of the first chapter (cf. Eq. 2.15).

Derivation of the model equations

1. Equation for c_B:

Introducing Eq. 5.28 into the free energy functional Eq. 5.1, the variations $\frac{\delta\tilde{\mathcal{F}}}{\delta\phi}$ and $\frac{\delta\tilde{\mathcal{F}}}{\delta c}$ which appear in the dynamic equations Eqs. 5.3, 5.4, can be easily calculated. The chemical potential density of the solute B in the model is defined as

$$\mu_v(\phi) = \frac{\delta\tilde{F}}{\delta c_B} = \frac{\partial\tilde{g}_v}{\partial c_B} = b(\phi) + \frac{RT}{v_m}\ln c_B. \tag{5.46}$$

which recovers the second expression in Eqs. 5.22 at the solid ($\phi = +1$) and liquid ($\phi = +1$) bulk phases. For dilute solutions, the mobility M introduced in Eq. 5.7 can be approximated by

$$M(\phi, c_B) = c_B \frac{\tilde{D}_L v_m}{RT} q(\phi), \tag{5.47}$$

and, introducing Eq. 5.46 and noting that g_v^B is constant, the Fick's law Eq. 5.5 reads

$$\tilde{\mathbf{j}} = -c_B \tilde{D}_L q(\phi)\tilde{\nabla}\mu_v(\phi) = -c_B\tilde{D}_L q(\phi)\tilde{\nabla}\left[\frac{v_m}{RT}b(\phi) + \ln c_B\right], \tag{5.48}$$

and the evolution of the solute concentration field is given by

$$\partial_{\tilde{t}} c_B = -\tilde{\nabla}\cdot\tilde{\mathbf{j}} = \tilde{D}_L\tilde{\nabla}c_B q(\phi)\tilde{\nabla}\left[\frac{v_m}{RT}b(\phi) + \ln c_B\right], \tag{5.49}$$

or, equivalently,

$$\partial_{\tilde{t}} c_B = \tilde{D}_L\tilde{\nabla}c_B q(\phi)\tilde{\nabla}\left[\frac{v_m}{RT}b(\phi)\right] + \tilde{D}_L\tilde{\nabla}q(\phi)\tilde{\nabla}c_B. \tag{5.50}$$

Reminding the definition of $q(\phi)$ in Eq. 5.7, we recover for $\phi = \pm 1$ the diffusion equations in the solid and liquid phases $\alpha = S, L$

$$\partial_{\tilde{t}} c_B^\alpha = \tilde{D}_\alpha\tilde{\nabla}^2 c_B^\alpha. \tag{5.51}$$

2. Equation for ϕ:

The equation for the dynamics of the ϕ field can also be obtained noting that the variation of the free energy with respect to ϕ is given by

$$\frac{\delta\tilde{F}}{\delta\phi} = -\tilde{K}\tilde{\nabla}^2\phi + \frac{\partial\tilde{g}_v}{\partial\phi}. \tag{5.52}$$

From Eq. 5.28, the last term in Eq. 5.52 is

$$\frac{\partial\tilde{g}_v}{\partial\phi} = -\partial_\phi a(\phi)(T - T_M^A) + \partial_\phi b(\phi)c_B, \tag{5.53}$$

and the time evolution of the phase field is given by

$$\tilde{\tau}\partial_{\tilde{t}}\phi = \frac{\tilde{K}}{\tilde{h}_0}\tilde{\nabla}^2\phi - \partial_\phi f(\phi) + \frac{1}{\tilde{h}_0}\partial_\phi a(\phi)(T - T_M^A) - \frac{1}{\tilde{h}_0}\partial_\phi b(\phi)c_B, \tag{5.54}$$

where we can check that all the terms are dimensionally correct by noting that both $a(\phi)$ and $b(\phi)$ have dimensions of energy per unit volume. Equation 5.54 can be interpreted as follows: The time evolution of the phase-field variable depends on the four factors at the right side of Eq. 5.54: The first term is a diffusive term which tends to eliminate the gradients in the phase-field ϕ by diffusing them. The derivative of the double-well potential $\partial_\phi f$ acts as a force which guarantees that the solid ($\phi = +1$) and liquid ($\phi = -1$) phases are the equilibrium phases of the system. The last two terms account for the deviations from the bulk equilibrium which turns metastable one of the phases making the other one grow. The $\partial_\phi a(\phi)$ term describes the free energy variation due to the mixing entropy density differences between the solid and liquid phases, whereas the $\partial_\phi b(\phi)$ term accounts for free energy variations produced by the variation in the mixing enthalpy of the system (regular systems) and in the free energy of the pure solute.

Equilibrium profiles for ϕ and c_B

Let us consider an equilibrium dilute binary heterogeneous system with equilibrium solute concentration at the liquid $c_B^{0,L}$. The equilibrium condition $\mu_v^S = \mu_v^L$ can be imposed by evaluating from Eq. 5.46 the chemical potential at the bulk phases $\phi = \pm 1$

$$\mu_v^0 = b(\phi = +1) + \frac{RT}{v_m}\ln c_B^{0,S} = b(\phi = -1) + \frac{RT}{v_m}\ln c_B^{0,L}, \tag{5.55}$$

where μ_v^0 is the equilibrium chemical potential. From the last equation, we see that the phase-field formulation recovers the equilibrium concentration at the solid as $c_B^{0,S} = kc_B^{0,L}$, where the segregation constant k is

$$k = \exp\left\{\frac{v_m}{RT}(\Delta g_v^B + \Delta\nu_v)\right\}, \tag{5.56}$$

The next step is to obtain the phase field profile $\phi_0(\tilde{z})$ of an equilibrium solid-liquid planar interface perpendicular to the z direction.

In equilibrium, we have

$$\left.\frac{\partial\tilde{g}_v}{\partial\phi}\right|_{\phi_0, c_B^0} = 0, \tag{5.57}$$

and the non-equilibrium terms in Eq. 5.54 cancel out leading to a relation between the functions a and b

$$\partial_\phi a(\phi_0(\tilde{z}))(T - T_M^A) = \partial_\phi b(\phi_0(\tilde{z}))c_B^0(\tilde{z}), \tag{5.58}$$

which is obviously satisfied at the bulk phases because we have imposed the condition $\partial_\phi g(\phi = \pm 1) = \partial_\phi p(\phi = \pm 1) = 0$ (cf. Eq. 5.42) to the functions g and p. Imposing now the stationarity of the phase-field $\partial_{\tilde{t}}\phi_0 = 0$, Eq. 5.54 can be written as

$$\frac{\tilde{K}}{\tilde{h}_0}\partial^2_{\tilde{z}}\phi_0 - \partial_\phi f(\phi)|_{\phi_0} = 0. \tag{5.59}$$

It is easy to show that, for the particular choice of $f(\phi)$ given in Eq. 5.2, the last equation has a kink-type solution given by

$$\phi_0(\tilde{z}) = -\tanh\left(\frac{\tilde{z}}{\sqrt{2}\tilde{W}}\right), \tag{5.60}$$

where $\tilde{W} = \sqrt{\frac{\tilde{K}}{\tilde{h}_0}}$ is the *thickness of the solid liquid interface* in the phase-field model. From the last equation, it follows that the solid and liquid bulks are located at $\tilde{z} \to -\infty$ and $\tilde{z} \to \infty$ respectively.

In order to find the equilibrium concentration profile $c^0_B(\tilde{z})$, we introduce the kink solution $\phi_0(\tilde{z})$ into the chemical potential Eq. 5.46, and impose the equilibrium condition $\mu_v(\phi_0) = \mu^0_v$

$$b(\phi_0(\tilde{z})) + \frac{RT}{v_m}\ln c^0_B(\tilde{z}) = \nu^L_v + g^{B,L}_v(T) + \frac{RT}{v_m}\ln c^{0,L}_B, \tag{5.61}$$

from which, using Eq. 5.34, we obtain

$$c^0_B(\tilde{z}) = c^{0,L}_B \exp\left\{\frac{(\Delta\nu_v + \Delta g^B_v)v_m}{2RT}[1 + p(\phi_0(\tilde{z})]\right\}. \tag{5.62}$$

Using the definition of the segregation constant k in Eq. 5.56, we can write the last equation as

$$c^0_B(\tilde{z}) = c^{0,L}_B k^{\frac{1}{2}[1+p(\phi_0(\tilde{z})]}. \tag{5.63}$$

The concentration and phase field equilibrium profiles ϕ_0, c^0_B can be now inserted into the condition Eq. 5.58 in order to obtain a relation between the $g(\phi)$ and $p(\phi)$ functions in Eqs. 5.33 and 5.34, which takes the form

$$\partial_\phi g(\phi_0(\tilde{z})) = \frac{T^A_M c^{0,L}_B(\Delta\nu_v + \Delta g^B_v)}{L_v(T - T^A_M)}\partial_\phi p(\phi_0(\tilde{z}))k^{\frac{1}{2}[1+p(\phi_0(\tilde{z})]}, \tag{5.64}$$

where we have used that $\Delta s_v = L_v/T^A_M$. By using from Eq. 5.56 that

$$\ln k = \frac{(\Delta\nu_v + \Delta g^B_v)v_m}{RT^A_M}, \tag{5.65}$$

and noting from the equation for the decrease of the melting point Eq. 5.25 that

$$T - T^A_M = -\frac{RT^{A\,2}_M}{v_m L_v}c^{0,L}_B(1-k), \tag{5.66}$$

the constant pre-factor of the right side term of Eq. 5.64 can be rewritten as

$$\frac{T_M^A c_B^{0,L}(\Delta\nu_v + \Delta g_v^B)}{L_v(T - T_M^A)} = -\frac{\ln k}{1-k}, \tag{5.67}$$

and the equation Eq. 5.64 adopts the simplified form

$$\partial_\phi g(\phi_0(\tilde{z})) = -\frac{\ln k}{1-k}\partial_\phi p(\phi_0(\tilde{z}))k^{\frac{1}{2}[1+p(\phi_0(\tilde{z})]}, \tag{5.68}$$

The last equation can be easily solved by performing the change of variable $y(\phi) = k^{\frac{1}{2}p}$. We can then write

$$\partial_\phi p(\phi_0)k^{\frac{1}{2}p(\phi_0)} = \frac{2\partial_\phi y}{\ln k}, \tag{5.69}$$

which, substituted in Eq. 5.68, leads to

$$\partial_\phi g(\phi_0) = -\frac{2\sqrt{k}}{1-k}\partial_\phi y, \tag{5.70}$$

which can be integrated over ϕ resulting in

$$g(\phi_0) = -\frac{2\sqrt{k}}{1-k}k^{\frac{1}{2}p(\phi_0)} + C, \tag{5.71}$$

where C is an integration constant which can be determined by imposing the conditions $g(\pm 1) = p(\pm 1) = \pm 1$ to be

$$C = \frac{1+k}{1-k}. \tag{5.72}$$

The desired relation between the functions g and p is finally given by

$$g(\phi_0) = \frac{1+k}{1-k}\left[1 - \frac{2\sqrt{k}}{1+k}k^{\frac{1}{2}p(\phi_0)}\right]. \tag{5.73}$$

As the condition Eq. 5.58 is a required condition for the equilibrium of the system, the last relation between g and p must be respected in the phase-field formulation. The relation Eq. 5.73 can be inverted in order to express the function p in terms of g

$$p(\phi_0) = \frac{2}{\ln k}\ln\left(\frac{1+k-(1-k)g(\phi_0)}{2}\right) - 1, \tag{5.74}$$

The equilibrium concentration profile Eq. 5.63 adopts a simpler form when written in terms of g

$$c_B^0(\tilde{z}) = \frac{c_B^{0,L}}{2}\left[1+k-(1-k)g(\phi_0(\tilde{z}))\right], \tag{5.75}$$

recovering the equilibrium concentration at both sides of the interface for $\phi = \pm 1$

$$c_B^0(\tilde{z} \to \infty) = c_B^{0,L} \tag{5.76}$$

$$c_B^0(\tilde{z} \to -\infty) = kc_B^{0,L}. \tag{5.77}$$

Compact form of the phase-field equations

With the help of relations Eq. 5.74 and Eq. 5.67, we can rewrite the free energy density Eq. 5.28

$$\begin{aligned}\tilde{g}_v(\phi, c_B, T) = \tilde{g}_A + \frac{TR}{v_m} c_B(\ln c_B - 1) - \frac{\Sigma s_v}{2}(T - T_M^A) + c_B\frac{(\Sigma\nu_v + \Sigma g_v^B)}{2} \\ + \frac{L_v(T - T_M^A)}{2T_M^A}\left[g(\phi) + \frac{c_B}{(k-1)c_B^{0,L}}\left[\ln\left(\frac{1+k-(1-k)g(\phi)}{2}\right) - 1\right]\right],\end{aligned} \tag{5.78}$$

and the equation for the phase-field evolution Eq. 5.54 adopts the form

$$\tilde{\tau}\partial_{\tilde{t}}\phi = \frac{\tilde{K}}{\tilde{h}_0}\tilde{\nabla}^2\phi - \partial_\phi f(\phi) + \frac{L_v(T - T_M^A)}{2T_M^A\tilde{h}_0}\partial_\phi g\left[\frac{2c_B}{c_B^{0,L}[1+k-(1-k)g]} - 1\right]. \tag{5.79}$$

Using Eq. 5.66, Eq. 5.79 can be written as

$$\tilde{\tau}\partial_{\tilde{t}}\phi = \frac{\tilde{K}}{\tilde{h}_0}\tilde{\nabla}^2\phi - \partial_\phi f(\phi) - \frac{RT_M^A\Delta c_0}{2v_m\tilde{h}_0}\partial_\phi g\left[\frac{2c_B}{c_B^{0,L}[1+k-(1-k)g]} - 1\right], \tag{5.80}$$

where we have introduced $\Delta c_0 = c_B^{0,L} - c_B^{0,S} = (1-k)c_B^{0,L}$. The last term in Eq. 5.79 can be interpreted as the total deviation from equilibrium of the system, and vanishes in the solid and liquid bulk regions due to the requirement $g(\pm 1) = 0$. Note that in an equilibrium situation, c_B is given by the equilibrium profile c_B^0 in Eq. 5.75, and the non-equilibrium driving force vanishes. The standard choice for the function $g(\phi)$ is given by the fifth order odd polynomial

$$g(\phi) = \frac{15}{8}(\phi - \frac{2}{3}\phi^3 + \frac{1}{5}\phi^5), \tag{5.81}$$

and its derivative appearing in the phase-field equation Eq. 5.79 is

$$\partial_\phi g(\phi) = \frac{15}{8}(\phi^2 - 1)^2. \tag{5.82}$$

The equation for the evolution of the solute field can also be rewritten by using the obtained relations between g and p. The concentration current $\tilde{\mathbf{j}}$ given in Eq. 5.48 can be expressed as

$$\begin{aligned}\tilde{\mathbf{j}} &= -c_B\tilde{D}_L q(\phi)\tilde{\nabla}\mu_v(\phi) = -c_B\tilde{D}_L q(\phi)\tilde{\nabla}\left[\frac{v_m}{RT}b(\phi) + \ln c_B\right] \\ &= -c_B\tilde{D}_L q(\phi)\tilde{\nabla}\ln\left(\frac{c_B}{[1+k-(1-k)g]}\right)\end{aligned} \tag{5.83}$$

where we have used the definition of $b(\phi)$ in Eq. 5.34 and the relation Eq. 5.65. Using the last expression for $\tilde{\mathbf{j}}$, the equation for c_B reads

$$\partial_{\tilde{t}}c_B = \tilde{D}_L\tilde{\nabla}q(\phi)\tilde{\nabla}c_B + (1-k)\tilde{D}_L\tilde{\nabla}\left[\frac{c_B q(\phi)\tilde{\nabla}g(\phi)}{[1+k-(1-k)g]}\right]. \tag{5.84}$$

The last equations Eqs. 5.84, 5.79 determine the time evolution of the ϕ and c_B fields and can be numerically solved to simulate the dynamical evolution of the solidification front. In the next chapter, we will present simulations of these equations in order to quantitatively check the phase-field results comparing them with the analytical predictions presented in the previous chapter.

Extension to Directional Solidification

As far, we have only considered a phase-field model for isothermal solidification processes. However, it is straightforward to extend the phase-field procedure to the directional solidification system discussed in Sec. 3.3. In such a system, the temperature at each point of the sample is determined by an externally imposed temperature gradient $\nabla T = \tilde{G}\hat{\mathbf{z}}$. Being $\tilde{z}$ the distance transversal to the planar front measured in the sample frame, the gradient is located at

$$T(\tilde{\mathbf{r}}, \tilde{t}) = T_M - m_L \frac{c_B^{0,L}}{k} + \tilde{G}\tilde{z}(\tilde{t}), \tag{5.85}$$

where $c_B^{0,L}$ is the solute concentration of the melt. A simple way to introduce the external gradient into the phase-field equation Eq. 5.79 is to add the term

$$\frac{\tilde{G}}{m_L c_B^{0,L}}\tilde{z}(\tilde{t}) \tag{5.86}$$

inside the factor between the brackets of the third term at the right side of Eq. 5.79. The equation for the phase-field then reads

$$\begin{aligned}\tilde{\tau}\partial_{\tilde{t}}\phi = &\frac{\tilde{K}}{\tilde{h}_0}\tilde{\nabla}^2\phi - \partial_\phi f(\phi) \\ &- \frac{RT_M^A \Delta c_0}{2v_m \tilde{h}_0}\partial_\phi g\left[\frac{2c_B}{c_B^{0,L}[1+k-(1-k)g]} - 1 + \frac{\tilde{G}}{m_L c_B^{0,L}}\tilde{z}(\tilde{t})\right],\end{aligned} \tag{5.87}$$

and in equilibrium, the bracketed expression cancels out and we recover the Gibbs-Thomson equation

$$c_B^L(\phi = -1, \tilde{t}) = c_B^{0,L} - \frac{\tilde{G}}{m_L}\tilde{\xi}(\tilde{t}), \tag{5.88}$$

being $\tilde{\xi}(\tilde{t})$ the front position in the sample frame which changes from an initial value of $\tilde{\xi}(\tilde{t}=0) = \tilde{l}_T$ to its final one $\tilde{\xi}(\tilde{t}\to\infty) = 0$. Using the definition of the gradient length $\tilde{l}_T = m_L\Delta c_0/\tilde{G}$, the phase-field equation adopts the form

$$\begin{aligned}\tilde{\tau}\partial_{\tilde{t}}\phi = &\frac{\tilde{K}}{\tilde{h}_0}\tilde{\nabla}^2\phi - \partial_\phi f(\phi) \\ &- \frac{RT_M^A \Delta c_0}{2v_m \tilde{h}_0}\partial_\phi g\left[\frac{2c_B}{c_B^{0,L}[1+k-(1-k)g]} - 1 + \frac{(1-k)}{\tilde{l}_T}\tilde{z}(\tilde{t})\right],\end{aligned} \tag{5.89}$$

Explicit dependence on the interface thickness $\tilde{W}$

The surface energy of the system can be easily calculated from the phase-field free-energy potential by subtracting from the total free energy the energy associated to the bulk phases. We therefore define the surface energy $\tilde{\sigma}$ as

$$\tilde{\sigma} = \tilde{\mathcal{F}}(\phi_0, c_B^0(\phi_0), T) - \tilde{\mathcal{F}}(\pm 1, c_B^0(\phi = \pm 1), T) = \int d\tilde{\mathbf{r}} \left[\frac{\tilde{K}^2}{2} \tilde{\nabla}^2 \phi_0 + \tilde{h}_0 (f(\phi_0) - f(\pm 1)) \right], \tag{5.90}$$

and inserting Eq. 5.60 and evaluating the integral, we obtain

$$\tilde{\sigma} = \sqrt{\tilde{K} \tilde{h}_0} I_1, \tag{5.91}$$

where I_1 is an integral constant defined as

$$I_1 = \int_{-\infty}^{\infty} d\eta (\partial_\eta \phi_0(\eta))^2. \tag{5.92}$$

If the potential $f(\phi)$ is chosen as $f = -\phi^2/2 + \phi^4/4$, the kink solution for the equilibrium phase-field is given by $\phi_0(\eta) = -tanh(\eta/2)$ and we have

$$I_1 = \frac{2\sqrt{2}}{3}. \tag{5.93}$$

As $\tilde{W} = \sqrt{\tilde{K}/\tilde{h}_0}$, equation Eq. 5.91 can be rewritten in terms of the interface thickness $\tilde{W}$ as

$$\tilde{\sigma} = \tilde{W} \tilde{h}_0 I_1, \tag{5.94}$$

and using the Clausius-Clapeyron relation, the pre-factor in the phase-field equation $\frac{RT_M^A \Delta c_0}{2 v_m \tilde{h}_0}$ can be finally written as

$$\frac{RT_M^A \Delta c_0}{2 v_m \tilde{h}_0} = \frac{I_1}{2(1-k)} \frac{\tilde{W}}{\hat{\tilde{d}}_0}, \tag{5.95}$$

where $\hat{\tilde{d}}_0 = \frac{\tilde{\sigma} T_M^A}{L_v m_L \Delta c_0}$ is the reduced chemical capillary length introduced in section Sec. 3.3.4 ($\hat{\tilde{d}}_0 = d_0^c / \Delta c_0$, with $\tilde{d}_0^c = \tilde{d}_0 / m_L$). The final form of the phase-field equation is therefore expressed in terms of the interface thickness as

$$\begin{aligned} \tilde{\tau} \partial_{\tilde{t}} \phi &= \tilde{W}^2 \tilde{\nabla}^2 \phi - \partial_\phi f(\phi) \\ &- \frac{I_1}{2(1-k)} \frac{\tilde{W}}{\hat{\tilde{d}}_0} \partial_\phi g \left[\frac{2 c_B}{c_B^{0,L} [1 + k - (1-k) g]} - 1 + \frac{(1-k)}{\tilde{l}_T} \tilde{z}(\tilde{t}) \right]. \end{aligned} \tag{5.96}$$

Introduction of anisotropies in the phase-field equations

A major advantage of the phase-field approach is that it can easily account for anisotropic thermophysical properties of the system. The two quantities which tipically depend on the cristalline structure of the solid are the surfece energy $\tilde{\sigma}$ and the kinetic attachment of the system $\tilde{\beta}$. The introduction of anisotropies in $\tilde{\sigma}$ and $\tilde{\beta}$ has been studied elsewhere [Karma98], and requires a convenient modification of the phase-field parameters $\tilde{W}$ and $\tilde{\tau}$ respectively. For the standard fourfold symmetry of these quantities, we define the anisotropic interface thickness $\tilde{W}(\mathbf{n})$ and $\tilde{\tau}(\mathbf{n})$ as

$$\tilde{W}(\mathbf{n}) = \tilde{W}_0(\mathbf{n}) f_a(\mathbf{n}) \tag{5.97}$$

$$\tilde{\tau}(\mathbf{n}) = \tilde{\tau}_0(\mathbf{n}) f_a(\mathbf{n}), \tag{5.98}$$

where $\mathbf{n}$ is a unit vector normal to the interface and $f_a(\mathbf{n}) = (1 + \delta\cos(\theta))$ being θ the angle between $\mathbf{n}$ and the y axis and δ the anisotropy strength.

5.2.2 Pure substances and symmetric alloys with constant miscibility gap

The solidification of pure substances and dilute alloys in the constant miscibility gap approximation can be modeled by a very simple variational phase-field. Let us consider the free-energy functional $\tilde{\mathcal{F}}$

$$\tilde{\mathcal{F}} = \int d\tilde{\mathbf{r}} \left[\frac{\tilde{K}}{2} |\tilde{\nabla}\phi|^2 + \tilde{h}_0 f(\phi) + \tilde{g}_v \right], \tag{5.99}$$

where $\tilde{g}_v$ stands for the free energy density of the system, and the double-well potential $f(\phi)$ is taken to be $f(\phi) = -\phi^2/2 + \phi^4/4$. The simplest variational form for the free energy density $\tilde{g}_v$ was first proposed by Langer [Langer86], and was further developed and studied in [Karma98]

$$\tilde{g}_v = \frac{\tilde{e}_0}{2} u^2. \tag{5.100}$$

Model for pure substances

For the case of a pure substance, u is the reduced temperature field defined by

$$u = \frac{T - T_M}{(L_v/c_v)}, \tag{5.101}$$

and $\tilde{e}_0$ is an energy density scale associated to the thermal field which will be determined in brief. Let us now introduce the physical field $\tilde{e}$, defined as

$$\tilde{e} = \tilde{e}_0 \left(u - \frac{1}{2} g(\phi) \right), \tag{5.102}$$

where $g(\phi)$ is the continuous function introduced in the last subsection satisfying the limit conditions $g(\phi = \pm 1) = \pm 1$ at the solid and liquid bulk phases and the additional condition $\partial_\phi g(\phi = \pm 1) = 0$ in order to ensure the stability of the two phases. As we know from the last section, in variational formulations, the standard choice for the function $g(\phi)$ is given by (cf. Eq. 5.81)

$$g(\phi) = \frac{15}{8}(\phi - \frac{2}{3}\phi^3 + \frac{1}{5}\phi^5), \tag{5.103}$$

Noting that the field $\tilde{e}$ takes different values at the solid and liquid phases

$$\tilde{e}_S = \tilde{e}_0\left(u - \frac{1}{2}\right) \tag{5.104}$$

$$\tilde{e}_L = \tilde{e}_0\left(u + \frac{1}{2}\right), \tag{5.105}$$

we can evaluate the free energy difference between the phases

$$\begin{aligned}\Delta\tilde{g}_v = \tilde{g}_v^L - \tilde{g}_v^S = \tilde{g}_v(\phi = -1) - \tilde{g}_v(\phi = +1) = \\ \frac{\tilde{e}_0}{2}\left(\frac{\tilde{e}_L}{\tilde{e}_0} - \frac{1}{2}\right)^2 - \frac{\tilde{e}_0}{2}\left(\frac{\tilde{e}_S}{\tilde{e}_0} + \frac{1}{2}\right)^2 = -\tilde{e}_0\frac{T - T_M}{(L_v/c_v)},\end{aligned} \tag{5.106}$$

where we have used that $\tilde{e}_L^2 - \tilde{e}_S^2 = 0$. Comparing the last equation with the free energy difference for an undercooled pure melt Eq. 2.15, which is given by

$$\Delta\tilde{g}_v = -\frac{L_v(T - T_M)}{T_M}, \tag{5.107}$$

we can determine the value of the constant $\tilde{e}_0$

$$\tilde{e}_0 = \frac{L_v^2}{T_M c_v}. \tag{5.108}$$

The dynamical evolution of the phase-field ϕ and of the diffusive variable $\tilde{e}$ are determined by the variational principle

$$\tilde{\tau}\partial_{\tilde{t}}\phi = -\frac{1}{\tilde{h}_0}\left(\frac{\delta\tilde{\mathcal{F}}}{\delta\phi}\right) \tag{5.109}$$

$$\partial_{\tilde{t}}\tilde{e} = D\tilde{e}_0\tilde{\nabla}^2\left(\frac{\delta\tilde{\mathcal{F}}}{\delta\tilde{e}}\right), \tag{5.110}$$

and the equations for ϕ and u can be expressed as

$$\tilde{\tau}\partial_{\tilde{t}}\phi = \frac{\tilde{K}}{\tilde{h}_0}\tilde{\nabla}^2\phi - \partial_\phi f(\phi) - \frac{1}{2}\frac{\tilde{e}_0}{\tilde{h}_0}\partial_\phi g(\phi)u \tag{5.111}$$

$$\partial_{\tilde{t}}u = \tilde{D}\tilde{\nabla}^2 u + \frac{1}{2}\partial_{\tilde{t}}g(\phi), \tag{5.112}$$

It interesting to insert $\tilde{e}_0$ into Eq. 5.111 and write the phase-field equation with the explicit dependence on the thermodynamical magnitudes

$$\tilde{\tau}\partial_{\tilde{t}}\phi = \frac{\tilde{K}}{\tilde{h}_0}\tilde{\nabla}^2\phi - \partial_\phi f(\phi) - \frac{L_v(T-T_M)}{2\tilde{h}_0 T_M}\partial_\phi g(\phi) \tag{5.113}$$

and note that is the same equation than the phase-field equation in the previous model for alloys Eq. 5.79 in the pure substance case $c_B = 0$. The phase-field equation Eq. 5.113 can be written in a simpler form by noting from the definition of u that $T - T_M = uL_v/c_v$ and that $\tilde{h}_0 = \tilde{\sigma}/\tilde{W}I_1$. It reads

$$\tilde{\tau}\partial_{\tilde{t}}\phi = \tilde{W}^2\tilde{\nabla}^2\phi - \partial_\phi f(\phi) - \frac{I_1}{2}\frac{\tilde{W}}{\tilde{d}_0^T}\partial_\phi g(\phi)u, \tag{5.114}$$

where $\tilde{d}_0^T = \frac{\tilde{\sigma}T_M^A c_v}{L_v^2}$ is the *reduced thermal capillary length* .

The parameters and fields that we have introduced so far have dimensions of

$$[\tilde{h_0}] \sim [\tilde{e}] \sim [\tilde{e}_0] \sim [\frac{\delta\tilde{\mathcal{F}}}{\delta\phi}] \sim \frac{E}{L^d} \tag{5.115}$$

$$[\frac{\delta\tilde{\mathcal{F}}}{\delta\tilde{e}}] \sim 1 \tag{5.116}$$

$$[\tilde{K}] \sim \frac{E}{L^{d-2}} \tag{5.117}$$

$$[\tilde{\mathcal{F}}] \sim E \tag{5.118}$$

$$[\tilde{\tau}] \sim T. \tag{5.119}$$

Model for alloys in the miscibility gap approximation

The model presented in this section can be easily extended for the solidification of a dilute alloy in the constant miscibility gap approximation introduced in Sec. 4.1.3. This approximation assumes that the solid and liquid slopes are equal $m_L = m_S$, which is equivalent to suppose that $\Delta c_0 = c_L^0 - c_S^0$ is constant in the phase diagram. Under this assumption, if the concentration at the liquid of a solid-liquid interface is $c_B^{0,L}$, the equilibrium concentration at the solid side will be given by $c_B^{0,S} = c_B^{0,L} - \Delta c_0$ instead $c_B^{0,S} = kc_B^{0,L}$. For such a system, we identify

$$\begin{aligned}
\tilde{e} &= \frac{\tilde{e}_0}{\Delta c_0}\left(c - \frac{c_S^0 + c_L^0}{2}\right) \\
\tilde{e}_0 &= \frac{RT_M^A(\Delta c_0)^2}{v_m c_L^0} \\
u &= \frac{\tilde{e}}{\tilde{e}_0} + \frac{1}{2}g(\phi),
\end{aligned} \tag{5.120}$$

With this change of variables, the phase-field equations for the alloy constant miscibility gap model adopt the same form as in the pure substance case Eqs. 5.111, 5.112. In particular, the phase-field equation written with all the thermodynamical constants is given by

$$\tilde{\tau}\partial_{\tilde{t}}\phi = \frac{\tilde{K}}{\tilde{h}_0}\tilde{\nabla}^2\phi - \partial_\phi f(\phi) - \frac{RT_M^A\Delta c_0}{2v_m\tilde{h}_0}\partial_\phi g(\phi)\left[\frac{c_B}{c_B^{0,L}} - \frac{c_B^{0,S}+c_B^{0,L}}{2c_B^{0,L}} - \frac{\Delta c_0}{2c_B^{0,L}}g(\phi)\right], \tag{5.121}$$

which is the constant miscibility gap version of Eq. 5.89. The last equation can be also rewritten with the help of Eq. 5.95 showing explicitely the dependence with the interface thickness, the phase field equation for the solutal case read

$$\tilde{\tau}\partial_{\tilde{t}}\phi = \tilde{W}^2\tilde{\nabla}^2\phi - \frac{I_1}{2}\frac{\tilde{W}}{\hat{\tilde{d}}_0}\partial_\phi g(\phi)\left[\frac{c_B}{\Delta c_0} - \frac{c_B^{0,S}+c_B^{0,L}}{2\Delta c_0} - \frac{g(\phi)}{2}\right], \tag{5.122}$$

where now it appears the solutal capillarity constant $\hat{\tilde{d}}_0 = \frac{\tilde{\sigma}T_M^A}{L_v m_L \Delta c_0}$ instead of the thermal capillarity $\tilde{d}_0$.

5.2.3 Introduction of fluctuations in variational models

In variational formulations such as those presented so far in this chapter, the introduction of fluctuations can be done by following the procedure proposed by Hohenberg, Halperin and Ma within the context of critical dynamics [Halperin74, Hohenberg77]. For a general reference concerning the introduction of noise in spatially extended systems, we refer to Ref. [García-Ojalvo99].

For the sake of clarity, we will refer to the model proposed in Sec. 5.2.2, which applies for both pure substances and symmetric dilute alloys in the miscibility gap limit. In order to use the results of this section for each of these situations, one simply has to use the definitions of $\tilde{e}, \tilde{e}_0$ and u in Eqs. 5.101, 5.102, 5.108 and 5.120.

Noise terms can be directly added to the variational equations Eqs. 5.109, 5.110, resulting in the stochastic dynamical equations

$$\partial_{\tilde{t}}\phi = -\frac{1}{\tilde{\tau}\tilde{h}_0}\left(\frac{\delta\tilde{F}}{\delta\phi}\right) + \tilde{s}(\tilde{\mathbf{r}},\tilde{t}) \tag{5.123}$$

$$\partial_{\tilde{t}}\tilde{e} = D\tilde{e}_0\tilde{\nabla}^2\left(\frac{\delta\tilde{F}}{\delta\tilde{e}}\right) - \tilde{\nabla}\cdot\tilde{\mathbf{q}}_e. \tag{5.124}$$

Note that the stochastic term in the phase-field equation is a non-conserved additive noise $\tilde{s}$, whereas in the equation for $\tilde{e}$ we have a conserved stochastic current $\tilde{\mathbf{q}}_e$. If the noises have a thermodynamical internal origin, we can assume that they are described by Gaussian white random variables. The statistical properties of the noise terms are then related with the deterministic parameters of the system by

the *Fluctuation-Dissipation theorem*, which can be used in order to determine the correlation of the stochastic terms in Eqs. 5.123, 5.124

$$\langle \tilde{s}(\tilde{\mathbf{r}},\tilde{t})\tilde{s}(\tilde{\mathbf{r}}',\tilde{t}')\rangle = \frac{2K_B T_M}{\tilde{\tau}\tilde{h}_0}\delta(\tilde{\mathbf{r}}-\tilde{\mathbf{r}}')\delta(\tilde{t}-\tilde{t}') \tag{5.125}$$

$$\langle \tilde{q}_e^i(\tilde{\mathbf{r}},\tilde{t})\tilde{q}_e^j(\tilde{\mathbf{r}}',\tilde{t}')\rangle = 2K_B T_M D\tilde{e}_0\delta_{ij}\delta(\tilde{\mathbf{r}}-\tilde{\mathbf{r}}')\delta(\tilde{t}-\tilde{t}'), \tag{5.126}$$

where the super-indexes i, j refer to the spatial components of the stochastic current $\tilde{\mathbf{q}}_e$. The dimensions of the new stochastic terms are given by

$$[\tilde{s}] \sim \frac{1}{T} \tag{5.127}$$

$$[\tilde{q_e}] \sim \frac{E}{L^{d-1}T}. \tag{5.128}$$

Introducing the new stochastic variables

$$\tilde{\mathbf{q}}_u = \frac{\tilde{\mathbf{q}}_u}{\tilde{e}_0} \tag{5.129}$$

$$\tilde{\eta} = \tilde{\tau}\tilde{s}, \tag{5.130}$$

the fluctuating phase-field equations adopt the form

$$\tilde{\tau}\partial_{\tilde{t}}\phi = \frac{\tilde{K}}{\tilde{h_0}}\tilde{\nabla}^2\phi - f'(\phi) - \frac{\tilde{e_0}}{2\tilde{h_0}}\partial_\phi g(\phi)u + \tilde{\eta}(\tilde{\mathbf{r}},\tilde{t}) \tag{5.131}$$

$$\partial_{\tilde{t}}u = \tilde{D}\tilde{\nabla}^2 u + \frac{1}{2}\partial_{\tilde{t}}g(\phi) - \tilde{\nabla}\cdot\tilde{\mathbf{q}}_u(\tilde{\mathbf{r}},\tilde{t})\ , \tag{5.132}$$

with the correlations

$$\langle \tilde{\eta}(\tilde{\mathbf{r}},\tilde{t})\tilde{\eta}(\tilde{\mathbf{r}}',\tilde{t}')\rangle = \frac{2K_B T_M\tilde{\tau}}{\tilde{h_0}}\delta(\tilde{\mathbf{r}}-\tilde{\mathbf{r}}')\delta(\tilde{t}-\tilde{t}') \tag{5.133}$$

$$\langle \tilde{\mathbf{q}}_u^i(\tilde{\mathbf{r}},\tilde{t})\tilde{\mathbf{q}}_u^j(\tilde{\mathbf{r}}',\tilde{t}')\rangle = \frac{2K_B T_M\tilde{D}}{\tilde{e_0}}\delta_{ij}\delta(\tilde{\mathbf{r}}-\tilde{\mathbf{r}}')\delta(\tilde{t}-\tilde{t}'). \tag{5.134}$$

A similar procedure can be applied to the model presented in section Sec. 5.2.1.

5.3 Non-variational Formulations

Although their appealing structure, variational phase-field formulations have some important drawbacks. As pointed by Almgren in Ref. [Almgren99], when the one-sided model presented in this section is asymptotically expanded to its sharp-interface projection, some spurious terms appear which can not be canceled by simply choosing the proper interpolation functions. That constitutes indeed a very

important problem, because without a proper sharp interface projection the phase-field simulations might present undesirable and uncontrolled finite thickness effects. A solution to this problem was presented by Karma in Ref. [Karma01], where he introduced an effective solute current which canceled the spurious solute trapping effect. With the introduction of this additional current, the choice of the potentials turned to be sufficient to eliminate the remaining finite-thickness effects.

5.3.1 Non-symmetric dilute binary alloys

The variational model presented in section 5.2.1 can be used as the basis for computationally improved, non-variational formulation. Taking the free-energy functional

$$\tilde{\mathcal{F}}[\phi, c_B, T] = \int d\tilde{\mathbf{r}} \left[\frac{\tilde{K}}{2} |\tilde{\nabla}\phi|^2 + \tilde{h}_0 f(\phi) + \tilde{g}_v(\phi, c_B, T) \right], \tag{5.135}$$

where the phenomenological free-energy density is now given by

$$\tilde{g}_v(\phi, c_B, T) = -\frac{RT_M^A \Delta c_0}{2v_m} g(\phi) \left[\frac{2c_B}{c_B^{0,L}[1 + k - (1-k)h(\phi)]} - 1 \right], \tag{5.136}$$

where we have introduced $h(\phi)$ as a new odd function satisfying the limiting conditions $h(\phi = \pm 1) = \pm 1$ but not $\partial_\phi h(\pm 1) = 0$. The stability of the $\phi = \pm 1$ solutions is guaranteed because the function $g(\phi)$ satisfies $\partial_\phi g(\pm 1) = 0$. The evolution of the phase-field variable can be determined from the following the variational principle

$$\tilde{\tau}\partial_{\tilde{t}}\phi = -\frac{1}{\tilde{h}_0} \left(\frac{\delta \tilde{\mathcal{F}}}{\delta \phi} \right), \tag{5.137}$$

and is given by

$$\tilde{\tau}\partial_{\tilde{t}}\phi = \frac{\tilde{K}}{\tilde{h}_0}\tilde{\nabla}^2\phi - \partial_\phi f(\phi) - \frac{I_1}{(1-k)} \frac{\tilde{W}}{\tilde{d}_0} \partial_\phi g \left[\frac{2c_B}{c_B^{0,L}[1 + k - (1-k)h]} - 1 \right]. \tag{5.138}$$

The evolution for the concentration field can not be derived from the equivalent variational principle, and will be assumed to have the form

$$\partial_{\tilde{t}} c_B = \tilde{D}_L \tilde{\nabla} q(\phi) \tilde{\nabla} c_B + (1-k)\tilde{D}_L \tilde{\nabla} \left[\frac{c_B q(\phi) \tilde{\nabla} h(\phi)}{[1 + k - (1-k)h(\phi)]} \right], \tag{5.139}$$

which is equivalent to Eq. 5.84 but where the function $g(\phi)$ has been changed by the better computationally behaved $h(\phi)$.

Finite-thickness effects and the anti-trapping current

Recently, some authors have pointed out some important problems which affect non-symmetric phase-field models when performing the sharp-interface asymptotics [Almgren99, Karma01].

In the next chapter, we will see that in symmetric phase-field models the choice of the functions f, g, h gives enough freedom to cancel out the finite thickness spurious terms which appear in the sharp-interface projection of the model. The cancellation of these terms is of course a necessary condition in order to obtain quantitative phase-field simulation results. As pointed by Almgren in Ref. [Almgren99], in non-symmetric models these finite thickness terms appear in an asymmetric form and can not be canceled in situations where the system presents large differences between the solid and liquid diffusivities (one-sided models). Therefore the interpolation functions f, g, h are not enough to proceed with this cancellation, and the performance of the phase-field simulations will be affected by these spurious terms.

In Ref. [Karma01], Karma proposed a solution to this problem consisting in the introduction of an additional term into the solute concentration equation. The form of this term is chosen in such a way that its sharp-interface projection cancels one of the finite thickness spurious terms. This explicit cancellation makes it possible to eliminate the remaining spurious terms by a proper choice of the interpolation functions f, g and h. This additional term is called the *anti-trapping current* $\tilde{\mathbf{j}}_a$, and has the form of an interfacial solute current going from the solid to the liquid phase and therefore in the opposite sense than a solute trapping effect. This extra current is oriented in the normal direction to the solidification front $\hat{n} = \tilde{\nabla}\phi/|\tilde{\nabla}\phi|$, and is proportional to the front velocity and to the local solute concentration. The proposed form for this term is given by

$$\tilde{\mathbf{j}}_a = -a\tilde{W}(1-k)\frac{c_B}{[1+k-(1-k)h(\phi)]}\frac{\partial\phi}{\partial\tilde{t}}\frac{\tilde{\nabla}\phi}{|\tilde{\nabla}\phi|}, \tag{5.140}$$

where a is a constant to be determined for a given choice of the interpolation potentials. The dependence on $\tilde{W}$ is due to the fact that the finite-thickness term that is canceled with the projection of $\tilde{\mathbf{j}}_a$ appears at second order in the asymptotic expansion in ε. After the introduction of the anti-trapping current, the total solute current in the model is given by

$$\tilde{\mathbf{j}}_T = \tilde{\mathbf{j}} + \tilde{\mathbf{j}}_a, \tag{5.141}$$

where $\tilde{\mathbf{j}}$ is defined by Eq. 5.83. The concentration equation after the introduction of $\tilde{\mathbf{j}}_a$ reads

$$\begin{aligned}\partial_{\tilde{t}}c_B = {} & \tilde{D}_L\tilde{\nabla}q(\phi)\tilde{\nabla}c_B + (1-k)\tilde{D}_L\tilde{\nabla}\left[\frac{c_B q(\phi)\tilde{\nabla}h(\phi)}{[1+k-(1-k)h(\phi)]}\right] \\ & + a\tilde{W}(1-k)\tilde{\nabla}\left[\frac{c_B}{[1+k-(1-k)h(\phi)]}\frac{\partial\phi}{\partial\tilde{t}}\frac{\tilde{\nabla}\phi}{|\tilde{\nabla}\phi|}\right].\end{aligned} \tag{5.142}$$

It can be shown (cf. Ref. [Echebarria04]), that for one-sided systems (i.e, $\tilde{D}_S = 0$,

$\tilde{D}_L = \tilde{D}$) and the usual choice of the potentials

$$f(\phi) = -\frac{1}{2}\phi^2 + \frac{1}{4}\phi^4 \tag{5.143}$$

$$\bar{g}(\phi) = \phi - \frac{2}{3}\phi^3 + \frac{1}{5}\phi^5 \tag{5.144}$$

$$h(\phi) = \phi, \tag{5.145}$$

all the spurious terms are canceled when the interpolation function $q(\phi)$ is chosen to be

$$q(\phi) = \frac{(1-\phi)}{[1+k-(1-k)h(\phi)]}, \tag{5.146}$$

and $a = \sqrt{2}$. Note that the function q satisfies the one-sided values of the diffusivity at the liquid and solid phases ($q(+1) = 0$, $q(-1) = 1$).

5.3.2 Pure substances and symmetric alloys with constant miscibility gap

Let us consider the free-energy functional $\tilde{\mathcal{F}}$

$$\tilde{\mathcal{F}} = \int d\tilde{\mathbf{r}} \left[\frac{\tilde{K}}{2} |\tilde{\nabla}\phi|^2 + \tilde{h}_0 f(\phi) + \tilde{g}_v \right], \tag{5.147}$$

where the free energy $\tilde{g}_v$ adopts now the form [Langer86, Karma98]

$$\tilde{g}_v = \frac{\tilde{e}_0}{2} g(\phi) u, \tag{5.148}$$

where the function $g(\phi)$ satisfies the conditions $g(\phi = \pm 1) = \pm 1$ and $\partial_\phi g(\phi = \pm 1) = 0$, and $u, \tilde{e}_0$ are defined for pure substances and symmetric alloys as in section Sec. 5.2.2. The equation for the phase-field can be derived as usual from the variational principle

$$\tilde{\tau}\partial_{\tilde{t}}\phi = -\frac{1}{\tilde{h}_0}\left(\frac{\delta\tilde{\mathcal{F}}}{\delta\phi}\right), \tag{5.149}$$

and takes the form

$$\tilde{\tau}\partial_{\tilde{t}}\phi = \frac{\tilde{K}}{\tilde{h}_0}\tilde{\nabla}^2\phi - \partial_\phi f(\phi) - \frac{1}{2}\frac{\tilde{e}_0}{\tilde{h}_0}\partial_\phi g(\phi) u. \tag{5.150}$$

The equation for the evolution of the u field is postulated to have the form

$$\partial_{\tilde{t}} u = \tilde{D}\tilde{\nabla}^2 u + \frac{1}{2}\partial_{\tilde{t}} h(\phi), \tag{5.151}$$

where the function $h(\phi)$ is odd and satisfies $h(\phi = \pm 1) = \pm 1$ and will be chosen in order to improve the computational efficiency of the numerical simulations. The best choice for this function is given by

$$h(\phi) = \phi. \tag{5.152}$$

For an interesting work discussing the computational efficiency of the different choices for the potentials, we refer to [Kim99]. We shall remark here that in this model the function $g(\phi)$ appears in the phase-field equation only, but not in the diffusion dynamics.

5.3.3 Introduction of fluctuations in non-variational models

The standard procedure to introduce fluctuations in phase field models has been traditionally restricted to variational formulations [Karma99, Pavlik99, Pavlik00, Elder94, Drolet00] analogous to the C model of critical dynamics [Halperin74, Wheeler92a, Wheeler92b], where the intensity of the fluctuations can be determined by using a fluctuation-dissipation relation. In more recent phase field formulations which do not maintain their variational structure, the fluctuation-dissipation relation cannot be used to infer the statistics of the noise appearing in the equations. We will refer on a recent calculus [Benítez04c] that projects the dynamics of a generic stochastic phase field model to the motion of the fluctuating interface. This procedure, which will be described in the next Chapter, provides a prescription for the intensity of the noise terms in the model, accounting for fluctuations of both internal and external origin. This approach has previously been used in both equilibrium [Benítez04c] and out of equilibrium situations [Benítez04a, Benítez04b].

Chapter 6

Sharp-Interface projection of a fluctuating phase-field model

We present in this chapter a derivation of the sharp interface limit of a fluctuating phase field model for solidification. In the result, the noise terms appear both in the diffusion equation and in the moving boundary conditions, and their intensities are computed from the phase field parameters. The procedure does not rely on any free energy functional, and hence can be applied to both external and internal fluctuations. In particular it can be applied to quantitatively account for thermodynamical internal fluctuations in non variational formulations of the phase field model, which could be numerically more efficient.

6.1 Introduction

Phase field models are constructed in order to recover the classical moving boundary dynamics in the so called sharp-interface limit as $\tilde{W} \to 0$ [Caginalp88]. This limit is taken by means of a systematic asymptotic expansion on the interface width, and allows in turn to determine the model parameters in terms of physical and substance parameters. On the other hand, it is well established the importance of interfacial and bulk fluctuations in the selection dynamics of morphological instabilities [Warren90, Warren93, Karma93b, Karma93c]. In this respect, one interesting characteristic of the phase-field model is the possibility of incorporating fluctuations without major modifications of the numerical scheme. In fact fluctuations were early introduced in phase-field models in an *ad hoc* way as a controlled source of interfacial perturbations [Kobayashi93b]. However, models accounting for internal thermodynamical fluctuations were not formulated until

recently [Elder94, Karma99, Pavlik99, Pavlik00]. These formulations have a variational structure, in the sense that they are derived from a single free-energy functional, and the properties of the fluctuating terms of the phase-field equations can be determined by using the fluctuation-dissipation theorem, following the procedure proposed by Hohenberg, Halperin and Ma in the context of critical dynamics [Halperin74, Hohenberg77]. Unfortunately, this variational structure is lost when improving the computational efficiency of the model [Karma98], or when introducing some specific physical situations such as one-sided solidification [Karma01] or viscous fingering [Folch99].

The aim of this chapter is to present a systematic procedure to deal with generic sources of noise in phase field models, not relying on any variational formulation. To this end, we will perform the classical sharp interface limit of a phase field model with fluctuations, obtaining explicitly the properties of the projected noise terms that will appear in the sharp interface equations. This projection will be carried out by means of an asymptotic expansion which combines a standard sharp interface limit up to second order in $\tilde{W}$ and a small noise expansion. The structure of the resulting sharp interface projection takes the form of a moving boundary problem which now includes bulk and interfacial stochastic terms. The statistical properties of these new terms are related with those of the noises appearing in the starting phase field equations. The extension of our procedure to a thin-interface asymptotics [Karma98] is straightforward and is not presented here for the sake of clarity.

This analytical technique will permit to give a prescription for the introduction of internal thermodynamical fluctuations in non-variational phase field models, subjected only to the constraint of giving the correct interface equilibrium fluctuations. This approach will also allow for considering more general noise sources of external origin, like experimental imperfections or controlled perturbations, which would not obey equilibrium statistics. It is worth pointing out that although the calculations will be performed in the framework of the symmetric model of solidification, the approach can be easily extended to consider one-sided formulations [Karma01].

6.2 Model equations

Our approach starts from the non-variational phase-field model introduced in section Sec. 5.3.2, which applies for both the solidification of a pure substance and for the symmetric alloy solidification in the constant miscibility gap approximation. We scale space and times in the model equations Eqs. 5.150 and 5.151 with a characteristic length $\tilde{l} = \tilde{D}/\tilde{v}_p$ and a time scale $\tilde{\gamma} = \tilde{l}^2/\tilde{D}$, being $\tilde{D}$ the thermal diffusivity of the substance. The *scaled interface thickness* is then defined as $\varepsilon = \tilde{W}/\tilde{l}$, and will be considered the small parameter in which the formal expansions will be

carried out. Introducing the parameters

$$\lambda = \frac{15}{16}\frac{I_1}{\hat{d}_0}, \tag{6.1}$$

and

$$\alpha = \frac{\tau}{\varepsilon^2}, \tag{6.2}$$

where $\tau = \tilde{\tau}/\tilde{\gamma}$, the dimensionless model equations adopt the form

$$\alpha\varepsilon^2\partial_t\phi = \varepsilon^2\nabla^2\phi - f'(\phi) - \varepsilon\lambda\bar{g}'(\phi)u + \varepsilon^{\frac{3}{2}}\eta(\mathbf{r},t) \tag{6.3}$$

$$\partial_t u = \nabla^2 u + \frac{1}{2}\partial_t h(\phi) - \nabla\cdot\mathbf{q}(\mathbf{r},t)\ , \tag{6.4}$$

where u is the reduced temperature field defined by $u = \frac{T-T_M}{(L_v/c)}$ in the pure substance system and by $u = (c - \frac{c_S^0+c_L^0}{2})/\Delta c_0 + \bar{g}(\phi)/2$ for symmetric alloys. The relation between the function $g(\phi)$ introduced in the last chapter and the new $\bar{g}(\phi)$ function is given by

$$\bar{g} = \frac{8}{15}g(\phi), \tag{6.5}$$

and the condition $g(\phi = \pm 1) = \pm 1$, will be now supplied by the requirement $\bar{g}(\phi = \pm 1) = \pm 8/15$. In Eq. 6.2, α does not depend on ε, and can therefore be understood as the assumption that the phase-field time scale $\tilde{\tau}$ is proportional to ε^2. All the dependence of the model equations on ε has been explicitely written, so the model parameters α, λ do not have any dependence on ε.

In the model, fluctuations appear as a non-conserved noise term η in the equation for the phase-field, and a conserved noise current $\mathbf{q}$ in the equation for the temperature. These fluctuations account for generic sources of noise of either internal or external origin. We assume that the noises are Gaussian with correlations given by

$$\langle\eta(\mathbf{r},t)\eta(\mathbf{r}',t')\rangle = 2\sigma_\phi^2\delta(\mathbf{r}-\mathbf{r}')\delta(t-t')\ , \tag{6.6}$$

$$\langle q_i(\mathbf{r},t)q_j(\mathbf{r}',t')\rangle = 2\sigma_u^2\delta_{ij}\delta(\mathbf{r}-\mathbf{r}')\delta(t-t')\ . \tag{6.7}$$

In order to carry out the calculations along this chapter, we will assume $\bar{g}(\phi)$ and $h(\phi)$ to be odd functions of ϕ, and the standard double-well potential for $f(\phi) = \phi^4/4 - \phi^2/2$. In addition, we must also assume that the functions g and h satisfy the limiting relation $g'(\pm 1) = 0$ and $h(\pm 1) = \pm 1$, respectively. These conditions will be used in different points during the asymptotic matching derived in this section. Although the whole derivation will be developed with generic expressions for the functions $f(\phi)$, $\bar{g}(\phi)$ and $h(\phi)$, in the numerical simulations will

be given by

$$f(\phi) = -\frac{1}{2}\phi^2 + \frac{1}{4}\phi^4 \tag{6.8}$$

$$\bar{g}(\phi) = \phi - \frac{2}{3}\phi^3 + \frac{1}{5}\phi^5 \tag{6.9}$$

$$h(\phi) = \phi. \tag{6.10}$$

6.3 Hybrid asymptotic expansion

In the presence of fluctuations, the classical sharp interface limit, based on a small interface width (small ε) expansion, must be complemented with a small noise assumption. To this end, noise intensities σ_ϕ and σ_u will also be taken as small parameters in the expansion. Namely we will assume the order relations

$$\sigma_\phi \sim O(\varepsilon^{3/2}), \tag{6.11}$$

$$\sigma_u \sim O(\varepsilon^2), \tag{6.12}$$

between the noise intensities and the interface thickness.

As usually, we proceed by dividing the system into two different regions: an outer region far away from the interface at distances much greater than ε, and an inner region located around the interface up to distances of order ε. Solutions for the fields in both regions should match at some intermediate radial distance r_M, which can be taken of order $r_M \sim \varepsilon^{1/2}$, in the limit $\varepsilon \to 0$.

6.3.1 Outer region

The equations for the outer region can be solved at each order by expanding the fields in ε as

$$u = u_0 + \varepsilon u_1 + O(\varepsilon^2) \tag{6.13}$$

$$\phi = \phi_0 + \varepsilon\phi_1 + O(\varepsilon^2). \tag{6.14}$$

The functions of ϕ (or u) like $\varphi(\phi)$ will also be expanded in Taylor

$$\varphi(\phi) \approx \varphi(\phi_0) + \varphi'(\phi_0)(\phi - \phi_0) + \frac{1}{2}\varphi''(\phi_0)(\phi - \phi_0)^2 + \cdots, \tag{6.15}$$

and using the expansions Eqs. 6.14 we get

$$\varphi(\phi_0) + \varepsilon\varphi'(\phi_0)\phi_1 + \varepsilon^2\left(\varphi'(\phi_0)\phi_2 + \frac{1}{2}\varphi''(\phi_0)\phi_1^2\right) + \cdots. \tag{6.16}$$

An equivalent expression will be used when expanding the functions of the inner fields. We next proceed to write the outer equations at each order.

Zero Order:

The outer equations at zero order in ε is given by:

$$f'(\phi_0) = 0 \tag{6.17}$$
$$\partial_t u_0 = \nabla^2 u_0. \tag{6.18}$$

As our function f satisfies $f'(\pm 1) = 0$, the first equation brings to $\phi_0 = \pm 1$.

First Order:

The outer equations at order ε are

$$f''(\phi_0)\phi_1 = -\lambda \bar{g}'(\phi_0) u_0 \tag{6.19}$$
$$\partial_t u_1 = \nabla^2 u_1 \,. \tag{6.20}$$

As we have chosen the functions f, $\bar{g}$ such that $f''(\pm 1) \neq 0$ and $\bar{g}'(\pm 1) = 0$, the first equation brings to $\phi_1 = 0$.

Second Order:

$$f''(\phi_0)\phi_2 = \lambda \bar{g}'(\phi_0) u_1 \tag{6.21}$$
$$\partial_t u_2 = \nabla^2 u_2 - \nabla \cdot \mathbf{q} \,, \tag{6.22}$$

which is solved by $\phi_2 = 0$. Compiling the results for ϕ at the three first orders, the outer phase-field is given up to second order by

$$\phi = \pm 1 + O(\varepsilon^3). \tag{6.23}$$

Similarly, the outer diffusion field u follows a diffusion equation with a stochastic current which contributes at second order in ε, *i.e.*

$$\partial_t u = \nabla^2 u - \nabla \cdot \mathbf{q}(\mathbf{r}, t) + O(\varepsilon^3) \,. \tag{6.24}$$

6.3.2 Inner region

For the inner region, it is convenient to write Eqs. 6.3 and 6.4 in a curvilinear coordinate system centered at the interface. The idea is that the solvability condition for the very existence of solutions of these transformed equations will provide the evolution of the coordinate system, *i.e.* of the interface, which in fact constitutes the solution we are looking for. To define this coordinate system maintaining it smooth at small scales, we use an auxiliary coarse grained field defined as a local spatial and temporal average of the fluctuating field ϕ. The surface corresponding to the level set of this coarse grained field $\langle \phi(\mathbf{r}, t) \rangle = 0$ then defines the 3D orthogonal curvilinear coordinate system (r, s_1, s_2), where r is a normal distance from

the surface and s_1, s_2 are the arclength distances measured along the maximum and minimum curvature directions of the surface. Furthermore, we introduce the scaled radial coordinate $\rho = r/\varepsilon$ and the scaled time $\tau = t/\varepsilon$ to measure radial distances and times in the inner region. We use capital letters to refer all the fields when written in the inner region, including the fluctuating fields. Appendix B is dedicated to derive the expressions of the differential operators written in curvilinear coordinates. After some algebraic manipulations (see Appendix B), we get the inner equations in the frame of the moving interface

$$\begin{aligned}\alpha\varepsilon[\frac{d}{d\tau} - v\partial_\rho]\Phi &= \partial_\rho^2\Phi + \varepsilon(\kappa_1+\kappa_2)\partial_\rho\Phi - \varepsilon^2\rho(\kappa_1^2+\kappa_2^2)\partial_\rho\Phi \\ &+ \varepsilon^2\partial_{s_1}^2\Phi + \varepsilon^2\partial_{s_2}^2\Phi - f'(\Phi) - \varepsilon\lambda\bar{g}'(\Phi)U + \varepsilon^{1/2}H(\rho,\mathbf{s},\tau)\end{aligned} \tag{6.25}$$

$$\begin{aligned}&\frac{1}{\varepsilon}[\frac{d}{d\tau} - v\partial_\rho - \varepsilon^2\rho(v_{s_1}\partial_{s_1} + v_{s_2}\partial_{s_2})]U = \\ &\frac{1}{\varepsilon^2}\partial_\rho^2 U + \frac{(\kappa_1+\kappa_2)}{\varepsilon}\partial_\rho U - \varepsilon^2\rho(\kappa_1^2+\kappa_2^2)\partial_\rho U + \partial_{s_1}^2 U + \partial_{s_2}^2 U \\ &+ \frac{1}{\varepsilon}\frac{dh(\Phi)}{d\tau} - \frac{v}{2\varepsilon}\partial_\rho h(\Phi) - \frac{1}{\varepsilon^2}\partial_\rho Q_\rho,\end{aligned} \tag{6.26}$$

where $v = v(\mathbf{s},\tau)$ is the normal (or radial) front velocity, and $\kappa_1(\mathbf{s},\tau)$, $\kappa_2(\mathbf{s},\tau)$ the main curvatures of the surface. The fluctuating functions $H(\rho,\mathbf{s},\tau)$ and $\mathbf{Q}(\rho,\mathbf{s},\tau)$ are the noises in the inner region and Q_ρ corresponds to the radial component of the stochastic current. The correlations of these scaled noise terms are

$$\langle H(\rho,\mathbf{s},\tau)H(\rho',\mathbf{s}',\tau')\rangle = 2\sigma_\phi^2\delta(\rho-\rho')\delta(\mathbf{s}-\mathbf{s}')\delta(\tau-\tau'), \tag{6.27}$$

$$\langle Q_i(\rho,\mathbf{s},\tau)Q_j(\rho',\mathbf{s}',\tau')\rangle = 2\sigma_u^2\delta_{ij}\delta(\rho-\rho')\delta(\mathbf{s}-\mathbf{s}')\delta(\tau-\tau'). \tag{6.28}$$

The inner and outer noises are related by

$$H = \varepsilon\eta \tag{6.29}$$

$$Q = \varepsilon q, \tag{6.30}$$

where we have used that

$$\delta(r-r') = \frac{1}{\varepsilon}\delta(\rho-\rho') \tag{6.31}$$

$$\delta(t-t') = \frac{1}{\varepsilon}\delta(\tau-\tau'). \tag{6.32}$$

The inner equations, keeping terms up to second order in ε can be written in a more compact form

$$\begin{aligned}\alpha\varepsilon[\frac{d}{d\tau} - v\partial_\rho]\Phi &= \partial_\rho^2\Phi + \varepsilon\kappa\partial_\rho\Phi - \varepsilon^2\rho(\kappa^2 - 2\Pi)\partial_\rho\Phi \\ &+ \varepsilon^2\sum_{i=1,2}\partial_{s_i}^2\Phi - f'(\Phi) - \varepsilon\lambda\bar{g}'(\phi)U + \varepsilon^{1/2}H(\rho,\mathbf{s},\tau),\end{aligned} \tag{6.33}$$

$$\frac{1}{\varepsilon}[\frac{d}{d\tau}-v\partial_\rho]U=\frac{1}{\varepsilon^2}\partial_\rho^2 U+\frac{1}{\varepsilon}[\kappa-\rho(\kappa^2-2\Pi)]\partial_\rho U+\sum_{i=1,2}\partial_{s_i}^2 U-\frac{v_r}{2\varepsilon}\partial_\rho h(\Phi)-\frac{1}{\varepsilon^2}\partial_\rho Q_\rho, \tag{6.34}$$

where we have introduced $\kappa=\kappa_1+\kappa_2$ and $\Pi=\kappa_1\kappa_2$ as the mean and Gaussian curvatures of the surface.

Expanding the inner fields in ε

$$U = U_0+\varepsilon U_1+\varepsilon^2 U_2+O(\varepsilon^3) \tag{6.35}$$
$$\Phi = \Phi_0+\varepsilon\Phi_1+\varepsilon^2\Phi_2+O(\varepsilon^3), \tag{6.36}$$

and the parameters

$$\kappa_i = \kappa_{i0}+\varepsilon\kappa_{i1}+O(\varepsilon^2)\ ,\ i=1,2 \text{ (curvatures)} \tag{6.37}$$
$$v = v_0+\varepsilon v_1+O(\varepsilon^2) \text{ (normal velocity)}$$
$$v_t = \varepsilon v_{t1}+O(\varepsilon^2) \text{ (tangential velocity)}, \tag{6.38}$$

we can determine the inner equations at each order in ε.

After solving the inner and outer equations at each order, the fields at each region are asymptotically matched at an intermediate distance r_M. The matching procedure can be described as follows: Let's consider the arbitrary inner and outer functions $a(r)$ and $A(\rho)$. The inner function $A(\rho)$ is then asymptotically expanded for $\rho\to\pm\infty$ as

$$A(\rho)\sim A_0+A_1\rho+A_2\rho^2+O(\rho^3), \tag{6.39}$$

and the outer function $a(r)$ is expanded in Taylor around $r=0^\pm$ by

$$a(r)\approx a(0^\pm)+\partial_r a(0^\pm)\cdot r+\frac{a}{2}\partial_r^2 a(0^\pm)\cdot r^2+O(r^3). \tag{6.40}$$

As $\varepsilon\to 0$, the inner and outer functions must take the same value at the intermediate distances $\rho_M\sim O(\varepsilon^{-1/2})$ and $r_M\sim O(\varepsilon^{1/2})$. This defines a matching condition which is given by

$$a(r_M)=A(\rho_M), \tag{6.41}$$

and permits to proceed to match the inner and outer solutions at each order by taking

$$A_0 = a(0^\pm) \tag{6.42}$$
$$A_1 = \varepsilon\partial_r a(0^\pm) \tag{6.43}$$
$$A_2 = \frac{1}{2}\varepsilon^2\partial_r^2 a(0^\pm) \tag{6.44}$$
$$\cdots \tag{6.45}$$
$$A_n = \frac{1}{n!}\varepsilon^n\partial_r^n a(0^\pm). \tag{6.46}$$

The last equations can be expanded in powers of ε to find the matching conditions at each order. During the solution of the inner equations, we will use some assumptions which are derived from these matching relations.

Zero order:

The inner equations at zero order (ε^0 for the Φ equation, ε^{-2} for the U one) are given by

$$\partial_\rho^2 \Phi_0 - f'(\Phi_0) = 0 \tag{6.47}$$

$$\partial_\rho^2 U_0 = 0. \tag{6.48}$$

From the first equation, and choosing $f(\phi) = -\phi^2/2 + \phi^4/4$, we obtain the zero-order kink solution for the phase-field

$$\Phi_0(\rho) = -\tanh\left(\frac{\rho}{\sqrt{2}}\right). \tag{6.49}$$

Note that the zero-order phase-field solution Φ_0 satisfies the matching conditions with the outer field $\phi_0 = \pm 1$ for $\rho \to \pm\infty$. Furthermore, the higher order solutions of the inner phase-field must satisfy the limiting condition

$$\Phi_i(\rho \to \pm\infty) = 0, \text{ for } i = 1, 2. \tag{6.50}$$

Integrating the second equation Eq. 6.48, we have

$$U_0(\mathbf{s}, \tau) = A(\mathbf{s}, \tau) + B(\mathbf{s}, \tau)\rho. \tag{6.51}$$

As the gradients of U_0 must vanish far away from the interface, it is necessary that $B(\mathbf{s}, \tau) = 0$, so we are left with

$$U_0(\mathbf{s}, \tau) = A(\mathbf{s}, \tau). \tag{6.52}$$

First Order:

The inner equations at order ε are

$$\Omega\Phi_1 = -(v_0\alpha + \kappa_0)\partial_\rho\Phi_0 + \lambda\bar{g}'(\Phi_0)U_0 \tag{6.53}$$

$$\partial_\rho^2 U_1 = \frac{dU_0}{d\tau} + \frac{v_0}{2}\partial_\rho h(\Phi_0), \tag{6.54}$$

where $\Omega = \partial_\rho^2 - f''(\Phi_0)$ and we have used that $d\Phi_0/d\tau = 0$. Φ_1 can be then isolated from Eq. 6.53 to give

$$\Phi_1 = \Omega^{-1}[-(v_0\alpha + \kappa_0)\partial_\rho\Phi_0 + \lambda\bar{g}'(\Phi_0)U_0]. \tag{6.55}$$

If we choose $\bar{g}'(\phi_0)$ and $f''(\phi)$ even in Φ, Ω is an even differential operator. As the functions $\partial_\rho\Phi_0$ and $\bar{g}'(\Phi_0)$ are even functions of ρ, we conclude that Φ_1 is even in ρ. Integrating twice over ρ the equation for U Eq. 6.54, we get

$$U_1 = D(\mathbf{s}, \tau) + C(\mathbf{s}, \tau)\rho + \frac{v_0}{2}\int_0^\rho d\rho' h(\Phi_0) + \frac{1}{2}\frac{dU_0}{d\tau}\rho^2 , \tag{6.56}$$

where $D(\mathbf{s}, \tau)$ and $C(\mathbf{s}, \tau)$ are the integration constants and we have used that $\partial_\rho U_0 = 0$.

Second order:

At second order in ε, the inner equations read

$$\begin{aligned}\Omega\Phi_2 = &-(\alpha v_1+\kappa_1)\partial_\rho\Phi_0-(\alpha v_0+\kappa_0)\partial_\rho\Phi_1+\alpha\frac{d\Phi_1}{d\tau}+\frac{1}{2}f'''(\phi_0)\Phi_1^2\\ &+\rho(\kappa_0-2\Pi_0)\partial_\rho\Phi_0+\lambda\bar{g}'(\phi_0)U_1+\lambda g''(\Phi_0)\Phi_1U_0+\varepsilon^{-3/2}H.\end{aligned} \tag{6.57}$$

$$\begin{aligned}\partial_\rho^2U_2 = &-(v_0+\kappa_0)\partial_\rho U_1+\frac{dU_1}{d\tau}+\frac{v_1}{2}\partial_\rho h+\frac{v_0}{2}\partial_\rho(h'(\Phi_0)\Phi_1)\\ &-\partial_s^2U_0-\frac{1}{\varepsilon^2}\partial_\rho Q_\rho.-h'(\Phi_0)\frac{d\Phi_1}{d\tau}\end{aligned} \tag{6.58}$$

The first equation will be used in the next section when imposing the solvability conditions of the problem. Integrating twice over ρ the equation for U_2 Eq. 6.58, we obtain

$$\begin{aligned}U_2 = &F+E\rho-(v_0+\kappa_0)\int_0^\rho d\rho' U_1+\int_0^\rho d\rho'\int_0^{\rho'}d\rho''\frac{dU_1}{d\tau}\\ &-\frac{1}{2}\partial_s^2U_0\rho^2+\frac{v_1}{2}\int_0^\rho d\rho' h(\Phi_0)+\frac{v_0}{2}\int_0^\rho d\rho' h'(\Phi_0)\Phi_1-\frac{1}{\varepsilon^2}\int_0^\rho d\rho' Q(\rho,s,\tau)\end{aligned} \tag{6.59}$$

6.3.3 Solvability conditions

We impose now the solvability conditions for the inner problem, which are given by

$$\int_{-\infty}^{\infty}(\partial_\rho\Phi_0)\Omega\Phi_j d\rho=0,\ \text{for } j=1,2. \tag{6.60}$$

From the first order solvability condition $\int_{-\infty}^{\infty}(\partial_\rho\Phi_0)\Omega\Phi_1 d\rho=0$ we get

$$-(\alpha v_0+\kappa_0)I_1-\lambda I_2 v_0=0, \tag{6.61}$$

which allows to determine U_0 as

$$U_0(\mathbf{s},\tau)=A=-\frac{\alpha I_1}{\lambda I_2}v_0-\frac{I_1}{\lambda I_2}\kappa_0, \tag{6.62}$$

where I_1 and I_2 are integral constants given by

$$I_1 = \int_{-\infty}^{\infty}d\rho(\partial_\rho\Phi_0)^2 \tag{6.63}$$

$$I_2 = -\int_{-\infty}^{\infty}d\rho\bar{g}'(\Phi_0)(\partial_\rho\Phi_0)=-\int_{-\infty}^{\infty}d\rho\partial_\rho\bar{g}(\Phi_0)=\bar{g}(1)-\bar{g}(-1). \tag{6.64}$$

Imposing the solvability condition at second order $\int_{-\infty}^{\infty}(\partial_\rho\Phi_0)\Omega\Phi_2 d\rho=0$, and taking into account that Φ_0, $\partial_\rho\Phi_1$, are odd in ρ, $\partial_\rho\Phi_0$, Φ_1 even in ρ, $\bar{g}(\phi)$, $g''(\phi)$,

$f'''(\phi)$, $h(\phi)$ are odd in ϕ ($\int_0^\rho d\rho h(\phi)$ is even in ϕ) and that $\bar{g}'(\phi)$ is even in ϕ, we obtain

$$D(\mathbf{s},\tau) = -(\alpha v_1 + \kappa_1)\frac{I_1}{\lambda I_2} + v_0\frac{I_3}{2I_2} + \frac{I_4}{2I_2} + \frac{\alpha I_5}{\lambda I_2} - \varepsilon^{-3/2}\frac{Z(\mathbf{s},\tau)}{\lambda I_2}, \tag{6.65}$$

where the integral constants I_3,I_4 and I_5 are defined by

$$I_3 = \int_{-\infty}^{\infty} d\rho\ (\partial_\rho \Phi_0)\ \bar{g}'(\Phi_0) \int_0^\rho d\rho' h(\Phi_0) \tag{6.66}$$

$$I_4 = \frac{dU_0}{d\tau}\int_{-\infty}^{\infty} d\rho\ (\partial_\rho \Phi_0)\bar{g}'(\phi_0)\rho^2 \tag{6.67}$$

$$I_5 = \int_{-\infty}^{\infty} d\rho\ (\partial_\rho \Phi_0)\frac{d\Phi_1}{d\tau}, \tag{6.68}$$

and Z is a stochastic term given by

$$Z(\mathbf{s},\tau) = \int_{-\infty}^{\infty} d\rho\ (\partial_\rho \Phi_0)\ H(\rho, s, \tau), \tag{6.69}$$

whose statistical properties are given by

$$\langle Z(\mathbf{s},\tau)Z(\mathbf{s}',\tau')\rangle = 2I_1\sigma_\phi^2\delta(\mathbf{s}-\mathbf{s}')\delta(\tau-\tau'). \tag{6.70}$$

In the outer region, the stochastic term Z gets an extra $\sqrt{\varepsilon}$ factor coming from the un-scaling of the time delta

$$\sqrt{\varepsilon}z(\mathbf{s},t) = Z(\mathbf{s},\tau). \tag{6.71}$$

6.3.4 Asymptotic matching of the inner and outer solutions

Expanding in ε the fields, velocities and curvatures, and introducing the expansions into Eqs. 6.25,6.26 we get the inner equations at each order. Following the classical sharp-interface procedure [Almgren99], the solutions should match with those of the outer equations order by order. For the phase field, direct matching with the outer ϕ_i solutions provides the boundary conditions for the Φ_i terms of the inner expansion. However, to match the diffusion field in the presence of fluctuations, we have to employ an auxiliary matching function defined in both regions as

$$\chi(r,\mathbf{s},t) = u(r,\mathbf{s},t) - \int_0^r dr' q_r(r',\mathbf{s}',t) \tag{6.72}$$

$$X(\rho,\mathbf{s},\tau) = U(\rho,\mathbf{s},\tau) - \int_0^\rho d\rho' Q_\rho(\rho',\mathbf{s},\tau), \tag{6.73}$$

which is smooth up to order ε^2 in the matching region r_M.

Explicitely, if X is asymptotically expanded for $\rho \to \pm\infty$ as

$$X \sim T + S\,\rho + R\,\rho^2 + O(\rho^3), \tag{6.74}$$

and the outer matching function χ is expanded in Taylor around $r = 0^{\pm}$ by

$$\chi \approx \chi(0^{\pm}) + \partial_r\chi(0^{\pm}) \cdot r + \frac{1}{2}\partial_r^2\chi(0^{\pm}) \cdot r^2 + O(r^3), \tag{6.75}$$

the different terms can be related to those of the Taylor expansion of χ at $r \to 0^{\pm}$ to obtain the relations

$$T = \chi(0^{\pm}) \tag{6.76}$$
$$S = \varepsilon\partial_r\chi(0^{\pm}) \tag{6.77}$$
$$R = \frac{\varepsilon^2}{2}\partial_r^2\chi(0^{\pm}). \tag{6.78}$$

These terms are then expanded in powers of ε to complete the matching at each order in ε.

Using the expression for the asymptotic expansion of an integral

$$\lim_{\rho\to\pm\infty}\int_0^{\rho} d\rho'\varphi(\rho') = \varphi(\pm\infty)\cdot\rho + J^{\pm}, \tag{6.79}$$

where the integration constant $J^{\pm}$ is given by

$$J^{\pm} = \int_0^{\pm\infty} d\rho[\varphi(\rho) - \varphi(\pm\infty)], \tag{6.80}$$

we can expand asymptotically for $\rho \to \infty$ the obtained expressions for the inner solutions U_0, U_1 and U_2 Eqs. 6.52, 6.56 and 6.59 to get

Zero Order:

At zero order we do not have any dependence in ρ and U_0 remains unchanged

$$U_0(\mathbf{s},\tau) = -\frac{\alpha I_1}{\lambda I_2}v_0 - \frac{I_1}{\lambda I_2}\kappa_0. \tag{6.81}$$

First Order:

$$U_1 \approx \frac{1}{2}\frac{dU_0}{d\tau}\rho^2 + \left[U_0(\mathbf{s},\tau) + \frac{v_0}{2}h(\Phi_0(\rho\to\pm\infty))\right]\rho + D + \frac{v_0}{2}J_1^{\pm} \tag{6.82}$$

where

$$J_1^{\pm} = \int_0^{\pm\infty} d\rho\left[h(\Phi_0(\rho)) - h(\Phi_0(\rho\to\pm\infty))\right], \tag{6.83}$$

which is a finite integral because the integrand vanishes at $\rho \to \pm\infty$. This assertion can be checked by noting that h satisfies $h(\pm1) = \pm1$ and $\Phi_0(\rho \to \pm\infty) = \pm1$. Choosing $h(\Phi(\rho))$ to be odd in ϕ, and noting that Φ_0 is odd in ρ, we have

$$J_1 = J_1^{+} = J_1^{-}. \tag{6.84}$$

Second Order:

$$\begin{aligned} U_2 \approx F + E\rho - (v_0 + \kappa_0) \int_0^\rho d\rho' \frac{dU_1}{d\tau} + \int_0^\rho d\rho' \int_0^{\rho'} d\rho'' \frac{dU_1}{d\tau} \\ - \frac{1}{2}\partial_s^2 U_0 \rho^2 - \int_0^\rho d\rho' \int_0^{\rho'} d\rho'' h'(\Phi_0) \frac{d\Phi_1}{d\tau} \\ + \frac{v_0}{2} J_2^{\pm} + \frac{v_1}{2} J_1 + \frac{v_1}{2} h(\Phi_0(\rho \to \pm\infty))\rho + \int_0^\rho d\rho' Q_\rho(\rho, \mathbf{s}, t). \end{aligned} \tag{6.85}$$

where

$$J_2^{\pm} = \int_0^\rho d\rho' h'(\Phi_0)\Phi_1, \tag{6.86}$$

and we have used that $\Phi_1(\rho \to \pm\infty) = 0$ from condition Eq. 6.50. By inserting the asymptotic expressions of U_0, U_1 and U_2 Eqs. 6.81, 6.82 and 6.85 into Eq. 6.74, we can construct the far field expansion of the matching function X and perform the matching with the outer function χ in Eq. 6.75.

Imposing the third matching condition Eq. 6.78 at first order, we determine that

$$\frac{dU_0}{d\tau} = 0, \tag{6.87}$$

and using the relation Eq. 6.55, it brings to

$$\frac{d\Phi_1}{d\tau} = 0, \tag{6.88}$$

so the integral constants I_4 and I_5 defined in Eqs. 6.67, 6.68 are zero

$$I_4 = I_5 = 0. \tag{6.89}$$

From the two first orders of the matching condition Eq. 6.76, we get a first order expression for the outer interfacial temperature

$$u(0^{\pm}) = -\frac{I_1}{\lambda I_2}(\alpha v + \kappa) + \frac{\varepsilon v_0}{2}\left(\frac{I_3}{I_2} + J_1\right) - \frac{z(\mathbf{s}, t)}{\lambda I_2} + O(\varepsilon^2), \tag{6.90}$$

where $z(\mathbf{s}, t)$ is a stochastic term whose statistical properties are given by

$$\langle z(\mathbf{s}, t) z(\mathbf{s}', t') \rangle = 2 I_1 \sigma_\phi^2 \delta(\mathbf{s} - \mathbf{s}')\delta(t - t'). \tag{6.91}$$

Note that as a consequence of choosing $h(\phi)$ as an odd function of ϕ, we have $J_1^+ = J_1^-$ and Eq.6.90 satisfies temperature continuity at the interface up to first order in ε. The calculation is completed by using the two first orders of the second matching conditions Eq. 6.77, from which we find a conservation equation to first order in ε,

$$v = v_0 + \varepsilon v_1 = [\partial_r u]_+^- - [q_r]_+^- + O(\varepsilon^2), \tag{6.92}$$

where the stochastic current q_ρ accounts for a conserved stochastic heat current at the interface.

6.4 Determination of the model parameters

As a main result of this chapter, the sharp-interface projection of the stochastic phase field Eqs. 6.3-6.7 is given by the diffusion Eq. 6.24, supplemented with two moving boundary conditions at the interface: the conservation condition Eq. 6.92, and the Gibbs-Thomson Eq. 6.90, where a new projected interfacial noise appears with correlation given by Eq. 6.91. Whereas the general lines of the calculation follow the standard sharp interface asymptotics, we have included along the procedure the fluctuating terms, which have been projected in the weak noise limit. In that sense, this calculation is similar to the projection of front dynamics performed in Ref. [Rocco02]. Indeed, projected interfacial noise appearing in Eq. 6.90 is the analogous counterpart of the noise term of the projected eikonal front equation of Ref. [Rocco02].

The noises considered in this work are intended to account for both external and internal sources of fluctuations. Nevertheless it is worth pointing out that the resulting stochastic sharp interface equations are similar to those postulated in the Langevin formulation of solidification due to Karma [Karma93b, Karma93c] (see also Ref. [Cherepanova76]), which was constructed to obey equilibrium statistics. This opens the possibility of using the results above to provide generic (not necessarily variational) phase-field models with the correct equilibrium fluctuations, without using the fluctuation dissipation theorem for its formulation.

Pure substances

To illustrate that, let us consider the Langevin equations for the solidification of a undercooled pure substance [Karma93b, Karma93c] scaled with $\tilde{l} = \tilde{D}/\tilde{v}_p$ and $\tilde{\gamma} = \tilde{l}^2/\tilde{D}$

$$\partial_t u_{si} = \nabla^2 u_{si} - \nabla \cdot \mathbf{q}_{si}(\mathbf{r},t) \tag{6.93}$$

$$v^{int} = [\partial_r u_{si}]_+^- - [q_{si}^r]_+^- \tag{6.94}$$

$$u_{si}^{L,int} = -d_0^T \kappa - \beta^T v + \theta(\mathbf{r},t)\ , \tag{6.95}$$

where $d_0^T = d_0/(L_v/c) = \frac{\tilde{\sigma} T_M c}{L_v^2 \tilde{l}}$ is the reduced thermal capillary length and $\beta^T = c/\tilde{\mu} L_v$ where $\tilde{\mu}$ is the reduced thermal kinetic coefficient. The fluctuating terms $\mathbf{q_{si}}$ and θ have correlations given by

$$\langle q_{si}^i(\mathbf{r},t) q_{si}^j(\mathbf{r}',t')\rangle = \frac{2K_B T_M^2 c}{L_v^2 \tilde{l}^d}\delta_{ij}\delta(\mathbf{r}-\mathbf{r}')\delta(t-t') \tag{6.96}$$

$$\langle \theta(\mathbf{s},t)\theta(\mathbf{s}',t')\rangle = \frac{2K_B T_M^2 c\beta^T}{L_v^2 \tilde{l}^d}\delta(\mathbf{s}-\mathbf{s}')\delta(t-t'). \tag{6.97}$$

The Gibbs-Thomson equation Eq. 6.95 can be compared with Eq. 6.90 and the heat conservation condition Eq. 6.94 with Eq. 6.92. This comparison allows to determine

the phase-field parameters in terms of physical and substance parameters

$$\begin{aligned}
\lambda &= \frac{I_1}{I_2 d_0^T} \\
\alpha &= \frac{\beta^T}{d_0^T} + \frac{\varepsilon}{2d_0^T}\left(\frac{I_3}{I_2} + J_1\right) \\
\sigma_u^2 &= \frac{K_B T_M^2 c}{L_v^2 \tilde{l}^d} \\
\sigma_\phi^2 &= \frac{I_1 K_B T_M^2\, c\, \beta^T}{(d_0^T)^2 L_v^2 \tilde{l}^d} = \frac{\beta^T I_1}{(d_0^T)^2}\sigma_u^2.
\end{aligned} \tag{6.98}$$

The first relation is obtained from the asymptotic matching and recovers the definition of λ in the formulation of the model. The second one determines the value of the parameter α (or equivalently, τ), defined by Eq. 6.2 in terms of the physical parameters of the sharp-interface problem. The last two relations determine the intensities of the phase-field noises which are required to recover the stochastic sharp-interface equations Eqs. 6.93, 6.94.

Symmetric alloys

As the model can be used for both pure substances and symmetric alloys, we can also compare the sharp-interface projection of the model with the Langevin equations corresponding to the solutal case. For the reduced concentration $u = \frac{c-c_\infty}{\Delta c_0}$, these equations are given by the dimensionless set of equations

$$\partial_t u_{si} = \nabla^2 u_{si} - \nabla \cdot \mathbf{j}_{si}(\mathbf{r},t)\ , \tag{6.99}$$

$$v^{int} = [\partial_r u_{si}]_+^- - [j_{si}^r]_+^- \tag{6.100}$$

$$u_{si}^{L,int} = -\hat{d}_0\kappa - \hat{\beta} v + \nu(\mathbf{r},t) \tag{6.101}$$

$$u_{si}^{S,int} = u_{si}^{L,int} - 1\ , \tag{6.102}$$

where $\hat{d}_0 = d_0^c/\Delta c_0 = d_0/m_L = \frac{\tilde{\sigma} T_M}{L_v m_L \Delta c_0 \tilde{l}}$ is the scaled reduced chemical capillary length, $\tilde{\sigma}$ the interfacial surface energy and

$$\hat{\beta} = \frac{\beta}{\Delta c_0} = \frac{\tilde{l}}{\tilde{\gamma}\tilde{\mu} m_L \Delta c_0} \tag{6.103}$$

is the (scaled) reduced chemical kinetic coefficient , being $\tilde{\mu}$ the interface mobility. The correlations of the fluctuations are now

$$\langle j_{si}^i(\mathbf{r},t) j_{si}^j(\mathbf{r}',t')\rangle = \frac{2c_L^0 v_m}{N_0 \Delta c_0^2 \tilde{l}^d}\delta_{ij}\delta(\mathbf{r}-\mathbf{r}')\delta(t-t')\ , \tag{6.104}$$

$$\langle \nu(\mathbf{s},t)\nu(\mathbf{s}',t')\rangle = \frac{2K_B T_M^2 \hat{\beta}}{L_v m_L \Delta c_0\ \tilde{l}^d}\delta(\mathbf{s}-\mathbf{s}')\delta(t-t'), \tag{6.105}$$

By comparing Eqs. 6.100 and 6.102 with the sharp-interface projection of the phase-field model Eqs. 6.92 and 6.90, we obtain the values for the phase-field parameters

$$\lambda = \frac{I_1}{I_2}\frac{1}{\hat{d}_0} \tag{6.106}$$

$$\alpha = \frac{\hat{\beta}}{\hat{d}_0} + \frac{\varepsilon}{2\hat{d}_0}\left(\frac{I_3}{I_2} + J_1\right) \tag{6.107}$$

$$\sigma_u^2 = \frac{c_L^0 v_m}{N_0(\Delta c_0)^2 \tilde{l}^d} \tag{6.108}$$

$$\sigma_\phi^2 = \frac{K_B T_M^2 \hat{\beta} I_1}{\hat{d}_0^2 L_v m_L \Delta c_0\, \tilde{l}^d} = \frac{\hat{\beta} I_1}{\hat{d}_0^2}\sigma_u^2. \tag{6.109}$$

6.5 Power spectrum of a stationary flat interface

As a test of our results, we perform 2D phase-field simulations to find the power spectrum of the interfacial fluctuations of a solid-liquid stationary flat interface. Introducing the Fourier transform of the interface position $\xi(\mathbf{r},t)$ as $\xi_k(t) = \int dk\ \xi(\mathbf{r},t)\ e^{-i\mathbf{kr}}$, the power spectrum of a flat stationary interface in scaled variables is given by

$$S(k) = \langle \xi_k \xi_{-k} \rangle = \int \frac{dk'}{2\pi} \langle \xi_k \xi_{k'} \rangle = \frac{K_B T_M}{\tilde{\gamma}} \frac{1}{k^2}, \tag{6.110}$$

where $\tilde{\gamma} = \frac{\tilde{l}^d L_v^2 d_0}{T_M c}$ is the scaled interfacial surface energy. We perform 2D simulations of the model Eqs. 6.3, 6.4 scaling spaces and times with $\tilde{l} = 10^{-8}\ m$ and $\tilde{\gamma} = 9 \times 10^{-10}\ s$ respectively. The functions f, g have been chosen to be $h(\phi) = \phi$ and $\bar{g}'(\phi) = (1-\phi^2)^2$ so that the model does not have a variational structure. The substance parameters are given by $d_0 = 0.2817$, $\beta = 3.0331$ and $\sigma_u^2 = 0.001432$, which correspond to the values of the pure SCN in the $d = 3$ case. For this choice, and using Eqs. 6.98, the phase-field parameters take the values $\lambda = 3.13$, $\alpha = 10.76$ and $\sigma_\phi^2 = 0.05158$. The interface thickness is taken to be $\varepsilon = 0.3$. The simulations have been implemented with a finite differences scheme on a 512×50 lattice with $\Delta y = \Delta x = 0.2$ and $\Delta t = 0.005$. Fluctuations have been included by adding in the equations independent zero-mean Gaussian random variables at each time step and at each grid point. We use the initial conditions $\phi(0) = -\tanh(\frac{x}{\varepsilon\sqrt{2}})$, $u(0) = 0$, and non-flux and periodic boundary conditions have been imposed in the x and y directions respectively. The power spectrum statistics has been obtained as a time average among the last 3×10^6 time steps in a long simulation of 3.5×10^6 steps. The dashed line in Fig. 6.1 reflects the theoretical result given by Eq. 6.110, whereas the solid line describes the stationary power spectrum calculated from the phase-field simulations. As it can be seen, good agreement is found between theoretical and numerical results. The vertical dashed line in the figure represents the wavelength associated to the effective thickness of the interface, and determines

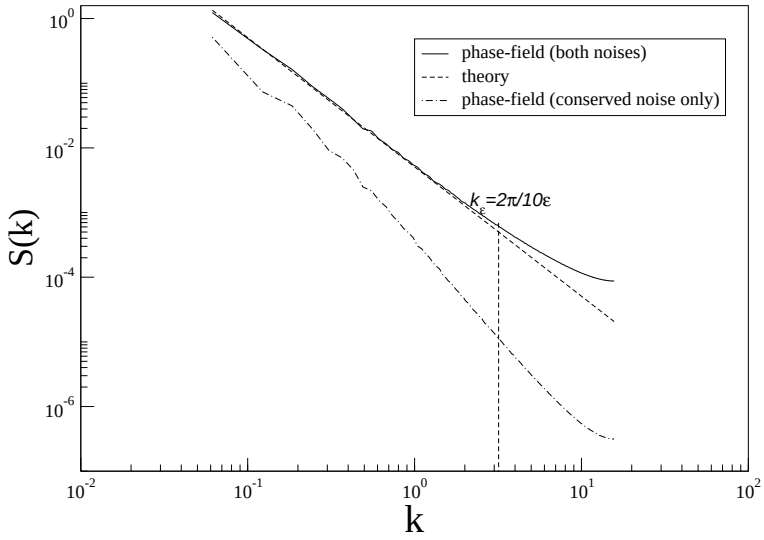

Figure 6.1: Comparison between the theoretical power spectrum of the stationary interface and the results from the phase-field simulations. Note that the incorporation of the phase-field (non-conserved) noise is necessary to recover the theoretical prediction.

qualitatively the breakdown of the phase-field description. The dot-dashed line in Figure 6.1 describes the power spectrum obtained by a phase-field simulations with only the conserved noise. This curve shows that, in general, the non-conserved noise is necessary to properly account for the correct equilibrium fluctuations of the system. Only in systems with a small attachment kinetics [Karma99], the noise in the diffusion equation becomes more relevant than the phase-field non-conserved noise and the power spectrum can be described without the contribution of the phase-field fluctuations.

6.6 Discussion

In this chapter, we have proposed an asymptotic procedure to obtain the sharp-interface projection of a stochastic phase-field model. This method can be used in both variational and non-variational phase-field formulations and permits to account for either internal or external fluctuations. Provided that the technique does not use the Fluctuation-Dissipation relation, it is therefore capable to account for the introduction of noise sources which do not obey equilibrium statistics. We

have tested the validity of our results by simulating the phase-field model to predict the interfacial correlations of a stationary planar interface.

The procedure might be used in more complex situations in which the presence of fluctuations is relevant, such as the apparition of dendritic sidebranching. We will devote Chapter 8 to another important problem in pattern formation, the wavelength selection during initial redistribution transients in the directional solidification of dilute alloys. In this case, our procedure will permit to perform quantitative simulations including fluctuations and properly describing the initial transient stages.

Chapter 7

Phase-field simulations of transient stages in alloy solidification

In this chapter, we present quantitative phase-field simulations of the early transient stages in a directional solidification process. To this extent, we will quantitatively compare the phase-field results with the analytical techniques described in Chapter 4. We will consider the three different non-variational phase-field models presented in Section 5.3 for one-sided, symmetric, and symmetric with constant miscibility gap systems. The substance and experimental parameters used in the simulations correspond to different realistic alloy systems used in several directional solidification experiments such as CBr_4-C_2Cl_6 [Faivre92, Akamatsu98, Akamatsu97], SCN-C152 [Losert98a, Losert98b, Losert98c], SCN-ACE [Han94a, Eshelman88a, Eshelman88b, Trivedi85], or 8CB [Figueiredo96, Figueiredo93, Oswald87, Simon88]. The first quantitative benchmark of the phase-field results is to compare the front position during the initial redistribution transient with the analytical prediction based in the Green's function techniques presented in Section 4.1.1. The Warren-Langer approximation presented in Section 4.2.1 will be used as reference for the comparison of the phase-field evolution of the concentration profiles during the initial transients. The transient dispersion relation derived in Section 4.2.1 from a linear stability analysis of the interface instability will be used as a benchmark for the phase-field evolution of the Fourier modes in the absence of noise. Simulation results for each of these models will be presented in Sections 7.2 (one-sided model), 7.3 (symmetric model) and 7.2 (symmetric model with constant gap).

7.1 Numerical simulation of the model equations

7.1.1 Selection of the model parameters

The sharp-interface limit performed in the last chapter determines the value of the deterministic (λ, α) and stochastic (σ_u, σ_ϕ) phase-field parameters in terms of physical properties of the system. For the sake of clarity, we shall distinguish the physical properties of the system in two different groups: The first group refers to the *substance parameters*, consisting in thermophysical properties of the system such as the melting temperature of the pure system T_M^A, the latent heat per unit volume L_v or the kinetic coefficient $\tilde{\mu}$. The values of these parameters for pure and alloy systems used in the simulations presented in this chapter can be found in Appendix A. The second class of parameters are the *experimental parameters*, which characterize the directional solidification set-up, and are given by the value of the external thermal gradient $\tilde{G}$, the solute concentration of the melt sample c_∞, and the pulling velocity of the sample frame with respect to the gradient frame $\tilde{v}_p$.

Assuming that we know all the substance and experimental parameters for a given directional solidification experiment, it is possible to determine all the phase-field parameters by using the relations Eqs. 6.106 - 6.109. Once the model parameters have been determined, one chooses the value of the interface thickness ε in order to perform the numerical simulation of the equations. As the value of the model parameters has been obtained by assuming $\varepsilon \to 0$, it is necessary to choose small values of ε in order to observe a good convergence of the phase-field dynamics to the Sharp-Interface prediction. For a given finite value of the interface thickness $\tilde{W}$, the phase-field simulations will only be reliable within the order at which the Sharp-Interface limit has been performed.

In order to understand the importance of the value of W, we first give a brief review of the main historical evolution of the phase-field simulations. The first Sharp-Interface asymptotic analysis was done for the pure substance model [Langer86, Caginalp89], and it was performed at first order in the interface thickness $\tilde{W}$. The obtained relations for the parameters were given by

$$\tilde{\lambda} = \frac{I_1}{I_2 \tilde{d}_0} \tag{7.1}$$

$$\tilde{\alpha} = \frac{\tilde{\beta}}{\tilde{d}_0}, \tag{7.2}$$

where $\tilde{\lambda}$ and $\tilde{\alpha}$ have dimensions of $[L^{-1}]$ and $[TL^{-2}]$ respectively and we have used the notation introduced in Chapter 6.

As the last equations are valid in the limit $\tilde{W} \to 0$, the main physical restriction on the interface thickness $\tilde{W}$ is that it has to be smaller than any relevant length scale in the problem. As in a solidification problem the smallest relevant scale is

the capillarity length $\tilde{d}_0$, the most restrictive condition for $\tilde{W}$ is then given by

$$\frac{\tilde{W}}{\tilde{d}_0} \ll 1. \tag{7.3}$$

Besides the last relation, there are other less restrictive conditions to be satisfied by $\tilde{W}$: For instance, we also need to choose a front thickness smaller than the radii of curvature of the front deformations $\tilde{W} \ll \frac{1}{\tilde{\kappa}}$, and obviously smaller than the diffusion length $\tilde{W} \ll \tilde{l}$.

The condition Eq. 7.3 expresses the physical requirement of the so called *classical Sharp-Interface limit*, and is responsible of the main problem of the early first-order phase-field formulations. As pointed out by some authors (see for instance [Wheeler93], [Wang96] and [Kobayashi93a] for the computation dendritic structures), quantitative phase-field simulations required a large amount of computational effort. The reason for that can be already explained by considering a 1D simulation of the model equations: On one hand, the simulation grid size $\Delta\tilde{z}$ must be taken to be smaller than $\tilde{W}$ in order to resolve the shape the phase-field kink. As $\tilde{W}$ must be smaller than $\tilde{d}_0$ for convergence reasons, the grid size $\Delta\tilde{z}$ must be therefore smaller than $\tilde{d}_0$. On the other hand, the size of the simulation domain $\tilde{L}_z$ needs to be of the order of the typical microstructures of the solidification front. These patterns typically appear at the diffusion scale $\tilde{l}$, which is at least two or three orders of magnitude larger than $\tilde{d}_0$, so we must impose the condition $\tilde{L}_z \gg \Delta\tilde{z}$. For instance, in a typical experiment with $\tilde{d}_0/\tilde{l} = 10^{-3}$, a fixed-grid simulation scheme with N_z simulation points ($\tilde{L}_z = N_z\Delta\tilde{z}$) will need at least $N_z > 1000$ simulation points. It turns then clear than extending the simulations to two and three dimensions will demand a huge amount of computational power.

Besides the large number of simulation points, requiring a small $\Delta\tilde{z}$ also imposes important restrictions in the simulation time-step of the simulations. In an explicit time-iteration algorithm, the numerical stability requires a simulation time-step $\Delta\tilde{t} < 2\tilde{D}/(\Delta\tilde{z})^2$ [Press92], which results in very long simulation times. This situation can be slightly improved by using implicit schemes which are more computationally stable and therefore not so restrictive in the value of the time-step. Another computational way of reducing the simulation time was proposed by Provatas et al. [Provatas98] and consisted in using an adaptive mesh, finite-elements method to solve numerically the phase-field equations. This procedure allowed to have more points around the interface and concentrate most of the computational power in solving the front dynamics instead spending time in calculating the fields in the bulk regions. In fact, adaptive finite-differences algorithms were already used by Braun and Murray in Ref. [Braun97]. Level-set techniques have been also used with the aim of reducing the computational time [Kim00]. Following this philosophy of decreasing the computational effort, the so-called mesh-less numerical techniques where also proposed: Plapp and Karma [Plapp00] proposed a Monte-Carlo simulation to calculate the diffusion field far from the solid-liquid interface, and calculated the phase-field equations only near the interface. Although

this procedure reduces the computational power dedicated to solve the far-field region, it requires rather complicated particle-averaging boundary conditions in order to match the phase-field solutions with the Monte-Carlo results and turns to be impractical. Benítez and Goldenfeld [Benítez03a] developed a hybrid method which simulated the model equations by writing them in a integral form and solving the multi-dimensional integrals by using importance-sampling, Monte-Carlo method with quasi-random sequences. Quasi-random sequences are based on low-discrepancy sequences [Niederreiter98] and present a better convergence than the classical pseudo-random sequences.

All these computational approaches, however, indicate that an improvement in the computational method do not necessary leads to an equivalent enhancement of the phase-field simulation results. In fact, the best way of increasing the computational efficiency of the phase-field simulations is to improve the accuracy of the sharp-interface limit. This can be done in two different ways, which turned to be equivalent:

- The first way was proposed by Karma and Rappel in Refs. [Karma96b, Karma98] and supposed an important gain in computation power. By assuming that the important length scales of the problem are the interface curvature and the diffusion length rather than the capillary length, they proposed an alternative Sharp-Interface asymptotic expansion in terms of a reduced interface thickness $p = \tilde{W}/\tilde{l}$ (*the interface Péclet number*) which was considered to be small ($p \ll 1$). The new asymptotic restriction was given by

$$\frac{\tilde{W}}{\tilde{l}} \ll 1, \tag{7.4}$$

  and replaced the most restrictive requirement of the classical limit $\tilde{W}/\tilde{d}_0 \ll 1$, thus providing more flexibility in the simulations. This approach was called *thin-interface limit* , and its main benefit remains in the fact that the limit $p \ll 1$ is taken while maintaining constant the value of $\tilde{W}/\tilde{d}_0$, therefore eliminating the hard restriction on $\Delta\tilde{z}$ that we have commented before.

- The second way of eliminating the hard restriction on $\tilde{W}/\tilde{d}_0$ is to perform the classical *Sharp-Interface limit up to second order* in ε as we did in the last chapter. This procedure yields to the same relations than the thin-interface procedure at first order, thus confirming that the capillary length restriction can be avoided.

The main relation between these two approaches was pointed out by Karma and Rappel [Karma96b], and is based in the fact that both asymptotic procedures introduce a term which acts as a non-constant temperature correction in the interface region. In the classical Sharp-Interface limit, this term appears at second order in ε and corresponds to the $\frac{\varepsilon v_0}{2}(\frac{I_3}{I_2} + J_1)$ term in Eq. 6.90. If the classical asymptotics is performed only up to first-order, the diffusion field is constant across the diffuse interface and imposes the restrictive condition in the value of $\tilde{W}$.

This can be explained by noting that if the u field is constant across the interface, its variation δu within the distance $\tilde{W}$ should be negligibly small. As the variation of u occurs in the scale of the diffusion length $\tilde{l}$, its gradient is proportional to $\tilde{l}^{-1}$ and δu is proportional to $\tilde{W}/\tilde{l}$. By comparing δu with the temperature variations due to kinetic effects $\tilde{\beta}\tilde{v}$, we arrive to the condition

$$\frac{\tilde{W}}{\tilde{l}} \ll \tilde{\beta}\tilde{v} \tag{7.5}$$

which can be reformulated using Eqs. 7.1 and 7.2 as

$$\frac{\tilde{W}}{\tilde{d}_0} \ll \tilde{\alpha}\tilde{D}, \tag{7.6}$$

which is an explicit version of the restriction Eq. 7.3.

7.2 Directional solidification of a one-sided dilute binary alloy

7.2.1 Dimensionless equations

The equations describing the directional solidification of a one-sided alloy ($\tilde{D}_S = 0$, $\tilde{D}_L \neq 0$) can be obtained from the non-symmetric model described in section 5.3.1 (cf. Eqs. 5.138, 5.84) by choosing the function $q(\phi)$ in such a way that its value ranges from zero at the solid to $\tilde{D}_L$ at the liquid phase. The phase-field equations are then given by

$$\begin{aligned}
&\partial_{\tilde{t}} c_B = \tilde{D}_L \tilde{\nabla} q(\phi) \tilde{\nabla} c_B + (1-k)\tilde{D}_L \tilde{\nabla}\left[\frac{c_B q(\phi)\tilde{\nabla} h(\phi)}{[1+k-(1-k)h]}\right] \\
&+ a\tilde{W}(1-k)\tilde{\nabla}\left[\frac{c_B}{[1+k-(1-k)h(\phi)]}\frac{\partial\phi}{\partial\tilde{t}}\frac{\tilde{\nabla}\phi}{|\tilde{\nabla}\phi|}\right] \\
&\tilde{\tau}\partial_{\tilde{t}}\phi = \tilde{W}^2\tilde{\nabla}^2\phi - \partial_\phi f(\phi) \\
&- \frac{I_1}{2(1-k)}\frac{\tilde{W}}{\hat{\tilde{d}}_0}\partial_\phi g\left[\frac{2c_B}{c_B^{0,L}[1+k-(1-k)h]} - 1 + \frac{(1-k)}{\tilde{l}_T}\tilde{z}(\tilde{t})\right],
\end{aligned} \tag{7.7}$$

where $\hat{\tilde{d}}_0$ is given by

$$\hat{\tilde{d}}_0 = \frac{\tilde{\sigma} T_M^A}{L_v m_L \Delta c_0}. \tag{7.8}$$

In the last model, the extension to directional solidification has been performed by using the arguments presented in section 5.2. Scaling space and times with

the diffusion length $\tilde{l} = \tilde{v}_p/\tilde{D}_L$ and the diffusion time $\tilde{\gamma} = \tilde{l}^2/\tilde{D}_L$ respectively, the dimensionless version of the equations is given by

$$\begin{aligned}
&\partial_t c_B = \nabla q(\phi)\nabla c_B + (1-k)\nabla\left[\frac{c_B q(\phi)\nabla h(\phi)}{[1+k-(1-k)h]}\right] \\
&+ a\varepsilon(1-k)\nabla\left[\frac{c_B}{[1+k-(1-k)h(\phi)]}\frac{\partial\phi}{\partial t}\frac{\nabla\phi}{|\nabla\phi|}\right] \\
&\tau\partial_t\phi = \varepsilon^2\nabla^2\phi - \partial_\phi f(\phi) \\
&- \frac{I_1}{2(1-k)}\frac{\varepsilon}{\hat{d}_0}\partial_\phi g\left[\frac{2c_B}{c_B^{0,L}[1+k-(1-k)h]} - 1 + \frac{(1-k)}{l_T}z(t)\right],
\end{aligned} \tag{7.9}$$

where $\varepsilon = \tilde{W}/\tilde{l}$, $\hat{d}_0 = \hat{\tilde{d}}_0/\tilde{l}$ and $\tau = \tilde{\tau}/\tilde{\gamma}$.
Following the notation introduced in Chapter 6, we use the dimensionless parameters

$$\lambda = \frac{15}{16}\frac{I_1}{\hat{d}_0}, \tag{7.10}$$

$$\alpha = \frac{\tau}{\varepsilon^2}, \tag{7.11}$$

and the function

$$\bar{g}(\phi) = \frac{8}{15}g(\phi), \tag{7.12}$$

and write the model equations in its final form

$$\begin{aligned}
&\partial_t c_B = \nabla q(\phi)\nabla c_B + (1-k)\nabla\left[\frac{c_B q(\phi)\nabla h(\phi)}{[1+k-(1-k)h]}\right] + \\
&a\varepsilon(1-k)\nabla\left[\frac{c_B}{[1+k-(1-k)h(\phi)]}\frac{\partial\phi}{\partial t}\frac{\nabla\phi}{|\nabla\phi|}\right] \\
&\alpha\varepsilon^2\partial_t\phi = \varepsilon^2\nabla^2\phi - \partial_\phi f(\phi) \\
&- \varepsilon\frac{\lambda}{(1-k)}\partial_\phi\bar{g}\left[\frac{2c_B}{c_B^{0,L}[1+k-(1-k)h]} - 1 + \frac{(1-k)}{l_T}z(t)\right].
\end{aligned} \tag{7.13}$$

For all the simulations presented in this chapter, the potentials and interpolation functions are chosen to be given by

$$f(\phi) = -\frac{1}{2}\phi^2 + \frac{1}{4}\phi^4 \tag{7.14}$$

$$\bar{g}(\phi) = \phi - \frac{2}{3}\phi^3 + \frac{1}{5}\phi^5 \tag{7.15}$$

$$h(\phi) = \phi. \tag{7.16}$$

In the case of non-symmetric models, we will take

$$q(\phi) = \frac{(1-\phi)}{[1+k-(1-k)h(\phi)]}, \tag{7.17}$$

and the anti-trapping constant a is taken to be

$$a = \sqrt{2} \text{ (normal gap models)}, \tag{7.18}$$
$$a = 0 \text{ (constant gap models)}. \tag{7.19}$$

7.2.2 Front position during the transient: Convergence to the Sharp-Interface

By performing 1D simulations of the model defined by Eqs. 7.13, we determine the position of the front during the initial redistribution transient. The phase-field results are then compared with both the Green's function prediction and with the Warren-Langer results. This quantitative comparison will be performed for different values of the convergence parameter ε, and will allow to determine the value of the interface thickness if we want to obtain quantitative simulation results. The simulations will be performed for different alloy systems and in different experimental regimes.

CBr_4-C_2Cl_6

The first set of simulations are performed for the organic alloy CBr_4-C_2Cl_6. The substance parameters for this substance are listed in Appendix A, Section A.2.1. The experimental values taken for the simulations are given by $\tilde{v}_p = 10^{-5}$ m/s, $\tilde{G} = 5.6 \times 10^3$ K/m and $c_\infty = 0.03$ mol, and the relevant parameters for the simulations are $\hat{\tilde{d}}_0 = 1.45 \times 10^{-7}$ m and $\tilde{l}_T = 10^{-4}$ m. The value of the interface mobility in this simulations is $\tilde{\mu} = 0.1503$ m/ K s ($\hat{\beta} = 1.18 \times 10^{-4}$, for $\hat{\beta} = \tilde{l}/(\tilde{\gamma}\tilde{\mu}m_l\Delta c_0)$). The diffusion length is $\tilde{l} = \tilde{D}_L/\tilde{v}_p = 5 \times 10^{-5}$ m and the diffusion time $\tilde{\gamma} = \tilde{D}_L/\tilde{v}_p^2 = 5s$, so the scaled thermal length and scaled capillary length are $l_T = \tilde{l}_T/\tilde{l} = 2$, $\hat{d}_0 = \hat{\tilde{d}}_0/\tilde{l} = 0.0029$ respectively. We have simulated the phase-field equations for different values of the interface thickness $\varepsilon = \tilde{W}/\tilde{l} \in [0.08, 0.04, 0.02, 0.01, 0.005]$ ($\tilde{W}/\hat{\tilde{d}}_0 \in [27.58, 13.79, 6.89, 3.44, 1.72]$). The equations have been discretized in a $N_z \times N_y = 6000 \times 2$ rectangular lattice with different dimensionless grid sizes for each interface thickness $\Delta y = \Delta\tilde{y}/\tilde{l} = \Delta z = \Delta\tilde{z}/\tilde{l} \in [0.064, 0.032, 0.016, 0.008, 0.004]$. For this choice of parameters, the ratio between the interface thickness and the grid size is given by $\Delta\tilde{z}/\tilde{W} = 0.8$, so as can be observed in Fig. 7.1, the kink solution for the phase-field is well resolved. Finally, the equations have been iterated in time by using an Euler explicit iteration scheme with dimensionless time-step $\Delta t = \Delta\tilde{t}/\tilde{\gamma} \in [2 \times 10^{-4}, 5 \times 10^{-5}, 1.25 \times 10^{-5}, 3.125 \times 10^{-6}, 7.8125 \times 10^{-7}]$, which keep the ratio $\Delta t/(\Delta x)^2 = 0.15625$. In Fig. 7.2 we have a comparison between the phase-field results and the Green's function profiles in the case of small kinetics ($\hat{\beta} = 1.18 \times 10^{-4}$) and for the different values of the interface thickness referenced before. The Sharp-Interface curves have been calculated by integrating the integral equation for the one-sided system Eq. introduced in Section 4.1.3. The initial conditions for the concentration field in both the phase-field and

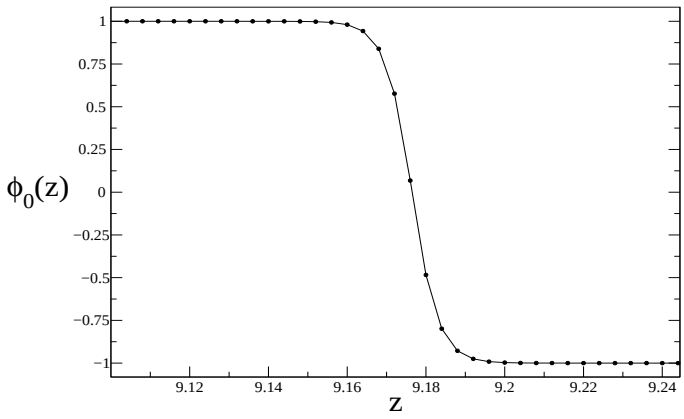

Figure 7.1: Profile of the phase-field kink solution and resolution and position of the simulation mesh points for $\Delta\tilde{z}/\tilde{W} = 0.8$.

Green's function simulations are $c_S(z, t = 0) = kc_\infty$ and $c_L(z, t = 0) = c_\infty$. It can be observed that the phase-field results converges to the sharp-interface prediction as the interface thickness ε decreases. In the simulations, the value of $\varepsilon = W/l$ is always small (interface thickness much smaller that the diffusion length), whereas the ratio $W/\hat{d}_0$ is reasonably near to the unity (interface thickness near the capillary length).

Generic substance

Figure 7.3 shows the convergence for a substance with segregation constant $k = 0.15$ and $\tilde{l}_T/\tilde{l} = 3.125$, $\tilde{\hat{d}}_0/\tilde{l} = 0.06923$. We have now plotted, in addition to the Green's function result, the profile obtained from the simulation of the Warren-Langer equations Eqs. 4.77 introduced in Chap. 4.2.1. The interface attachment has been supposed to be instantaneous $\tilde{\mu} = \infty$ (kinetic coefficient $\hat{\beta} = 0$). The phase-field simulation has been performed for $\varepsilon = 0.125$ ($W/\hat{d}_0 = 1.8053$) $\Delta z = \Delta y = 0.4$, $\Delta t = 0.008$. Note that now the ratio $\Delta\tilde{z}/\tilde{W} = 0.4$ is smaller than in the previous case, so the kink is better resolved. As depicted in the inset graph, the differences between theoretical and simulation curves are only appreciable at smaller scales.

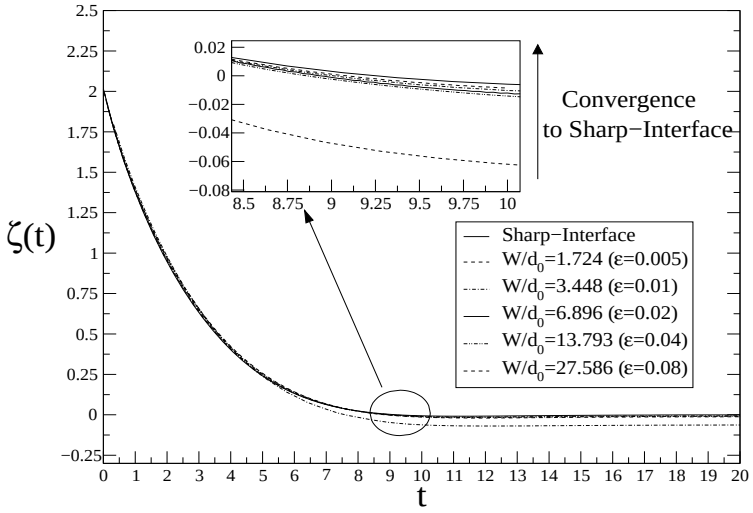

Figure 7.2: Convergence of the phase-field simulations to the Sharp-Interface prediction for the front position during the transient. The physical parameters chosen in the simulations correspond to a diluted CBr_2-C_2Cl_6 solution.

Different kinetic coefficients

In Fig. 7.4 we present a comparison between the phase-field and Sharp-Interface results in the case of having small ($\hat{\beta} = 1.18 \times 10^{-4}$) and large ($\hat{\beta} = 0.0805$) kinetic effects. The values of the interface mobility are taken in the collision-limited and diffusion-limited regimes (cf. Section 2.1.4 and Ref. [Aziz94]) are given by $\tilde{\mu} = 0.1503$ m/ K s and 2.2×10^{-4} m/ K s respectively, corresponding to the dimensionless kinetic coefficients $\hat{\beta} = 1.18 \times 10^{-4}$ and $\hat{\beta} = 0.0805$, where $\hat{\beta} = \tilde{l}/(\tilde{\gamma}\tilde{\mu}m_l\Delta c_0)$. The phase-field parameters correspond to the CBr_2-C_2Cl_6 system performed for $\varepsilon = 0.005$ ($\tilde{W}/\hat{\tilde{d}}_0 = 1.724$), and the phase-field results present a good quantitative agreement with the Green's function prediction.

Different segregation constants

Figure 7.5 plots $\xi(t)$ for two systems with $\tilde{l}_T/\tilde{l} = 3.125$, $\hat{\tilde{d}}_0/\tilde{l} = 0.06923$ but different values of the partition constant $k = 0.5$ and $k = 0.75$. The computational parameters are $\varepsilon = 0.125$ ($W/\hat{d}_0 = 1.8053$) $\Delta z = \Delta y = 0.4$, $\Delta t = 0.008$ (ratio $\Delta\tilde{z}/\tilde{W} = 0.4$).

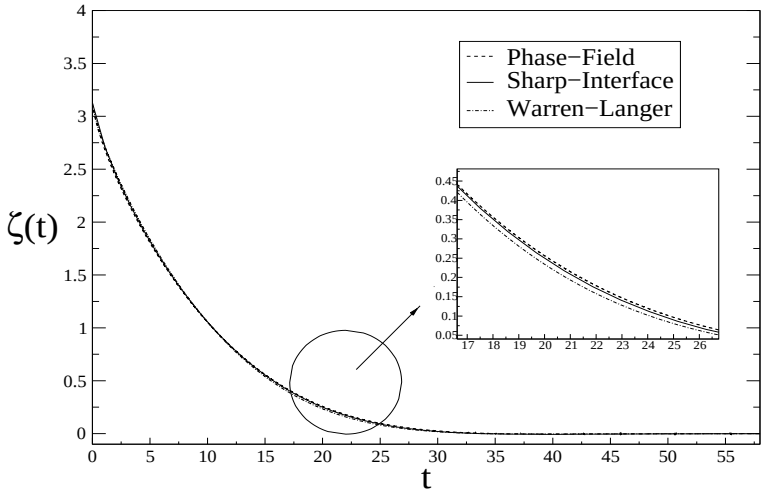

Figure 7.3: Phase-field, Warren-Langer and Sharp-Interface curves for $\tilde{l}_T/\tilde{l} = 3.125$ in a binary alloy with segregation constant $k = 0.15$.

7.2.3 Concentration profiles

Fig. 7.6 plots the concentration profiles for the CBr_2-C_2Cl_6 phase-field simulations at six different times $t = 0.25, 1.25, 2.5, 5, 7.5$ and 10 during the initial solute redistribution transient. The simulations are performed here for $\varepsilon = 0.005$ ($W/\hat{d}_0 = 1.724$), and are compared with the Warren-Langer's ansatz Eq. 4.72. Note that the concentration at the solid side of the interface varies from $c_\infty = 0.03$ to $c_\infty/k = 0.04$ during the initial transient ($k = 0.75$), and that the dimensionless size of the boundary layer in the stationary state is of the order of the dimensionless diffusion length $l = \tilde{l}/\tilde{l} = 1$.

7.2.4 Transient dispersion relation

The next step is to perform 2D simulations of the equations in order to observe if the morphological stability of the interface in the phase-field simulations agrees

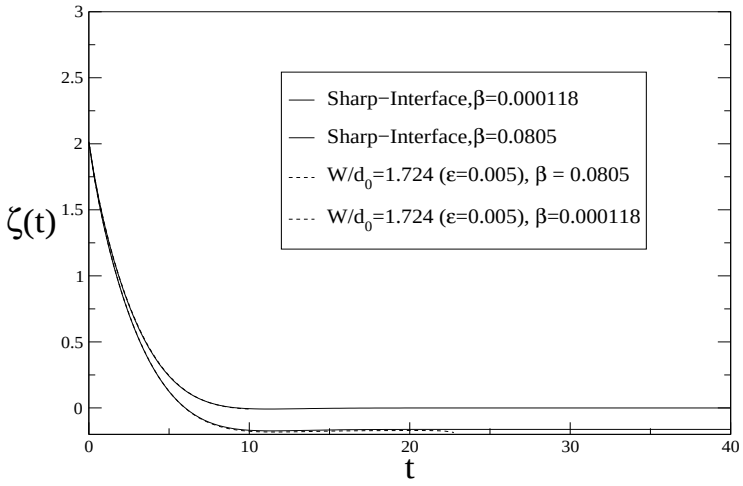

Figure 7.4: Comparison of the transient front positions for a CBr_2-C_2Cl_6 one-sided alloy and for two different values of the kinetic coefficient $\hat{\beta} = 1.18 \times 10^{-4}$ and $\hat{\beta} = 0.0805$.

with the theoretical predictions formulated in Section 4.2.1. The phase-field simulations are now performed in a rectangular lattice of size 2000×50. The parameters are now taken for the case $\tilde{l}_T/\tilde{l} = 3.125$ and $\hat{\tilde{d}}_0/\tilde{l} = 0.06923$. In order to calculate the transient dispersion relation from the phase-field simulations, the solid-liquid interface is perturbed in the simulations at different times with a sinusoidal modulation with a certain wavelength $\tilde{k}\tilde{l}$. For convenience reasons, the wavelength of the sinusoidal perturbation is taken to be equal the size of the system in the transversal direction, so the dimensionless wavelength of the perturbation is given by

$$k_{pert} = \frac{2\pi}{N_y \Delta y} \tag{7.20}$$

where N_y is the number of simulation points in the y direction, which in this section is $N_y = 50$. Figure 7.8 depicts the form of an initially perturbed interface at different times. As it can be observed, the amplitude of the perturbation decays indicating that the perturbed wavelength is stable at this time. The linear amplification or decay of the amplitude of the perturbed mode allows to determine the growth rate corresponding to the wavelength of the perturbation at this precise time. The amplitude of the mode $A(k,t)$ is calculated at each time by obtaining the Discrete Fourier Transform of the implicit interface curve $\phi(z,y,t) = 0$. As

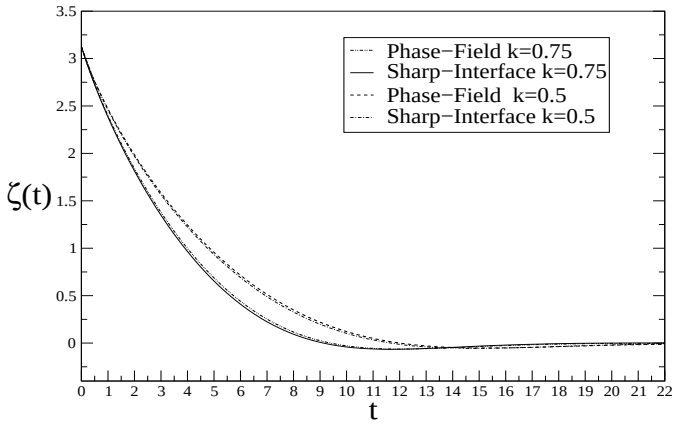

Figure 7.5: Phase-field and sharp-interface front position curves for two generic one-sided alloys with $\tilde{l}_T/\tilde{l} = 3.125$ and different segregation constants $k = 0.5$, $k = 0.75$.

shown in the Figure 7.9, the growth of the mode is linear only during a certain time after the perturbation. In the figure we can observe the evolution for a perturbation of wavelength $\tilde{k}\tilde{l} = 10.053$ introduced at different times during the intial transient $t = 0.3125, 1.5625, 9.375, 15.625$ and 21.875. In these simulations, we have used a generic substance with $\tilde{l}_T/\tilde{l} = 3.125$, and we have chosen a scaled interface thickness of $\varepsilon = 0.03125$. The sign of the $\frac{dA(k,t)}{dt}$ determines if the perturbed wavelength is stable ($\frac{dA(k,t)}{dt} < 0$) or unstable ($\frac{dA(k,t)}{dt} > 0$) at the time at which the front has been perturbed. After this linear growth regime, the interface enters in a non-linear stage where the amplitude of other wavelengths will eventually be comparable with the inverse of the perturbation wavelength. This procedure permits to calculate the transient growth rate $\omega(k,t)$ for a given set of parameters and compare the phase-field result with the theoretical prediction of the transient dispersion relation derived in Sec. 4.2.1. Theoretical and simulation curves for $\omega(k,t)$ are shown in Figs. 7.10, 7.11. In both cases, the wavelength of the perturbation is $\tilde{k}\tilde{l} = 10.053$ and the ratio $\tilde{l}_T/\tilde{l} = 3.125$. Both simulations have been performed with $\varepsilon = 0.03125$, and the difference between the simulations is that in Figure 7.10 the segregation constant is $k = 0.9$ whereas in Fig. 7.11 we have $k = 0.5$.

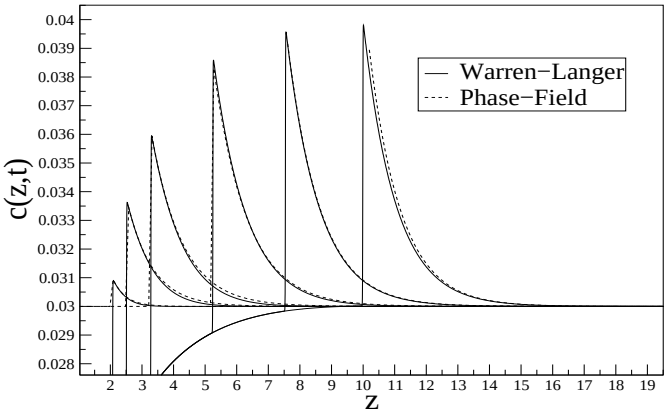

Figure 7.6: Comparison between the phase-field concentration profiles and the Warren-Langer approximation profile Eq.4.72 at six different times $t = 0.25, 1.25, 2.5, 5, 7.5$ and 10 during the initial solute redistribution transient. The simulations correspond to the one-sided CBr_2-C_2Cl_6 as described in Sec. 7.2.3.

7.3 Directional solidification of a symmetric dilute alloy

The symmetric model is appropriate to describe the solidification of liquid crystal alloys. The model equations can be obtained from the non-symmetric model by taking $q = 1$.

7.3.1 Dimensionless equations

In order to obtain the symmetric solutal model ($\tilde{D}_S = \tilde{D}_L = \tilde{D}$), we take $q(\phi) = 1$ and $a = 0$ in the previous model and find

$$\begin{aligned}
&\partial_t c_B = \nabla^2 c_B + (1-k)\nabla\left[\frac{c_B \nabla h(\phi)}{[1+k-(1-k)h]}\right].\\
&\alpha\varepsilon^2\partial_t\phi = \varepsilon^2\nabla^2\phi - \partial_\phi f(\phi)\\
&-\varepsilon\frac{\lambda}{(1-k)}\partial_\phi\bar{g}\left[\frac{2c_B}{c_B^{0,L}[1+k-(1-k)h]} - 1 + \frac{(1-k)}{l_T}z(t)\right].
\end{aligned} \tag{7.21}$$

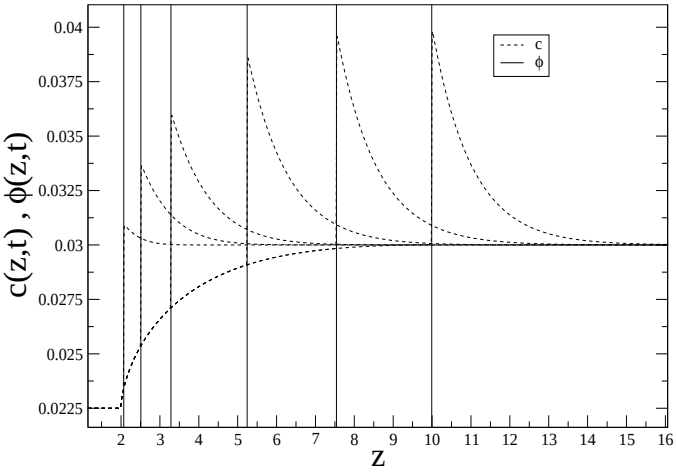

Figure 7.7: Profiles of the concentration and phase-field at six different times $t = 0.25, 1.25, 2.5, 5, 7.5$ and 10 during the initial transient. The profiles correspond to the system described in Sec. 7.2.3.

7.3.2 Front position during the transient

In this section we use the parameters corresponding to the commercial 8CB liquid crystal, which has been extensively used in directional solidification experiments [Figueiredo96, Figueiredo93, Oswald87, Simon88]. The substance parameters for this substance can be found in Appendix A, Section A.2.2. The experimental values taken for the simulations are given by $\tilde{v}_p = 6 \times 10^{-5}$ m/s, $\tilde{G} = 2.3 \times 10^3$ K/m and $c_\infty = 0.012$ mol.

The relevant parameters for the simulations are then $\hat{\tilde{d}}_0 = 2.696 \times 10^{-7}$ m and $\tilde{l}_T = 5.128 \times 10^{-5}$ m. The interface mobility is given by $\tilde{\mu} = 1.51$ m/ K s, and the values of the diffusion length and diffusion time are $\tilde{l} = \tilde{D}_L/\tilde{v}_p = 6.666 \times 10^{-6}$ m and $\tilde{\gamma} = \tilde{D}_L/\tilde{v}_p^2 = 0.111s$ respectively. The model parameters correspond to $\tilde{l}_T/\tilde{l} = 7.692$, $\hat{\tilde{d}}_0/\tilde{l} = 0.04044$, and the computational parameters are $\varepsilon = \tilde{W}/\tilde{l} \in [0.15, 0.075, 0.00375]$ ($\tilde{W}/\hat{\tilde{d}}_0 \in [3.709, 1.8545, 0.9272]$). The equations have been simulated in a 600×2 rectangular lattice with a dimensionless grid size $\Delta y = \Delta\tilde{y}/\tilde{l} = \Delta z = \Delta\tilde{z}/\tilde{l} \in [0.12, 0.06, 0.03]$. The dimensionless time-step is $\Delta t = \Delta\tilde{t}/\tilde{\gamma} \in [2.5\times10^{-6}, 6.7\times10^{-4}, 1.5\times10^{-4}]$. Figure 7.12 shows the convergence of this model for $\varepsilon = 0.15, 0.075$ and 0.00375 to the Sharp-Interface results which

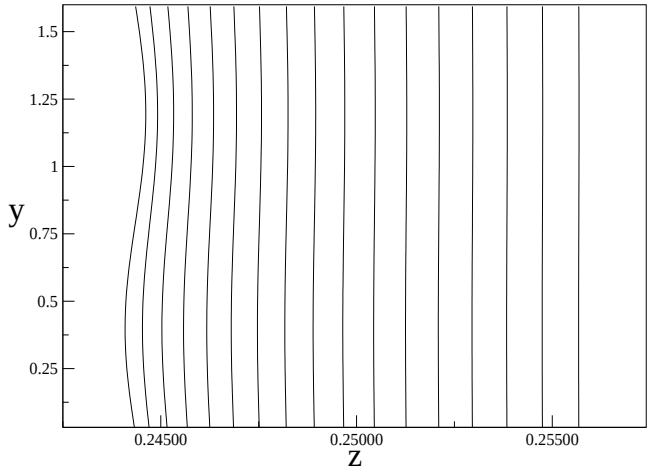

Figure 7.8: Dynamical evolution of a sinusoidal perturbation of the solidification front. The curves correspond to the numerical linear stability analisis described in Section 7.2.4.

have been obtained by solving the integral equation for the symmetric case and normal miscibility gap Eq. 4.68.

7.4 Directional solidification of symmetric alloys with constant miscibility gap

This model is completely equivalent to the pure substance model and only be used in symmetric alloy systems with segregation coefficients near the unity such as in solutions of liquid crystals. The results presented in this section are presented in Ref. [Benítez03b].

7.4.1 Dimensionless equations

The symmetric solutal model with constant gap is described in section 5.3.2 and in its dimensionless form reads

$$\begin{aligned} \alpha\varepsilon^2\partial_t\phi &= \varepsilon^2\nabla^2\phi - \partial_\phi f(\phi) - \varepsilon\lambda\partial_\phi\bar{g}(u+\frac{z}{l_T}) \\ \partial_t u &= \nabla^2 u + \frac{1}{2}\partial_t h(\phi). \end{aligned} \tag{7.22}$$

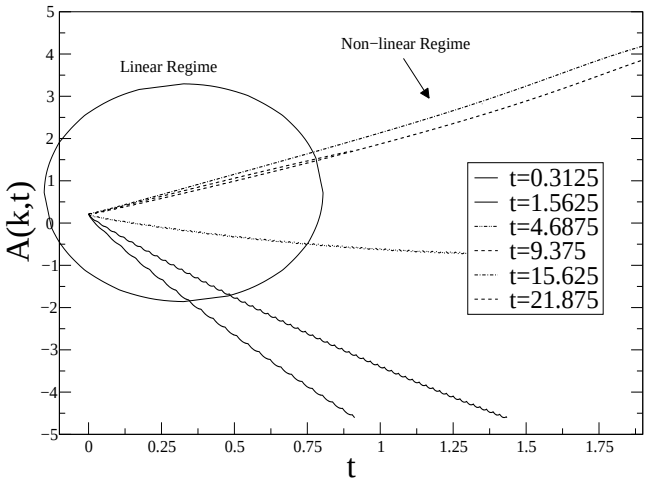

Figure 7.9: Time evolution of the amplitude of the Fourier mode of wavelength $\tilde{k}\tilde{l} = 10.053$ when perturbing the interface at times $t = 0.3125, 1.5625, 9.375, 15.625$ and 21.875.

7.4.2 Front position during the transient

Figure 7.13 plots the convergence of the phase-field simulations to the Sharp-Interface prediction made by solving the symmetric-constant gap boundary integral formulation Eq. 4.57. The interface thickness has been maintained constant ($W/d_0 = 1.8053$) and the convergence has been achieved by modifying the diffusion and thermal lengths l, l_T so that the value of ε decreases taking the values $\varepsilon = 0.5, 0.25, 0.125$ maintaining unchanged the ratio $l_T/l = 12.5$.

7.4.3 Transient dispersion relation

Using the same procedure as in Section 7.2.4, we evaluate the time evolution of two different modes $\tilde{k}\tilde{l} = 2.5$ and $\tilde{k}\tilde{l} = 1.25$ in the symmetric model with constant miscibility gap. The set of parameters is the same as in the previous case $\tilde{l}_T/\tilde{l} = 12.5$ and $\varepsilon = 0.125$, and the phase-field growth rate has been calculated at times $t = 0, 6.25, 12.5, 18.75, 25, 31.125, 37.5, 50$ and 62.5. The results are shown in Fig. 7.14 where it is shown that the phase-field simulations present a qualitative agreement with the theoretical predictions.

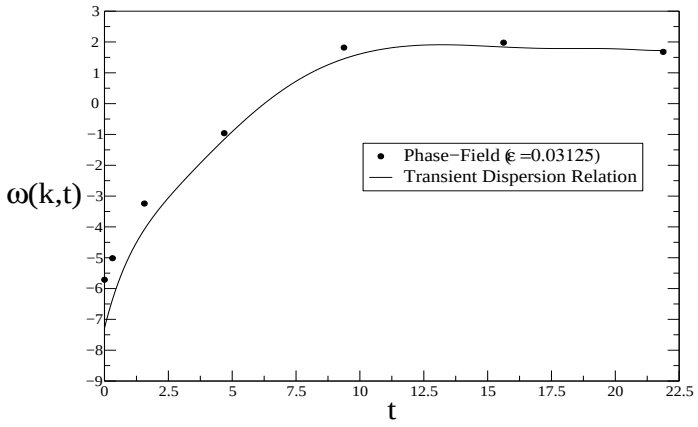

Figure 7.10: Time evolution of the growth rate of the wavelength $\tilde{k}\tilde{l} = 10.053$ during the initial transient. The system is a one-sided alloy and the simulation parameters are $\tilde{l}_T/\tilde{l} = 3.125$ and $\varepsilon = 0.03125$, and the segregation constant of the alloys is $k = 0.9$. The phase-field growth rate has been evaluated at times $t = 0, 0.3125, 1.5625, 9.375, 15.625$ and 21.875.

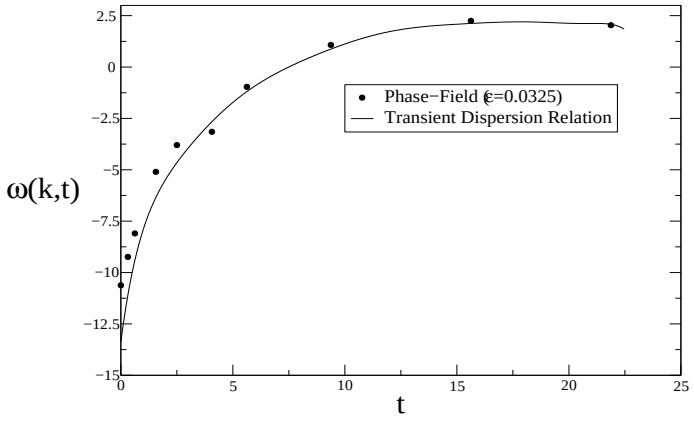

Figure 7.11: Time evolution of the growth rate of the wavelength $\tilde{k}\tilde{l} = 10.053$ during the initial transient. The system is a generic one-sided alloy, and the simulation parameters are $\tilde{l}_T/\tilde{l} = 3.125$ and $\varepsilon = 0.03125$, and the segregation constant of the alloys is $k = 0.5$. The phase-field growth rate has been calculated at times $t = 0, 0.3125, 0.625, 1.5625, 2.5, 4.0625, 5.625, 9.375, 15.675$ and 21.875.

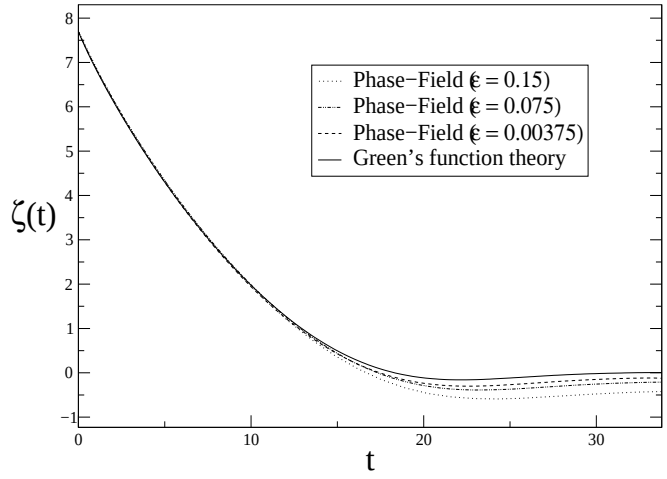

Figure 7.12: Sharp-interface convergence of the symmetric phase-field simulations of the front position for the 8CB liquid crystal. The simulations have been performed with the symmetric,normal gap model, and the parameters are described in Sec. 7.3.2.

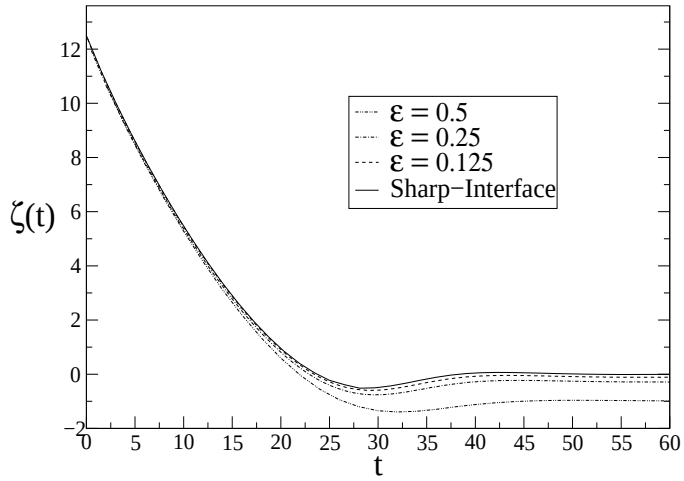

Figure 7.13: Convergence to the sharp-interface of the transient front position for the symmetric phase-field model with the constant miscibility gap approximation. The system parameters and simulation values are described in Sec. 7.4.2.

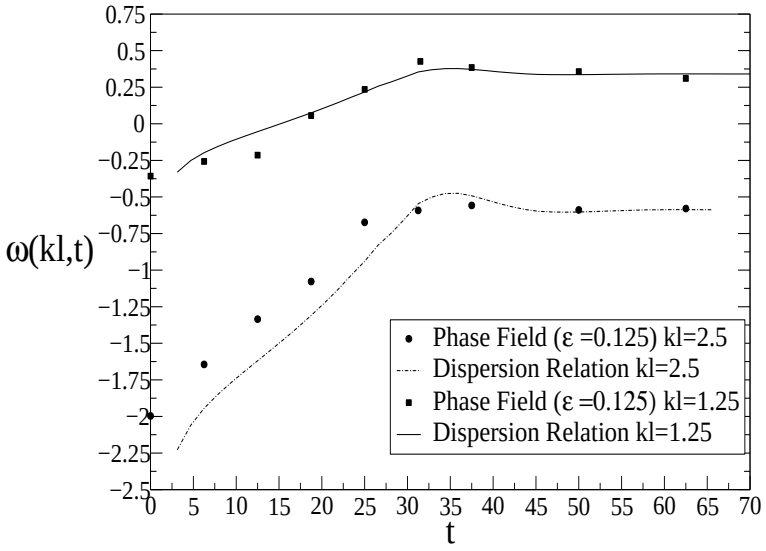

Figure 7.14: Time evolution of the growth rate of the wavelengths $\tilde{kl} = 2.5$ and $\tilde{kl} = 1.25$ in the symmetric model with constant miscibility gap.

Chapter 8

Stochastic phase-field simulations of the wavelength selection during transient stages

8.1 Introduction

In the last chapter, we have shown that phase-field models provide a quantitative description of the solidification process during early transient stages. It is specially important that the phase-field dynamics recovers quantitatively the sharp-interface transient behavior, accounting for the correct non-steady growth rate for the morphological deformations of the interface. On the other hand, a quantitative method to include fluctuations in non-variational phase-field formulations has been introduced in Chapter 6, which allows to perform simulations with the proper thermodynamical fluctuations of the system.

The aim of the present chapter is to study the transient dynamics of the solidification front in the presence of the correct thermodynamical fluctuations of the system. As we have already seen, under certain conditions, the interface becomes morphologically unstable under perturbations of a given wavelength, giving rise to complex cellular or dendritic structures. Several experimental results indicate that the selected final state depends on this loose of stability that happens during early transient stages while the concentration boundary layer builds up. This morphological destabilization process can be divided into four well defined stages: 1) At the beginning of the solidification process, the planar interface is stable under the microscopical perturbations produced by the internal thermodynamical fluctuations of the system. 2) At a certain time, which we shall refer as the *instability*

time, the growth rate of a certain wavelength becomes positive and the system becomes unstable under perturbations of this type. Therefore, the internal noise acts as an initiation mechanism for the morphological destabilization of the interface. The instability time can be precisely determined by following the time evolution of the interfacial spectrum. 3) After the instability time, the amplitude of the unstable modes growth linearly with time. During this linear amplification regime, the deformations are amplified by several orders of magnitude from the initial microscopic perturbations, and all the Fourier modes growth independently. 4) The linear regime finishes when the amplitude of one of these modes become comparable with its own wavelength. At this time, known as the *crossover time* $\tilde{t}_0$, the interface deformations are typically of the order of few microns and can be observable with the help of a microscope. After this moment, the front begins a coarsening process which dynamically selects the final steady cellular or dendritic structure.

The three first stages happen at early times of the solidification process, and in most cases the solute concentration profiles are not well developed. During the linear regime, the front dynamics can be studied from a theoretical framework. As we have studied in Section 4.2, Warren and Langer were the first in studying analytically this linear noise amplification process. The first section of this chapter Sec. 8.2 is devoted to compare the phase-field transient interfacial power spectrum and compare it with the theoretical predictions of the Warren and Langer's theory.

After the crossover time, the evolution of the front becomes non-linear, and the morphological modes begin to interact one to each other. This regime is studied by means of phase-field simulations in Section 8.3 of this chapter. In the non-linear regime, the mode interactions become complex and the dynamics of the whole system selects dynamically different values of the interfacial wavelength. During this regime, the system presents a coarsening process between the initial wavelength λ_0 at the crossover time t_0 and the final wavelength of the pattern λ_1. This crossover is studied for two different systems in Section 8.3.

As we will see, depending on the growth conditions and the thermophysical properties of the system, the final steady pattern might be a cellular or a dendritic structure with a definite wavelength λ_1. The first difference between cells and dendrites is perhaps that dendrites present secondary instabilities in the form of sidebranches, whereas cell solutions are similar to the Saffmann-Taylor fingers observed in a Hele-Shaw cell. Dendrites, moreover, have a well-defined tip radius which is selected by means of the microscopic solvability theory introduced in Section 1.2.1. The aim of Section 1.2.1 is to compare the results of phase-field numerical experiments with real experimental data and theoretical predictions of different aspects during the non-linear regime. In particular, we will study the coarsening process of the cellular or array pattern from the crossover time t_0 to the steady state of the system at which a well defined wavelength λ_1 is selected. This process has been studied experimentally in a quantitative way by some authors [Trivedi84, Somboonsuk85, Trivedi85, Somboonsuk84, Eshelman88c, Huang93, Han94b, Rios97, Losert98b, Ding96, Kauerauf01b, Kauerauf01a], and

some of the experimental findings are compared with the numerical results obtained from the phase-field model, as well as with recent theoretical descriptions of the problem [Kurz81, Warren90, Ding97, Lu92, Hunt96, Losert96].

8.2 Noise amplification during the initial recoil transient: The linear regime

8.2.1 Introduction

We next investigate the amplification of the fluctuations during the initial redistribution transient. It is well known that the final properties of the pattern are determined while the initial redistribution transient is still building the solute boundary layer. The simulations are compared with theoretical predictions based on the Warren and Langer's work on noise amplification [Warren93]. In that theoretical work, the time evolution of the interface correlations is described by a transient power spectrum function

$$S(k,t) = S_0(k) \int_{-\infty}^{t} dt' \exp\left\{ 2 \int_{t'}^{t} \omega(k,t) dt' \right\}, \tag{8.1}$$

where $\omega(k,t)$ is the transient growth rate of the different Fourier modes present in the system (cf. Sec. 4.2.1), and $S_0(k)$ is a physical pre-factor given by

$$S_0(k) = \frac{|\omega^e| K_B T_M^2}{LG(1 + d_0^c \, l_T \, k^2)}, \tag{8.2}$$

being $\omega^e = \omega(k, t = \infty)$ the amplification rate at $t \to \infty$ or stationary dispersion relation Eq. 4.113 derived in Section 4.2.1.

8.2.2 One-sided model

We first consider the parameters of the organic alloy CBr_4-C_2Cl_6. The experimental values for the simulations are given by $\tilde{v}_p = 10^{-3}$ m/s, $\tilde{G} = 5.6 \times 10^3$ K/m and $c_\infty = 0.03$ mol, and the relevant parameters for the simulations are $\hat{\tilde{d}}_0 = 1.45 \times 10^{-7}$ m and $\tilde{l}_T = 10^{-4}$ m. The value of the interface mobility is $\tilde{\mu} = 0.1503$ m/ K s ($\hat{\beta} = 1.18 \times 10^{-4}$). The diffusion length is $\tilde{l} = \tilde{D}_L/\tilde{v}_p = 5 \times 10^{-7}$ m and the diffusion time $\tilde{\gamma} = \tilde{D}_L/\tilde{v}_p^2 = 5 \times 10^{-4} s$, so the dimensionless control parameters are $l_T = \tilde{l}_T/\tilde{l} = 200$ and $\hat{d}_0 = \hat{\tilde{d}}_0/\tilde{l} = 0.29$. The interface thickness is $\varepsilon = \tilde{W}/\tilde{l} = 0.005$ ($\tilde{W}/\hat{\tilde{d}}_0 = 1.724$). The equations have been discretized in a $N_z \times N_y = 128 \times 512$ rectangular lattice with a dimensionless grid size of $\Delta y = \Delta\tilde{y}/\tilde{l} = 0.4$ and $\Delta z = \Delta\tilde{z}/\tilde{l} = 0.4$ ($\Delta\tilde{z}/\tilde{W} = 0.8$), and a time step $\Delta t = \Delta\tilde{t}/\tilde{\gamma} = 0.032$. Figure 8.1 shows the amplification of the interfacial fluctuation spectrum at six different physical times during the initial transient ($\tilde{t}$= 0, 0.01866, 0.03433, 0.05, 0.0912,

0.1059 and 0.12 s). The dashed lines represent the power spectrum at these times obtained from the phase-field simulations, whereas the solid lines correspond to the theoretical prediction described in Section 4.2.2 at the same times. The phase-field power spectrum is noisy because the curves are direct spectral properties of the fluctuating interface at each time and no average or filtering has been used. The results shown in Fig. 8.1 present a rather good quantitative agreement between the theoretical predictions and the phase-field simulations. For clarity reasons, the inset graph depicts the enlarged amplification region of the spectrum. At $\tilde{t} = 0$, the stationary power spectrum is given by the theoretically predicted power spectrum of a stationary planar interface, given by Eq. 8.2. As time evolves, some of the modes are located in the range of wavenumbers $\tilde{k} \in [0.5, 1]$ μm^{-1}. These perturbations correspond to morphological deformations in the front of wavelengths in the range $\tilde{\lambda} \in [3.14, 6.28]$ μm.

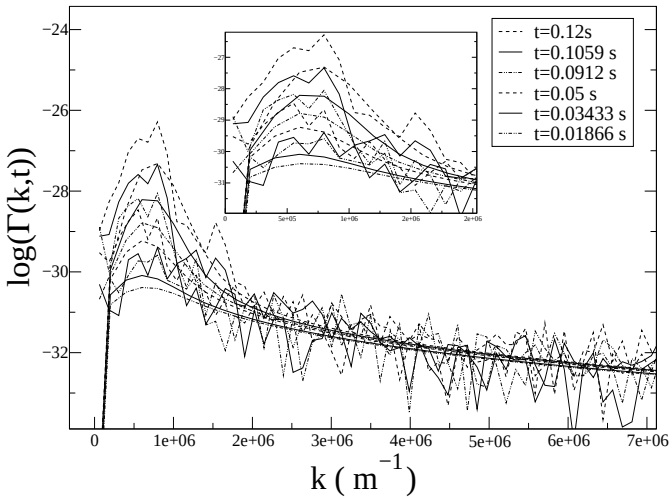

Figure 8.1: Amplification of the initial noise and selection of a preferred wavelength during the transient.

8.2.3 Symmetric model with normal gap

In this section we use the parameters corresponding to the commercial 8CB liquid crystal. The simulations have been carried out by using the symmetric phase-field model with the correct miscibility gap. The experimental values taken for the sim-

ulations are given by $\tilde{v}_p = 6 \times 10^{-5}$ m/s, $\tilde{G} = 2.3 \times 10^3$ K/m and $c_\infty = 0.012$ mol. The relevant parameters for the simulations are then $\hat{\tilde{d}}_0 = 2.696 \times 10^{-7}$ m and $\tilde{l}_T = 5.128 \times 10^{-5}$ m. The interface mobility is given by $\tilde{\mu} = 1.51$ m/ K s, and the values of the diffusion length and diffusion time are $\tilde{l} = \tilde{D}_L/\tilde{v}_p = 4 \times 10^{-6}$ m and $\tilde{\gamma} = \tilde{D}_L/\tilde{v}_p^2 = 0.04s$ respectively. The model parameters correspond to $\tilde{l}_T/\tilde{l} = 12.82$, $\hat{\tilde{d}}_0/\tilde{l} = 0.0674$, and the computational parameters are $\varepsilon = \tilde{W}/\tilde{l} = 0.25$ ($\tilde{W}/\hat{\tilde{d}}_0 = 3.709$). The equations have been simulated in a 500×256 rectangular lattice with a dimensionless grid size $\Delta y = \Delta\tilde{y}/\tilde{l} = \Delta z = \Delta\tilde{z}/\tilde{l} = 0.15$. The dimensionless time-step is $\Delta t = \Delta\tilde{t}/\tilde{\gamma} = 3.75 \times 10^{-3}$. Figure 8.2 shows the amplification of the interfacial fluctuation spectrum at three different physical times during the initial transient ($\tilde{t}$= 0, 1.8 s and 2.7 s). Dashed lines are obtained by integrating $S(k,t)$ in the adiabatic regime $\omega \ll k^2$. As it can be observed, quantitative agreement is achieved between theory and simulations in the early time amplification of fluctuations as well as in the wavelength selection of the cellular pattern. After

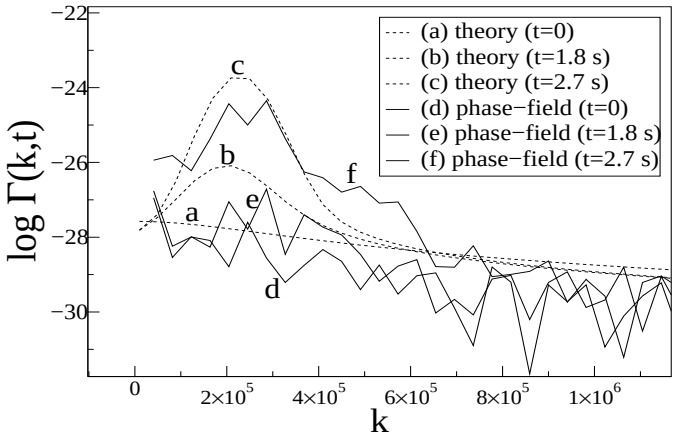

Figure 8.2: Amplification of the initial noise and selection of a preferred wavelength during the transient in the symmetric model and for the parameters of the 8CB liquid crystal.

the early stages where the growth of fluctuations is linear, the system enters in a non-linear regime and a cellular pattern with a certain wavelength sets in the system. The change from linear to non-linear evolution can be observed in Figure 8.3 where the interface presents a morphological destabilization which gives rise to the apparition of a cellular pattern. The end of the linear regime can be defined as the time at which the amplitude of the most unstable Fourier mode is compa-

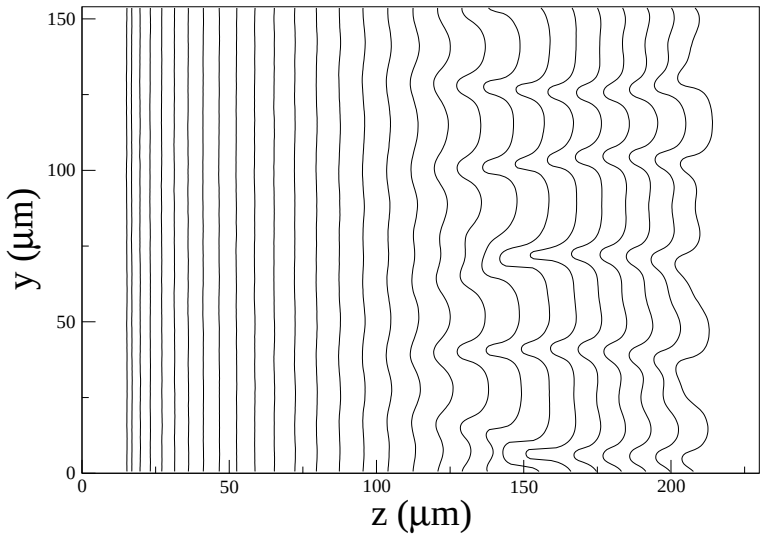

Figure 8.3: Morphological destabilization of the interface by the amplification of the initial thermodynamical fluctuations. After the linear regime, a cell-like pattern sets up and evolves towards a dendritic regime.

rable with its wavelength. This condition defines a crossover time t_0 which can be theoretically determined by the condition

$$< \delta z^2(t_0) >^{1/2} \sim \tilde{\lambda}_{max}, \tag{8.3}$$

where

$$< \delta z^2(t) > = \int \frac{d^2k}{(2\pi)^2} S(k,t) \tag{8.4}$$

is the mean-square fluctuation amplitude and λ_{max} is the wavelength of the largest spectral mode in the system. Figure 8.4 shows the time evolution of these two magnitudes in our system, and the intersection between the two curves determines the crossover time $\tilde{t}_0$ in physical units.

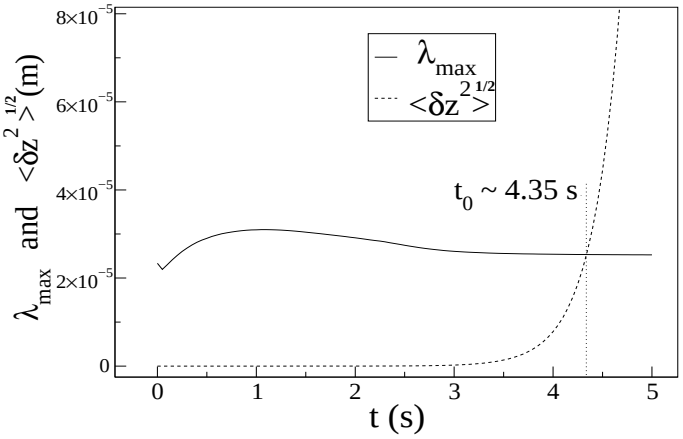

Figure 8.4: Determination of the crossover time at which the amplitude of the most unstable mode becomes of the order of its wavelength.

8.3 Primary spacing selection of the dendritic array: The non-linear regime

8.3.1 Introduction

The next two subsections present the simulation results of the non-linear front evolution for two distinct solidification systems. The first one is a CBr_4-based alloy (we have considered CBr_4-C_2Cl_6, but the solute might also be taken to be Br_2 as in Ref.[deCheveigné86]), which has extensively been studied experimentally in Refs. [deCheveigné86, Faivre92, Akamatsu97, Akamatsu98]. The thermophysical properties of this substance are listed in Appendix A, and can be found in the previously commented references. The second substance is the succinonitrile-acetone mixture (SCN-ACE), which has also been used to perform quantitative experimental studies of the cellular and dendritic coarsening structures directional solidification [Somboonsuk84, Eshelman88a, Eshelman87, Eshelman88c, Seetharaman88].

Our purpose is to perform realistic phase-field simulations of these two solidification systems and compare the results with the previous experimental observations in the literature. Besides the standard computational problems concerning phase-field simulations (convergence to the sharp-interface, system size, numerical discretization, allowed range of wavelengths, proper introduction of noise, etc.), the main difficulty in this set of simulations is the same that the one reported by the experimentalists: When decreasing the pulling velocities, the response times

of these solidification systems become very long. This response time τ_r can be defined as the time necessary to reach a well defined concentration profile and a established morphological structure. Ignoring thermal effects, this time can be estimated in directional solidification as $\tau_r \sim D_L/k\tilde{v}_p^2$ [Tiller53], which in the case of the CBr_4 alloy predicts a response time of $\tau_r = 11.1$ min. for a pulling velocity of $\tilde{v}_p = 10^{-6}$ m/s and $\tau_r = 6.6$ s for $\tilde{v}_p = 10^{-5}$ m/s. It turns then clear that considering situations at low pulling speeds requires numerical experiments with very large simulation times.

The numerical experiments reported in this section start with an equilibrium solid-liquid interface with $c_S^0 = kc_\infty$ and $c_L^0 = c_\infty$ located at $\tilde{z} = \tilde{l}_T$. At $\tilde{t} = 0$, sample is pulled along the gradient at the pulling velocity $\tilde{v}_p$, and the initial recoil transient begins. Once that the system has reached the crossover time, the evolution of the morphological perturbations becomes non-linear. This opens a dynamic coarsening process where the system modifies its wavelength by means of a process of creation and annihilation of cells. In our simulations, we will focus in the determination of the crossover time and in the evolution of the cellular spacing during the non-linear coarsening process.

8.3.2 Numerical experiments with the CBr_4-C_2Cl_6 alloy

In the CBr_4-C_2Cl_6 mixture, the numerical experiments have been carried out for $c_\infty = 0.08$ mol and $\tilde{G} = 11 \times 10^3$ K/m, the same values used in reference [Akamatsu98]. We have carried out simulations for two values of the pulling velocity $\tilde{v}_p = 10^{-5}$ m/s and $\tilde{v}_p = 3.1 \times 10^{-5}$ m/s above the critical value which is located at $\tilde{v}_p^c = 2.8 \times 10^{-6}$ m/s. Although anisotropy in the attachment kinetics might be relevant for this substance, in this set of simulations we have considered an isotropic kinetic mobility of $\tilde{\mu} = 2 \times 10^{-4}$ m/K s. Surface energy has been also taken to be isotropic. The physical interface thickness in these phase-field simulations is $\tilde{W} = 1.5 \times 10^{-6}$ m (1.5 μm), and the equations have been simulated in a 2000×512 rectangular lattice with a physical grid size of $\Delta\tilde{y} = \Delta\tilde{z} = 1.2 \times 10^{-6}$ m (1.2 μm), being the ratio $\Delta z/\varepsilon = 0.8$. Each simulation step corresponds to a physical time of $\Delta\tilde{t} = 4.5 \times 10^{-4}$ s. We have implemented periodic boundary conditions for all the fields in the y direction and non-flux conditions at the two z boundaries of the system.

Simulations for $\tilde{v}_p = 10^{-5}$ m/s:

The simulations shown in the figures Figs. 8.5, 8.6 and 8.7 correspond to a pulling velocity of $\tilde{v}_p = 10^{-5}$ m/s. In this case, the dimensionless thermal length is given by $l_T = \tilde{l}_T/\tilde{l} = 3.86$, and the dimensionless interface thickness is $\varepsilon = \tilde{W}/\tilde{l} = 0.03$. The dimensionless grid size $\Delta y = \Delta\tilde{y}/\tilde{l} = \Delta z = \Delta\tilde{z}/\tilde{l} = 0.024$, and the dimensionless time-step is $\Delta t = \Delta\tilde{t}/\tilde{\gamma} = 9 \times 10^{-5}$.

Figure 8.5 shows snapshots of the front shape taken each 1.8 seconds, and it can be appreciated how the number of cells in the system (and therefore its

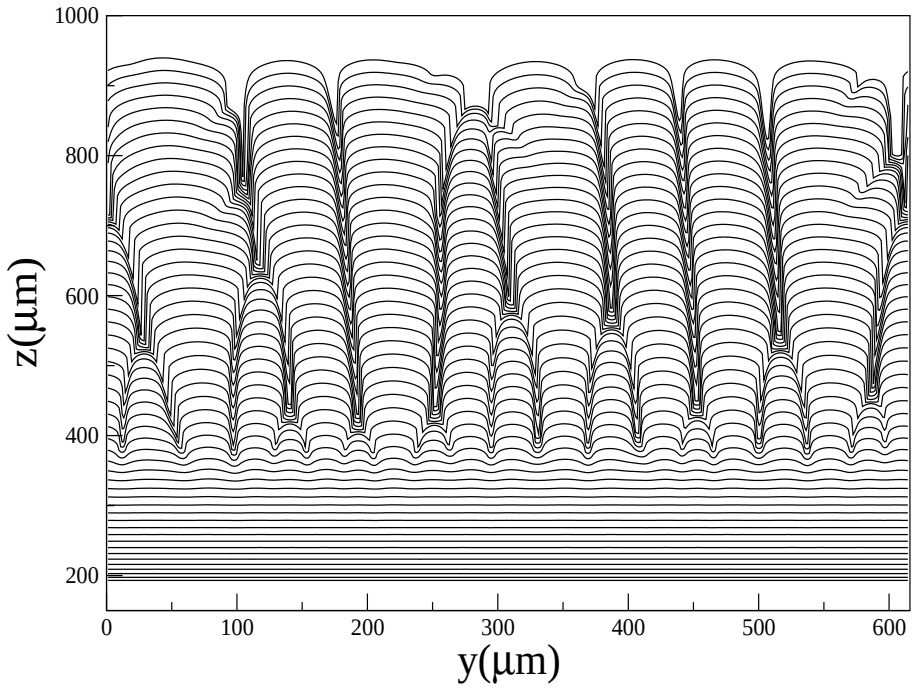

Figure 8.5: The curves show snapshots of the solid-liquid interface taken each 1.8 s for the CBr_4-C_2Cl_6 system at $\tilde{v}_p = 10^{-5}$ m/s. The interface is initially located at $\tilde{z}_0 = \tilde{l}_t = 1.939 \times 10^{-4}$ m, and the final profile corresponds to the front at $\tilde{l}_T$=90 s.

primary wavelength) changes dynamically as the cellular front advances. At the crossover time, which is now located around $\tilde{t}_0 = 30$ s, the front destabilizes and the system adopts a small wavelength shape with wavelength $\tilde{\lambda}_0 \sim 30$ μm. This can be observed in the upper graph in Figure 8.6, which represents the time evolution of the most relevant Fourier modes in the system (i.e, those with the larger amplitudes during the coarsening process).

The lower graph in Fig. 8.6 shows the evolution of the wavelength of the most important Fourier mode in the system, i.e, the one which has the largest amplitude at each time. This primary wavelength determines the spacing of the different cellular shapes at different moments of the dynamical coarsening process. As it can be appreciated in Fig. 8.6, at $\tilde{t} = 35$ s the system has passed the crossover time and the mode with a largest amplitude corresponds to a wavelength $\tilde{\lambda} = 34.13$ μm. Few seconds later, this mode vanishes and the mode $\tilde{\lambda} = 43.85$ μm determines the main cellular spacing of the system. This change of stability can be seen in the two

lower curves of Figure 8.7, which represents the shape of the system at two times $\tilde{t} = 33.75$ s and $\tilde{t} = 42.35$ s before and after the change of spacing, respectively. Note that the amplitude of this second mode becomes about twice larger than the largest amplitude of the first mode. At $\tilde{t} = 42.35$ s, the shape of the front clearly shows the non-linear nature of the growth dynamics.

At later times, some of the cells are annihilated producing an increase of the primary wavelength, and a mode with wavelength $\tilde{\lambda} = 68.26$ μm sets up in the system. At the last stages, there is a competition between this mode and the mode $\tilde{\lambda} = 102.4$ μm, which can be interpreted as a period-doubling instability which happens by means of the annihilation of one of every two cells in the system (see Fig. 8.5). This period-doubling mechanism, which was theoretically predicted in [Warren90, Warren93] and observed experimentally in Ref. [Losert96], has been observed in our numerical experiments as the main spacing adjustment mechanism in the selection dynamics.

At the end of the simulation, the primary wavelength of the pattern was $\tilde{\lambda}_1 = 104.2$ μm, which is in qualitative agreement with the experiments carried out by Faivre and Akamatsu in reference Ref. [Akamatsu98] in which the final wavelength was $\tilde{\lambda}_1^{exp} \sim 80$ μm. This spacing, however, might be reduced at later stages as a consequence of the tip splitting in the system. Whereas cell elimination increases the wavelength of the pattern, tip-splitting is the mechanism by which the cellular front decreases its spacing. This phenomena can be observed in the upper curves of Fig. 8.5, where some of the cells present an instability which divides the cell in two parts. Tip splitting and cell elimination were first reported as space adjusting mechanisms by Jackson and Hunt [Jackson65] and observed experimentally by Eshelman *et al.* in Refs. [Eshelman88a, Eshelman88b].

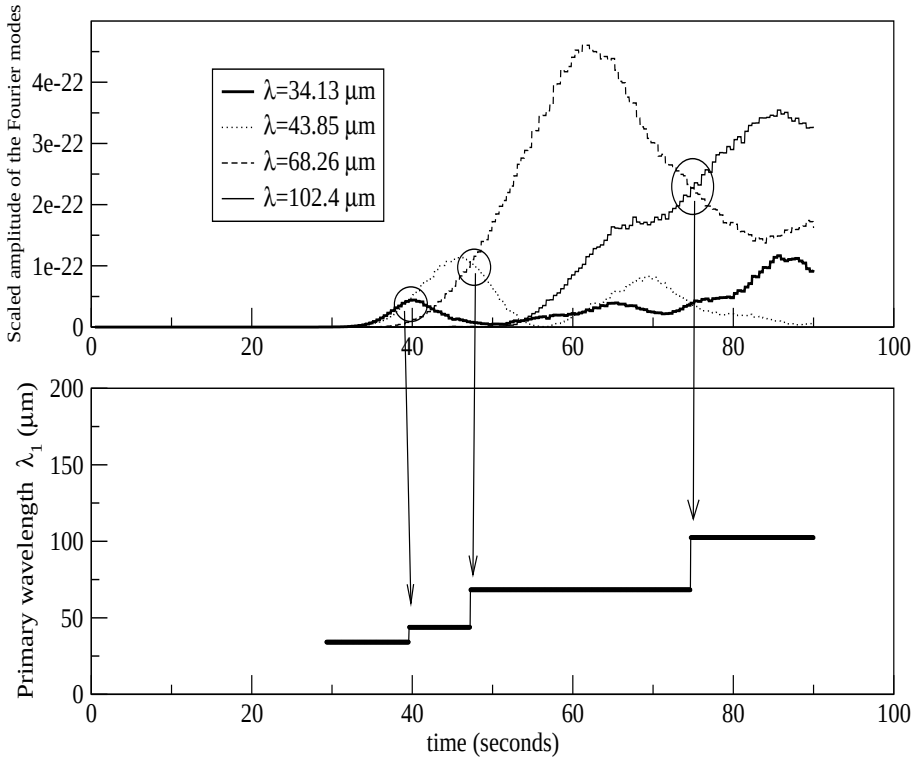

Figure 8.6: Time evolution of the primary interdendritic mode (CBr_4-C_2Cl_6, $\tilde{v}_p = 10^{-5}$ m/s). After the crossover time, the system evolves by means of process of creation and annihilation of cells. The time evolution of the most relevant Fourier modes is depicted in the upper graph. As can be seen, the main primary spacing of the system changes suddenly at different times.

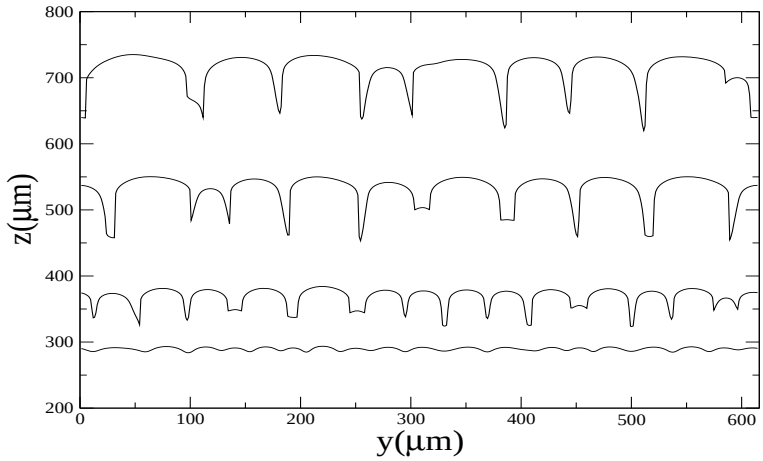

Figure 8.7: Interface shapes at four different times $\tilde{t}$=33.75, 42.75, 58.5 and 76.5 seconds, corresponding to the three different primary wavelengths selected during the coarsening described in Fig. 8.6. The curves correspond here to the CBr_4-C_2Cl_6 system at a pulling velocity $\tilde{v}_p = 10^{-5}$ m/s.

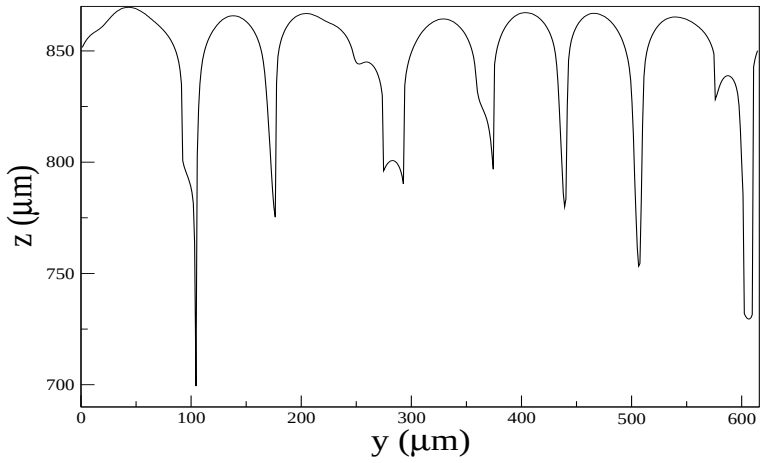

Figure 8.8: Shape at the end of the simulation of the CBr_4-C_2Cl_6 system with $\tilde{v}_p = 10^{-5}$ m/s.

Simulations for $\tilde{v}_p = 3.1 \times 10^{-5}$ m/s:

The figures Figs. 8.9 and 8.10 represent simulations for a larger pulling velocity $v_p = 3.1 \times 10^{-5}$ m/s. In this case, the dimensionless thermal length is given by $l_T = \tilde{l}_T/\tilde{l} = 12.06$, and the dimensionless interface thickness is $\varepsilon = \tilde{W}/\tilde{l} = 0.093$. The scaled grid size $\Delta y = \Delta\tilde{y}/\tilde{l} = \Delta z = \Delta\tilde{z}/\tilde{l} = 0.075$, and the scaled time-step is $\Delta t = \Delta\tilde{t}/\tilde{\gamma} = 3.75 \times 10^{-3}$.

The front evolution is shown in Figure 8.9, where the x and y axis have been scaled differently in order to see the complete advance of the front. We can see how the initial instability develops and gives rise to a well defined periodic pattern. After an initial transient of about 20 seconds, the system selects a fixed spacing of $\tilde{\lambda}_1 = 87.77$ μm. The primary wavelength dynamics is represented in Figure 8.10. The saturation of all the important spectral modes indicates that the system has already reached the steady state cellular structure. The final shape of the front can be better appreciated in Figure 8.11 and consists in a regular cellular structure with cells of about 30 μm deep.

The experimental results reported in Ref. [Akamatsu98] present an intercellular spacing of $\tilde{\lambda}_1^{exp} \sim 50$ μm, which is slightly smaller than the one obtained by our numerical experiments. We think that this difference might be due to the presence of anisotropic effects in the attachment kinetics, which has not been considered in the present simulations.

It is interesting to note that the steady cellular structure obtained in this experiment presents a traveling wave which crosses the pattern in the transversal direction of the advancing front. This can be appreciated in Fig. 8.9, which presents a clear phase shift in the cells which evolves from right to left in the system as the solidification front advances. A more systematic study of these kind of traveling modes is needed in order to understand the basic mechanisms determining their apparition.

Additionally, we have included in Fig. 8.12 the solute concentration profiles along the z direction corresponding to a longitudinal cut at half of the system size in the y direction. The curves have been taken at intervals of 0.9 s, and show the perturbations in the concentration due to the apparition of the cellular structure. We observe that the concentration at the front position decreases as a consequence of the increment of the mean position of the interface.

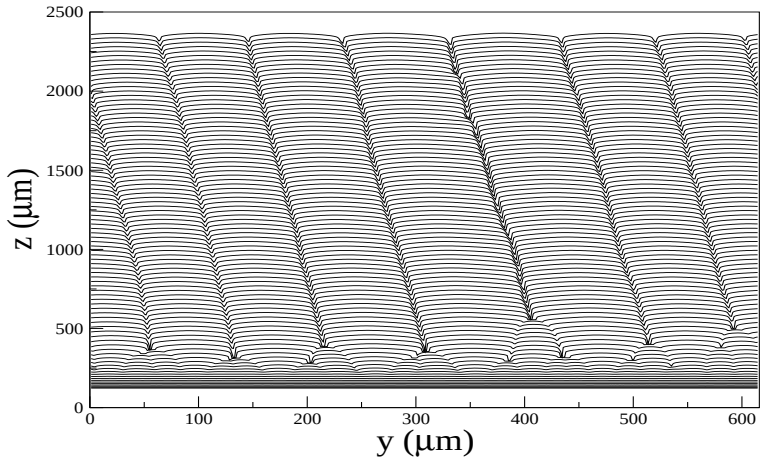

Figure 8.9: Interface shapes of the CBr_4-C_2Cl_6 system at $v_p = 3.1 \times 10^{-5}$ m/s taken each 0.9 seconds. Note that in order to see the time evolution of the front the distances along the z and y directions are not proportional.

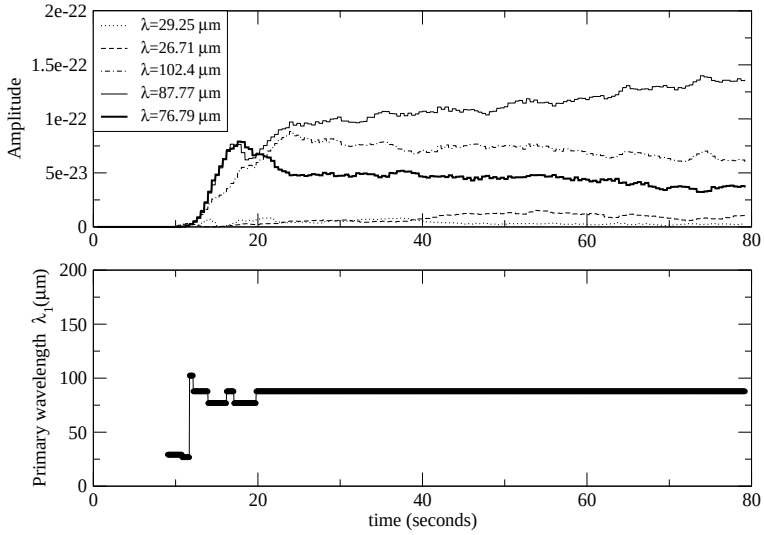

Figure 8.10: Time evolution of the most relevant Fourier modes (upper graph) and of the primary selected wavelength during the coarsening of the cellular structure (lower graph). The system is here CBr_4-C_2Cl_6 at $\tilde{v}_p = 3.1 \times 10^{-5}$ m/s.

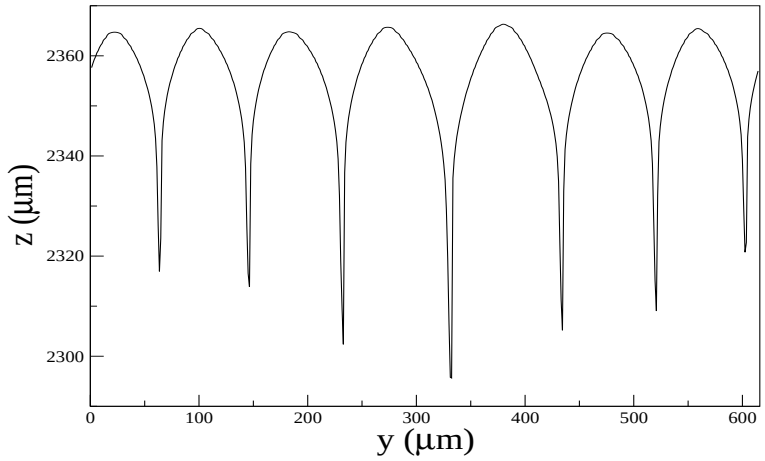

Figure 8.11: Final shape of the cellular structure in the CBr_4-C_2Cl_6 system at $\tilde{v}_p = 3.1 \times 10^{-5}$ m/s. The amplitude of the cells can be here appreciated better than in Fig. 8.9.

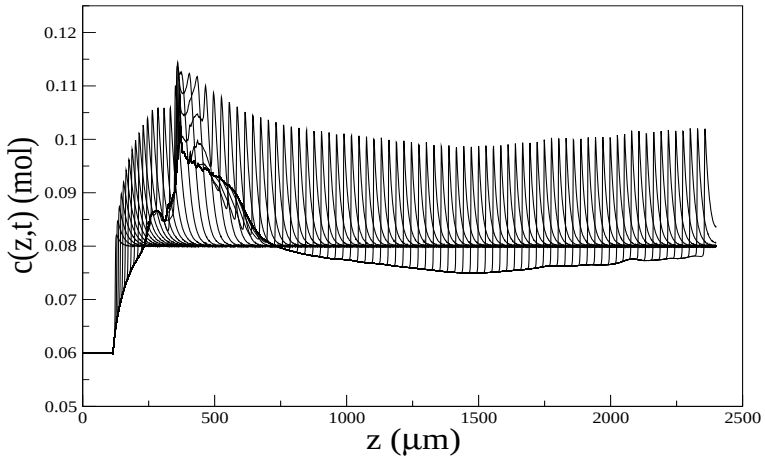

Figure 8.12: Solute concentration profiles during the coarsening process of the CBr_4-C_2Cl_6 system at $\tilde{v}_p = 3.1 \times 10^{-5}$ m/s. The snapshots are taken at intervals of 0.9 s.

8.3.3 Numerical experiments with the SCN-ACE alloy

In the SCN-ACE system, the numerical experiments have been carried out for $c_\infty = 0.055$ mol, $\tilde{G} = 6.7 \times 10^3$ K/m, the same values used in reference [Somboonsuk84]. These experiments were used as a benchmark of the Warren-Langer theory [Trivedi85, Somboonsuk84, Somboonsuk85]. We have also carried out simulations for two values of the pulling velocity $\tilde{v}_p = 6.510^{-5}$ m/s and $\tilde{v}_p = 10^{-4}$ m/s above the critical value which is located at $\tilde{v}_p^c \sim 10^{-7}$ m/s. A four-fold anisotropy $\tilde{\sigma}(\mathbf{n}) = \tilde{\sigma}(1+\delta\cos(4\theta))$ with $\delta = 0.05$ has been considered for the surface energy of the system. The kinetic mobility is assumed to be isotropic and has a value of of $\tilde{\mu} = 0.01$ m/K s. The physical interface thickness in these simulations is $\tilde{W} = 10^{-6}$ m (1 μm), and the equations have been simulated in a 2000×512 rectangular lattice with a physical grid size of $\Delta\tilde{y} = \Delta\tilde{z} = 0.8 \times 10^{-6}$ m (0.8 μm), being the ratio $\Delta z/\varepsilon = 0.8$. Each simulation step corresponds to a physical time of $\Delta\tilde{t} = 7.87 \times 10^{-5}$ s. We have also implemented periodic boundary conditions for all the fields in the y direction and non-flux conditions at the two z boundaries of the system.

Simulations for $\tilde{v}_p = 6.5 \times 10^{-5}$ m/s:

At this velocity, we observe that the front shape presents three clearly different spacings during the coarsening (see Fig. 8.13). At early stages, the front selects a wavelength $\tilde{\lambda} \sim 40$ μm, which stays in the system for about 40 seconds. After this time one of each two cells grows faster overtaking the intermediate cells, and the system presents a kind of period-doubling instability resulting in a wavelength jump from $\tilde{\lambda} \sim 40$ μm to $\tilde{\lambda} \sim 100$ μm. A final spacing adjustment is produced by the annihilation of an additional intermediate cell, and the system has a definite wavelength $\tilde{\lambda}_1 \sim 136$ μm at the end of the simulation. This value presents a rather good agreement with the wavelength predicted by the Somboonsuk experiments [Eshelman88a], which is $\tilde{\lambda}_1^{exp} = 125$ μm.

As we can see in Figure 8.14, the spacing presents three well-defined plateau corresponding to the three basic modes appearing in the system. In the upper graph of Fig. 8.14, we see how the amplitude of the final mode grows and the others decrease.

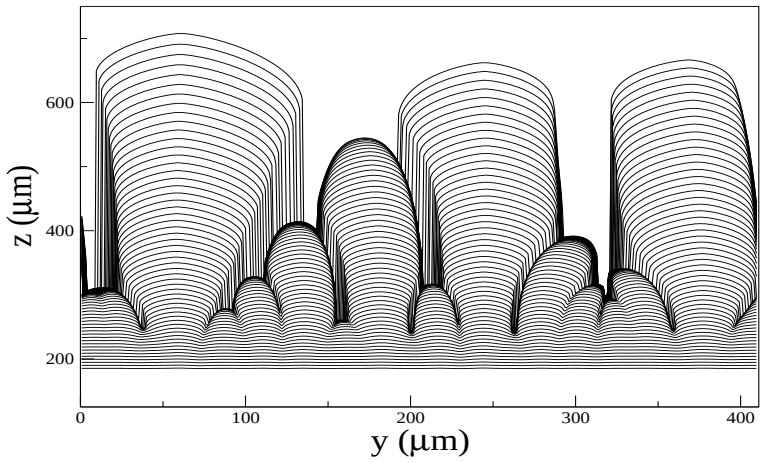

Figure 8.13: Interface shapes of the SCN system at $v_p = 6.5 \times 10^{-5}$ m/s experiment taken each 0.78 seconds.

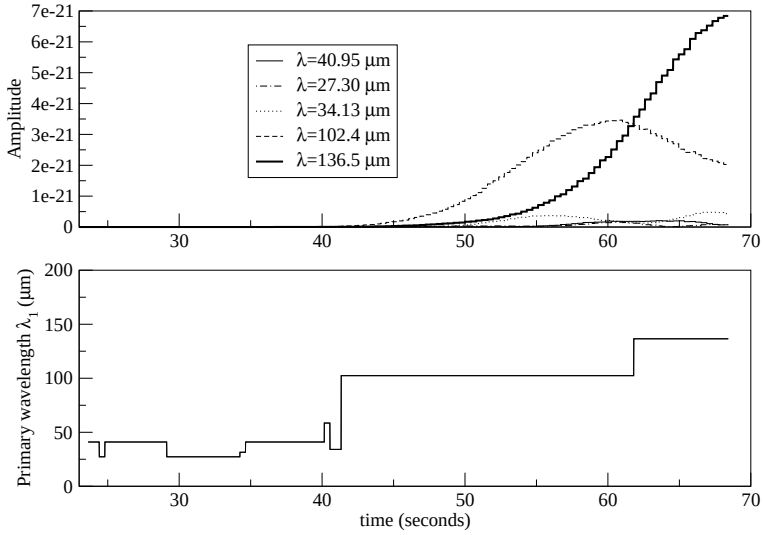

Figure 8.14: Time evolution of the most relevant Fourier modes (upper graph) and primary selected wavelength during the coarsening of the cellular structure (lower graph). The curves correspond to the SCN system with a pulling velocity of $\tilde{v}_p = 6.5 \times 10^{-5} m/s$.

Simulations for $\tilde{v}_p = 10^{-4}$ m/s:

In this last case, the evolution of the front is represented in Figure 8.15, and the final state presents a well defined mode with two single cells in the system. A very interesting feature of this coarsening process is that the spacing of the system uniquely evolves by means of period-doubling instabilities. This is clearly shown in the lower graph of Figure 8.16, in which we observe three plateau corresponding to three wavelengths $\tilde{\lambda} = 51.2$ μm, $\tilde{\lambda} = 102.4$ μm and $\tilde{\lambda} = 204.8$ μm. This sequence of two period-doubling jumps turns to be a very effective mechanism to increase the cellular spacing of the system.

However, the wavelength predicted by the Somboonsuk experiments [Eshelman88a] under the same conditions is $\tilde{\lambda}_1^{exp} = 96.8$ μm, which differs in a factor of 2 from our final wavelength $\tilde{\lambda}_1 = 204.8$ μm.

Although at the end of the simulation the final steady state of the system was not yet reached, we think that it would be difficult to observe a change in the final wavelength by increasing the computational time of the numerical experiment. This could happen by means of a tip-splitting instability, which does not seem to be the case here. In order to study the reasons of this mismatch, one would need larger grids in the y direction so that the final state has more cells. This would allow for a more precise determination of the wavelength based in a combined study of statistical cell counting and spectral analysis.

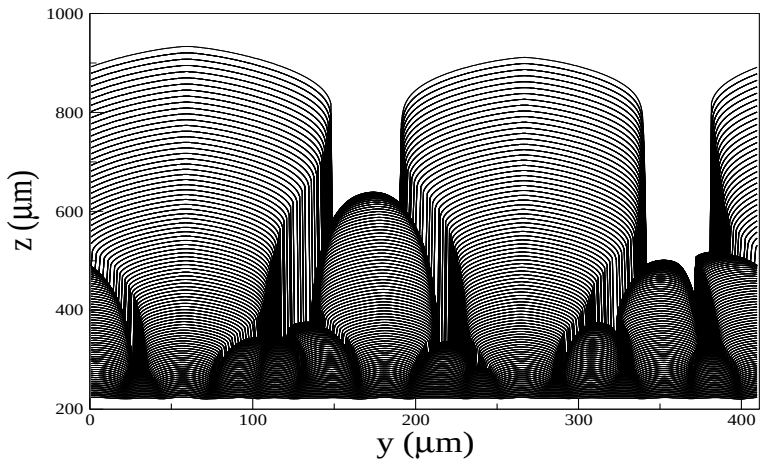

Figure 8.15: Interface shapes of the SCN system at $v_p = 10^{-4}$ m/s experiment taken each 0.078 seconds.

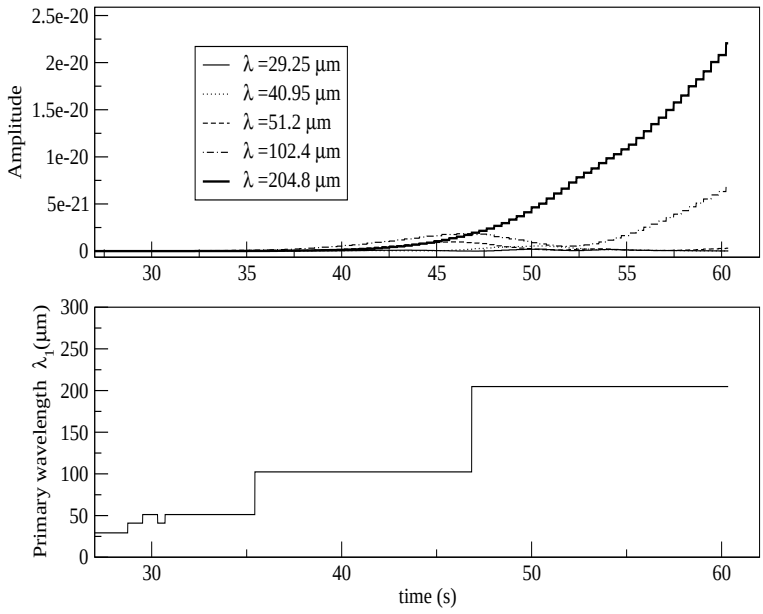

Figure 8.16: Time evolution of the most relevant Fourier modes (upper graph) and primary selected wavelength during the coarsening of the cellular structure (lower graph). The curves correspond to the SCN system with a pulling velocity of $\tilde{v}_p = 10^{-4} m/s$.

8.4 Discussion

The main aim of this chapter has been to use the phase-field approach to quantitatively determine the wavelength selection properties in directional solidification experiments. In particular, we have focused in the transient behavior during initial stages and in the physical fluctuations which are the origin of the initial morphological instabilities.

A good quantitative agreement has been found in the determination of the crossover time by means of phase-field simulations. This agreement would not have been possible without a correct introduction of fluctuations in the stochastic formulation of the model. In this sense, we would like to remark here that the results obtained in this chapter provide a sound confirmation of the stochastic sharp-interface procedure described in Section 6.

This analytic approach, in addition with the quantitative phase-field results presented in Section 7, provided the possibility of simulating the coarsening dynamics in directional solidification obtaining a reasonable agreement with previous

experimental works. The whole procedure provide us the tools to start a systematic study of many interesting problems in pattern-formation in solidification. These studies are beyond the scope of this thesis, and will be carried out in the future.

In the spacing selection studies, we observe that the agreement between experiments and simulations is worse for large pulling velocities. This happens for both the SCN and the CBr_4 systems. As kinetic effects become more important as velocity increases, we think that the origin of this mismatch could be due to the assumption of an isotropic kinetic attachment in the system. Indeed, experimental measures of the anisotropy in the kinetic attachment are quite complicated and are reported only for few solidification systems. In our opinion, the incorporation of such effects should give the possibility of performing numerical studies in rapid solidification conditions. In this respect, it would be interesting to investigate a hypothetical change in the attachment kinetics from diffusion-limited to collision-limited regimes (cf. Sec. 2.1.4) in rapid solidification conditions, as well as the subsequent effects in the properties of the selected pattern.

Chapter 9

Conclusions and perspectives

This final chapter means to be a brief summary of the main results obtained in this thesis and the new perspectives which are derived from it. The first section gives a general description of the main conclusions which can be derived from this thesis, as well as a summary of the most relevant results. We next comment the current work in progress, and describe some of the topics and problems which we want to study in the future.

9.1 Conclusions and summary of results

The general conclusion of this thesis is that the phase-field approach provides a quantitative technique to simulate interfacial phenomena in solidification processes, allowing to account for the correct transient stages and the proper statistical fluctuations of the system. Therefore, phase-field models constitute a very convenient approach to simulate the selection dynamics of the morphological instabilities appearing in solidification processes. In addition, they can be used as a quantitative tool in order to predict and control the apparition of microstructures in material processing technologies.

Throughout this thesis, we have focused on the importance of transient and fluctuations in the apparition of morphological instabilities during solidification phenomena. Due to the difficulty of accounting for the correct transient dynamics, several theoretical and numerical approaches in the literature have been based in a steady-state assumption. This approximation states that the front deformations occur when the solute boundary layer is already formed, ignoring the initial recoil transient of the solidification front. Although that might be the case under some particular conditions, the experiments show that the interface becomes morphologically unstable at early transient stages. In order to study that non-steady period, we have tested the validity of the phase-field approach in order to account for the proper transient behavior (Chapter 7). We have performed a quantitative

comparison between the phase-field results and the integration of the non-steady moving boundary equations, finding an excellent agreement. Therefore, we conclude that phase-field method is a feasible approach to investigate transient stages, avoiding the necessity of using front tracking techniques and permitting the study of complex interfacial regimes.

However, considering the correct transient stages is a necessary, but not a sufficient condition to account for the correct morphological evolution of the front. In addition, we must take into account the thermodynamical fluctuations of the system, which are the basic microscopic mechanism by which the interfacial perturbations are initiated. Indeed, fluctuating mass and heat currents are stochastic interfacial forces which act during the evolution of the solidification front. A straightforward incorporation of such noise terms in the phase-field equations is only possible in the particular case of variational formulations. Unfortunately, variational models present a rather poor computational efficiency and do not permit to obtain quantitative results during the initial transient stages. To this extent, we have derived a stochastic sharp-interface projection which prescribes how to introduce the fluctuations in both variational and non-variational phase-field formulations (Chapter 6). In this sense, a major conclusion of this thesis is that the standard asymptotic matching procedure, based in a small interface thickness expansion, must be complemented with a small noise assumption in order to account for the correct stochastic terms in the phase-field equations.

When all these considerations have been included, the phase-field model properly accounts for the correct transients and fluctuations of the system, and can be used to simulate the complete dynamical evolution of the front from the initial transient stages to the final non-linear coarsening dynamics.

From our phase-field simulations of the front destabilization during the transient (Chapter 8), we conclude that the initial front perturbations become observable at very early times during the initial recoil stages, as predicted by the Warren-Langer theory. Numerical experiments on the non-linear coarsening process show that the system presents a dynamical selection mechanism which depends on the previous history of the front. As the selected cellular wavelengths obtained from the simulations are in good agreement with the experimental observations, we finally conclude that the phase-field approach is a powerful technique to carry out quantitative studies on interfacial pattern formation.

The main results of this thesis, which are described in the following subsections, can be divided in computational and analytical results. Both approaches have been complemented during the whole work, in such a way that the final computational findings are a direct consequence of the previous analytical studies of the problem.

Theoretical and analytical results

- The main analytical result concerns to the derivation of a sharp-interface limit of a generic phase-field model with fluctuations and has been described in

detail in Chapter 6. We have proposed an asymptotic procedure which allows to obtain the sharp-interface projection of a generic stochastic phase-field model. This procedure allows to determine the deterministic and stochastic phase-field parameters, and does not rely in the variational character of the model. Moreover, our hybrid asymptotic projection can be used in order to account for noises of both an internal or an external origin, providing the possibility of accounting for noises which might not follow an equilibrium statistics. This work has been submitted for publication [Benítez04c].

- We have derived the complete boundary integral equations describing the front evolution during transient stages. In particular, we have derived such boundary integral equations in the following cases which were not reported in the previous literature:

  i) Symmetric systems in the constant miscibility gap approximation.

  ii) Symmetric systems with normal miscibility gap.

  iii) Incorporation of kinetic attachment effects.

  The derivation and simulation of the resulting integral equations is described in detail in Chapter 4, and have been used as a benchmark of our phase-field simulations during early transient stages.

- We have derived analytical expressions for the transient growth rate (Section 4.2.1). This mathematical expressions determine the front stability during the early transient stages at the beginning of the solidification process.

Computational and modelization results

The second block of results are obtained by means of numerical simulations of the phase-field method. These results are compared with different theoretical and experimental works, and can be divided in three parts:

- The first part is devoted to the study of the quantitative convergence of the phase-field approach to the transient moving boundary dynamics, and is reported in the Chapter 7 of the thesis. To this end, we have performed phase-field simulations in different models and compared the results with theoretical predictions derived from the moving boundary problem. These theoretical predictions have been obtained by formulating and solving numerically the Boundary Integral Problems associated to the different moving boundary equations. In particular, we have focused in the transient position of the solidification front, considering kinetic attachment effects (Sections 7.2.2, 7.3.2 and 7.4.2). We have also simulated the transient build-up of the solute boundary layer ahead of the solidification front, obtaining a quantitative agreement between the phase-field simulations and the evolution of the theoretical profiles (Sections 7.2.3). As shown in Sections 7.2.4 (one-sided

model) and 7.4.3 (symmetric model), quantitative agreement is also obtained for the transient growth rate of the morphological deformations of the advancing front. The results obtained in this part have been reported in the references [Benítez03b, González-Cinca04].

- In the second part of the numerical results, we have focused in the amplification of the initial fluctuations during the solute redistribution transient. As explained in Section 8.2, we have observed that the initial wavelength is selected in very early stages, not following the Mullins-Sekerka prediction and thus confirming the Warren and Langer's theory. We have determined the crossover time at which the morphological deformations of the interface become non-linear, and a good quantitative agreement has been obtained when comparing with the Warren-Langer theory of noise amplification. These studies have been performed in both symmetric (liquid crystal) and one-sided (organic alloy) systems, and are presented in the references [Benítez04b, Benítez04a].

- The third section of the computational results is described in Section 8.3 and concerns to the study of the non-linear coarsening stages in directional solidification. We have studied two different organic substances in different regimes of the pulling velocity. These phase-field simulations are carried out until the system reaches a well defined pattern-forming cellular structure. The dynamical evolution of the primary spacing of the cellular patter has been studied by means of spectral techniques which allow to determine the main primary spacing between the cells. We have found a reasonably good agreement with the equivalent experiments reported in the literature, and conclude that the phase-field approach is a suitable tool for predicting microstructure formation in material processing. Additionally, we have observed in the simulations two of the most important spacing adjustment mechanisms of the cellular front, i.e. cell creation by tip-splitting and cell elimination by cellular overgrowth. We have also observed the period-doubling instability which seems to be one of the basic mechanisms in the wavelength selection of the interfacial pattern.

In all these previous situations, we have the possibility of including anisotropy, kinetic effects and fluctuations from the thermophysical parameters of the solidification process. Moreover, we have used different phase-field formulations for

- One-sided systems in the constant gap approximation.
- One-sided systems with normal miscibility gap.
- Symmetric systems in the constant gap approximation.
- Symmetric systems with normal miscibility gap,

using each model to perform simulations of the corresponding physical systems in each case.

9.2 Work in progress

We are currently working in several interesting problems which have been already started during the realization of this thesis. Some of them are in a rather advanced situation, and others will still require to dedicate more efforts. The main work in progress can be structured as follows:

- Extension of the stochastic phase-field limit to one-sided models. We have already done this calculation, and the result is essentially the same to the one for the symmetric case. Some technical details, however, still need to be refined before the complete derivation could be submitted for publication.

- A complete understanding of the relation between the higher order corrections in the deterministic (kinetic effect) and fluctuating (interfacial noise) terms in the Gibbs-Thomson equation. At second order, the classical sharp-interface limit presents a second-order finite thickness correction which results in an effective increase of the interface kinetic mobility. In order to satisfy the fluctuation-dissipation theorem, an increment in the kinetic attachment must result in an increase of the interfacial fluctuations. However, the corresponding finite ε fluctuating correction might not appear at the same order in the asymptotic expansion, and a higher-order expansion might be required.

- Phase-field simulations of the non-linear selection of the dendritic spacing. Comparison with experiments and importance of the kinetic and surface tension anisotropies.

- Systematic studies of the nature of the planar-cellular bifurcation. This is the first bifurcation which suffers the solidification front, and has been extensively studied by some authors from both theoretical [Wollkind70, Caroli82, Liu94] and experimental [deCheveigné85, deCheveigné86, Eshelman87] points of view. It is already clear that in many situations this bifurcation is subcritical, i.e., presents a hysteretic behavior when crossing the critical velocity by increasing or decreasing the pulling velocity. Under some circumstances (different values of the segregation constant, different bulk sample concentrations), however, it is theoretically predicted that the nature of the bifurcation can be changed and present a normal supercritical behavior. In a subcritical scenario, the cellular pattern appears suddenly with a certain finite amplitude above the critical point, and the amplitude of the pattern can not be assumed to be proportional to the distance from the instability threshold. As a consequence, the subcritical nature of the transition makes it difficult to give a theoretical description of the system in terms of amplitude equations, and requires some special analytical techniques.

- Study the history-dependent character of the pattern selection during the non-linear coarsening regime. For a given set of experimental and substance parameters, the system does not select a definite wavelength [Eshelman88a,

Seetharaman88, Warren90, Losert96]. Instead, the selection process depends on the history of actions which has suffered the front. In this third part, the front is to a sequence of actions before imposing the final pulling velocity. As it can be observed, the final wavelength selected by the system is different depending on the sequence for each experiment.

- Controlled numerical experiments of the period-doubling instability predicted by Warren and Langer [Warren90] and observed experimentally by Losert *et al.* [Losert96].

9.3 Perspectives

Interfacial pattern formation is a very active topic in which there are always new interesting problems. In particular, the study of microstructure formation in solidification is a highly active area of research. There are some interesting problems concerning the effect of fluctuations in the apparition of microstructures, and some of them might be solved by using our hybrid sharp-interface projection. As an example, some of the interesting problems are the following:

- The study of sidebranching structures in directional solidification. In a dendritic array structure, the shape and growth of each dendrite is dynamically selected by a non-steady process. Although the conditions under which the sidebranches appear have already been studied, the origin itself of these perturbations is not completely understood.

- 3D simulations of the wavelength selection problem in dendritic directional solidification. As the power of computers is continously increasing, 3D phase-field simulations will be soon performed without much computational effort.

- Influence of the experimental and external fluctuations in the wavelength selection of the final cellular or dendritic pattern. This would give an explanation of the discrepancies observed between experiments and theory. As experimentalists affirm, there some uncontrolled experimental variables which might induce some perturbations to the advance of the solidification front.

Finally, the method could be applied to phase-field formulations of other interesting problems, not related to solidification, to study the effects of internal and/or external fluctuations, such as crack propagation, biological membranes, etc.

Appendix A

Substance and experimental parameters

A.1 Parameters for pure substances

The Gibbs-Thompson equation reads

$$u^{int} = \frac{T^{int} - T_M}{(L_v/c_v)} = -\tilde{d}_0^T \tilde{\kappa} - \tilde{\beta}^T \tilde{v}_n, \tag{A.1}$$

where

$$\tilde{d}_0^T = \frac{\tilde{\sigma} T_M c_v}{L_v^2}, \tag{A.2}$$

$$\tilde{\beta}^T = \frac{c_v}{\tilde{\mu} L_v}. \tag{A.3}$$

The physical parameters relevant for the solidification of pure substances are collected in Table A.1.

A.2 Parameters for dilute alloys

We remind here the Gibbs-Thompson equation

$$u^{int} = \frac{c^{int} - c_\infty}{\Delta c_0} = 1 - \frac{1}{\tilde{l}_T}\tilde{\xi} - \tilde{\hat{d}}_0 \tilde{\kappa} - \tilde{\hat{\beta}} \tilde{v}_n, \tag{A.4}$$

where $\Delta c_0 = c_L^0 - c_S^0$, $\tilde{\hat{d}}_0 = \tilde{\sigma} T_M / L_v m_L \Delta c_0$, $\tilde{\hat{\beta}} = 1/(\tilde{\mu} m_L \Delta c_0)$ and $\tilde{l}_T = m_L \Delta c_0 / \tilde{G}$. The physical parameters relevant for some one-sided and symmetric alloy systems are collected in the next tables.

Parameter	**Units**	**Symbol**	**SCN**	**Al**
Melting temperature	K	T_M	331.23	933.6
Density	Kg/m^3	ρ	9.7×10^2	2.55×10^3
Specific heat density	J/Km^3	$c_v = \rho \cdot c_m$	2×10^6	2.92×10^6
Thermal conductivity	J/Ksm	$\tilde{\kappa}_T$	0.22	210
Thermal diffusivity	m^2/s	$\tilde{D}_T$	1.11×10^{-7}	7×10^{-5}
Latent heat density	J/m^3	L_v	4.6×10^7	9.5×10^8
Interfacial free energy	J/m^2	$\tilde{\sigma}$	9×10^{-3}	9.3×10^{-2}
Capillary length	m	$\tilde{d}_0^T$	2.81×10^{-9}	2.74×10^{-10}
Interfacial mobility	m/sK	$\tilde{\mu}$	10^{-2}	4.3
Kinetic coefficient	s/m	$\tilde{\beta}^T$	4.3	6.95×10^{-4}

Table A.1: Physical parameters for the pure SCN and Al from [Kurz85]

A.2.1 One-sided systems: Organic alloys

Parameter	**Units**	**Symbol**	**SCN-ACE**	**SCN-C152**	**CBr_4-C_2Cl_6**
Melting temperature	K	T_M	331.24	331.24	365.5
Partition coefficient		k	0.1	0.05	0.75
Density	g/m^3	ρ	1.016×10^6	1.016×10^6	3×10^6
Liquidus slope	K/mol	m_L	202.77	543	81
Molecular weight	g	Z	80.09-58	80.09-257	336-237
Solutal diffusivity	m^2/s	$\tilde{D}_L$	1.27×10^{-9}	4.5×10^{-10}	5×10^{-10}
Latent heat density	J/m^3	L_v	4.6×10^7	4.6×10^7	2.95×10^7
Interfacial free energy	J/m^2	$\tilde{\sigma}$	8.95×10^{-3}	8.95×10^{-3}	6.6×10^{-3}
Interfacial mobility	m/s K	$\hat{\tilde{\mu}}$	10^{-2}	4.3	2.24×10^{-4}
Kinetic coefficient	s/m	$\tilde{\beta}$	4.3	6.95×10^{-4}	2.09×10^3

Table A.2: Substance parameters for three organic alloys. The values have been obtained from the references [Somboonsuk84, Warren90] (SCN-ACE), [Losert98a, Losert98b] (SCN-C152) and [Akamatsu98, Faivre92, Akamatsu97] (CBr_4-C_2Cl_6).

A.2.2 Symmetric systems: Liquid crystals

Parameter	**Symbol**	**Value**	**units**
Segregation Constant	k	0.9	dimensionless
liquidus slope	m_L	88.46	K/mol
Melting temperature	T_M	313.5	K
Surface tension	$\tilde{\sigma}$	2.2×10^{-4}	J/m^2
interface mobility	$\tilde{\mu}$	10^{-4}	m/Ks
Diffusion constant	$\tilde{D}_L$	4×10^{-10}	m^2/s
Latent heat	L_v	2.2×10^6	J/m^3
Specific heat	c_v	5×10^6	J/Km^3
Molecular weight	Z	291.44	g
density	ρ	10^6	g/m^3

Table A.3: Substance parameters for the 8CB liquid crystal obtained from Refs. [Oswald87, Simon88, Figueiredo96]

Appendix B

Differential operators in 3D curvilinear coordinates

In this appendix, we give the expressions of the most common differential operators written in the curvilinear coordinates system introduced in Chapter 6. For a further information about the derivation of the relations presented in this chapter, we refer to Refs. [Fife95, Folch99]. The change from Cartesian (x,y,z) to curvilinear (r,s_1,s_2) coordinates is defined by the conversion factors

$$h_1 = \left|\frac{\partial \mathbf{r}}{\partial r}\right| = 1, \tag{B.1}$$

$$h_2 = \left|\frac{\partial \mathbf{r}}{\partial s_1}\right| = 1 + r\kappa_1, \tag{B.2}$$

$$h_3 = \left|\frac{\partial \mathbf{r}}{\partial s_2}\right| = 1 + r\kappa_2. \tag{B.3}$$

These factors will be used in this section to write down the differential operators in the curvilinear coordinate system introduced in Section 6.3.2. These operators will be written in both the inner and outer regions of the matching asymptotic analysis introduced in Capter 6.

B.1 Outer Region

We next write the time derivatives and space differential operators in the outer region written in curvilinear coordinates.

B.1.1 Partial time derivative

The partial derivative operator can be written as

$$\partial_t = \frac{d}{dt} + (\partial_t r)\partial_r + (\partial_t s_1)\partial_{s_1} + (\partial_t s_2)\partial_{s_2}, \tag{B.4}$$

where the functions $\partial_t r$, $\partial_t s_1$ and $\partial_t s_2$ are given by

$$\partial_t r = -v_r \text{ (radial velocity)} \tag{B.5}$$

$$\partial_t s_1 = -v_{1t} = -\frac{r v_{s_1}}{1 + r\kappa_1} \text{ (tangential velocity along } s_1) \tag{B.6}$$

$$\partial_t s_2 = -v_{2t} = -\frac{r v_{s_2}}{1 + r\kappa_2} \text{ (tangential velocity along } s_2). \tag{B.7}$$

B.1.2 Space differential operators

Gradient

The gradient, written in curvilinear corrdinates, takes the form

$$\nabla\varphi = \frac{\partial_r \varphi}{h_1}\,\hat{\mathbf{r}} + \frac{\partial_{s_1}\varphi}{h_2}\,\hat{\mathbf{s}}_1 + \frac{\partial_{s_2}\varphi}{h_3}\,\hat{\mathbf{s}}_2 = \partial_r\varphi\,\hat{\mathbf{r}} + \frac{\partial_{s_1}\varphi}{1 + r\kappa_1}\,\hat{\mathbf{s}}_1 + \frac{\partial_{s_2}\varphi}{1 + r\kappa_2}\,\hat{\mathbf{s}}_2 \tag{B.8}$$

Divergence

The divergence of a curvilinear vector $\mathbf{a} = a^r\hat{\mathbf{r}} + a^{s_1}\hat{\mathbf{s}}_1 + a^{s_2}\hat{\mathbf{s}}_2$ is given by

$$\begin{aligned} &\nabla\cdot\mathbf{a} = \frac{1}{h_1 h_2 h_3}\left[\partial_r(h_2 h_3 a^r) + \partial_{s_1}(h_1 h_3 a^{s_1}) + \partial_{s_2}(h_1 h_2 a^{s_2})\right] = \\ &\nabla^2 r\; a^r + \partial_r a^r + \frac{r(a^{s_1}\partial_{s_1}\kappa_2 + a^{s_2}\partial_{s_2}\kappa_1)}{(1 + r\kappa_1)(1 + r\kappa_2)} + \frac{\partial_{s_1} a^{s_1}}{1 + r\kappa_1} + \frac{\partial_{s_2} a^{s_2}}{1 + r\kappa_2}. \end{aligned} \tag{B.9}$$

Laplacian

The Laplacian of a scalar field φ is given by

$$\begin{aligned} &\nabla^2\varphi = \nabla\cdot(\nabla\varphi) = \\ &\frac{1}{h_1 h_2 h_3}\left[\partial_r\left(\frac{h_2 h_3}{h_1}\partial_r\varphi\right) + \partial_{s_1}\left(\frac{h_1 h_3}{h_2}\partial_{s_1}\varphi\right) + \partial_{s_2}\left(\frac{h_1 h_2}{h_3}\partial_{s_2}\varphi\right)\right] = \\ &|\nabla r|^2\partial_r^2 + \nabla^2 r\partial_r + |\nabla s_1|^2\partial_{s_1}^2 + |\nabla s_2|^2\partial_{s_2}^2 + \nabla^2 s_1\partial_{s_1} + \nabla^2 s_2\partial_{s_2}, \end{aligned} \tag{B.10}$$

where the factors $|\nabla r|^2$, $\nabla^2 r$, $|\nabla s_i|^2$, $\nabla^2 s_i$ are given by

$$|\nabla r|^2 = 1 \tag{B.11}$$

$$\nabla^2 r = \frac{\kappa_1(1+r\kappa_2)+\kappa_2(1+r\kappa_1)}{(1+r\kappa_1)(1+r\kappa_2)} \tag{B.12}$$

$$\nabla^2 s_1 = \frac{r\partial_{s_1}\kappa_2}{(1+r\kappa_1)^2(1+r\kappa_2)} - \frac{r\partial_{s_1}\kappa_1}{(1+r\kappa_1)^3} \tag{B.13}$$

$$\nabla^2 s_2 = \frac{r\partial_{s_2}\kappa_1}{(1+r\kappa_2)^2(1+r\kappa_1)} - \frac{r\partial_{s_2}\kappa_2}{(1+r\kappa_2)^3} \tag{B.14}$$

$$|\nabla s_1|^2 = \frac{1}{(1+r\kappa_1)} \tag{B.15}$$

$$|\nabla s_2|^2 = \frac{1}{(1+r\kappa_2)}. \tag{B.16}$$

$$\tag{B.17}$$

B.2 Inner Region

In the inner region, the radial coordinate and time are scaled using the relations

$$\rho = \frac{r}{\varepsilon} \tag{B.18}$$

$$\tau = \frac{t}{\varepsilon}, \tag{B.19}$$

and the change or coordinates is (x,y,z) $\rightarrow$ (ρ,s_1,s_2). Writing the inner differential operators in terms of τ and ρ, we get the conversion relations

$$h_1 = 1 \tag{B.20}$$

$$h_2 = 1+\varepsilon\rho\kappa_1 \tag{B.21}$$

$$h_3 = 1+\varepsilon\rho\kappa_2. \tag{B.22}$$

B.2.1 Partial time derivative

$$\partial_t = \frac{1}{\varepsilon}\partial_\tau = \frac{1}{\varepsilon}\frac{d}{d\tau} + \frac{\partial_\tau\rho}{\varepsilon}\partial_\rho + \frac{1}{\varepsilon}\partial_\tau s_1\partial_{s_1} + \frac{1}{\varepsilon}\partial_\tau s_2\partial_{s_2}, \tag{B.23}$$

where the pre-factors are now given by

$$\partial_\tau\rho = \partial_t r = -v_r \tag{B.24}$$

$$\partial_\tau s_1 = \varepsilon\partial_t s_1 = -\varepsilon v_{1t} = -\frac{\varepsilon^2\rho v_{s_1}}{1+\varepsilon\rho\kappa_1} \approx -\varepsilon^2\rho v_{s_1} + O(\varepsilon^3) \tag{B.25}$$

$$\partial_\tau s_2 = \varepsilon\partial_t s_2 = -\varepsilon v_{2t} = -\frac{\varepsilon^2\rho v_{s_2}}{1+\varepsilon\rho\kappa_2} \approx -\varepsilon^2\rho v_{s_2} + O(\varepsilon^3) \tag{B.26}$$

As noted in reference Ref. [Elder01], the tangential velocity v_t is at least of order ε, which is consistent with the requirement of a vanishing value for $\varepsilon = 0$.

B.2.2 Space differential operators

Gradient

$$\begin{aligned}\nabla\varphi = \frac{\partial_\rho\varphi}{\varepsilon h_1}\,\hat{\rho} + \frac{\partial_{s_1}\varphi}{h_2}\,\hat{\mathbf{s}}_1 + \frac{\partial_{s_2}\varphi}{h_3}\,\hat{\mathbf{s}}_2 = \\ \frac{1}{\varepsilon}\partial_\rho\varphi\,\hat{\mathbf{r}} + \frac{\partial_{s_1}\varphi}{1+\varepsilon\rho\kappa_1}\,\hat{\mathbf{s}}_1 + \frac{\partial_{s_2}\varphi}{1+\varepsilon\rho\kappa_2}\,\hat{\mathbf{s}}_2\end{aligned} \tag{B.27}$$

Divergence

$\mathbf{a} = a^\rho\hat{\rho} + a^{s_1}\hat{\mathbf{s}}_1 + a^{s_2}\hat{\mathbf{s}}_2$

$$\begin{aligned}\nabla\cdot\mathbf{a} = \frac{1}{h_1h_2h_3}\left[\frac{1}{\varepsilon}\partial_\rho(h_2h_3a^r) + \partial_{s_1}(h_1h_3a^{s_1}) + \partial_{s_2}(h_1h_2a^{s_2})\right] = \\ \nabla^2 r\;a^\rho + \frac{1}{\varepsilon}\partial_\rho a^\rho + \frac{\varepsilon\rho(a^{s_1}\partial_{s_1}\kappa_2 + a^{s_2}\partial_{s_2}\kappa_1)}{(1+\varepsilon\rho\kappa_1)(1+\varepsilon\rho\kappa_2)} + \frac{\partial_{s_1}a^{s_1}}{1+\varepsilon\rho\kappa_1} + \frac{\partial_{s_2}a^{s_2}}{1+\varepsilon\rho\kappa_2}\end{aligned} \tag{B.28}$$

Laplacian

$$\begin{aligned}&\nabla^2\varphi = \nabla\cdot(\nabla\varphi) = \\ &\frac{1}{h_1h_2h_3}\left[\frac{1}{\varepsilon}\partial_\rho(\frac{h_2h_3}{\varepsilon h_1}\partial_\rho\varphi) + \partial_{s_1}(\frac{h_1h_3}{h_2}\partial_{s_1}\varphi) + \partial_{s_2}(\frac{h_1h_2}{h_3}\partial_{s_2}\varphi)\right] = \\ &|\nabla r|^2\frac{1}{\varepsilon^2}\partial_\rho^2 + \nabla^2 r\frac{1}{\varepsilon}\partial_\rho + |\nabla s_1|^2\partial_{s_1}^2 + |\nabla s_2|^2\partial_{s_2}^2 + \nabla^2 s_1\partial_{s_1} + \nabla^2 s_2\partial_{s_2}.\end{aligned} \tag{B.29}$$

The factors $|\nabla r|^2$, $\nabla^2 r$, $|\nabla s_i|^2$, $\nabla^2 s_i$ can be expanded for $\varepsilon \ll 1$ up to second order to obtain

$$|\nabla r|^2 = 1 \tag{B.30}$$

$$\begin{aligned}\nabla^2 r &= \frac{\kappa_1(1+\varepsilon\rho\kappa_2)+\kappa_2(1+\varepsilon\rho\kappa_1)}{(1+\varepsilon\rho\kappa_1)(1+\varepsilon\rho\kappa_2)} \approx \\ &\kappa_1+\kappa_2-\rho(\kappa_1^2+\kappa_2^2)\varepsilon+\rho^2(\kappa_1^3+\kappa_2^3)\varepsilon^2+O(\varepsilon^3)\end{aligned} \tag{B.31}$$

$$\begin{aligned}\nabla^2 s_1 &= \frac{\varepsilon\rho\partial_{s_1}\kappa_2}{(1+\varepsilon\rho\kappa_1)^2(1+\varepsilon\rho\kappa_2)} - \frac{\varepsilon\rho\partial_{s_1}\kappa_1}{(1+\varepsilon\rho\kappa_1)^3} \approx \\ &\rho(\partial_{s_1}\kappa_2-\partial_{s_1}\kappa_1)\varepsilon+\rho^2[2\kappa_1\partial_{s_1}\kappa_2+\kappa_2\partial_{s_1}\kappa_2-3\kappa_1\partial_{s_1}\kappa_1]\varepsilon^2+O(\varepsilon^3)\end{aligned} \tag{B.32}$$

$$\begin{aligned}\nabla^2 s_2 &= \frac{\varepsilon\rho\partial_{s_2}\kappa_1}{(1+\varepsilon\rho\kappa_2)^2(1+\varepsilon\rho\kappa_1)} - \frac{\varepsilon\rho\partial_{s_2}\kappa_2}{(1+\varepsilon\rho\kappa_2)^3} \approx \\ &\rho(\partial_{s_2}\kappa_1-\partial_{s_2}\kappa_2)\varepsilon+\rho^2[2\kappa_2\partial_{s_2}\kappa_1+\kappa_1\partial_{s_2}\kappa_1-3\kappa_2\partial_{s_2}\kappa_2]\varepsilon^2+O(\varepsilon^3)\end{aligned} \tag{B.33}$$

$$|\nabla s_1|^2 = \frac{1}{(1+\varepsilon\rho\kappa_1)} \approx 1-2\rho\kappa_1\varepsilon+3\rho^2\kappa_1^2\varepsilon^2+O(\varepsilon^3) \tag{B.34}$$

$$|\nabla s_2|^2 = \frac{1}{(1+\varepsilon\rho\kappa_2)} \approx 1-2\rho\kappa_2\varepsilon+3\rho^2\kappa_2^2\varepsilon^2+O(\varepsilon^3). \tag{B.35}$$

Appendix C

Parameter definitions and notation

C.1 Thermodynamic magnitudes

G	Total Gibbs' free energy
G_v	Gibbs' free energy per unit volume
g	Molar Gibbs' free energy
g_v	Molar Gibbs' free energy density
S, H	Total entropy, total enthalpy
S_v, H_v	entropy and enthalpy per unit volume
s, h	Molar entropy and enthalpy
L	Latent heat
L_m	Molar latent heat
L_v	Latent heat per unit volume
c_p	Specific heat
c_v	Specific heat per unit volume
W	Work
Q	Heat
T	Temperature

P	Pressure
Ω	Probability
v_m	Molar volume
Z	Molecular weight
ρ	Density
N_0	Avogadro's number
k_B	Boltzmann's constant
R	Gas constant
N_A, N_B	Number of A,B particles
n_A, n_B	Number of A,B moles
c, x	Solute molar fraction
$\tilde{c}$	Solute concentration per unit volume
k	Segregation constant
m_L	Absolute value of the liquidus slope (molar)
$\tilde{m}_L$	Absolute value of the liquidus slope (volume)
T_M	Melting temperature
$\tilde{\mu}$	Interface mobility

C.2 Solidification parameters

$\tilde{D}_\alpha$	Solute diffusivity at the phase α
$\tilde{\kappa}_\alpha$	Thermal conductivity at the phase α
$\tilde{D}_\alpha^T$	Thermal diffusivity at the phase α
$\tilde{l}$	Diffusion length
$\tilde{\gamma}$	Diffusion time
$\tilde{G}$	External temperature gradient
$\tilde{l}_T$	Thermal length
$\tilde{\kappa}$	Interface curvature
$\tilde{v}_p$	Pulling velocity
$\tilde{\beta}$	Kinetic coefficient
$\tilde{\beta}^T$	Reduced thermal kinetic coefficient
$\hat{\tilde{\beta}}$	Reduced solutal kinetic coefficient
$\tilde{d}_0$	Capillary length
$\tilde{d}_0^T$	Reduced thermal capillary length
$\tilde{d}_0^c$	Thermal capillary length
$\hat{\tilde{d}}_0$	Reduced chemical capillary length

C.3 Physical variables

$\tilde{\mathbf{r}}$	Position in the sample frame
$\tilde{\mathbf{r}}_g$	Position in the gradient frame
$\tilde{v}$	Front velocity in the sample
$\tilde{v}_g$	Front velocity in the gradient frame
$\tilde{\rho}$	x,y plane position in the sample frame
$\tilde{t}$	Time
$\tilde{\xi}$	Front position in the sample frame
p	Space-time point
x	x,y space-point
$\tilde{\mathbf{k}}$	Wave-vector
$\tilde{\xi}_k$	Fourier transform of the interface position
$\tilde{\omega}$	Growth rate
$\tilde{\Gamma}$, S	Power spectrum

List of Figures

List of Tables

Bibliography

[Akamatsu97] S. Akamatsu and T. Ihle, *Phys. Rev. E*, **56**(4), 4479–4485 (1997).

[Akamatsu98] S. Akamatsu and G. Faivre, *Phys. Rev. E*, **58**(3), 1–14 (1998).

[Almgren99] R. F. Almgren, *SIAM J. Appl. Math.*, **59**, 2086 (1999).

[Amar88] M. B. Amar and B. Moussallam, *Phys. Rev. Lett.*, **60**(4), 317–320 (1988).

[Amar93] M. B. Amar and E. Brener, *Phys. Rev. Lett.*, **71**, 589 (1993).

[Aranson00] I. S. Aranson, V. A. Kalatsky and V. M. Vinokur, *Phys. Rev. Lett.*, **85**, 118–121 (2000).

[Aranson02] I. Aranson and L. Kramer, *The world of the complex ginzburg landau equation*, *Rev. Mod. Phys.*, **74**, 99–143 (2002).

[Aziz88] M. J. Aziz and T. Kaplan, *Acta Metall.*, **36**(8) (1988).

[Aziz94] M. Aziz and W. J. Boettinger, *Acta Metall. Mater.*, **42**(2), 527–537 (1994).

[Aziz96] M. Aziz, *Metall. and Mater. Trans. A*, **27A**, 671–686 (1996).

[Barber87] M. Barber, A. Barbieri and J. Langer, *Phys. Rev. A*, **36**(7), 3340–3349 (1987).

[Ben-Jacob84] E. Ben-Jacob, N. Goldenfeld, B. Kotliar and J. Langer, *Phys. Rev. Lett.*, **53**, 2110 (1984).

[Bender99] C. Bender and S. Orszag, *Advanced Mathematical Methods for Scientists and Engineers* (Springer, 1999).

[Benítez03a] R. Benítez and N. Goldenfeld, *Hybrid quasi-monte-carlo method for a solidification phase-field model* (2003), in preparation.

[Benítez03b] R. Benítez and L. Ramírez-Piscina, *Interface and transport dynamics*, volume 32 of *Lecture Notes in Computational Science and Engineering*, pp. 160–164 (Springer, 2003).

[Benítez04a] R. Benítez and L. Ramírez-Piscina, in Z. Gingl, J. Sancho, L. Schimansky-Geier and J. Kertesz, editors, *Noise in complex systems and stochastic dynamics II*, volume 5471 of *SPIE Proceedings*, pp. 58–67 (The International Society for Optical Engineering, 2004).

[Benítez04b] R. Benítez and L. Ramírez-Piscina, *Fluct. Noise Lett.*, **4**(3), L505–L510 (2004).

[Benítez04c] R. Benítez and L. Ramírez-Piscina, *Sharp-interface projection of a fluctuating phase-field model* (2004), submitted to Phys. Rev. E.

[Biben03] T. Biben and C. Misbah, *Phys. Rev. E*, **67**, 031908 (2003).

[Boettinger00] W. Boettinger, S. Coriell, A. Greer, A. Karma, W. Kurz, M.Rappaz and R. Trivedi, *Acta Mater.*, **48**, 43–70 (2000).

[Bragard02] J. Bragard, A. Karma, Y. H. Lee and M. Plapp, *Interface Science*, **10**, 121–136 (2002).

[Braun97] R. J. Braun and B. T. Murray, *J. Crys. Growth*, **174**, 41–53 (1997).

[Büeler98] L. Büeler and S. Davis, *J. Crys. Growth*, **186**, 629–647 (1998).

[Buka96] A. Buka and L. Kramer, editors, *Pattern formation in liquid crystals* (Springer, 1996).

[Busse84] F. Busse and E. Bolton, *J. Fluid Mech.*, **146**, 115 (1984).

[Caginalp84] G. Caginalp, *Applications of field theory to statistical mechanics*, pp. 216–226, number 216 in Lecture Notes in Physics (Springer Berlin, 1984).

[Caginalp86a] G. Caginalp, *Arch. Rational Mech. Anal.*, (92), 205 (1986).

[Caginalp86b] G. Caginalp, *Annals of Physics*, **172**, 136–155 (1986).

[Caginalp86c] G. Caginalp and P. Fife, *Phys. Rev. B*, **33**(11), 7792–7794 (1986).

[Caginalp86d] G. Caginalp and P. Fife, *Phys. Rev. B (Rapid Communications)*, **34**(7), 4940–4943 (1986).

[Caginalp88] G. Caginalp and P. Fife, *SIAM J. Appl. Math.*, **48**, 506 (1988).

[Caginalp89] G. Caginalp, *Phys. Rev. A*, **39**(11), 5887–5896 (1989).

[Caginalp90] G. Caginalp, *IMA Journal of Applied Mathematics*, **44**, 77–94 (1990).

[Cahn58] J. W. Cahn and J. E. Hilliard, *J. Chem. Phys.*, **28**(2), 258–267 (1958).

[Carlslaw50] H. Carlslaw and J. Jaeger, *Heat Conduction in Solids*, chapter IX (Oxford University Press, 1950).

[Caroli82] B. Caroli, C. Caroli and B. Roulet, *J. Phys. Paris*, (43), 1767 (1982).

[Caroli86a] B. Caroli, C. Caroli and B. Roulet, *J. Crys. Growth*, **76**, 31–49 (1986).

[Caroli86b] B. Caroli, C. Caroli, B. Roulet and J. Langer, *Phys. Rev. A*, **33**(1), 442–452 (1986).

[Caroli90] B. Caroli, C. Caroli and B. Roulet, *J. Phys. France*, **51**, 1865–1876 (1990).

[Caroli92] B. Caroli, C. Caroli and B. Roulet, *Solids far from equilibrium*, chapter 2, pp. 155–296 (Cambridge University Press, 1992).

[Caroli93] B. Caroli, C. Caroli and L. Ramírez-Psicina, *J. Crys. Growth*, **132**, 377–388 (1993).

[Cherepanova76] T. A. Cherepanova, *Dokl. Akad. Nauk SSSR*, **226**, 1066–1068 (1976), [Sov. Phys. Dokl. v21(2),109(1976)].

[Chernov04] A. A. Chernov, *J. Crys. Growth*, **264**, 499–518 (2004).

[Collins85] J. Collins and H. Levine, *Phys. Rev. B*, **31**(9), 6119–6122 (1985).

[Crank84] J. Crank, *Free and moving boundary problems* (Oxford Science Publications, 1984).

[Cross93] M. Cross and P. Hohenberg, *Pattern formation outside of equilibrium*, *Rev. Mod. Phys.*, **65**(3), 851–1112 (1993).

[Davis84] S. Davis, U. Mueller and C. Dietsche, *J. Fluid Mech.*, **144**, 133–151 (1984).

[Davis01] S. Davis, *Theory of soldification*, Cambridge Mongraphs on Mechanics (Cambridge University Press, 2001).

[deCheveigné85] S. de Cheveigné, C. Guthmann and M.-M. Lebrun, *J. Crys. Growth*, **73**, 242–244 (1985).

[deCheveigné86] S. de Cheveigné, C. Guthmann and M.-M. Lebrun, *J. Physique*, **47**, 2095–2103 (1986).

[Dee83] G. Dee and R. Mathur, *Phys. Rev. B*, **27**(12) (1983).

[Ding96] G. Ding, W. Huang, X. Huang, X. Lin and Y. Zhou, *Acta Mater.*, **44**(9), 3705–3709 (1996).

[Ding97] G. Ding, W. Huang, X. Lin and Y. Zhou, *J. Crys. Growth*, **177**, 281–288 (1997).

[Dombre87] T. Dombre and V. Hakim, *Phys. Rev. A*, **36**(6), 2811–2817 (1987).

[Drolet00] F. Drolet, K. R. Elder, M. Grant and J. M. Kosterlitz, *Phys. Rev. B*, **61**(6), 6705–6720 (2000).

[Echebarria04] B. Echebarria, R. Folch, A. Karma and M. Plapp, */cond-mat/0404164* (2004).

[Einstein56] A. Einstein, *Investigations on the theory of the Brownian movement* (Dover Publications, Inc., 1956).

[Elder94] K. R. Elder, F. Drolet, J. M. Kosterlitz and M. Grant, *Phys. Rev. Lett.*, **72**, 677 (1994).

[Elder01] K. R. Elder, M. Grant, N. Provatas and J. M. Kosterlitz, *Phys. Rev. E*, **64**, 021604 (2001).

[Eshelman87] M. Eshelman and R.Trivedi, *Acta. Metall.*, **35**(10), 2443–2452 (1987).

[Eshelman88a] M. Eshelman, V. Seetharaman and R. Trivedi, *Acta Metall.*, **36**(4), 1165–1174 (1988).

[Eshelman88b] M. Eshelman, V. Seetharaman and R. Trivedi, *Acta Metall.*, **36**(4), 1175–1185 (1988).

[Eshelman88c] M. Eshelman and R. Trivedi, *Scripta Metallurgica*, **22**, 893–898 (1988).

[Faivre92] G. Faivre and J. Mergy, *Phys. Rev. E*, **46**(2), 963–972 (1992).

[Fermi56] E. Fermi, *Thermodynamics* (Dover Publications Inc., 1956).

[Field85] R. Field and M. Burger, editors, *Oscillations and travelling waves in chemical systems* (Wiley, New York, 1985).

[Fife95] P. C. Fife and O. Penrose, *Electr. Jour. Diff. Eq.*, **1**(16), 1–49 (1995).

[Figueiredo93] J. M. A. Figueiredo, M. B. L. Santos, L. O. Ladeira and O. N. Mesquita, *Phys. Rev. Lett.*, **71**(26), 4397 (1993).

[Figueiredo96] J. M. A. Figueiredo, A. Vidal and O. N. Mesquita, *J. Crys. Growth*, **166**, 222 (1996).

[Fix83] G. Fix, *Phase field methods for free boundary problems*, in A. Fasano and M. Primicerio, editors, *Free boundary problems: Theory and applications*, volume 2 of *Research notes in mathematics*, pp. 580–589 (Pitman, 1983).

[Folch99] R. Folch, J. Casademunt, A. Hernández-Machado and L. Ramírez-Piscina, *Phys. Rev. E*, **60**, 1724 (1999).

[García-Ojalvo99] J. García-Ojalvo and J. M. Sancho, *Noise in spatially extended systems* (Springer-Verlag, 1999).

[Gardiner04] C. Gardiner, *Handbook of stochastic methods*, Springer series in Synergetics (Springer Verlag, 2004), 3rd edition.

[Ginzburg50] V. Ginzburg and L. D. Landau, *Sov. Phys. JETP*, **20**, 1064 (1950).

[Glicksman93] M. Glicksman and S. Marsh, *Fundamentals. Thermodynamics and Kinetics*, volume 1a of *Handbook of Crystal Growth*, pp. 1075–1122 (North-Holland, 1993).

[González-Cinca01] R. González-Cinca, L. Ramírez-Piscina, J. Casademunt and A. Hernández-Machado, *Phys. Rev. E*, **63**, 051602 (2001).

[González-Cinca04] R. González-Cinca, R. Folch, R. Benítez, L. Ramírez-Piscina, J. Casademunt and A. Hernández-Machado, *Phase-field models in interfacial pattern formation out of equilibrium*, in E. Korutcheva and R. Cuerno, editors, *Advances in Condensed Matter and Statistical Mechanics*, pp. 203–236 (Nova Science Publishers, 2004).

[Guckenheimer83] J. Guckenheimer and P. Holmes, *Nonlinear oscilations, dynamical systems, and bifurcations of vector fields*, volume 42 of *Applied Mathematical Sciences* (Springer-Verlag, 1983).

[Guiggiani95] M. Guiggiani, *Comp. Mech.*, **16**, 245–248 (1995).

[Hadamard23] J. Hadamard, *Lectures on Cauchy's problem in linear partial differential equations* (Yale University Press, New Haven, 1923).

[Haken75] H. Haken, *Cooperative phenomena in systems far from equilibrium and in nonphysical systems*, *Rev. Mod. Phys.*, **47**, 67–121 (1975).

[Halperin74] B. Halperin, P. Hohenberg and S. Ma, *Phys. Rev. B*, **10**, 139 (1974).

[Hamina00] M. Hamina, *J. Comp. Appl. Math.*, **115**, 229–243 (2000).

[Han94a] S. Han and R. Trivedi, *Acta Metall. Mater.*, **42**(1), 25–41 (1994).

[Han94b] S. Han and R. Trivedi, *Acta Metall. Mater.*, **42**(1), 25–41 (1994).

[Haug89] P. Haug, *Phys. Rev. A*, **40**(12), 7253–7264 (1989).

[Hohenberg77] P. C. Hohenberg and B. I. Halperin, *Theory of critical phenomena*, *Rev. Mod. Phys.*, **49**, 435 (1977).

[Huang81a] S. Huang and M. Glicksman, *Acta Metall. Mater.*, **29**, 701–716 (1981).

[Huang81b] S. Huang and M. Glicksman, *Acta Metall. Mater.*, **29**, 717–731 (1981).

[Huang93] W. Huang, X. Geng and Y. Zhou, *J. Crys. Growth*, **134**, 105–115 (1993).

[Huang97] W. Huang, Y. Inatomi and K. Kuribayashi, *J. Crys. Growth*, **182**, 212–218 (1997).

[Hunt96] J. Hunt and S.-Z. Lu, *Metal. Mater. Trans. A*, **27A**, 611–623 (1996).

[Hurle93a] D. Hurle, editor, *Fundamentals. Thermodynamics and Kinetics*, volume 1a of *Handbook of Crystal Growth* (North-Holland, 1993).

[Hurle93b] D. Hurle, editor, *Fundamentals. Transport and Stability*, volume 1b of *Handbook of Crystal Growth* (North-Holland, 1993).

[Hurle93c] D. Hurle, E. Jakeman and A. Wheeler, *Phys. Fluids*, **26**, 624–626 (1993).

[Ivantsov47] G. Ivantsov, *Dokl. Akad. Nauk SSSR*, **58**, 567 (1947).

[Jackson65] K. Jackson and J. Hunt, *Acta Metall.*, **13**, 1212 (1965).

[Jackson66a] K. Jackson and J. Hunt, *Trans. Metall. Soc. AIME*, **236**, 843 (1966).

[Jackson66b] K. Jackson and J. Hunt, *Trans. Metall. Soc. AIME*, **236**, 1129 (1966).

[Jackson04] K. Jackson, *J. Crys. Growth*, **264**, 519–529 (2004).

[Karma86] A. Karma, *Phys. Rev. Lett.*, **57**(7), 858–861 (1986).

[Karma90] A. Karma and P. Pelcé, *Phys. Rev. A*, **41**(12), 6741–6748 (1990).

[Karma92] A. Karma and A. Sarkissian, *Phys. Rev. Lett.*, **68**(17), 2616 (1992).

[Karma93a] A. Karma, *Phys. Rev. Lett.*, **70**(22), 3439–3442 (1993).

[Karma93b] A. Karma, *Phys. Rev. Lett.*, **70**, 3439 (1993).

[Karma93c] A. Karma, *Phys. Rev. E*, **48**, 3441 (1993).

[Karma93d] A. Karma and A. Sarkissian, *Phys. Rev. E*, **47**(1), 513 (1993).

[Karma96a] A. Karma and W. Rappel, *Phys. Rev. Lett.*, **77**(19), 4050–4053 (1996).

[Karma96b] A. Karma and W. Rappel, *Phys. Rev. E (Rapid Communications)*, **53**(4), R3017 (1996).

[Karma96c] A. Karma and A. Sarkissian, *Metall. Mater. Trans. A*, **27**, 625–656 (1996).

[Karma97] A. Karma and W. Rappel, *J. Crys. Growth*, **174**, 54–64 (1997).

[Karma98] A. Karma and W. J. Rappel, *Phys. Rev. E*, **57**, 4323 (1998).

[Karma99] A. Karma and W. J. Rappel, *Phys. Rev. E*, **60**(4), 3614–3625 (1999).

[Karma01] A. Karma, *Phys. Rev. Lett.*, **87**, 115701–1 (2001).

[Kassner91a] K. Kassner and C. Misbah, *Phys. Rev. A*, **44**, 6513–6532 (1991).

[Kassner91b] K. Kassner and C. Misbah, *Phys. Rev. A*, **44**, 6533–6543 (1991).

[Kauerauf01a] B. Kauerauf, G. Zimmermann, S. Rex, B. Billia, H. Jamgotchian and J. Hunt, *J. Crys. Growth*, **223**, 277–284 (2001).

[Kauerauf01b] B. Kauerauf, G. Zimmermann, S. Rex, M. Mathes and F. Grote, *J. Crys. Growth*, **223**, 265–276 (2001).

[Kerszberg83a] M. Kerszberg, *Phys. Rev. B*, **27**(6), 3909–3912 (1983).

[Kerszberg83b] M. Kerszberg, *Phys. Rev. B*, **28**(1), 247–254 (1983).

[Kerszberg83c] M. Kerszberg, *Phys. Rev. B*, **27**(11), 6796–6810 (1983).

[Kessler85] D. Kessler, J. Koplik and H. Levine, *Phys. Rev. A*, **31**, 1712 (1985).

[Kessler89a] D. Kessler and H. Levine, *Phys. Rev. A*, **39**(6), 3041–3052 (1989).

[Kessler89b] D. Kessler and H. Levine, *Phys. Rev. A (Brief Reports)*, **39**(6), 3208–3210 (1989).

[Kessler90] D. Kessler and H. Levine, *Phys. Rev. A*, **41**(6), 3197–3205 (1990).

[Kim99] Y. Kim, N. Provatas, N. Goldenfeld and J. Dantzig, *Phys. Rev. E (Rapid communications)*, **59**(3), R2546–R2549 (1999).

[Kim00] Y. Kim, N. Goldenfeld and J. Dantzig, *Phys. Rev. E.*, **62**(2), 2471–2474 (2000).

[Kobayashi93a] R. Kobayashi, *Physica D*, **63**, 410 (1993).

[Kobayashi93b] R. Kobayashi, *Physica D*, **63**, 410 (1993).

[Koch94] A. Koch and H. Meinhardt, *Biological pattern formation: from basic mechanisms to complex structures*, *Rev. Mod. Phys.*, **66**(4), 1481–1507 (1994).

[Kurz81] W. Kurz and D. Fisher, *Acta Metall.*, **29**, 11–20 (1981).

[Kurz85] W. Kurz and D. Fisher, *Fundamentals of solidification* (Trans Tech Publications, 1985).

[Kurze96] D. Kurze, *Phys. Rev. Lett.*, **77**(1), 63–66 (1996).

[Lamé31] G. Lamé and B. Clapeyron, *Ann. Chem. Phys.*, **47**, 250–256 (1831).

[Landau80] L. Landau and E. Lifshitz, *Statistical Physics* (Pergamon, NY, 1980).

[Langer78] J. Langer (1978), unpublished notes.

[Langer80a] J. Langer, *Phys. Rev. Lett.*, **44**, 1023–1026 (1980).

[Langer80b] J. Langer, *Instabilities and pattern formation in crystal growth*, *Rev. Mod. Phys.*, **52**(1), 1–28 (1980).

[Langer86] J. S. Langer, *Directions in condensed matter physics*, chapter 5, pp. 165–176 (World Scientific, 1986).

[Langer87] J. Langer, *Lectures in the theory of pattern formation*, chapter 10, Les Houches Chance and Matter 1986, Session XLVI (Elsevier Science Publishers, 1987).

[Li99] Q. Li and C. Beckermann, *Acta Mater.*, **47**(8), 2345–2356 (1999).

[Liu94] D. Liu, L. Williams and H. Cummins, *Phys. Rev. E*, **50**(6), R4286–R4289 (1994).

[Losert96] W. Losert, B. Shi, H. Cummins and J. Warren, *Phys. Rev. Lett.*, **77**(5), 889–891 (1996).

[Losert98a] W. Losert, B. Q. Shi and H. Z. Cummins, *Proc. Natl. Acad. Sci. USA*, **95**, 431–438 (1998).

[Losert98b] W. Losert, B. Q. Shi and H. Z. Cummins, *Proc. Natl. Acad. Sci. USA*, **95**, 439–442 (1998).

[Losert98c] W. Losert, D. Stillman, H. Cummins, P. Kopczyński, W. Rappel and A. Karma, *Phys. Rev. E*, **58**(6), 7492–7506 (1998).

[Lu92] S. Lu and J. Hunt, *J. Crys. Growth*, **123**, 17–34 (1992).

[Mashaal90] M. Mashaal, M. B. Amar and V. Hakim, *Phys. Rev. A*, **41**(8), 4421–4432 (1990).

[Moloney92] J. Moloney and A. Newell, *Nonlinear optics* (Addison Wesley, Reading, MA, 1992).

[Mullins63] W. Mullins and R. Sekerka, *J. App. Phys.*, **34**(2), 323–329 (1963).

[Murray95] B. Murray, A. Wheeler and M. Glicksman, *J. Crys. Growth*, **154**, 386–400 (1995).

[Murray02] J. Murray, *Mathematical biology I.*, volume 17 of *Interdisciplinary Applied Mathematics* (Springer, 2002), 3rd edition.

[Murray03] J. Murray, *Mathematical biology II*, volume 18 of *Interdisciplinary Applied Mathematics* (Springer, 2003), 3rd edition.

[Niederreiter98] H. Niederreiter, *Monte Carlo and Quasi-MonteCarlo methods 1996*, volume 127 of *Lecture Notes in Statistics* (Springer-Verlag, 1998).

[Niu04] Z. Niu and H. Zhou, *Comp. Struct.*, **82**, 315–323 (2004).

[Nozières91] P. Nozières, *Solids far from equilibrium* (Cambridge University Press, 1991).

[Oswald87] P. Oswald, J. Bechhoefer and A. Libchaber, *Phys. Rev. Lett.*, **58**(22), 2318 (1987).

[Pavlik99] S. G. Pavlik and R. F. Sekerka, *Physica A*, **268**, 283–290 (1999).

[Pavlik00] S. G. Pavlik and R. F. Sekerka, *Physica A*, **277**, 415–431 (2000).

[Penrose90] O. Penrose and P. Fife, *Physica D*, **43**, 44–62 (1990).

[Penrose93] O. Penrose and P. Fife, *Physica D*, **69**, 107–113 (1993).

[Plapp00] M. Plapp and A. Karma, *Phys. Rev. Lett.*, **84**(8), 1740–1743 (2000).

[Pocheau01] A. Pocheau and M. Georgelin, *Eur. Phys. J. B*, **21**, 229–240 (2001).

[Pomeau79] Y. Pomeau and P. Manneville, *J. Phys. Lett.*, **40**, 609 (1979).

[Porter92] D. Porter and K. Easterling, *Phase Transformations in Metals and Alloys* (Chapman & Hall, 1992), 2nd edition.

[Press92] W. H. Press, S. A. Teukolsky, W. T. Vetterling and B. P. Flannery, *Numerical Recipes in FORTRAN* (Cambridge University Press, 1992), 2nd edition.

[Provatas98] N. Provatas, N. Goldenfeld and J. Dantzig, *Phys. Rev. Lett.*, **80**(15), 3308–3311 (1998).

[Qian89] X. Qian, H. Chou, M. Muschol and H. Cummins, *Phys. Rev. B*, **39**(4), 2529–2531 (1989).

[Rios97] C. Rios and R. Caram, *J. Crys. Growth*, **174**, 65–69 (1997).

[Rocco02] A. Rocco, L. Ramírez-Psicina and J. Casademunt, *Phys. Rev. E*, **65**, 056116 (2002).

[Rutter53] J. Rutter and B. Chalmers, *Can. J. Phys.*, **31**, 15 (1953).

[Rytov56] S. M. Rytov, *Dokl. Akad. Nauk SSSR*, **110**, 371 (1956), [Sov. Phys. JETP v2(2),225-235(1956)].

[Seetharaman88] V. Seetharaman, M. Eshelman and R. Trivedi, *Acta Metall.*, **36**(4), 1175–1185 (1988).

[Simon88] A. J. Simon, J. Bechhoefer and A. Libchaber, *Phys. Rev. Lett.*, **61**(22), 2574 (1988).

[Sinha03] A. Sinha, *Physical Metallurgy Handbook* (McGraw-Hill, 2003).

[Somboonsuk84] K. Somboonsuk, J. Mason and R. Trivedi, *Metall. Trans. A*, **15A**, 967–975 (1984).

[Somboonsuk85] K. Somboonsuk and R. Trivedi, *Acta Metall.*, **33**(6), 1051–1060 (1985).

[Stefan91] J. Stefan, *Annalen der Physik und Chemie*, **42**, 269–286 (1891).

[Temkin60] D. Temkin, *Dokl. Akad. Nauk SSSR*, **132**, 1307 (1960).

[Tiller53] W. A. Tiller, K. A. Jackson, J. W. Rutter and B. Chalmers, *Acta Metall.*, **1**, 428–437 (1953).

[Trivedi70] R. Trivedi, *Acta Metall.*, **18**, 287 (1970).

[Trivedi84] R. Trivedi, *Metall. Trans. A*, **15A**, 977–982 (1984).

[Trivedi85] R. Trivedi and K. Somboonsuk, *Acta Metall.*, **33**(6), 1061–1068 (1985).

[Wang93] S. Wang, R. Sekerka, A. Wheeler, B. Murray, S. Coriell, R. Braun and G. McFadden, *Physica D*, **69**(1-2), 189–200 (1993).

[Wang96] S. Wang and R. F. Sekerka, *Phys. Rev. E*, **53**, 3760 (1996).

[Warren90] J. A. Warren and J. S. Langer, *Phys. Rev. A*, **42**(6), 3518–3525 (1990).

[Warren93] J. A. Warren and J. S. Langer, *Phys. Rev. A*, **47**(4), 2702–2712 (1993).

[Warren03] J. A. Warren, R. Kobayashi, A. E. Lobkovsky and W. C. Carter, *Acta Mater.*, **51**, 6035–6058 (2003).

[Weeks91] J. Weeks and W. van Saarloos, *J. Crys. Growth*, **112**, 244–282 (1991).

[Wheeler92a] A. A. Wheeler, W. J. Boettinger and G. B. McFadden, *Phys. Rev. A*, **45**, 7424–7439 (1992).

[Wheeler92b] A. A. Wheeler, W. J. Boettinger and G. B. McFadden, *Phys. Rev. E*, **47**, 1893–1909 (1992).

[Wheeler93] A. A. Wheeler, B. T. Murray and R. J. Schaefer, *Physica D*, **66**, 243–262 (1993).

[Wollkind70] D. Wollkind and L. Segel, *Philos. Trans. R. Soc. A*, **268**, 351 (1970).

[Zemansky81] M. Zemansky and R. Dittman, *Heat and Thermodynamics* (McGraw-Hill, 1981).

Index